2019

Three-dimensional Transient Heat Transfer Characterization of Crossflow Minichannel Heat Exchanger Apparatus

Mohammed Ismail
University of Windsor

Recommended Citation

Ismail, Mohammed, "Three-dimensional Transient Heat Transfer Characterization of Crossflow Minichannel Heat Exchanger Apparatus" (2019). *Electronic Theses and Dissertations*. 7709.
https://scholar.uwindsor.ca/etd/7709

Three-dimensional Transient Heat Transfer Characterization of Crossflow Minichannel Heat Exchanger Apparatus

By

Mohammed Ismail

A Dissertation
Submitted to the Faculty of Graduate Studies
through the Department of Mechanical, Automotive and Materials Engineering
in Partial Fulfillment of the Requirements for
the Degree of Doctor of Philosophy
at the University of Windsor

Windsor, Ontario, Canada

2019

Optimal Three-dimensional Transient Heat Transfer in Crossflow Minichannel Heat Exchanger Apparatus

by

Mohammed Ismail

APPROVED BY:

M. Islam, External Examiner
Ahsanullah University of Science and Technology

A. A. Asfour
Department of Civil & Environmental Engineering

J. Johrendt
Department of Mechanical, Automotive & Materials Engineering

B. Zhou
Department of Mechanical, Automotive & Materials Engineering

A. Fartaj, Advisor
Department of Mechanical, Automotive & Materials Engineering

May 16, 2019

DECLARATION OF CO-AUTHORSHIP / PUBLICATION

I. Co-Authorship Declaration

I hereby declare that this dissertation incorporates the outcome of research undertaken under the supervision of Dr. A. Fartaj, University of Windsor and in collaboration with S. Fotowat and M. Khan. In all cases, I certify that I am the principal author and have had a major role in the preparation and writing of the manuscripts. The key ideas, primary contributions, model designs, numerical simulations, data analyses, interpretation and graphing results were performed by the author. The contributions of the co-authors in the associated journal and conference publications were primarily through the provision of comments on refinement of ideas, discussions on technical issues, and editing of the manuscripts.

I am aware of the University of Windsor Senate Policy on Authorship and I certify that I have properly acknowledged the contribution of other researchers to my dissertation, and have obtained written permission from each of the co-author(s) to include the above material(s) in my dissertation.

I certify that, with the above qualification, this dissertation, and the research to which it refers, is the product of my own work.

II. Declaration of Publications

This dissertation includes the following original papers that have been previously published/submitted for publication in peer-reviewed journals and conference proceedings:

Publication title/full citation	Publication, Copyright status
M. Ismail, S. Fotowat, A. Fartaj, “Numerical simulation of Al_2O_3/automatic transmission fluid and Al_2O_3/water nanofluids in a compact heat exchanger”, Journal of Fluid Flow, Heat and Mass Transfer, 3: 34-43, 2016, doi: 10.11159/jffhmt.2016.005.	Published. Copyright permission included in Appendix A
M. Ismail, S. Fotowat, A. Fartaj, “Transient response of minichannel heat exchanger using Al_2O_3/EG-W nanofluid”, SAE Technical Paper 2016-01-0229, 2016, doi:10.4271/2016-01-0229.	Published. Copyright permission included in Appendix A
M. Ismail, S. Fotowat, A. Fartaj, “Simulation of Al2O3-ATF Nanofluid in a Compact Heat Exchanger”, In Proceedings of the 2nd International Conference on Fluid Flow, Heat and Mass Transfer, Ottawa, Ontario, Canada, 2015, Paper No. 149.	Published. Presented. Authors hold copyright.
M. Ismail, S. Fotowat, A. Fartaj, “Effect of channel size on heat transfer and pressure drop in thin slabs MICHX”, International	Published. Copyright permission

Journal of Mechanical Engineering and Mechatronics, 2: 1, 33-42, 2014, doi: 10.11159/ijmem.2014.004.	included in Appendix A
M. Ismail, S. Fotowat, A. Fartaj, “CFD modeling and validation of a multipass compact heat exchanger”, 23rd Annual Conference of the Computational Fluid Dynamics Society of Canada (CFDSC), June 7-10, 2015, Waterloo, ON, Canada.	Presented. Authors hold copyright.
M. Ismail, S. Fotowat, A. Fartaj (2013), “Uniformity of flow and heat transfer distribution in minichannel heat exchanger slab. A numerical approach”, In Proceedings of IASTED International Conference, Modelling and Simulation, MS 2013, 296-301, Banff, AB, Canada, 2013, DOI: 10.2316/P.2013.802-073.	Published. Presented. Copyright permission included in Appendix A
M. Ismail, S. Fotowat, A. Fartaj (2013), “Effect of Channel Size on Heat Transfer in Thin Slabs”, In Proceedings of the International Conference on Mechanical Engineering and Mechatronics, Toronto, Ontario, Canada, 2013, Paper No. 180.	Published. Presented. Authors hold copyright.
M. Ismail, M. Khan, A. Fartaj, “Transient heat transfer phenomena of crossflow minichannel heat exchanger due to incremental and decremental hot fluid mass flow rates”, International Journal of Thermal Sciences.	To be submitted
M. Ismail, M. Khan, A. Fartaj, “Numerical investigation of enhanced thermal performance of a novel crossflow minichannel heat exchanger”, Numerical Heat Transfer; Part A: Applications.	To be submitted

I certify that I have obtained a written permission from the copyright owner(s) to include the above published material(s) in my dissertation. I certify that the above material describes work completed during my registration as a graduate student at the University of Windsor.

III. General

I declare that, to the best of my knowledge, my dissertation does not infringe upon anyone’s copyright nor violate any proprietary rights and that any ideas, techniques, quotations, or any other material from the work of other people included in my dissertation, published or otherwise, are fully acknowledged in accordance with the standard referencing practices. Furthermore, to the extent that I have included copyrighted material that surpasses the bounds of fair dealing within the meaning of the Canada Copyright Act, I certify that I have obtained a written permission from the copyright owner(s) to include such material(s) in my dissertation.

I declare that this is a true copy of my dissertation, including any final revisions, as approved by my dissertation committee and the Graduate Studies office, and that this dissertation has not been submitted for a higher degree to any other University or Institution.

ABSTRACT

Heat exchangers are the key components in automotive, residential and industrial applications. These are employed in vehicle thermal management systems, thermal regulation process as well as heating, ventilation, air conditioning and refrigeration systems. It is important to assess their performance and behavior in transient situation, especially when a sudden change in their operating conditions takes place.

This research advances steady state and transient heat transfer in minichannel heat exchanger (MICHX) with the aim of improving heat transfer and exploring transient response. This study uses three-dimensional (3D) computational models to resolve flow and heat transfer in air-to-liquid crossflow MICHX. A finite volume method based ANSYS FLUENT computational fluid dynamics (CFD) code is used to perform the numerical simulations. Models are verified and validated with both the steady state and the transient experimental data and results available in scientific literatures to represent the real world applications. Very good agreements in numerical predictions have been achieved for all models.

The current research consists of five stages. In Stage I, the fundamental laminar heat transfer and flow features are focused and modeled in MICHX and conventional flat tube heat exchanger (FTHX) as a benchmark. For a given Reynolds number within the laminar flow regime, MICHX displays significant enhancement of heat transfer coefficient than that of FTHX. In Stage II, computations of 3D flow and heat transfer are carried out in a 5-pass 3-loop air-to-liquid crossflow MICHX, which is equivalent in size of an automotive radiator. The distributions of fluid flow, liquid-side temperature drop, and heat transfer rate are predicted fairly uniform in each loop of the MICHX. The numerical prediction suggests that a single-loop can be applied to represent the multi-loop for further investigations on similar crossflow MICHX. In Stage III, Aluminum oxide ($\mathrm{Al_2O_3}$) nanoparticles are incorporated with base fluids to improve heat transfer. Significantly improved thermal performance is predicted for inclusion of the Al_2O_3 nanoparticles. In Stage IV, two distinct heat exchanger modules, sequential and simultaneous, are modeled to improve their thermal performance. For an identical module size, such as similar frontal area and volume, the simultaneous module provides superior thermal performance compared to the conventional sequential module as a benchmark.

Finally, in Stage V, transient behaviour of crossflow MICHX for perturbations in hot fluid inlet temperature and mass flow rate are investigated. Faster response time has been observed for higher step variations. After considering the step variations and detailed regression analyses with important variables and parameters, new correlations for transient temperature and Nusselt number have been developed in the current study.

The simultaneous module of MICHX can significantly reduce the energy requirements in automotive applications. The correlations for transient heat transfer can be useful tools for the engineers to design control devices in transient situations.

DEDICATION

Dedicated to my beloved

father the late Md Abdul Jalil,

mother Zohara Khatoon,

wife Shamima Akhter, and

sons Aljami Ismail and Miraj Ismail

who are the source of my inspiration and

sacrificed a lot for my dream to come true

ACKNOWLEDGEMENTS

First and above all, the author is greatly thankful to the Almighty, the Creator, and the Sustainer for giving him the opportunity to move forward to the end of his PhD degree.

The author would like to express his sincere appreciation and gratitude to his advisor Dr. Amir Fartaj for his sincere guidance, distinctive supports, and judicious suggestions throughout the research. His intellectual academic input, expert supervision, and continuous inspiration led the author to a successful completion of the research.

The author likes to deeply acknowledge his advisory committee members, Dr. Biao (Bill) Zhou, Dr. Jennifer Johrendt, and Dr. Abdul-Fattah Asfour for their valuable suggestions and comments at the various stages of the research. The author thankfully recognize the generous dedication of their time in reviewing the dissertation write-up.

The author also thankfully recognizes Dr. Ronald Barron for providing technical guidance through his applied computational fluid dynamics course as well as various projects that founded the basis for this research.

The author offers his intense acknowledgement to Angela Haskell for providing friendly secretarial supports and Mark Gryn for software and technical supports. Thanks also go to Andy Jenner for providing technical services associated with key controls.

The author is thankful to the Natural Sciences and Engineering Research Council of Canada (NSERC) for providing discovery grant (DG) for conducting the research work. The author also gratefully acknowledges the Ontario Graduate Scholarship (OGS), University of Windsor Postgraduate Tuition Scholarship, and Doctoral Entrance

Scholarship (Canadian). Thanks also go to the department of Mechanical, Automotive, and Materials Engineering at University of Windsor for providing the financial supports in the form of Graduate and Teaching Assistantships.

Sincere appreciation and intense acknowledgement to Dr. M. Khan, Dr. F. Siddiqui, Dr. S. Bhowmick, Shahram Fotowat and Serena Askar for providing the author wonderful companies, inspiration, and supports.

Last but not least, the author extends his sincere gratitude to his wife Shamima Akhter and sons Aljami Ismail and Miraj Ismail for their inspiration, patience, and caring throughout the period of this research to make his PhD dream come true.

TABLE OF CONTENTS

LIST OF TABLES

LIST OF FIGURES

LIST OF APPENDICES

NOMENCLATURE / ABBREVIATIONS

NOMENCLATURE

2D	Two dimensional
3D	Three dimensional
A	Area $[\mathrm{m}^2]$, Coefficient, Constant
$\mathrm{A_c}$	Cross-sectional area of a channel $[\mathrm{m}^2]$; $\left(\frac{\pi \mathrm{D}^2}{4}\right)$
$\mathrm{A_{fr}}$	Frontal area of MICHX $[\mathrm{m}^2]$
Al	Aluminum
$\mathrm{Al_2O_3}$	Aluminum oxide
$\mathrm{A_s}$	Heat transfer surface area $[\mathrm{m}^2]$; (πDL)
ATF	Automatic transmission fluid
B	Constant
Br	Brinkman number
C	Fluid heat capacity $[\mathrm{J/K}]$, Coefficient, Constant
$\mathrm{C_1}$	Dispersion coefficient
$\mathrm{C_1}$ - $\mathrm{C_5}$	Coefficients
CHF	Critical heat flux $[\mathrm{kW/m^2}]$
$\mathrm{c_p}$	Fluid specific heat $[\mathrm{J/kgK}]$
Cu	Copper
CuO	Copper oxide
d	Channel diameter $[\mathrm{m}]$
$\mathrm{D_1}$ - $\mathrm{D_5}$	Exponents

D_h	Hydraulic diameter [m]
DI	Deionized
EG	50% ethylene glycol
EO	Engine oil
Expon	Exponential
Expt	Experimental
G	Mass flux $[\mathrm{kg/m^2 s}]$
h	Heat transfer coefficient $[\mathrm{W/m^2K}]$
h(t)	Transient heat transfer coefficient $\left(\frac{\dot{Q}}{A_s\{T_{h,m}(t)-T_s(t)\}}\right)$
HVAC	Heating, ventilation and air conditioning
HVAC&R	Heating, ventilation, air conditioning and refrigeration
HT	High temperature
HX	Heat exchanger
k	Thermal conductivity [W/mK]
	Turbulence kinetic energy $[\mathrm{m^2 / s^2}]$, or [J/kg]
K_B	Boltzmann constant [j/K]
l	Mean free path [nm]
L	Channel length [m]
L_{hy}	Hydrodynamic entrance length [m]
LT	Low temperature
L_{th}	Thermal entrance length [m]
m	Mass [kg]

$\dot{m}$	Mass flow rate [kg/s]
MFR	Mass flow rate
MICHX	Minichannel heat exchanger
MMT CO_2	Million metric tonnes of carbon dioxide
MR	Mass flow rate step ratio
Mtoe	Million tonnes of oil equivalent
NTU	Number of transfer unit
Nu	Nusselt number $\left(\frac{hd}{k}\right)$
$Nu(t)$	Transient Nusselt number $\left(\frac{h(t)d}{k(t)}\right)$
num	Numerical
Pe	Peclet number $(VD/\alpha = Re.Pr)$
PG	Propylene glycol
Pr	Prandtl number $\left(\frac{c_p\mu}{k}\right)$
$\dot{Q}$	Heat transfer rate [w]
Re	Reynolds number $(\rho Vd/\mu)$ or $(4\dot{m}/n\pi\mu d)$, for circular channel
Si	Silicon
SiO_2	Silicon dioxide
T	Temperature [°C]
TR	Temperature step ratio
T^*	Dimensionless temperature $\left(T^* = \frac{T - T_{c,in}}{T_{h,i} - T_{c,in}}\right)$

$T^*_{c,o}(t)$	Cold fluid dimensionless outlet temperature $\left(T^*_{c,o}(t) = \frac{T_{c,o}(t) - T_{c,in}}{T_{h,i} - T_{c,in}}\right)$
$T^*_{h,o}(t)$	Hot fluid dimensionless outlet temperature $\left(T^*_{h,o}(t) = \frac{T_{h,o}(t) - T_{c,in}}{T_{h,i} - T_{c,in}}\right)$
t	Time [s], Transient or function of time
t_{res}	Residence time [s]
t^*	Dimensionless time (t/t_{res})
$T_{c,i}$	Cold fluid inlet temperature [℃]
$T_{c,o}$	Cold fluid outlet temperature [℃]
$T_{h,i}$	Hot fluid inlet temperature [℃]
$T_{h,o}$	Hot fluid outlet temperature [℃]
T_i	Fluid inlet temperature [℃]
T_o	Fluid outlet temperature [℃]
T_m	Mass weighted average temperature of fluid [℃]
T_s	Channel inner surface temperature [℃]
U	Overall heat transfer coefficient $[W/m^2K]$
V	Fluid mean velocity $[m/s]$
V_{Br}	Brownian velocity $[m/s]$
$\dot{\forall}$	Volume flow rate $[m^3/s]$
x	Physical length of heat exchanger in x-direction [m]
y	Physical length of heat exchanger in y-direction [m]
ZnO	Zinc oxide

0	Initial
∞	Final, steady state

Greek letters

α	Thermal conductivity ratio $\left(\mathrm{k_{np}/k_{bf}}\right)$
β	Coefficient of thermal expansion $[1/\mathrm{k}]$
	Field factor $\left(\frac{\alpha-1}{\alpha+2}\right)$
γ	Interim parameter
ρ	Density $[\mathrm{kg/m^3}]$
μ	Fluid dynamic viscosity $[\mathrm{kg/m.\,s\ or\ N.\,s/m^2}]$
ν	Fluid kinematic viscosity or momentum diffusivity $[\mathrm{m^2/s}]$
λ	Molecular mean free path [µm]
ε	Turbulence kinetic energy dissipation rate $[\mathrm{m^2/s^3}]$
Δ	Change in variable, final-initial
Δp	Pressure difference or Pressure Drop [kPa]
ΔT	Temperature difference between two locations [°C]

Subscripts

0	Initial
∞	Final, steady state
a	Air
atf	Automatic transmission fluid
bf	Basefluid
c	Cold fluid

ch	Channel
eff	Effective
eg	50:50 ethylene glycol
enh	Enhancement
expt	Experimental
fthx	Flat tube heat exchanger
g	50% ethylene glycol
h	Hot fluid, hydraulic
hy	Hydrodynamic
ht	High temperature water
i	Inlet
l	Liquid
lt	Low temperature water
m	Mean, mass weighted average
max	Maximum
michx	Minichannel heat exchanger
min	Maximum
nf	Nanofluid
np	Nanoparticle
num	Numerical
o	Outlet
oil	Engine oil
s	Channel inner surface

ser	Serpentine
seq	Sequential
sim	Simultaneous
th	Thermal
w	Water, wall

CHAPTER 1

INTRODUCTION

Heat is one of the most significant energy forms that has versatile applications in daily life. Industries cannot be envisioned without the use of heat energy. The Global Energy Statistical Yearbook 2018 [1] reported, in 2017, the global total primary energy consumption was 14,126 million tonnes of oil equivalent (Mtoe), which is increased by 2.3% compared to that of 2016. The world energy consumption from 2009 to 2017 is presented in Figure 1.1 [1].

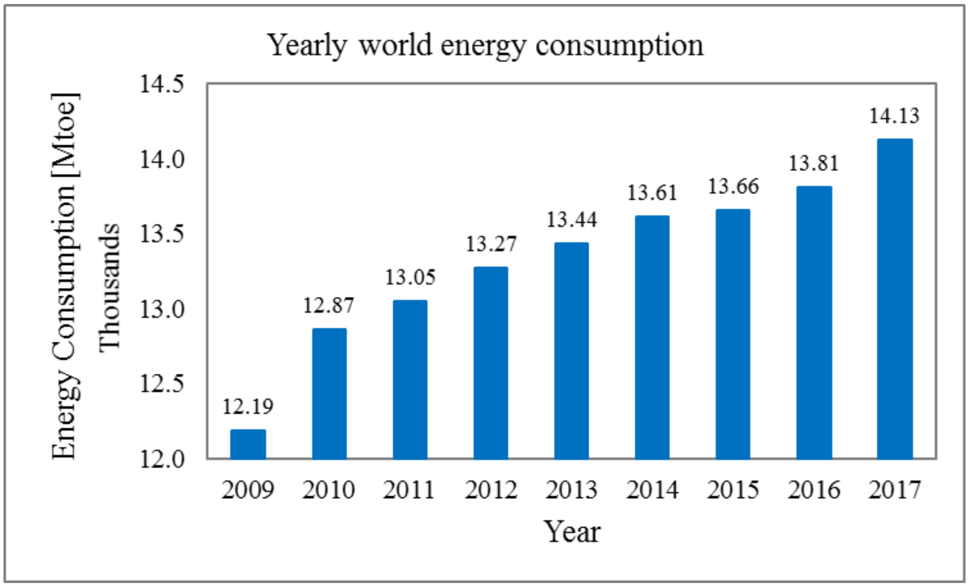

Figure 1.1: World total primary energy consumption in each year

This devoured energy comes from different sources, for example, fossil fuels, nuclear, and renewable energy. Fossil fuels are explicitly connected to global warming and environmental problems [2]. In 2017, fossil fuel was the worldwide single source for 85.2% of the energy produced as reported by BP Statistical Review of World Energy 2018 [3] as shown in Figure 1.2.

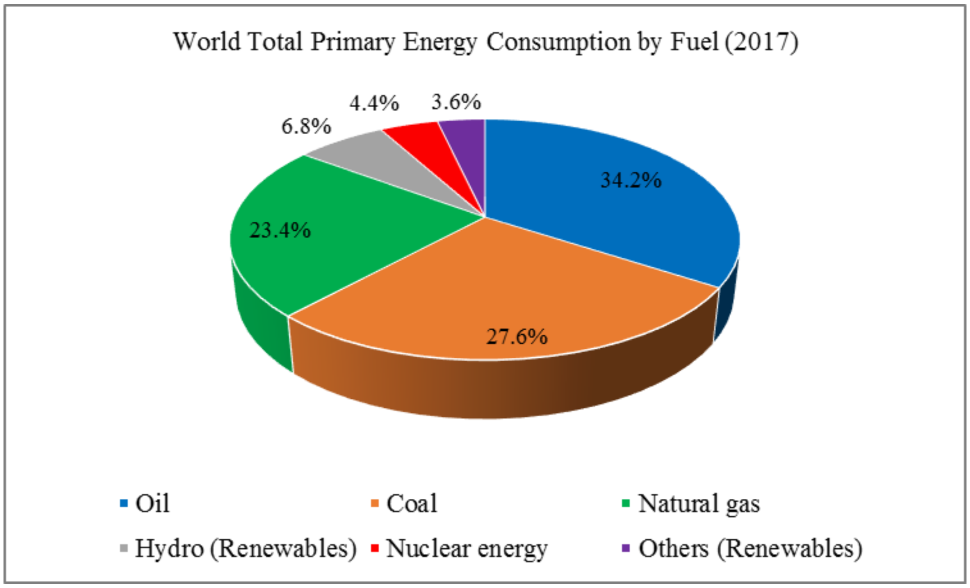

Figure 1.2: World total primary energy consumption by fuels in 2017

Even though natural renewable energy sources, such as sunlight, wind, waves and geothermal heat are widely available, the reserves of non-renewable energy, for example, fossil fuel and other mineral energy resources are being reduced day by day. The reserves of energy sources have been gradually diminished because of their continuous use in domestic, commercial, transportation and industrial sectors on a daily basis. In any case, energy sources are limited and should be conserved. Appropriate use of energy is the key to sustainable cost-effective as well as socio-economic development.

It is considered that fossil fuel is the major contributor to the ozone layer damaging substances, and there is a connection between energy use and the environment [2]. The U.S. Greenhouse Gas Inventory Report: 1990-2015 reported that in 2015, U.S. greenhouse gas emissions totaled 6,586.7 million metric tonnes of carbon dioxide (MMT CO_2) equivalents. It was also reported that U.S. emissions decreased by 2.3% from 2014 to 2015.

The following Figure 1.3 [2] shows the amount of carbon emissions in the U.S.A. and Canada.

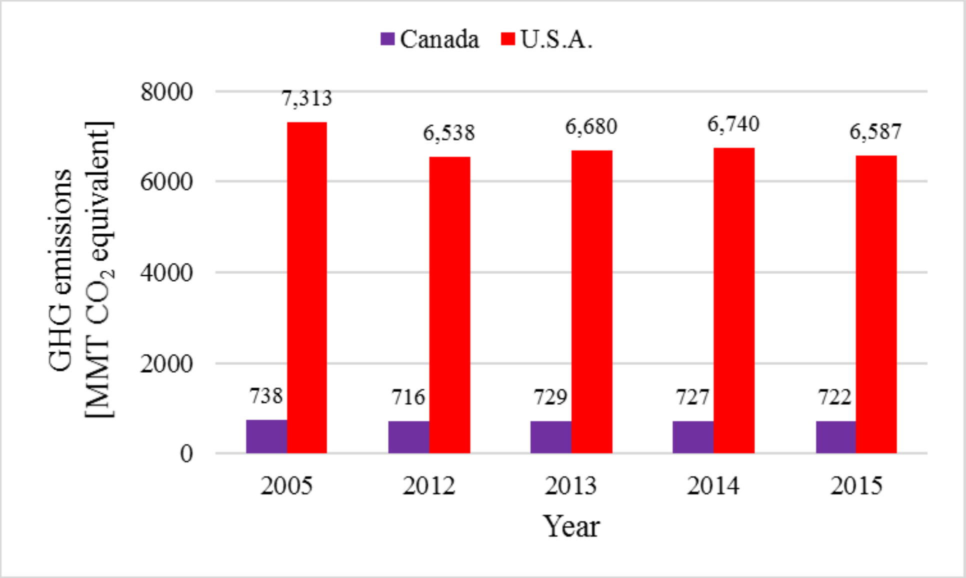

Figure 1.3: Greenhouse gas (GHG) emission in the U.S.A. and Canada

It was reported that Canada's Green House Gas (GHG) emissions profile is similar to that of the most industrialized nations [4]. Canada represented about 1.6% of total world GHG emissions in 2013, even though it is one of the topmost per capita emitters. In 2015, the latest yearly dataset in this report, Canada's GHG emissions were 722 MMT CO_2 equivalent, which was 727 MMT in 2014. The report also stated that total emissions decreased by 16 MMT or 2.2% during the period 2005–2015. Carbon dioxide (CO_2), 79% of total emissions, is the highest contributor to Canada's GHG emissions, which mostly results from the combustion of fossil fuel. CH_4 emissions in 2015 amounted to 14% of Canada's total. A summary of the GHG emissions contributors is shown in Figure 1.4 [4].

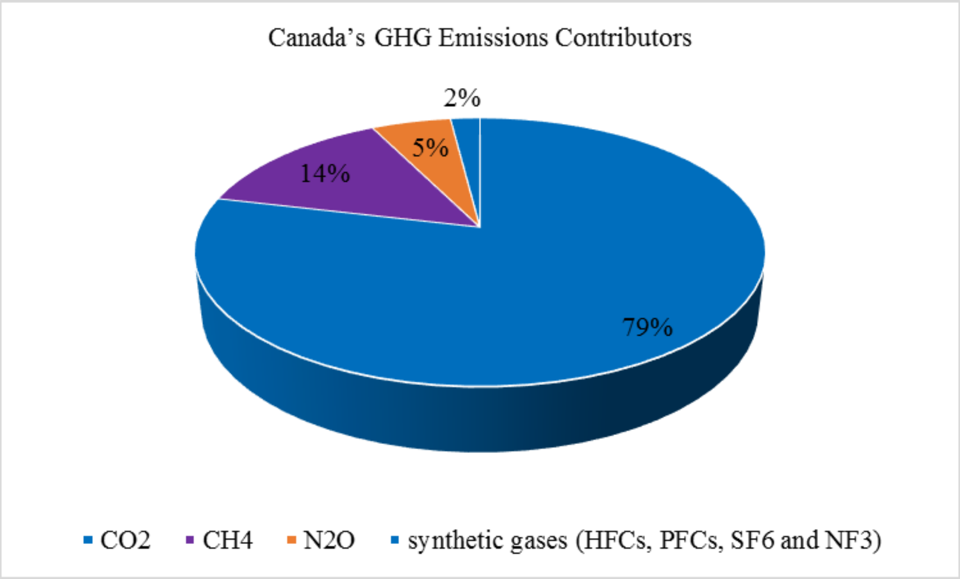

Figure 1.4: Contributors to Canada's GHG emissions in 2015

In accordance with the International Organization of Motor Vehicle Manufacturers' OICA statistics [5], the total world motor vehicle production and sales in the 2016 manufacturing year were 95 million and 93.9 million, respectively. The Global Auto Report (January 30, 2018) stated that 79.02 million cars were sold in 2017 statistical year and projected sales spikes to be 81.6 million in 2018. These vehicles use a huge amount of fossil fuel to produce their operating power.

An automobile engine is considered as a heat engine, which burns fuel and air inside a combustion chamber of an engine block to produce power. In this process, the working temperature inside the combustion chamber reaches an extremely high level. The maximum flame temperatures for a compression ratio of 3.86:1 have been experimentally measured by Hershey and Paton [6]. They recorded the maximum flame temperatures from 2066℃ to 2454℃ with the richest and leanest air-fuel ratio from 13.9 to 1. The temperature during the combustion process may reach as high as 2760℃ [7]. A modern automobile engine at its operating temperature generates about 44 kWh of heat energy when traveling at 97 km/h. Ideally, it is anticipated to run the engine as warm as possible without overheating that causes the engine coolant to boil at 125℃ [7].

It is desired to make the engine as efficient as possible and consecutively, yield the maximum power with the minimum pollution. However, in the real world, a heat engine cannot be hundred per cent efficient according to the second law of thermodynamics. There must always be some heat transfer to the environment, which is known as waste heat. As fuel burns in the engine, about 30% of heat energy is converted into useful power, about 30% goes out the exhaust, about 10% is absorbed through the engine lubrication oil and friction losses, and the rest, and about 30% is absorbed into the engine coolant and released into the cooling system [7].

A cooling system is necessary for any automotive engine. If no cooling system is provided, parts would melt and pistons would expand due to excessive heat of the burning fuel, and cylinder head or block would get cracked while it gets cooled. On the other hand, it is undesired to run the engine at a very low temperature that may create poor oil flow, sludge formation in the oil, and poor fuel vaporization. In order to make the engine most efficient with the least amount of pollution, it is preferred to run the engine as warm as possible without overheating. For the proper functioning of the engines, vehicles need appropriate thermal management systems.

Proper devices permit easy heat transfer. Heat exchangers are the devices that transfer heat energy between two or more fluids or between fluid and solid surface due to temperature differences [8]. The heat transfer takes place from a higher temperature fluid to a lower temperature fluid separated by a wall, in general.

In the automotive industry, heat exchangers are employed in engine cooling systems as a radiator, charge air cooler, and transmission oil cooler to remove excessive heat from the transmission systems. Heat exchangers are also used in automotive air conditioning systems as a condenser, evaporator, and heater core to keep the passenger compartment comfortable.

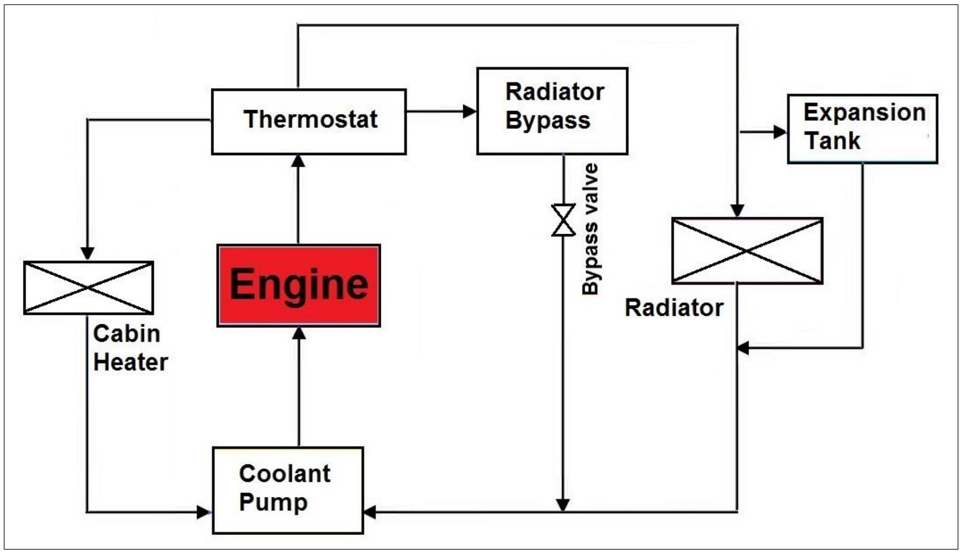

Figure 1.5: Block diagram of an automotive cooling systems

The radiator is the heart of the cooling system for transporting excess engine heat from the coolant to the atmosphere. The main purpose of the automotive cooling system is to remove excessive combustion heat from the engine, to keep the engine running at its most efficient temperature, and to warm the engine up to the optimum temperature as quickly as possible after starting.

In modern engines, turbochargers are used in order to increase both the engine's efficiency and power output. It is achieved by pushing excess compressed air through the combustion cylinder. Besides the intensification of the charge air density, the turbocharger and supercharger rise the intake manifold air temperature [9]. Consequently, this excessive temperature decreases charge air density and increases combustion temperature, which affects the torque, power, and emissions. In order to meet the strict emission standards set by the Environmental Protection Agency (EPA) and the California Air Resources Board (CARB), the air temperature of the intake manifold needs to be cooled. The charge air cooler (CAC), another type of heat exchangers, is a key component of the boosted engines to fulfill the growing demand for developments in fuel economy and exhaust emissions. This heat exchanger is employed to reduce the engine air temperature after passing through the turbocharger before entering the engine as shown in Figure 1.6. It transports heat from the intake charge to an intermediate fluid, which finally releases heat to the atmosphere.

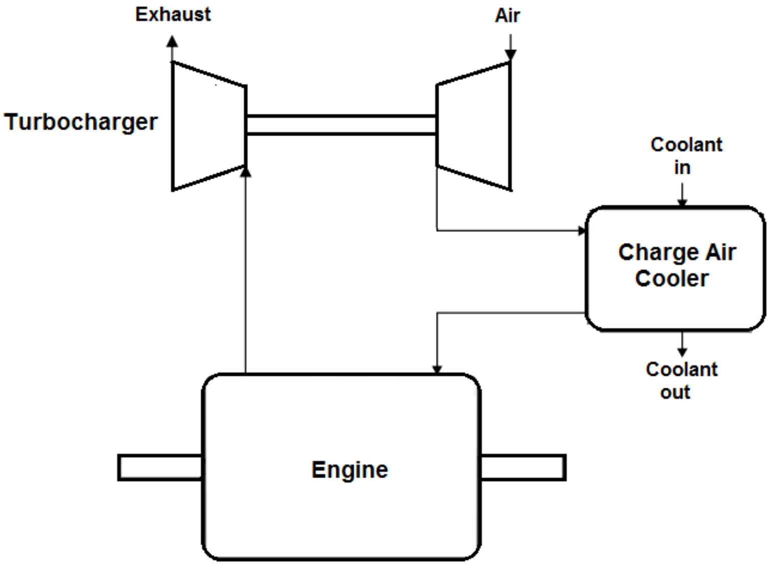

Figure 1.6: Schematic illustration of charge air cooler and turbocharger

The transmission oil cooler, usually placed inside the radiator loop, is an important device to protect the transmission system from overheating while things become excessively hot under heavy loads. Performance of motor vehicle is generally evaluated in terms of fuel consumption and emissions. The stringent emission regulations set by the EPA and CARB can be fulfilled by increasing the efficiency of the power train system, especially by improving the cooling performance of the automatic transmission fluid.

Evaporator and condenser are the main components of a mobile air conditioning system. The evaporator, also known as the evaporator core, is usually situated inside the passenger compartment, fairly concealed under the instrument panel. The main function of the evaporator, in a car, is to keep the passenger compartment cool and comfortable by removing heat and humidity from the inside of the vehicle.

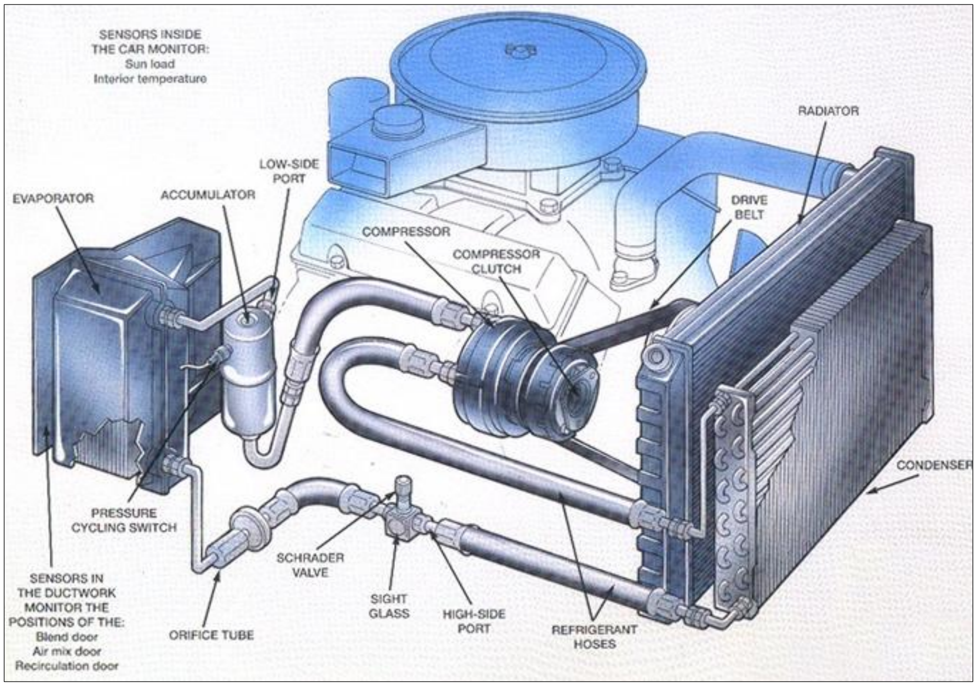

Image source [10] : http://www.79-85gm-ebodies.org/articles/a/basicairconditioning.html

Figure 1.7: A 6ypical automotive air conditioning systems

The condenser, which is commonly placed in front of the radiator, releases heat to the atmosphere from the hot air conditioning system that the refrigerant absorbs while passing through the evaporator. The radiator, evaporator, and condenser in the automotive thermal management systems are illustrated in Figure 1.7 [10]. The heater core, which is located in the plenum section of the HVAC module, is employed for heating the passenger compartment of a vehicle using the engine heat by means of hot coolant passing through the winding tube of the heat exchanger.

The thermal performance of heat exchangers plays a vital role on the underhood vehicle thermal management systems, which mainly depends on working fluid, geometry and channel size, module arrangement and fluid flow rate or engine speed. Heat transfer can be increased by minimizing entropy generation and maximizing the heat transfer coefficient. This can be achieved by minimizing pressure drops and friction losses, improving fabrication technologies, reducing channel size, changing module arrangement and adopting advanced fluids. The financial and environmental issues in the current industry consign the needs for system compactness and further performance improvement.

Nusselt number (Nu), a paramount important dimensionless characteristic parameter of convective heat transfer, represents the intensification of heat transfer due to convection over conduction across the fluid boundary layer thickness [11–14]. The relationship among Nu, heat transfer coefficient (h), thermal conductivity of the fluid (k) and hydraulic diameter of the minichannel ($\mathrm{D_h}$) is expressed as $\mathrm{h} = \frac{\mathrm{Nuk}}{\mathrm{D_h}}$. The fluid flow inside a minichannel can be considered as laminar due to the small channel hydraulic diameter [15]. For fully developed laminar flow in a circular channel subjected to constant surface temperature or constant surface heat flux, the Nusselt number is a constant [12]. In these circumstances, the heat transfer coefficient of a fluid can be improved by increasing the thermal conductivity of the working fluid and/or decreasing the hydraulic diameter of the flow passage.

Energy conversion and transportation primarily take place at atomic or molecular levels. Nanoscience and nanotechnology are likely to play a vital role in stimulating conventional energy industries as well as emerging renewable energy industries [16]. Heat transfer in various circumstances can be intensified by applying active and passive techniques. For the active method, external energy is required to enhance heat transfer, improve the efficiency of heat pumps, separators and reactors and make the process faster. However, this method is expensive and challenging under miniature situations, in particular. It involves mechanical mixing, rotation, and vibration as well as the external electrostatic or magnetic field.

For the passive method, heat transfer enhancement can be accomplished by improving fluid properties, modifying shape and roughness of the surface of flow passage or attaching the structure to increase heat transfer surface area and turbulence. However, the commonly used working fluids hold their characteristic drawback of moderately low thermal conductivity. Even though water owns the highest thermal conductivity among these working fluids, it is several orders lower than that of most metals or metal oxides. Probably, that is why a concept of adding particular solid particles in the base fluids to intensify their thermal conductivity has been experienced for a long time.

At the early stage of investigations, suspensions of milli- or micro-meter sized particles were used, which led to poor stability of suspensions, clog flow passage and create serious problems in small channels. Nanofluids are dispersions of nanoparticles smaller than 100 nm, developed a couple of decades ago with the certain aim of intensifying the thermal conductivity of heat transfer fluids [17]. Properly engineered nanofluid holds several benefits over the typical solid-fluid suspensions for heat transfer enhancement. These provide higher dispersion stability with leading Brownian motion of nanoparticles. These also offer higher surface between nanoparticles and base fluids, elevated heat transfer coefficient and reduced pumping power for equivalent heat duty as compared to the base fluid. In addition, engineered nanofluids minimize clogging of flow passage ash compared to typical slurries, and hence stimulate system miniaturization. Adaptable properties of nanofluids by changing nanoparticle concentrations brand these fluids appropriate for versatile applications.

Flow arrangement also plays a vital role in heat transfer between two or more fluids. According to flow arrangement, heat exchangers can primarily be classified as parallel flow, counterflow, and crossflow heat exchangers. The fundamental element of a heat exchanger can be seen as a tube with one fluid flowing through inside it and the other fluid running over the outside. In automotive applications, heat exchangers are generally subjected to air-to-liquid and air-to-gas crossflow orientation. Three mechanisms are involved in heat transfer processes. First, convective heat transfer takes place between hot fluid and the tube wall (inner surface). Then conductive heat transfer occurs through the wall from the hot side to the cold side of the tube. Finally, convective heat transfer takes place between the tube wall (outer surface) and the cold fluid.

Generally, in a vehicle, the condenser is placed in front of the radiator in a sequential arrangement. In this pattern, condenser releases heat to the ambient air, and the air gets warmer before entering the radiator. As a result, performance of the radiator, which also releases heat from the engine coolant, goes down compared to the situation when the radiator faces fresh ambient ram air. The performance of the radiator can be improved by modifying the arrangement of the heat exchangers module. In the current study, the radiator and condenser are proposed to place in a simultaneous arrangement, where both heat exchangers will face similar approach or ram air with the equivalent ambient conditions.

The thermal performance of an entire heating and cooling system is strongly influenced by the heat exchanger performance. Characterization of the transient behavior of crossflow heat exchangers is of great significance in many applications, particularly, due to sudden change in their operating conditions. Evaluation of transient performance and modeling the heat exchangers at a varied mass flow rate and temperature are important because it commonly happens in real-world applications. It is essential for the design of thermal control systems in order to enhance energy efficiency as well as thermal reliability [18]. Numerical simulations predict the in-depth understanding of various thermal parameters associated with the performance of heat exchangers.

This study and resultant analysis provide fundamental insights into a crossflow heat exchanger, which can be used to improve heat exchanger performance and support the design of thermal management systems.

1.1 Motivation

Although energy sources are limited, energy demands are increasing day by day. Therefore, energy conservation and appropriate use of energy are crucial to sustainable cost-effective development.

The necessity of heat transfer devices, which can provide elevated heat transfer and higher performance in a reduced size, is paramount for many industries. The augmentation of heat transfer is associated with modifications of thermal design that reduce entropy generation and enhance the convective heat transfer coefficient. In order to mitigate industry energy requirements through intensifying heat transfer and improving the performance of heat exchangers, the following approaches are considered for the optimal design of crossflow MICHX apparatus used in the current study:

- Circular cross-sectional channels are used for liquid transport because these can withstand larger pressure differences between the inside and the outside without undergoing any deformation.
- Conventional tubes are replaced by minichannels because they possess a higher heat transfer coefficient.
- MICHXs are the focus of diversified investigation and application interest due to their miniaturized geometry and lightweight, enhanced transfer characteristics, and versatile applications.
- Minifluidic devices have several advantages over traditional larger sized systems. One of the most important aspects of MICHX is higher volumetric

heat transfer due to its higher heat transfer surface area. The area density of the MICHX ($4000\ \mathrm{m}^2/\mathrm{m}^3$) used in the current study is several times higher than that of conventional heat exchangers ($1000\ \mathrm{m}^2/\mathrm{m}^3$). The larger surface-to-volume ratio results in higher heat transfer efficiencies and makes it possible to enhance heat transfer with a relatively low fluid flow rate [19]. The small dimensions and slab type mini-channel devices also provide safe operation with highly reactive or hazardous products [20, 21].

- Aluminum oxide nanoparticles are introduced in the base fluid due to the higher thermal conductivity of nanoparticles that gives elevated heat transfer coefficients than those of the base fluids. Nanofluids possess a higher heat transfer surface area between nanoparticles and base fluids. Nanofluids reduce pumping power compared to the base fluid to achieve the same heat duty. Nanofluids deliver adaptable properties by changing the volume fraction of nanoparticles in order to suit the versatile applications.

- An initiative is proposed to develop new type of heat exchanger module that abundantly exploits the benefits of minichannel flow passages. The simultaneous arrangement of heat exchangers module is considered to have similar ambient conditions of approach air for each heat exchanger. In the traditional arrangement, radiator and condenser are placed sequentially; as a result, only the frontal heat exchanger, i.e. the condenser faces the ambient conditions of approaching air while the radiator gets the hot air, which exits from the condenser.

- Transient simulation has been performed as it provides the characteristic behavior of heat transfer flow parameters when the heat exchanger is subjected to a sudden change in any operating conditions, such as mass flow rate and temperature. This can be analogous with the thermostat operation, which regulates the operating temperature of the engine by opening and closing in response to the step-change in the coolant flow rate.

1.2 Research Objectives

The main goal of current research is to optimize three-dimensional (3D) transient heat transfer in crossflow MICHX. It is also desired to compare the performance of the heat exchanger modules to fulfill the potentiality in real-world applications.

The objectives of the current study are as follows:

- Characterize transient performance and behavior of heat transfer parameters in MICHX. These include dynamic responses of fluid outlet temperature, channel surface temperature, heat transfer rate, heat transfer coefficient, and Nusselt number.

- Design multiple models of heat exchangers with different sizes and different arrangements. The intention is to develop a simultaneous MICHX module as well as to characterize transient performance and behavior of MICHX.

- Validate both the steady state and the transient models with experimentally measured steady state and transient data. This is to replace the need for experimental work, which is expensive, time consuming, and difficult to measure data of intricate thermal and flow fields.

- Develop new correlations for convective heat transfer for both steady state and transient situations
- Investigate thermal and flow performance of MICHX and conventional heat exchanger as a benchmark under steady state conditions
- Evaluate the effect of Al_2O_3-based nanofluid on the thermal performance of heat exchanger

1.3 Method of Reaching the Research Goal

Researchers have never discontinued or decelerated their struggles to improve the design and performance of heat transport devices. The experimental work is very expensive, and it requires a long time for the development of a test facility. It is also very hard to attain the in-depth data of thermal and flow fields of crossflow MICHX, especially in transient mode. Fortunately, the computational fluid dynamics (CFD) have become available in the last couple of decades to simulate the complicated problems and attain desired results. With the help of these technological advancements, this research has numerically been completed by CFD simulation, which provides sophisticated data and information on this matter.

In order to successfully accomplish the research objectives, a step-by-step action plan was developed. The flow chart of the action plan, which was strictly followed to meet the current research goal, is illustrated in Figure 1.8.

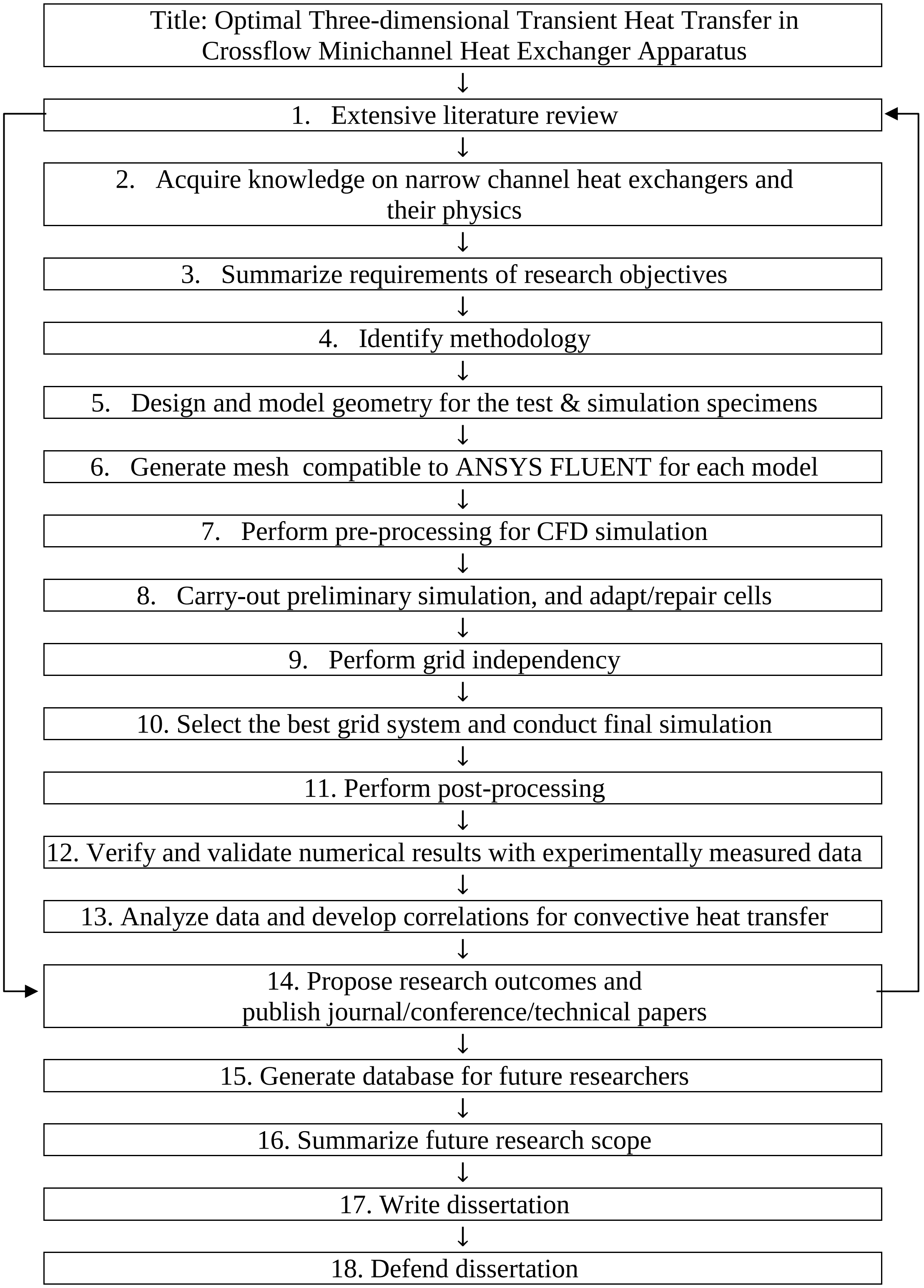

Figure 1.8: Step-by-step action plan to achieve research goal

1.4 Significance of the Current Research

This research has been carried out because of the current lack of comprehensive scientific numerical literature on 3D transient heat transfer in air-to-liquid crossflow MICHX. This dissertation is intended to fill this research gap as much as possible. Key research outcomes are intended to be published in scientific journals and proceedings. Several articles have already published in journals and presented in conferences for dissemination purposes.

A simultaneous module of MICHX has been modeled in the current study with the purpose of improving the thermal performance, especially for automotive HVAC and cooling systems. In this arrangement, both heat exchangers face incoming air of similar ambient conditions, such as quality, velocity, and temperature. The simultaneous module can play a significant role to mitigate the industry's energy needs by means of energy conservation and reduced exergy destruction. Incorporating the simultaneous module of MICHX in vehicle thermal management systems can be considered as a novel one.

New correlations for transient dimensionless temperature and Nusselt number for perturbation in both the mass flow rate and the inlet temperature of hot fluid have been developed. These correlations can be useful sources for future researchers. It is also anticipated that the designers can utilize the transient results to develop process control strategies for heat transport devices due to a sudden change in operating conditions.

CHAPTER 2

LITERATURE REVIEW AND SCOPE OF CURRENT RESEARCH

This chapter aims to introduce the present state and potential of minichannels available in published literature in order to enhance heat transfer. Some aspects and technological improvements of convective heat transfer in heat exchangers are presented. Based on the literature survey, an air-to-liquid crossflow minichannel heat exchanger is modeled. Literature pertaining to research on advanced fluid (nanofluid) and transient heat transfer are then introduced. It signifies the needs and scope of current research.

2.1 Flow and Heat Transfer Characteristics in Minichannel Heat Exchanger

Energy transfer and its applications are continuous and ever growing processes of global environmental sustainability and cost-effective development [22]. Researchers are very concerned about energy and environment. Energy generation, preservation, transmission and appropriate use play the vital role in cost-effective and sustainable development. Heat exchangers, one of the key components of energy conservation processes, are widely used in many engineering applications. In order to fulfil the increasing energy demand, the performance of such devices needs to be improved. Researchers [19, 23–43] have been taken great attention from the past decades for miniaturized, energy efficient environmentally friendly narrow-channel heat exchangers that provide elevated heat transfer for a given heat duty.

2.1.1 Heat Transfer Augmentation

Researchers started the investigation of heat transfer augmentation in heat exchanger in early 1920s, and their efforts continue to present day [23, 44, 45]. The benefits of this streak of work began to be appeared in industrial arena as well as in open literature in the 1980s [46]. The amount of published papers including articles, proceedings, reviews, and editorial materials on the field of heat transfer enhancement or augmentation hits more than 20 thousand during the past several decades [47].

Numerous researchers [22, 37, 46, 48–54] have offered reviews of the state-of-the-art techniques for intensifying heat transfer in past years. Bergles et al. [51] complied more than five thousand research papers on convective heat transfer from the open literature. They categorized the enhancement mechanisms into two types: passive and active techniques. In his recent work, Bergles [50] offered the fourth generation of heat transfer intensification. The author used a combination of different techniques and suggested to extend the field by combining different individual methods for further augmentation of heat transfer coefficients. The use of multiple techniques in single-phase flows is an attractive possibility.

Balaras [48] reviewed intensification techniques for heat transfer surfaces in single-phase heat transport devices. The augmentation techniques are categorized in several kinds, such as fluid, surface, compound and combined mechanisms. The fluid technique included vibration and electrostatic force of external fluid. The surface technique used variations to the heated surfaces including surface vibration, surface roughness, extended surfaces, and swirl-flow devices. The compound and combined techniques involved injection, suction, and a combination of the different techniques. Tao et al. [53] proposed three possible techniques for the single-phase heat transfer augmentation. These are: reducing the thermal boundary layer, growing flow interruptions, and growing the velocity gradient adjacent to the heated surface. A summary of the heat transfer intensification methods is presented in Appendix B.

The channel classification was presented by some researchers [19, 55] for a guideline of a flow passage related to the size in term of hydraulic diameter. The commonly used classification was offered by Kandlikar et al. [19]. The author divided the channel sized into three categories. Hydraulic diameter is greater than 3.0 mm for a conventional channel flow passage. For minichannel and microchannel passage, the hydraulic diameters $(\mathrm{D_h})$ are $200\mu\mathrm{m} < \mathrm{D_h} \leq 3.0\mathrm{mm}$ and $10\mu\mathrm{m} < \mathrm{D_h} \leq 200\mu\mathrm{m}$.

The fundamental equation of the heat transfer rate $(\dot{\mathrm{Q}})$ in a particular heat exchanger is expressed in the following form:

$$\dot{\mathrm{Q}} = \mathrm{UA\Delta T} \tag{2.1}$$

where U, A and $\Delta\mathrm{T}$ represent the overall heat transfer coefficient, the heat transfer surface area, and the temperature difference between inlet and outlet fluid of the liquid-side or air-side.

The overall heat transfer coefficient is a function of fluid heat transfer coefficient, fouling resistance, fin efficiency, and thermal resistance of the separating wall [29].

The heat transfer coefficient (h) of a given fluid in the heat exchanger is defined as

$$h = \frac{Nuk}{D_h} \tag{2.2}$$

where, Nu and k denote the Nusselt number and thermal conductivity of the fluid, respectively. D_h is the hydraulic diameter of the minichannel.

The fluid flow can be considered laminar inside a minichannel because of the small channel hydraulic diameter [15]. In order to evaluate the effects of the heat transfer augmentation due to channel size reduction, flow is assumed to be fully developed laminar. Since, the Nu is constant for a fully developed laminar flow [11, 56, 57], it is obvious from the above equation that the heat transfer coefficient is inversely proportional to the hydraulic diameter of a minichannel. The effect of channel hydraulic diameter on heat transfer and pressure drop in a crossflow minichannel heat exchanger (MICHX) under laminar regime was studied by Ismail et al. [26]. For a specific Reynolds number of 1300, the variation of heat transfer coefficient with channel size are shown in Figure 2.1.

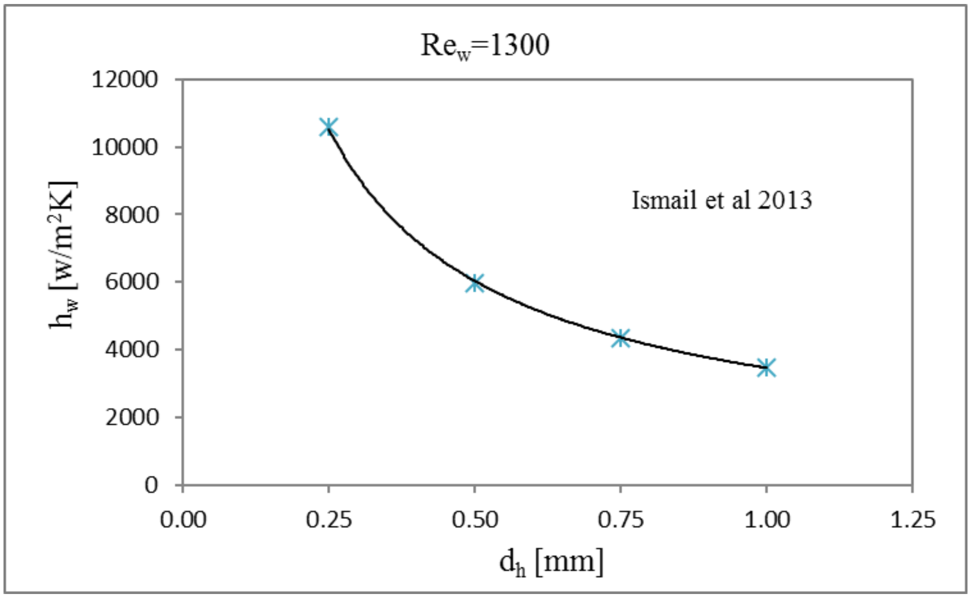

Figure 2.1: Effect of channel diameter on heat transfer coefficient at Re=1300

The heat transfer coefficient with water in a 1.00mm diameter channel is $\sim 3500\ \mathrm{w/m^2K}$; whereas, it increases to $\sim 10500\ \mathrm{w/m^2K}$ for a 0.25mm diameter channel with the expense of a higher pressure drop. It is necessary to carefully evaluate the pressure drop penalty along with the heat transfer intensifications for selecting the channel size. The pressure gradient drastically increases with the decrease of channel size. In order to limit the overall pressure drop, MICHXs have to be properly designed to deliver short flow lengths [58]. Nowadays, miniature heat exchangers are effectively and fruitfully employed in many applications, and elevated pressure gradients in MICHXs basically turn into a design control in accomplishment of an appropriate heat exchanger design.

One of the most important benefits offered by the minichannels is the overall size reduction of the heat exchanger. Neglecting the intermediate header and manifolds, the heat transfer surface area available per unit volume of a heat exchanger with circular channels of diameter, d and length, l is expressed by the following equation.

$$\frac{\mathrm{A}}{\mathrm{V}} = \frac{\pi \mathrm{dl}}{(\mu \mathrm{d}^2/4)\mathrm{l}} = 4\mathrm{d} \tag{2.3}$$

The ratio of available surface area to volume, $\mathrm{A/V}$ indicates the compactness of a particular heat exchanger, and usually uses in the open literature in the field of compact heat exchanger [59]. Kandlikar [29] presented the variations of surface are to volume ratio with the channel diameter. The authors reported the area to volume ratio of $400\ \mathrm{m^2/m^3}$ for the commonly used channel size of $\sim 10\ \mathrm{mm}$; whereas, this ratio turned out to be $4000\ \mathrm{m^2/m^3}$ and $8000\ \mathrm{m^2/m^3}$ for the channel diameters of $1.0\ \mathrm{mm}$ and $0.5\ \mathrm{mm}$, respectively. For the identical internal flow volume, it is obvious that a 1 mm diameter channel delivers $10-$fold higher surface area than that of a $10\ \mathrm{mm}$ diameter channel, which is normally used in the present day's stationary refrigeration applications.

Furthermore, the heat transfer rate of the heat exchanger with fluid mean temperature, $\mathrm{T_m}$ and surface temperature, $\mathrm{T_s}$ is given by the following equation.

$$\dot{\mathrm{Q}} = \mathrm{hA}(\mathrm{T_m} - \mathrm{T_s}) \tag{2.4}$$

The ratio of heat transfer rate to volume, $\frac{\dot{\mathrm{Q}}}{\mathrm{V}}$ is given by

$$\frac{\dot{\mathrm{Q}}}{\mathrm{V}} = \mathrm{h}(\mathrm{T_m} - \mathrm{T_s})\left(\frac{\mathrm{A}}{\mathrm{V}}\right) \tag{2.5}$$

This ratio clearly indicates that $\dot{\mathrm{Q}}/\mathrm{V}$ is directly proportional to A/V, which increases with decrease in channel diameter as seen earlier. For example, if all other factors remain constant, a 10-times reduction in the channel diameter from will yield a 10-times enhancement in heat transfer rate per unit volume. The actual increase in performance depends on additional parameters, including the other side heat transfer coefficient as well as redesign parameters to limit the pressure drop constraints [60].

2.1.2 The Effects of Channel Sizes on Pressure Drop and Heat Transfer

Numerous studies dealing with the single-phase forced convection heat transfer in mini and micro devices have been published in the previous decades, owing to the rapid development of micro-electromechanical devices during the last several years. This growth has great influence on micro scale devices, including microelectronic cooling systems and micro heat exchangers. Many researchers [56, 61–68] offered friction factor, pressure drop and heat transfer correlations. Single-phase heat transfer coefficients in six rectangular channels with a hydraulic diameter ($\mathrm{D_h}$) of 0.31 to 0.75 mm for water and methanol were reported by Wang and Peng [63]. Their Nusselt numbers were only 35% of that predicted by Dittus-Boetler [68] equation. However, Webb and Zhang [62] discussed the capability of commonly accepted correlations to predict single-phase and two-phase heat transfer and friction in channels with small hydraulic diameters between 0.1 mm and 2.0 mm. They found that their experimental results were adequately predicted by the established correlations for single-phase flow in multiple tubes with $0.96\ \mathrm{mm} < \mathrm{D_h} < 2.1\ \mathrm{mm}$.

The flow and the heat transfer characteristics for the run of nitrogen gas in heat exchangers were measured by Wu and Little [69]. They found that for laminar flow with a Reynolds number (Re) less than 600, Nu was lower than that predicted by traditional correlations, whereas for $600 < \mathrm{Re} < 1000$, Nu was higher than the standard values. Several effects that had been neglected when considering macro scale flow were identified by Papautsky et al. [70]. For example, micro scale phenomena may include two- or three-dimensional transport effects, and the temperature dependent variations of the transport fluid properties along a microchannel may invalidate the often used assumption of constant properties, so that to provide conclusive evidence of micro scale effects, amended measurement accuracies are required.

The liquid flow friction factor and heat transfer coefficient in circular and rectangular mini-channels with hydraulic diameters between 0.77 and 2.01 mm were quantified by Agostini et al. [71]. They found good agreement between their experimental results in the turbulent regime and the Gnielinski [72] correlation. Conversely, in the laminar regime, no precise prediction was found, and most of the heat transfer test results were expressively divergent from those predicted by the traditional forced convection heat transfer correlations. However, three main causes were explained for the differences between the experimental results obtained in minichannel heat exchanger compared to macro-tubes: uncertainties on the channel dimensions, inlet and outlet singular pressure losses, and longitudinal heat conduction. Good agreement was found with standard correlations and theories, when these elements were taken into account [71] .

Experimental and numerical studies were conducted by Li et al. [73] to characterize the flow and heat transfer behaviors of liquid laminar flow in microtubes. The smooth fused silica and rough stainless steel microtubes were used with hydraulic diameters of 50–100 μm and 373–1570 μm, respectively. The experiment was conducted with deionized water at the Reynolds number from 20 to 2400. They established that the experimental results of local Nu distribution along the axial direction of the stainless steel tubes did not comply with the conventional results when Reynolds number was low and the relative thickness of the tube wall was high. The numerical study revealed that the large ratio of wall thickness over tube diameter in low Reynolds number region causes significant axial heat conduction in the tube wall, leading to a non-linear distribution of the fluid temperature along the axial direction. The axial heat conduction effect was gradually weakened with the increase of Reynolds number and the decrease of the relative tube wall thickness.

Harirchian and Garimella [74] experimentally investigated the effects of channel size, heat flux, and mass flux (225-1420 $\mathrm{kg/m^2s}$) on flow boiling regimes in mini and micro-channels flow boiling regimes using high speed photography. Seven dissimilar silicon test pieces with a depth of 400 μm with parallel channels widths from100 to 5850 μm were used. The picturing and the heat transfer data show that nucleate boiling is dominant, flow regimes are similar in the channels of width 400 μm and large and differ from 100-250 μm wide channels, over a wide range of heat flux. It is also stated that with increase of channel width, bubbly flow substitutes slug flow and intermittent churn/wispy-annular flow substitutes intermittent churn/annular flow. For channels width of 400 μm and larger, the heat transfer coefficient is independent of mass flux regardless of the flow pattern for the range of heat fluxes in which nucleate boiling occurs on the channel walls,

The various mechanisms for the departure of flow and heat transfer correlations for flow in microchannels from the standard ones were categorized into two groups by Guo and Li [75]. First, if the characteristic length of the flow and the molecular mean free path are on the same order of the magnitude, the Navier-Stokes equations and the Fourier heat conduction equation are ineffective. As a result, the flow and heat transfer behaviour change significantly. This is the so-called rarefaction effect which can be shown by the Knudsen number, expressed by the ratio of the molecular mean free path and the characteristic length of the flow. Secondly, the size effect on the flow and heat transfer correlations is attributed to the disparity of the governing factors in the flow and heat transfer as the scale decreases even if the continuum assumption is still applicable. For example, forces employed on the fluid that affect the flow and heat transfer whose result on the convection changes at different scales, and also axial heat conduction in the tube wall, which are usually neglected for normal-sized devices, may become significant on a micro scale. Consequently, micro scale flow and heat transfer correlations vary from those of normal-sized devices.

The experiment of water flow in circular microtubes of fused silica and stainless steel with the hydraulic diameter of 50 to 254 μm was executed by Mala et al. [76]. The mean surface roughness of the tubes was ±1.75 μm, and the relative roughness of the tubes with $\mathrm{D_h} = 254$ μm and $\mathrm{D_h} = 50$ μm were from 1.36% to 1.70%, respectively. They noted that for low Re, there is a nonlinear trend between pressure drop and flow rate, and the friction factors were steadily higher than those predicted by the standard correlations. The authors predicted the transition from laminar to turbulent flow at $\mathrm{Re} > 300 - 900$, and the fully developed turbulent flow at $\mathrm{Re} > 1000 - 1500$ due to the effect of the surface roughness of the microtubes. Lelea et al. [77] experimentally and numerically studied developing and laminar flow regime for distilled water as the working fluid and stainless steel as the tube material with Reynolds number range up to 800 in microtubes with diameter of 0.1, 0.3, and 0.5 mm. They designed the experimental setup such a way to facilitate the study of friction factor and developing heat transfer. The experimental results have been compared both with numerical and theoretical predictions from literature for conventional tubes. It is stated that the conventional theories are valid for water flow through microtubes obtained by numerical modeling of their experiment.

The effects of diameter on two phase pressure drop in narrow circular tubes using air and water was investigated by Venkatesan et al. [78]. They employed the inner diameters of 0.6, 1.2, 1.7, 2.6, and 3.4 mm and the superficial velocity of 0.01–50 $\mathrm{m/s}$ and 0.01–3 $\mathrm{m/s}$ for the gas and liquid, respectively. Also a high-speed CMOS camera used to visualize the two phase flow. A correlation for predicting Chisholm parameter in slug annular flow pattern included surface-tension effect, mass flux effect and superficial velocities applicable for mini tubes was suggested in two-phase flow depending on the analysis of experimental frictional pressure drop data.

Minichannel flow passages of compact evaporators for two phase flow pattern, pressure drop and heat transfer was studied by Kandlikar [79]. He explored an inclusive literature review in small-diameter passages on evaporation together with some results obtained by the author for water evaporating in 1 mm hydraulic diameter multichannel passages. It was found that heat transfer rate in the minichannels may be anticipated using the flow boiling correlations established for large-diameter tubes, nevertheless, in the multichannel evaporators, it is different from that in the single-channel evaporators under the same set of operating conditions. It is also established that the length-to-diameter ratio for evaporator design in small-diameter channels is influenced by the heat transfer and pressure drop characteristics.

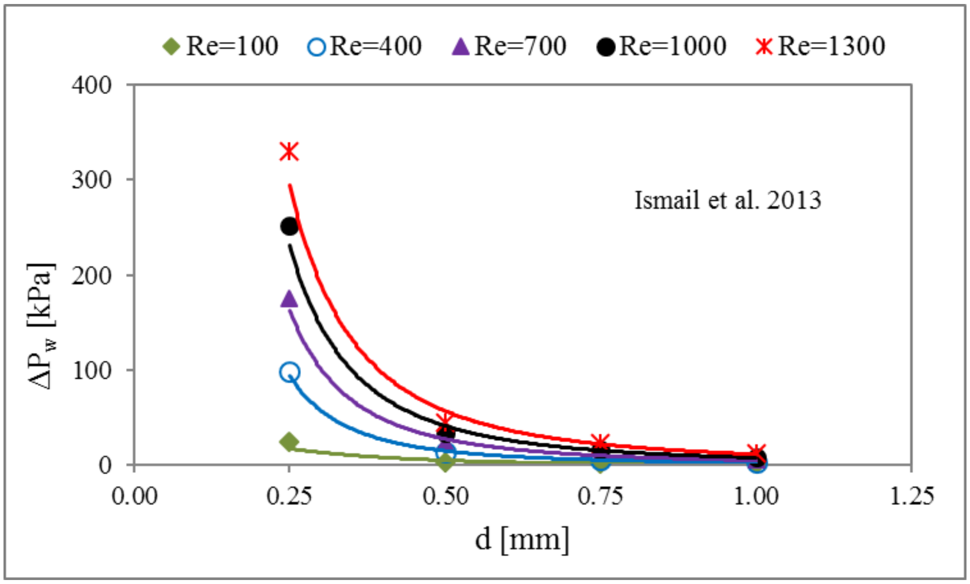

Figure 2.2: Effect of channel diameter on pressure drop at laminar regime

The effect of channel size on pressure drop and convective heat transfer behaviour were numerically studied by Ismail et al. [26] in a serpentine minichannel heat exchanger. For a particular Reynolds number of 1300, the variation of pressure drop with channel size are illustrated in Figure 2.2.

Authors used De-ionized water and air as the working fluids for the numerical investigation of thermal and flow characteristics. They considered four distinct channel diameters from 0.25 mm to 1.00 mm for the liquid side Reynolds number within the range of $100 \leq \mathrm{Re} \leq 1300$. They found that the changes in pressure gradient drastically increases with the decrease of channel size. However, it is found to be negligible for higher diameter and lower Reynolds number. It is necessary to evaluate the pressure drop penalty with judgment in conjunction with the heat transfer augmentations for selecting the channel size. In order to accommodate the overall pressure drop, MICHXs need to be accurately designed to provide small flow lengths [58].

2.1.3 Uniformity of Flow and Thermal Distribution in MICHX

Uniform flow distribution is a desirable field in numerous engineering devices, such as solar thermal collectors, fuel cells, heat sinks for cooling electronic devices, and more [21]. In cooling electronic chips, a nonuniform flow distribution in microchannel heat sinks can cause nonuniform heat transfer situation and produce undesirable temperature gradients which lead to lower performance [80]. The financial and environmental issues in current industry consign the needs for system compactness and further performance improvement. Minifluidic devices have several advantages over traditional larger scale systems. Generally, the most important aspect of compact systems is the large surface-to-volume ratio that results in high heat and mass transfer efficiencies, makes it possible to enhance heat transfer with relatively low fluid flow rate [19]. Numerical simulations have also been used to investigate the effect of geometrical parameters of a microstructure on flow uniformity [21].

The degree of flow uniformity that can be attained pertains to how small the pressure drop in the channels in comparison with the pressure drop in the manifold is [81]. The effect of Reynolds number on flow distribution was investigated by numerous researchers [19, 21, 82–84]. The effect of microchannel structures with triangular and trapezoidal manifolds on flow distribution uniformity, have been conducted by several examiners [85–87]. In the area of heat transfer and fluid flow characteristics, channel geometry, hydraulic diameter, and channel orientation are imperative parameters [32, 88]. Numerical modeling was used by Mohammadi et al. [89] to quantitatively investigate the effect of the geometry of the right triangular manifold and the dimensions of microchannels on desired uniformity and pressure drop. The simulations were performed within the low-Reynolds number of $5 \leq \mathrm{Re} \leq 25$. Studies have also been performed on the effect of inlet configuration on distribution of air-water annular flow in a header of a parallel flow heat exchanger, and found that besides the inlet direction, several parameters as well as both flow and geometry, will influence the flow distribution in a parallel flow heat exchanger [90]. It is found that performance reduction by flow mal-distribution can be as large as 20% [91]. Pressure drop in a MICHX impacts the heat transfer, operation, size, mechanical characteristics, and economic considerations; it entails the improvement of heat transfer and minimization of pressure drop [8]. If the pressure drop is small, laminar flow is overcome, yielding low thermal resistance. On the other hand, when the pressure drop is large, optimal thermal resistance is created in the turbulent region [92].

The hydraulic diameter is not an appropriate geometric modeling parameter. The annular geometry yields to a lower pressure drop than the trefoil geometry for the same hydraulic diameter [93]. The relationship between the heat transfer and the ratio of length to diameter (L/D) of shell and tube heat exchangers with 10, 20, 30, 40, 50 tubes were studied by Jiang and Deng [94]. Their results showed that heat transfer performance decreases and pressure drop increases with the decrease of L/D, and critical point of deep heat transfer state is achieved when L/D is at some point between 3.08 and 4.62. One common assumption typically made in the design and analysis of heat exchangers is that fluid properties are independent of temperature. Nevertheless, a number of a fluid's physical properties may have significant variations with temperature. For liquids, only the temperature effect on viscosity is significant [37]. Gao et al. experimentally studied the scale effects in two-dimensional mini- and micro-channels with channel height of 0.1 to 1 mm and found that the conventional laws of hydrodynamics and heat transfer can be applied to channels with the height of 0.4 mm and greater [95].

It is seen that many investigations on single phase heat transfer and flow distributions in minichannels have been conducted. However, the study on uniformity of mass and heat transfer in multi-port MICHX slab is rare in open literature. Therefore, in the present study, three-dimensional numerical simulations have been performed for cooling of ATF, ethylene glycol, and water to predict the uniformity of heat and mass transfer distribution in circular minichannels.

2.1.4 Benefits of Crossflow MICHXs

The necessity of size and weight reduction and thermal improvement of each component as well as overall system drives the advancement of compact heat exchangers [25, 37, 41]. These necessities are also significantly applicable in refrigeration and air conditioning systems. The refrigerant charge reduction and performance enhancement in conjunction with key safety and operating considerations are the primary concern of the urban architects. Minichannels offer a sustainable solution to address these concerns and are likely to be commonly used in residential, commercial, and industrial applications [29].

Minichannel heat exchanger leads to reduction of size and improvement of performance in air-conditioning systems [29]. Kim and Bullard [96] evaluated the performance of MICHX and finned round-tube condenser as a benchmark. They [96] reported 35% reduction of refrigerant charge in the MICHX design and 35–55% reduction of core volume and weight for the identical energy efficiency ratio (EER). The performance of a unitary split system using MICHX with a conventional fin-tube outdoor coils for air conditioning and heat pumping applications were compared by Kim and Groll [97]. Authors reported that MICHX needed 23% less face area and 32% less refrigerant-side volume than that of the baseline heat exchanger. The improvement in EER ranged from 1∼6%, depending on the air-side fin density and heat exchanger orientation.

An air-to-liquid crossflow MICHX provides several benefits over a typical heat exchanger. These benefits include intensified heat transfer rate, reduced air blower capacity, minimized liquid pump power for a particular flow rate, reduced weight, and smaller unit size [41, 97, 98].

The flat slab of the multi-port minichannels can reduce the airside pressure drop resulting lesser blower power. For a certain heat duty, the elevated heat transfer characteristic of minichannels results in shorter channel lengths. These reduce the fluid residence time and subsequently, minimize the unexpected axial conduction. Minichannels also allow the entire fluid to be stayed in close contact with the channel wall. The parallel and typically well-distributed fluid flow in minichannels reduces the fluid velocity in each channel and results the shorter liquid side pressure drop and minimize the liquid side pumping power [33].

2.1.5 Summary

A comprehensive overview of the heat transfer and fluid flow characteristics of the minichannel heat exchanger (MICHX) have been presented. The optimization methods and disadvantages, pressure drop in particular, of the MICHX have also been analyzed. Massive stimulating characteristics and benefits of minichannel heat exchanger (MICHX) have been reported in the scientific literatures. Minichannel heat exchangers provide elevated and efficient heat transfer rate, compactness, robust structure and lower cost for the same heat duty. These benefits are increasingly attracting wide spread applications of MICHX in automotive, HVAC&R and industrial fields. The enriched heat transfer coefficient accompanying with narrow channel flow miniaturizes the heat transport devices in size. Since heat exchanger is one of the key component of energy conversion systems, research on MICHXs can be improved and extended through exploring novel schemes that exhibit more compact and enhanced heat transfer.

2.2 Nanofluid

Nanofluid is a new class of fluids containing nanoparticles dispersed in basefluid [17, 99–101]. Over the past decade, investigations on nanofluid have been expanded very rapidly due to the primary reports of unusual thermal conductivity improvement in nanofluids by a small volume fraction of nanoparticles [102, 103]. Nanofluids have better potential for enhancement heat transfer and suitable for real-world application in heat transfer processes [103].

Regardless of some inconsistency in the reported results and inadequate comprehension of the techniques of the heat transfer in nanofluids, they have been developed as a promising heat transfer liquid. This chapter illustrates recent researches on potential applications and challenges, synthesis, stability, thermophysical properties, pressure drop and heat transfer characteristics of nanofluids. Innovative models, numerical approaches, and techniques of the thermal improvement of nanofluids have also been proposed.

2.2.1 Brief History of Nanofluids

Nanofluids are engineered colloidal suspensions of nanometer-sized nanoparticles or nanoparticles with an average particle size less than 100 nm in basefluids [104]. The Environmental Protection Agency (EPA) of the United States has defined four terms for classifying particles of different sizes. Table 1 [105] displays the EPA terminology along with the corresponding particle sizes.

Table 1: EPA particle size terminology

EPA Description	**Particle Size**
Supercoarse particles	$d_p > 10\ \mu m$
Coarse particles	$2.5\ \mu m < d_p \leq 10\ \mu m$
Fine particles	$0.1\ \mu m < d_p \leq 2.5\ \mu m$
Ultrafine particles (UFP) [106] Nanoparticles (after 1990s)	$d_p \leq 0.1 \mu m$

Nanoparticles used in nanofluids are usually made of metals, oxides, nitrides, carbides, or carbon nanotubes [107]. Conventional basefluids incorporate water, ethylene glycol, and oil. The inherently low thermal conductivity of these fluids place a crucial boundary on heat transfer. As a result, for more than a century since Maxwell's theoretical work in 1873 [108], researchers have made countless efforts to break the essential limits by dispersing milimeter- or micrometer-sized particles in liquids to increase their thermal conductivities. However, these sorts of fluids have not conventionally been employed in real-world heat transfer applications because of the issues associated with erosion, sedimentation, fouling, and higher pressure drop related to its flow through the channels [109]. Modern developments in the approaches for production of small particles have permitted us to produce nanoparticles that suspended into base fluids can avoid the said issues [109].

In 1974, Scientist Norio Taniguchi, first used the term Nanotechnology. After that, Choi conceived the innovative idea of nanofluids in 1993. Later in 1995, S.U.S. Choi and

J.A. Eastman [17], first, successfully prepared nanofluid at Argonne National Laboratory Argonne Laboratory. After the foundation of such a milestone in the history of nanoscience, nanofluid gets the attention of the scientists and engineers around the world. I recent years, researchers in the areas of rapidly growing nanofluids have made scientific revolution in finding amazing thermal properties and enhancing friction and erosion characteristics of nanofluids [110]. The amount of published articles, journal papers, proceedings, reviews, and editorial articles on the nanofluid arena hits about 12 thousand during the previous couple of decades [111]. The trend of nanofluid research has moved to such a place that in 2018 (as on December) alone, more than 25 hundred research papers were published [111]. The trend indicate an exponential development in nanofluid research from 10 in 2003, 303 in 2010, 1336 in 2015 and 2438 in 2017 [111]. Figure 2.3 [111] presents a breakneck growth in nanofluid research.

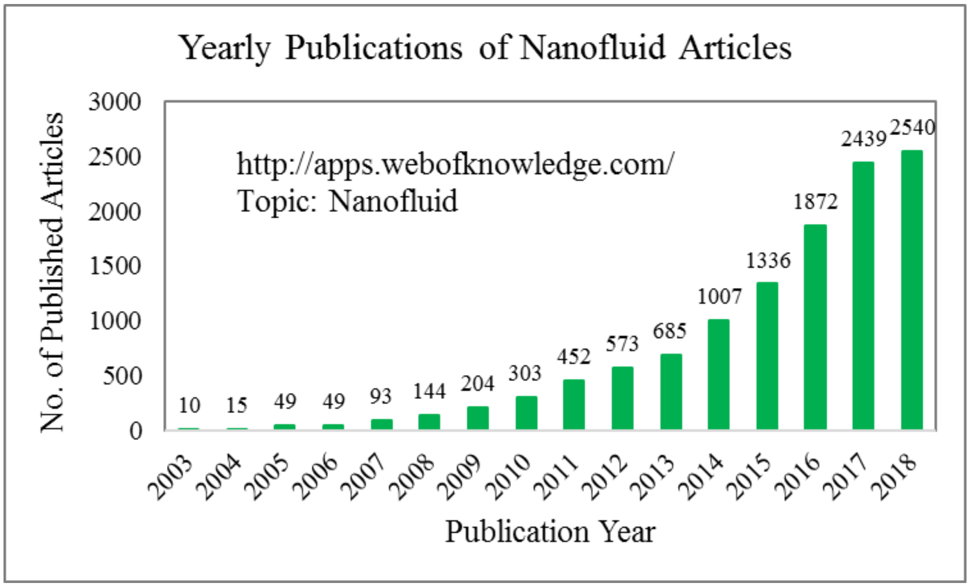

Figure 2.3: Yearly published research papers on nanofluid investigations

A quick review of research on nanofluid heat transfer in past years is presented in Figure 2.4 [111].

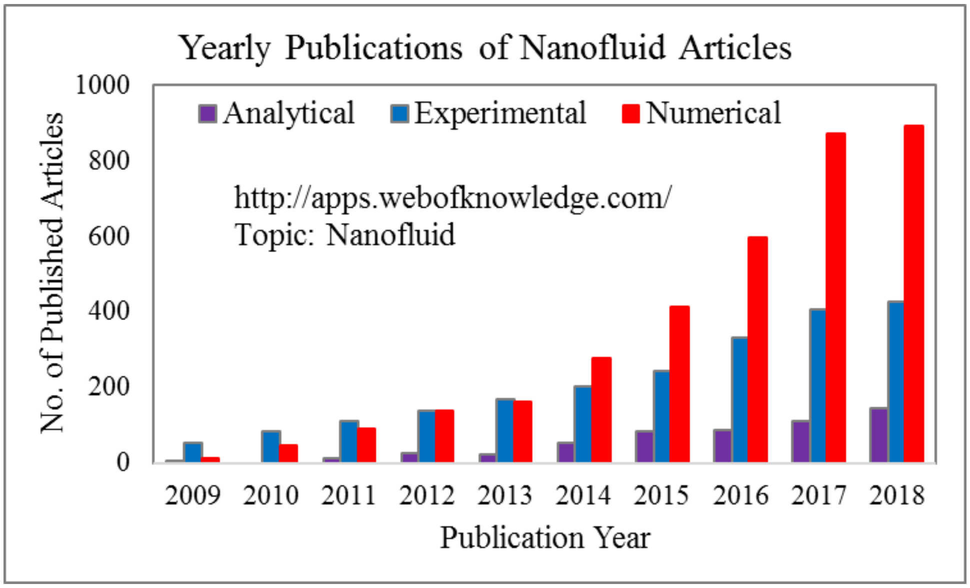

Figure 2.4: Summery of nanofluid articles in the field of heat transfer

In all areas including experimental, analytical, and numerical, the attention of research on nanofluid heat transfer are growing exponentially.

2.2.2 Characteristics and Challenges of Usages of Nanofluids

At the early stage of nanofluid investigations, researchers believed that the volume concentration and size of the nanoparticles are the two key factors which significantly impact the effective thermal conductivity of the nanofluids. However, from the recent experimental investigations, it is revealed that numerous factors, including types and shapes of the nanoparticles, thermophysical properties of the nanofluids, and working temperature also significantly effect on the heat transfer performance of nanofluids. It is still ambiguous, which factor is more vital. Scientist and engineers realized that the precise mechanism of heat transfer in nanofluids is ambiguous, uncertain, and complex; the conventional model cannot properly predict the anomalous improvement of the effective thermal conductivity of nanofluids.

Many researchers [107, 112–114] reported that in turbulent flow, fluids with larger particle of mm-sized and above are not appropriate as heat transfer fluids; it is because the large particles result erosion on the devices and deposit on the walls. Nanofluids have overcome these disadvantages in the light of the fact that they are made out of smaller particles (usually less than 100µm) that do not have significant sedimentation velocities to deposit promptly; as a result of their low mass and inertia, they do not cause device erosion.

The enhanced heat and mass transfer characteristics of nanofluids are because of two factors: (a) the significantly improved thermal conductivity of the fluid by the addition of very high conductivity nanoparticles; and (b) the neighborhood agitation due to the relative movement of the nanoparticles in the fluid [115].

2.2.3 Thermophysical Properties of Nanofluids

Since the suspended particles in nanofluid are very fine, the particles may easily be fluidized; subsequently, by overlooking the slip motion between particles and fluid and assuming the base fluid and the nanoparticles are in thermal equilibrium, the nanofluid has been treated as a homogenous fluid [116–118].

In this section, four thermophysical properties namely, density, specific heat, thermal conductivity, and dynamic viscosity of different nanofluids are discussed.

Density of nanofluids: Many researchers [119–125] have applied the principle of mass conservation in order to calculate the density of nanofluids. The total mass ($\mathrm{m_{nf}}$) within a finite control volume ($\mathrm{V_{nf}}$) of the nanofluid continuum is the sum of nanoparticles and basefluid masses which is expressed as

$$\mathrm{m_{nf}} = \left[\emptyset \rho_{\mathrm{np}} + (1-\emptyset)\rho_{\mathrm{bf}}\right]\mathrm{V_{nf}} \tag{2.6}$$

where $\emptyset$ is the volumetric fraction of nanoparticles in the base fluid, ρ_{np} is the density of nanoparticles, and ρ_{bf} is the density of basefluid.

The bulk density (ρ_{nf}) of nanofluid as the ratio of the its mass to volume is obtained from following correlation [126];

$$\rho_{\mathrm{nf}} = \frac{\mathrm{m_{nf}}}{\mathrm{V_{nf}}} = \emptyset \rho_{\mathrm{np}} + (1-\emptyset)\rho_{\mathrm{bf}} \tag{2.7}$$

This equation is frequently used by researchers for calculating the density of nanofluids.

Specific heat of nanofluids: A few researchers [127, 128] have used the volume-averaged specific heat ($\mathrm{c_{p_{nf}}}$) of nanofluid expression offered by Pak and Cho [126] in order to calculate the $\mathrm{c_{p_{nf}}}$ as follows;

$$\mathrm{c_{p_{nf}}} = \emptyset \mathrm{c_{p_{np}}} + (1-\emptyset)\mathrm{c_{p_{bf}}} \tag{2.8}$$

where $\mathrm{c_{p_{np}}}$ and $\mathrm{c_{p_{bf}}}$ represent the specific heat of nanoparticles and basefluid, respectively.

This volume-averaged specific heat may not applied directly to calculate the specific heat of nanofluid of the two constituent phases [129]. It is necessary to apply the principle of thermal energy conservation. The thermal conservation of energy of the two species in a finite control volume yields the overall specific heat of the nanofluid [123, 129]. Referring to the total mass ($\mathrm{m_{nf}}$) in the control volume ($\mathrm{V_{nf}}$), the enthalpy ($\mathrm{h_{nf}}$) and specific heat ($\mathrm{c_{p_{nf}}}$) of a nanofluid are defined as

$$\mathrm{h_{nf} = m_{np}h_{np} + m_{bf}h_{bf}} \tag{2.9}$$

$$\mathrm{c_{p_{nf}}} = \frac{1}{\mathrm{m_{nf}}}\left(\frac{\partial \mathrm{h_{nf}}}{\partial \mathrm{T}}\right)_{\mathrm{P}} = \frac{1}{\mathrm{m_{np}+m_{bf}}}\left(\mathrm{m_{np}c_{p_{np}} + m_{bf}c_{bf}}\right) \qquad ((2.10)$$

Expressing the masses of the basefluid (liquid) and the nanoparticles (solid) phases corresponding to their volume fractions and densities, the specific heat of the nanofluids yield the following correlation [130]:

$$\mathrm{c_{p_{nf}}} = \frac{\emptyset(\rho \mathrm{Cp})_{\mathrm{np}}+(1-\emptyset)(\rho \mathrm{Cp})_{\mathrm{bf}}}{\emptyset\rho_{\mathrm{np}}+(1-\emptyset)\rho_{\mathrm{bf}}} \tag{2.11}$$

It is an advanced form of Pak and Cho 1998 correlation and used by many researchers [121–123, 131, 132]. The equation (2.10) predicts specific heat of a nanofluid very well and supported by most of the experimental data available in the open literatures as stated by the authors [121–123, 131, 132].

Thermal conductivity of nanofluids: Nanofluids became the immense research interest during the past decade, mostly due to the strange enhancement of thermal conductivity of the nanofluid reported by early experimental studies. The thermal conductivities of some of the constituent materials, which are frequently used in nanofluids are listed below Table 2 [129].

Table 2: Thermal conductivities of some common materials used in nanofluids.

Solids (nanoparticles)	Thermal conductivity k_{np} [w/mK]	Liquids (Basefluids)	Thermal Conductivity k_{bf} [w/mK]
Sliver (Ag)	427	Water	0.613
Copper (Cu)	395	Ethylene glycol	0.253
Aluminum (Al)	237	Alcohol	0.115
Carbon nanotubes (CNT)	3,200–3,500	Glycerol	0.285
Brass (Cu_3Zn_2)	120		
Nickel (Ni)	91		
Alumina (Al_2O_3)	39		

It is obvious that the thermal conductivity of the nanoparticle is very high compared to the thermal conductivity of the basefluid. As a result, it is anticipated that the addition of a fraction of nanoparticles in the basefluid would significantly increase the thermal conductivity of the nanofluids [133]. The highest intensification in the thermal conductivity is found with carbon nanotubes (CNT) suspension – both single-and multi-walled, which has significantly high thermal conductivity of more than 3,000 w/mK in the longer fibers with elevated aspect ratio. S. Iijima [117] proposed a convenient technique to manufacture the carbon nanotubes; many investigators measured effective thermal conductivity; and they concluded that these synthesis are highly promising in the fiend of heat transfer.

High thermal conductivity metals including silver (Ag), copper (Cu), and gold (Au) and their chemical compounds also significantly increase the effective thermal conductivity of nanofluids [129]. Chopkar et al. [134] investigated thermal conductivity of 2% Ag_2Al nanoparticle and Al_2Cu nanoparticle suspensions, and evaluated the enhancement of thermal conductivity by 100%. Likewise, Patel et al. [135] conducted experimental investigation on pure silver (Ag) and gold (Au) nanoparticles. They found $5-21\%$ enhancement of thermal conductivity with 0.025% vol concentration of Ag nanoparticles and $7-14\%$ enhancement with 0.01% vol concentration of Au nanoparticles. Effective thermal conductivity enhancement is retrieved from several sets of experimental investigations [134, 136–142] and presented in Figures 2.5 to 2.7.

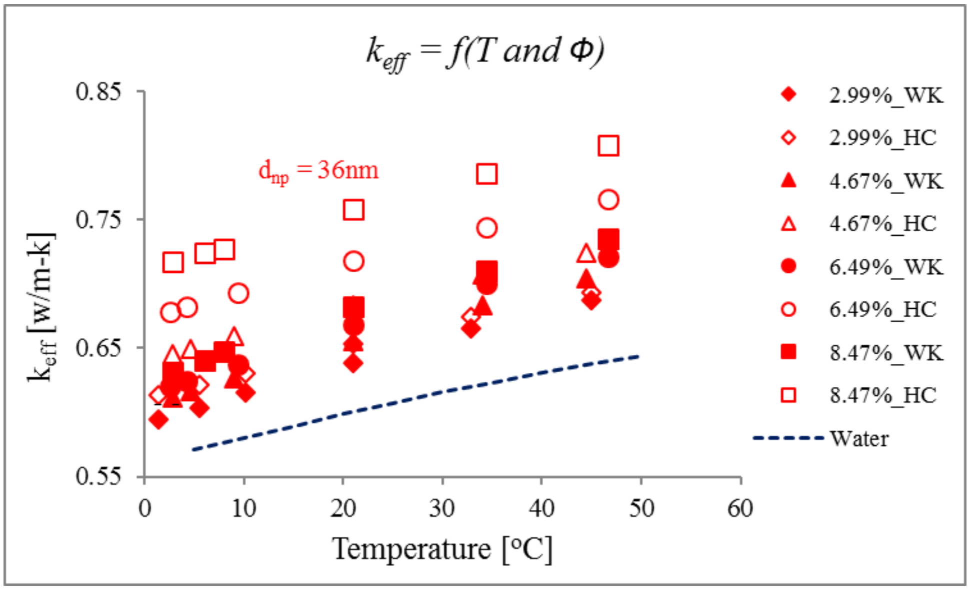

Figure 2.5: Effect of volume concentration of nanofluids on effective thermal conductivity

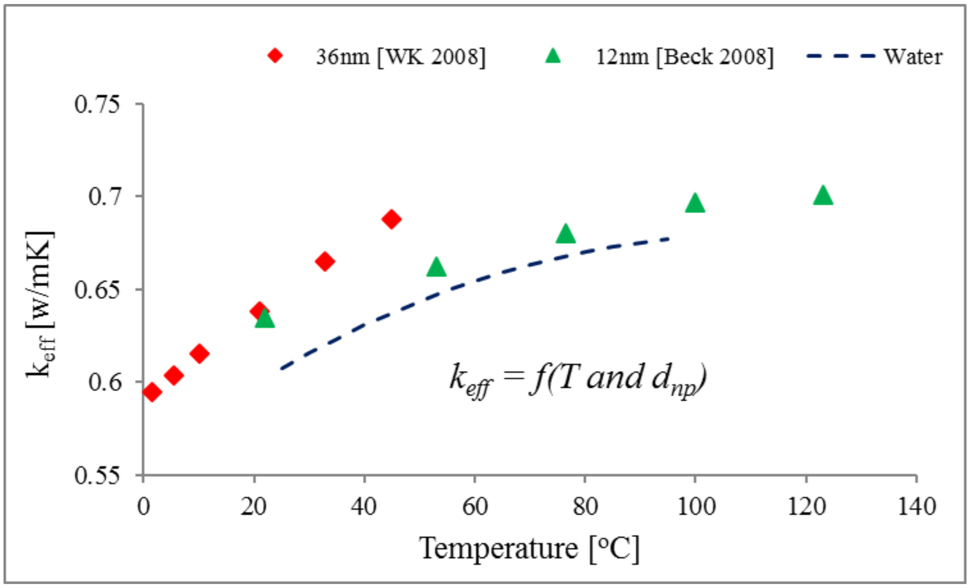

Figure 2.6: Effect of particle size on effective thermal conductivity of nanofluids

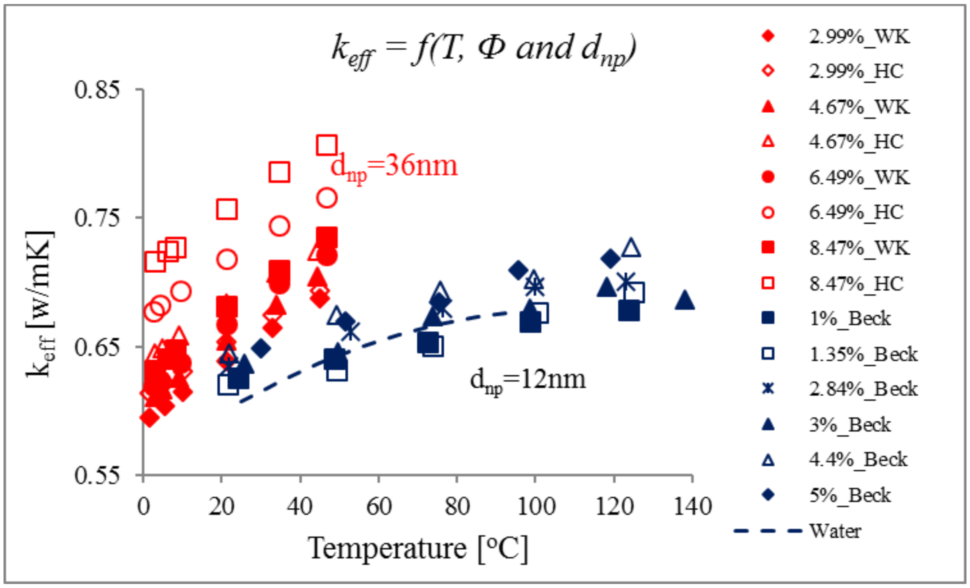

Figure 2.7: Effect of concentration and particle size on effective thermal conductivity

The preliminary investigations reported 100–200% heat transfer enhancement in nanofluids is due to the addition of nanoparticles even with a small percentage [129]. Many experiments [109, 126, 139–141, 143–153] have been done for the determination of thermal conductivity of various nanofluids. Majority of the experimental investigations have been conducted on spherical shaped nanoparticles with diameter range of $20\text{nm} \leq d_p \leq 170\text{nm}$, temperature range of $20℃ \leq T_{nf} \leq 70℃$ and volume concentration of $\emptyset \leq 4.0\%$. The experiments have been mostly conducted on Al_2O_3, CuO, Cu, TiO_2, SiC, ZrO_2 particles dispersed in water [123].

There are several controversial reports of anomalous enhancement in thermal conductivity [102]. Several experimental studies reported that the most influential parameters of thermal conductivity enhancement in nanofluids include the type, size, properties, and volume fraction of nanoparticles as well as the type of the basefluid and the articles. The heat transfer enhancement of nanofluid also significantly depends on many other factors such as, preparation mechanism, synthesis, the pH and the type of surfactants to stabilize the nanofluid [133, 154–160].

Analytical expressions and correlations: Several techniques have been offered in order to explain the thermal conductivity enhancement. An expression for the electrical conductivity of composite mixture of spherical particles in a fluid were derived by Maxwell [108]. Maxwell's expression for nanofluid, where the thermal conductivity of nanoparticles (k_{np}) are greater than the thermal conductivity basefluid (k_{bf}), is

$$k_{nf} = k_{bf}\left[1 + \frac{3(k_{np} - k_{bf})\emptyset}{k_{np} + 2k_{bf} - (k_{np} - k_{bf})\emptyset}\right] \tag{2.12}$$

where k_{nf} is the thermal conductivity of a nanofluid in w/mK and ø is the nanoparticles concentration in volume fraction of nanoparticles [%vol].

More precise analytical expression for the electrical conductivity of particles has been derived by Bruggeman [161]. This expression can be applied for the thermal conductivity of cylindrical or spherical nanoparticle suspension as below:

$$\mathrm{k_{nf}} = \mathrm{k_{bf}}\left[\frac{\mathrm{k_{np}}+(\mathrm{n}-1)\mathrm{k_{bf}}+(\mathrm{n}-1)\emptyset(\mathrm{k_{np}}-\mathrm{k_{bf}})}{\mathrm{k_{np}}+(\mathrm{n}-1)\mathrm{k_{bf}}-\emptyset(\mathrm{k_{np}}-\mathrm{k_{bf}})}\right] \qquad (2.13)$$

where, $\mathrm{n} = 3$ and $\mathrm{n} = 6$ for spherical and cylindrical particles, respectively.

Xuan et al. [162] performed an analytical study on the Langevin equation of the Brownian motion along with the concept of the stochastic Brownian motion of nanoparticles in the basefluid. The influence of the Brownian motion has been superimposed to the Maxwell's model of conductivity. The effects of size and volume fraction of nanoparticles on the effective thermal conductivity have also been taken into account. The authors derived the following correlation for the effective thermal conductivity of the nanofluids [162] :

$$\mathrm{k_{eff}} = \mathrm{k_{bf}}\left[1+\frac{3(\mathrm{k_{np}}-\mathrm{k_{bf}})\emptyset}{\mathrm{k_{np}}+2\mathrm{k_{bf}}-(\mathrm{k_{np}}-\mathrm{k_{bf}})\emptyset}\right]+\frac{9\emptyset \mathrm{h}\mathrm{k_B}\mathrm{T}}{8\pi\rho_{\mathrm{np}}\alpha^4} \qquad (2.14)$$

where h represents the convective heat transfer coefficient of nanofluid.

Many other researchers [163–170] also derived various models for determination of effective thermal conductivity of nanofluid suspensions as shown in Table 3.

Table 3: Correlations of effective thermal conductivity of nanofluid suspensions

Model	Expressions
Hamilton and Crosser [163]	$\mathrm{k_{eff}} = \left[\frac{\mathrm{k_{np}} + (\mathrm{n}-1)\mathrm{k_{bf}} - (\mathrm{n}-1)\emptyset(\mathrm{k_{bf}} - \mathrm{k_{np}})}{\mathrm{k_{np}} + (\mathrm{n}-1)\mathrm{k_{bf}} + \emptyset(\mathrm{k_{bf}} - \mathrm{k_{np}})}\right]\mathrm{k_{bf}}$ where, shape factor, $\mathrm{n} = \frac{3}{\psi}$, and sphericity, $\psi = \frac{\text{surface area}}{\text{volume}}$
Yu and Choi [167]	$\mathrm{k_{eff}} = \left[\frac{\mathrm{k_{np}} + 2\mathrm{k_{bf}} + 2(\mathrm{k_{np}} - \mathrm{k_{bf}})\emptyset}{\mathrm{k_{np}} + 2\mathrm{k_{bf}} - (\mathrm{k_{np}} - \mathrm{k_{bf}})\emptyset}\right]\mathrm{k_{bf}}$
Jeffrey [168]	$\mathrm{k_{eff}} = \left[1 + 3\beta\emptyset + \left(3\beta^2 + \frac{3\beta^3}{4} + \frac{9\beta^3}{16}\frac{\alpha+2}{2\alpha+3} + \frac{3\beta^4}{2^6} + \cdots\right)\emptyset^2\right]\mathrm{k_{bf}}$ where, the field factor, $\beta = (\alpha - 1)/(\alpha + 2)$
Davis [169]	$\mathrm{k_{eff}} = \left(1 + \frac{3(\alpha-1)}{(\alpha+2) - (\alpha-1)\emptyset}\left[\emptyset + \mathrm{f}(\alpha)\emptyset^2 + \mathrm{o}(\emptyset^3)\right]\right)\mathrm{k_{bf}}$ where, thermal conductivity ratio, $\alpha = \mathrm{k_{np}}/\mathrm{k_{bf}}$
Lu and Lin [170]	$\mathrm{k_{eff}} = [1 + \mathrm{a}\emptyset + \mathrm{b}\emptyset^2]\mathrm{k_{bf}}$

Khanafer and Vafai [171] derived another expression for the effective thermal conductivity of suspensions by using several sets of data of $\mathrm{Al_2O_3}$ and CuO nanoparticles in water at ambient temperatures:

$$\frac{\mathrm{k_{eff}}}{\mathrm{k_{bf}}} = 1 + 1.0112\emptyset + 2.4375\emptyset\frac{47}{\mathrm{d_{np}}} - 0.0248\emptyset\frac{\mathrm{k_{np}}}{\mathrm{k_{bf}}} \tag{2.15}$$

where $\mathrm{d_{np}}$ is the particle size in nm and $\mathrm{k_{bf}}$ is the thermal conductivity of basefluid, $\mathrm{k_{bf}} = 0.613$ w/mK for water.

Azmi et al. [123] performed a regression analysis on available data the thermal conductivity of nanofluid in open literature. They developed a correlation of effective thermal conductivity of nanofluid by taking the influence of material, volume concentration, particle size and temperature. The effect of the thermal diffusivity ratio of particle to water (α_p/α_w) is also accounted for the nanofluid thermal conductivity evaluation. The authors developed the following correlation in order to determine the thermal conductivity of nanofluid (k_{nf});

$$k_{eff} = k_{bf}\left[0.8938\left(1+\frac{\emptyset}{100}\right)^{1.37}\left(1+\frac{T_{nf}}{70}\right)^{0.2777}\left(1+\frac{d_p}{150}\right)^{-0.0336}\left(\frac{\alpha_p}{\alpha_{bf}}\right)^{0.01737}\right] \tag{2.16}$$

where, ø is the nanoparticle concentration in %vol, T_{nf} is temperature in °C, d_p is nanoparticle size in nm, and $\frac{\alpha_p}{\alpha_{bf}}$ is the thermal diffusivity ratio of the nanoparticle to the water.

Another correlation for the effective thermal conductivity of Al_2O_3 nanofluids developed by Chon et al. [148]. The authors choose several samples of water based Al_2O_3 nanofluid containing $11\,nm$, $47\,nm$ and $150\,nm$ sized Al_2O_3 nanoparticles at temperature range of $21°C$ to $71°C$ with $\pm 0.01°C$ accuracy. They developed the correlation based on the Buckingham-Pi theorem using linear regression for the experimental results as

$$k_{eff} = \left(1 + 64.7 \cdot \emptyset^{0.7460} \cdot \left(\frac{d_{bf}}{d_{np}}\right)^{0.3690} \cdot \left(\frac{k_{np}}{k_{bf}}\right)^{0.7476} \cdot Pr^{0.9955} \cdot Re^{1.2321}\right) k_{bf} \tag{2.17}$$

where d_{bf} is the molecular diameter of base fluid, d_{np} is the nanoparticles diameter, k_{eff} is the effective thermal conductivity of nanofluid, k_{bf} is the thermal conductivity of base fluid, k_{np} is the nanoparticle thermal conductivity, and $\emptyset$ is the nanoparticle volume fraction. The Prandtl number (Pr) is defined as

$$\Pr = \frac{\mu}{\rho_{BF}\alpha} \tag{2.18}$$

where μ is the base fluid viscosity given as

$$\mu = A10^{B/(T-C)} \tag{2.19}$$

For water, constants A, B and C are 2.414×10^{-5}, 247.8 and 140, respectively.

The Reynolds number is defined as

$$Re = \frac{\rho_{bf} V_{Br} d_{np}}{\mu} = \frac{\rho_{bf} K_B T}{3\pi\mu^2 l_{bf}} \tag{2.20}$$

where, the mean free path for water, $l_{bf} = 0.17\text{nm}$, Boltzmann constant, $K_B = 1.3807 \times 10^{-23}\ \text{j/K}$, V_{Br} is the Brownian velocity of the nanoparticles based on the Einstein diffusion theory given by

$$V_{Br} = \frac{k_{bT}}{3\pi\mu d_{np} l_{bf}} \tag{2.21}$$

A model for prediction of the effective thermal conductivity of nanofluid was presented by Abbaspoursani et al. [172]. The authors considered that the effective thermal conductivity of nanofluid (k_{eff}) depends on the thermal conductivity of nanoparticle (k_{np}), basefluid (k_{bf}), and interfacial shell (k_i), as well as the nanoparticle diameter (d_{np}), volume concentration (Φ), interfacial shell thickness (t), nanofluid temperature (T), and the half of the boiling temperature of basefluid (Tc). Their expression is presented below:

$$\mathrm{k_{eff}} = \mathrm{k_{bf}}\left[1 + \mathrm{m}\frac{\emptyset^{\alpha}}{\mathrm{d_{np}}^{\beta}}\mathrm{T}^{\delta} + \mathrm{n}\emptyset\ 1 - \frac{\mathrm{d_c}}{\mathrm{d_{np}}}\mathrm{T}\right] \text{ for } \mathrm{d_{np}} \geq \mathrm{d_c} \qquad (2.22)$$

where, m, α, β, n, $\mathrm{d_c}$ and δ are the model parameters given in Table 4.

Table 4: Model parameters for TiO_2/water and Al_2O_3/water systems

Parameters	Quantity	
	TiO_2/water system Based on data [173–175]	Al_2O_3/water system Based on data [176, 177]
m	515	10
α	0.912	0.350
β	51.9	2.6
n	4	0.0121
$\mathrm{d_c}$	20	21
δ	0	1

In numerical investigations, researchers [116, 118, 120, 121, 154, 178–249] commonly used either single-phase or two-phase models for nanofluid flow and heat transfer. In single-phase models, some researchers considered the nanofluid as a homogeneous fluid; whereas, others considered dispersion models in order to determine the effective thermal conductivity of nanofluid. Following expressions have been used;

$\mathrm{k_{eff}} = \mathrm{k_{static}} = \mathrm{k_{nf}}$, for the homogeneous single-phase model

$\mathrm{k_{eff}} = \mathrm{k_{nf}} + \mathrm{k_{disp}}$, for dispersion models

$k_{disp} = C_1 (\rho c_p)_{nf} \emptyset_{np} d_{np} uR$, proposed by Xuan and Roetzel [130]

$k_{disp} = C_1 (\rho Cp)_{nf} \emptyset_{np} \frac{\partial u}{\partial r} \frac{R}{d_{np}}$, proposed by Mokmeli and Saffar-Avval [219]

where, k_{disp} denotes the thermal conductivity of a nanofluid due to the dispersion effects, C_1 is the dispersion coefficient, R is the channel or tube radius in m, u is the fluid velocity in m/s, d_{np} is the nanoparticle size in nm.

Figure 2.8 illustrates the k_{eff} of 2%volume. Al_2O_3/W nanofluids for homogeneous single-phase and dispersion models. The dispersion model predicts higher k_{eff}.

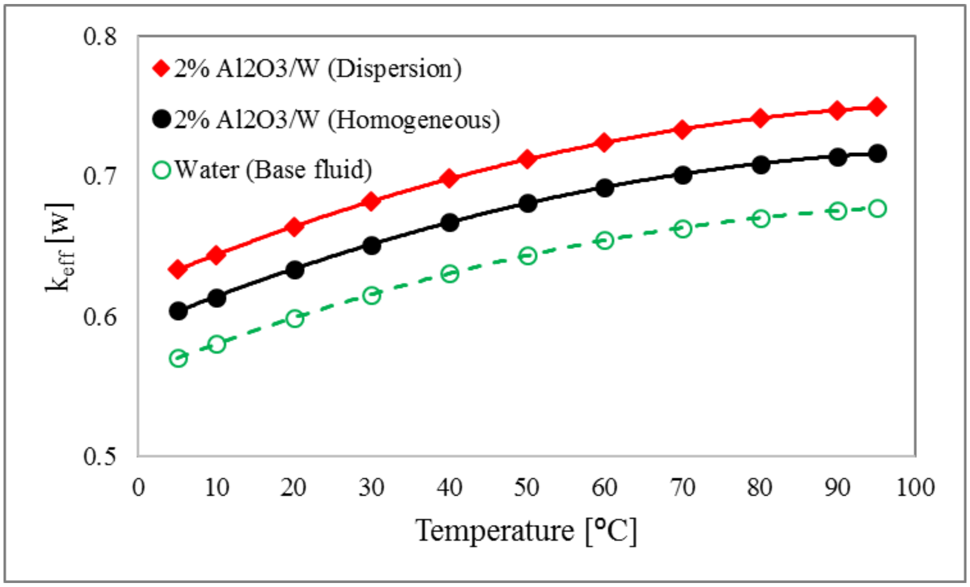

Figure 2.8: Effective thermal conductivity of Al_2O_3/W nanofluids at single-phase homogeneous and dispersion approaches

The thermal conductivity of nanofluid due to Brownian motion ($k_{Brownian}$ or $k_{dynamic}$) was derived by Koo and Kleinstreuer [250] and superimposed to the effective thermal conductivity of nanofluid as

$$\mathrm{k_{eff}} = \mathrm{k_{static}} + \mathrm{k_{dynamic}} = \mathrm{k_{nf}} + \mathrm{k_{Brownian}} \tag{2.23}$$

where, $\mathrm{k_{Brownian}} = 5 \times 10^4 \beta \emptyset \rho_{bf} c_{p_{bf}} \sqrt{\frac{k_B T}{\rho_p d_p}} f(T, \emptyset, \text{etc.})$

$\beta = 0.0017(100\emptyset)^{-0.0841}$, $\emptyset > 1\%$ [233] and

$f(T, \emptyset) = (-6.04\emptyset + 0.4705)T + (1722.3\emptyset - 134.63)$ [250]

In two-phase approaches such as, Volume of Fraction (VOF), Eulerian-Mixture, Eulerian-Eulerian, Eulerian-Lagrangian models, the effective thermal conductivity as well as other thermophysical properties have been considered for two distinct phases, solid (nanoparticle) and liquid (basefluid).

Dynamic viscosity of nanofluid: Viscosity of a fluid is its resistance to motion. The dynamic viscosity (μ) of a homogeneous fluid is defined as the local shear stress (τ) developed by the fluid motion and the local velocity gradient ($\partial u/\partial y$).

$$\mu = \frac{\tau}{(\partial u/\partial y)} \tag{2.24}$$

The above equation for the dynamic viscosity applies at every point of Newtonian fluids. Most of the base fluids used in nanofluids are Newtonian [129]. As the dynamic viscosity of a base fluid is strongly depends on temperature, the viscosity of the nanofluid is a strong function of the temperature. The viscosity of a nanofluid is also a strong function of the dispersion of the nanoparticles in the basefluid. This is because the particles move with different velocities than the fluid molecules. The relative velocity of the nanoparticles develop secondary velocity field, interaction and collision, which effects the shear stress nearby the particles. The models for determining the viscosity of nanofluid are as belows:

Brinkman [251]: $\mu_{nf} = \mu_{bf}/(1 - \emptyset)^{2.5}$, for $\emptyset<4\%$ (2.25)

Einstein [252]: $\mu_{nf} = (1 + 2.5\emptyset)\mu_{bf}$, for $\emptyset<2\%$ (2.26)

Batchelor [253]: $\mu_{nf} = (1 + 2.5\emptyset + 6.5\emptyset^2)\mu_{bf}$ (2.27)

Lundgren [254]: $\mu_{nf} = (1 + 2.5\emptyset + \frac{25}{4}\emptyset^2 + 0\emptyset^3)\mu_{bf}$ (2.28)

It is noticeable that there is no significant difference in the nanofluid viscosities among the above models. Some other models are also presented below:

Graham [255]: $\mu_{nf} = (1 + 2.5\emptyset + 4.5\left[\frac{1}{\left(\frac{h}{d_p}\right)\cdot\left(2+\frac{h}{d_p}\right)\cdot\left(1+\frac{h}{d_p}\right)^2}\right])\mu_{bf}$ (2.29)

Maiga et al. [209]: $\mu_{nf} = (123\emptyset^2 + 7.36\emptyset + 1)\mu_{bf}$ (2.30)

Nguyen et al. [256]: $\mu_{nf} = (0.904e^{0.1483\emptyset})\mu_{bf}$, for 47nm (2.31)

$\mu_{nf} = (1 + 0.025\emptyset + 0.015\emptyset^2)\mu_{bf}$, for 36nm (2.32)

$\mu_{nf} = (1.125 - 0.0007T)\mu_{bf}$, for $1\%\emptyset$ (2.33)

$\mu_{nf} = (2.1275 - 0.0215T + 0.0002T^2)\mu_{bf}$, for $4\%\emptyset$ (2.34)

Masoumi et al. [257]: $\mu_{nf} = \mu_{bf} + \mu_{apparent} = \mu_{bf} + \frac{\rho_p V_B d_p^2}{72C\delta}$ (2.35)

where, $V_B = \frac{1}{d_p}\sqrt{\frac{18K_bT}{\pi\rho_p d_p}}$, $\delta = \sqrt[3]{\frac{\pi}{6\emptyset}}d_p$, and $C = \frac{a\emptyset+b}{\mu_{bf}}$

Azmi et al. [123]: $\mu_{nf} = \mu_{bf}\left(1 + \frac{\emptyset}{100}\right)^{11.3}\left(1 + \frac{T_{nf}}{70}\right)^{-0.038}\left(1 + \frac{d_p}{170}\right)^{-0.061}$

for $\emptyset < 4\%$ (2.36)

2.2.4 Synthesis of Nanofluids

In order to synthesize stable nanofluids with enhanced thermophysical properties, varieties of combinations of nanoparticles and heat transfer fluids (base fluids) are used in the open literature. Nanoparticles prepared from metals, oxides, nitrites, carbides and carbon nanotubes are dispersed in base fluids, including water, ethylene glycol, engine oil, transmission fluid, and hydrocarbons with the presence or absence of surfactants (stabilizing agents) [159].

Two synthesized methods are used to prepare nanofluids: the two-step method and the one-step direct evaporation method. In two-step technique, nanoparticles are made first and then dispersed them into the base fluids. Whereas, in one-step method, nanoparticles are simultaneously made and dispersed them directly into the base fluids. In either technique, a properly mixed and homogeneously dispersed nanofluid is necessary for effective reproduction of properties and analysis of experimental data [258]. The first and the most common synthesis process of nanofluids used in the experimental investigations is two-step method [259]. Generally, dispersability of nanoparticles, chemical compatibility of nanoparticles and base fluids, stability of nanoparticles in base fluids, and thermal stability of nanofluids are considered for the improvement of the synthesis of nanofluids [259].

2.2.5 Stability of Nanofluids

Particles in dispersion may stick together and form cluster of larger size which may settle down because of the gravity. Stability means that the particles do not aggregate at an extensive rate. The agglomeration of nanoparticles results settlement and clogging of microchannels and reduces thermal conductivity of nanofluids [260]. Therefore, the research on the stability that influences the properties of nanofluids is one of the most important issues; it is essential to investigate the influencing factors to the dispersion stability of nanofluids. In this section, (a) the evaluation methods of stability, (b) the ways to enhance the stability, and (c) the mechanisms of stability for nanofluids are described.

Several methods, including sedimentation and centrifugation, zeta potential analysis, and spectral absorbency analysis have been developed to evaluate the stability of nanofluids. Among the various stability evaluation methods, sedimentation is the simplest one [155, 157]. The volume or weight of the sediment of nanoparticles in an external force field indicates the stability of the nanofluids. Nanofluids are considered to be stable when the concentration or particle size of the supernatant particles remain constant. A usual method of observing the stability of nanofluids is photography of sedimentation of nanofluids in test tubes [155]. Singh and Raykar applied the centrifugation method to observe the stability of silver nanofluids prepared by the microwave synthesis in ethanol by reduction of $AgNO_3$ with polyvinylpyrrolidone (PVP) as stabilizing agent [261]. Authors observed that the nanofluids were stable for more than 1 month in stationary condition and more than 10 hours under centrifugation at 3,000 rpm. Li and Kaner also used the centrifugation method to evaluate the stability of the aqueous polyaniline colloids [262]. Authors reported that the electrostatic repulsive forces between nanofibers empowered the long-term stability of the colloids.

Zeta potential is one of the key parameters that influences the stability of nanofluids. Zeta potential is electric potential in the interfacial double layer at the slipping's area versus a point in the bulk fluid away from the interface; it indicates the potential difference between the dispersion fluid and the stationary layer of fluid attached to the dispersed particles. It measures the magnitude of the electrostatic or charge attraction or repulsion between particles. The stability of colloidal dispersions depends on the value of zeta potential. High zeta potential (negative or positive) colloids are electrically stabilized; whereas, low zeta potential colloids have a tendency to coagulate or flocculate [260]. Yu and Xie [260] suggested that a positive or negative value of 25 mV can be considered as the margin of low-charged surfaces and highly charged surfaces. The authors also stated that the colloids with zeta potential of 40-60 mV exhibited good stability, and those with greater than 60 mV displayed outstanding stability.

Kim et al. [263] prepared gold (Au) nanofluids with an excellent stability due to a large negative zeta potential of Au nanoparticles in water. Authors observed no dispersants even after 1 month. Wang et al. [264] investigated the influence of pH and sodium dodecylbenzene sulfonate (SDBS) on the stability of $\mathrm{Al_2O_3/water}$ and $\mathrm{Cu/water}$ nanofluids. Authors reported that potential analysis could become increasingly important for enhanced heat transport. Water based aluminum oxide nanofluids were synthesized and their zeta potentials were measured by Zhu et al. [265]. Investigations were performed under different pH values and sodium dodecylbenzene sulfonate (SDBS) concentrations. Authors used the Derjaguin–Landau–Verwey–Overbeek (DLVO) theory used to evaluate repulsive and attractive potentials. They observed that the stability of $\mathrm{Al_2O_3/water}$ nanofluids were extremely dependent on the pH values as well as the concentration of SDBS dispersant of nanofluids. Higher absolute value of zeta potential were found at pH value of 8.0.

2.2.6 Numerical Approaches of Nanofluids

Several approaches have been used in the literature for the numerical studies of heat transfer and fluid flow characteristics of a nanofluid. Due to easiness and simplicity, most of the engineers and scientists have used the single-phase model. In this model, the fluid phase and nanoparticles are assumed to be at the same velocity and in thermal equilibrium. Nanofluid is considered as a single fluid homogeneous mixture. It is also assumed that the continuity and energy equations of the base fluid are not affected by the presence of the nanoparticles. On the other hand, in two-phase model, the base fluid and the nanoparticles are considered at two different phases, liquid and solid, respectively with different motion. The Eulerian-Lagrangian approach is used in two-phase model where each phase is treated as an interpenetrating continuum with distinct transport equations [194].

Different numerical methods used in open the literature are compiled in Table 5.

Table 5: Numerical approaches used in simulations of nanofluids

I. Single Phase Approaches i. Single Phase Homogeneous ii. Single Phase Dispersion
II. Two Phase Approaches i. Eulerian-Eulerian ▪ Volume of Fraction (VOF) ▪ Mixture ▪ Eulerian ii. Eulerian-Lagrangian
III. Lattice Boltzmann Method (LBM)

I. Single Phase Approaches

Since the suspended nanoparticles inside the base fluids are very fine, it has been considered that these nanoparticles may easily be fluidized. Subsequently, in many researches, nanofluids have been treated as a homogenous fluid by ignoring the relative motion between particles and fluid, and assuming the thermal equilibrium between them [266]. In this approach, the conservation equations of nanofluids are assumed to be similar to those of homogenous fluids; however, the effective properties of the nanofluids are applied for thermo-physical properties. Many researchers claimed that this method is simpler compared to the other approaches, needs less time for calculations, and provides relatively close results to the experimental ones. As a result, this method has attracted the attention of many researchers [266]. Mojarrad et al. [267] performed numerical studies using single-phase homogeneous and dispersion models. The authors studied the effect of nanoparticle concentration and Reynolds number on the convective heat transfer coefficient of nanofluids and compared their predictions with experimental results. They claimed that the homogeneous model is underestimated, whereas the dispersion approach provides more precise predictions.

II. Two Phase Approaches

In nanofluid, a number of factors including friction between the solid particles and basefluid, Brownian force, dispersion, thermophoresis and sedimentation can occur. Hence researchers are also using two-phase approaches in order to achieve more accurate results [266]. In the open literature, Eulerian–Eulerian and Eulerian–Lagrangian approaches are generally used in the two-phase methodologies on the nanofluid investigations. Eulerian–

Eulerian methods include three distinct models: volume of fluid (VOF), mixture, and Eulerian.

In the Eulerian–Lagrangian method, the dispersed nanoparticles are individually tracked in Lagrangian structure, whereas the fluid is computed in Eulerian frame. The Eulerian–Lagrangian is an appropriate approach for low concentration two-phase mixtures; however, it is challenging to directly use this method in the nanofluid simulation due to extremely high computational time caused by the presence of a huge number of particles even at a low concentration.

In order to investigate convective heat transfer of nanofluids in a horizontal circular tube with constant surface temperature, a numerical study was performed by Mojarrad et al. [267]. They carried out their numerical analysis using the two-phase models including mixture and Eulerian-Lanrangian models. They concluded that the mixture model was overestimated; however, the Eulerian–Lagrangian approach reasonably predicted the thermal behavior of nanofluids.

III. Lattice Boltzmann Method (LBM)

In Lattice Boltzmann Method (LBM) of nanofluid investigations, the interactions among the nanoparticles as well as the effective forces including gravity, buoyancy, and Brownian force are taken into account.

2.2.7 Applications of Nanofluids

The potential applications of nanofluids in heat transfer have increasingly been attracted the attention of researchers since the beginning of the nanofluid concept. Nanofluids have theoretically, numerically, and experimentally been shown to have enhanced heat transfer with enhanced thermophysical properties and better energy efficiency in heat transfer processes in a variety of transportations, industrial, nuclear reactors, residential as well as biomedicine and food applications [107, 159, 268–271]. Based on available literatures, the applications of nanofluids in various sectors are explicitly explained in this section.

Transportation and automotive applications:

In United States of America, Ford Motor Company and General Motors are running their own researches on nanofluids for the real-world applications in transportation. A C8.3 million FP7 project, NanoHex (Nanofluid Heat Exchange), involved 12 organizations from Europe and Israel. NanoHex is solving the technological challenges encountered in improvement and application of reliable and safe nanofluids intended for more environmentally friendly, energy efficient, and sophisticated products and services [260]

The conventional heat transfer fluids used in automotive and heavy-duty truck engines, radiators, and heating, ventilation and air-conditioning (HVAC) systems include engine oils, coolants, automatic transmission fluids, lubricants, and other synthetic high-temperature heat transfer fluids which possess inherently low heat transfer properties [260]. These could be benefitted from the high thermal conductivity displayed by nanofluids resulted from addition of nanoparticles [272, 273].

Nanofluid coolant: Vehicle cooling has a vital technological importance because it directly or indirectly affects engine performance, driver/passenger comfort, fuel economy, safety and reliability, emissions, vehicle aerodynamics, maintenance, and component life. Numerical simulations from the US department of energy’s office of vehicle technology predicted that nanofluid coolants could decrease the size of vehicle radiators by 5% resulted in a 2.5% fuel saving at highway speeds [271, 274, 275]. Therefore, an effective and responsive cooling system that is fuel-efficient and meet increasingly stringent emissions standards is crucial to the design and operation of over-the-road vehicles.

Nanofluids possess incredible possibilities to enhance automotive and heavy-duty engine cooling rates by reducing the weight, bringing down the complexity, and enhancing the efficiency of the thermal management systems. The enhanced heat transfer rates could be used to eliminate more heat from higher horsepower engines with the same size of cooling system which is beneficial to design more compact thermal management system for auto and truck [260]. The nanofluids possess high boiling point, elevate normal coolant operating temperature, and reject more heat through the existing coolant system [276].

Researchers have been attracted by ethylene glycol (EG) based nanofluids as engine coolant [277, 278] due to the less pressure drop compared to a 50/50 mixture of EG and water, which is the most commonly used automotive coolant. In 2010, Kole and Dey [279] prepared car engine coolant using $\mathrm{Al_2O_3}$ nanoparticles in a standard car engine coolant (HP KOOLGARD) and investigated the thermal conductivity and viscosity of the coolant. They observed that the nanofluid containing only 3.5% volume fraction of $\mathrm{Al_2O_3}$ nanoparticles showed a fairly higher thermal conductivity compared to the base fluid. They also claimed a maximum enhancement ($\mathrm{k_{nf}/k_{bf}}$) of 10.41% at room temperature. Tzeng et al. 2005 investigated the cooling of automatic transmissions applying dispersed CuO and $\mathrm{Al_2O_3}$ nanoparticles into engine transmission oil. The experiment was performed in the transmission system of a four-wheel drive vehicle. Authors measured the temperature distribution at the outside of the rotary-blade-coupling at four engine working speeds (400 rpm, 800 rpm, 1200 rpm, and 1600 rpm). They observed that CuO nanofluids generated lower transmission temperatures both at low and high rotational speeds. They reported that the use of nanofluid in the transmission has a clear advantage from the thermal performance viewpoint.

In searching for approaches to enhance the aerodynamic designs of vehicles, and successively the fuel efficiency, manufacturers must reduce the amount of energy required to overcome wind resistance on the road. At high speeds, about 65% of the aggregate energy yield from a vehicle is consumed in defeating the aerodynamic drag [268]. This is mostly because of the expansive radiator in front of the engine located to maximize the cooling effect of approaching air [268]. A research team of Argonne National Laboratory have evaluated the applications of nanofluids for transportation. They reported that the frontal area of a radiator can be reduced by up to 10% using the high-thermal conductive nanofluids. They also stated that up to 5% fuel can be saved due to the decrease in aerodynamic drag that opens the door to design novel aerodynamic automotive that reduce emissions.

Detection of knock occurrence in a SI engine: Ollivier et al. [280] numerically investigated the transient thermal signal around a spark ignition engine cylinder using a 5% $\text{Al}_2\text{O}_3/\text{water}$ nanofluid in order to detect knocks. Authors [280] reported that the variations of thermal signal for knock detection were increased by 15% over that predicted using water because of higher thermal diffusivity of nanofluids.

Brake nanofluids: Brake nanofluid has a higher demand for braking systems with greater efficient heat dissipation mechanisms and properties due to improved vehicle aerodynamics and reduced drag forces. The kinetic energy of a vehicle is dispersed through the heat produced during the process of braking and transmitted throughout the brake fluid in the hydraulic braking system. A vapor-lock is created when the heat causes the brake fluid to reach its boiling point; such an occurrence retards heat dissipation from the hydraulic system, causes a brake malfunction, and poses a safety hazard in vehicles. Nanofluids with enhanced characteristics maximize heat transfer performance and eliminate any safety concerns [268].

Kao et al. [281] conducted an experiment to examine the characteristics of Aluminum-oxide brake nanofluids (AOBN) produced by a home-made machine, a plasma arc system. Kao et al. [282] performed another experiment to investigate the characteristics of copper-oxide brake nanofluid (CBN) which was prepared by the arc-submerged nanoparticle synthesis system (ASNSS). Authors reported that both ABON and CBN have higher boiling point, higher viscosity, and a higher conductivity than that of traditional brake fluid. These enhanced properties of both nanofluids reduce the occurrence of vapor lock and offer increased safety while driving.

Nanofluid in fuel: Researchers have been working on the application of nanofluids as fuel additives that can improve the fuel efficiency. The scientists of nanoscale science, engineering, and technology council in USA have achieved increase of 10-25% combustion efficiency using 0.5% of aluminum nanoparticles to a rocket’s solid fuel [274]. Burning of fossil fuels have a significant contribution to produce the harmful gases including CO and $\mathrm{NO_x}$. Researchers experimentally proved that the production of such harmful gases can be minimized by using water based aluminum nanofluid as fuel additives. It is because aluminum nanoparticles possesses a high oxidation activity which allows increased decomposition of hydrogen from water during the combustion process [283]. Gan and Qiao [284] investigated the combustion characteristics of fuel droplets of ethanol and n-decane containing nano- and micron-sized aluminum particles. Authors found that the fuel completely burnt by suspending the aluminum nanoparticles with the fuel which may serve to improve fuel economy to an extent. Selven et al. [285] investigated the effects of cerium oxide nanoparticle addition in diesel and diesel-biodiesel-ethanol blends on the performance and emission characteristics of a comprssion ignition engine. Authors also found reduced emission of CO and $\mathrm{NO_x}$ gases. Cerium oxide absorbs oxygen for reduction of $\mathrm{NO_x}$ and provides oxygen for the oxidation of CO.

Friction and lubrication: Zhang and Que [286] investigated synthesis, structure and lubricating characteristics of dialkyldithiophosphate (DDP) modified Mo-S compound nanoclusters by a chemical method. Authors reported that MO-S compound nanocluster as an additive in paraffin oil significantly reduced wear and friction of the steel balls. Recently, many of researches have focused on improvement of tribological properties of nanolubricants. The performance and life span of vehicles increase due to the use of nanopowders suspended lubricants. Battez et al. [287] investigated the friction reduction characteristics of a NiCrBSi coating lubricated by CuO nanolubricant in a polyalphaolefin (PAO6). Authors reported that addition of CuO nanoparticles to the polyalphaolefin (PAO6) reduced friction compared to the base oil for a tribological contact steel–NiCrBSi coating; the antifriction characteristics of the nanoparticles on the wear surfaces act as third body (nano-bearings). They also stated that nanoparticles can react with surfaces forming antifriction compounds and deposit on the wear surfaces by tribosinterization. Kao and Lin [288] evaluated the tribological properties of spherical titanium oxide ($\mathrm{TiO_2}$) nanoparticles suspended paraffin oil. Authors reported that $\mathrm{TiO_2}$ nanoparticles applied as additives offer a rolling function, can fill the surface crack, increase viscosity as a lubricant, and reduce surface roughness, which leads to minimize the friction. They concluded that spherical $\mathrm{TiO_2}$ nanoparticles suspended in base oil are appropriate for tribological and lubrication applications in the mechanical industry.

Industrial Cooling Applications

The applications of nanofluids in industrial cooling may be greatly beneficial in energy savings and emissions reductions [260]. For US industry, the replacement of cooling and heating water with nanofluids has the potential to conserve 1 trillion Btu of energy [268, 289]. Authors reported that approximately 10–30 trillion Btu/year, equivalent to the energy consumption of about 50,000–150,000 households/year could be saved for the US electric power industry by using nanofluids in closed loop cooling cycles. They also stated that related emissions reductions would be about 5.6 million metric tons of $\mathrm{CO_2}$, 8,600 metric tons of $\mathrm{NO_x}$, and 21,000 metric tons of $\mathrm{SO_2}$ [268, 289]. For Michelin North America tire plants, more than 2 million gallons of heat transfer fluids is required to cool the rubber efficiently during numerous industrial processes. So, Michelin set a goal for the project to increase 10% productivity in its rubber processing plants using appropriate water-based nanofluids.

Han et al. [259] used phase-changeable nanofluids to enhance the effective thermal conductivity as we as the specific heat of the fluids. Authors synthesized a suspension of polyalphaolefin based indium (melting temperature of 157 ℃) nanofluids. They experimentally measured the temperature dependency as well as the thermophysical properties of fluids, such as thermal conductivity, specific heat, and viscosity. The authors observed that the melting-freezing phase transition of the indium nanoparticles significantly improved the effective specific heat of the fluid.

In 2007, Ma and Liu offered the concept of nanoliquid-metal fluid to launch an engineering route to produce the highest conductive coolant. Authors predicted the enhanced thermal conductivity of the liquid-metal fluid due to addition of several dozen times larger thermal conductivity nano particles [290]. The liquid metal with low melting point was anticipated to be a perfect base fluid for producing superconductive solution, which may extensively lead to the essential coolant of improved heat transfer area.

Application in Domestic Refrigerator

Bi et al. [291] reported that nanoparticles can normally and safely be used in domestic refrigerators to significantly reduce energy consumption. Jiang et al. [292] performed an experiment to investigate and make a model for predicting the thermal conductivity of carbon nanotube (CNT) nanorefrigerants. The experimental results showed that the thermal conductivities of CNT nanorefrigerants are much greater than those of sphericalnanoparticle-R113 nanorefrigerants or CNT/water nanofluids. Authors reported that the smaller the diameter (or the larger the aspect ratio) of CNT, the greater the thermal conductivity enhancement of CNT nanorefrigerant.

Several researches [293, 294] were carried out using nanoparticles in refrigeration systems to run-through the advantageous properties of nanoparticles to improve the efficiency and reliability of refrigerators. Wang et al. [293] performed an experimental investigation of the boiling heat transfer characteristics of R22 refrigerant base Al_2O_3 nanofluids, and reported that the nanoparticles reduced the bubble sizes, moved them rapidly near the heat transfer surface, and enhanced the heat transfer performance of the refrigerant. Park and Jung [294] investigated the effects of carbon nanotubes (CNTs) in R123 and HFC134a refrigerants on the nucleate boiling heat transfer. Authors found that CNTs increased the nucleate boiling heat transfer coefficients of those refrigerants. They observed up to 36.6% enhancement at low heat fluxes of less than 30kW/m^2.

Some investigations [295, 296] were also carried out performed using energy consumption tests and freezer capacity tests to examine the refrigerator performance with the nanoparticles. Authors found that the mixture of HFC134a and mineral oil in TiO_2 nanoparticles works normally without harm in the refrigerator. They also observed that the refrigerator using 0.1% mass fraction of TiO_2 nanoparticles consumed 26.1% less energy compared to the HFC134a and POE oil system. However, the same experiment with Al_2O_3 nanoparticles exhibited a little effect on the refrigerator performance.

Peng et al. [295] studied the effect of CuO nanoparticles on the heat transfer performance of R113 refrigerant refrigerant flow boiling in a horizontal smooth tube. Authors found a higher heat transfer coefficient of refrigerant-based CuO nanofluids compared to that of pure refrigerant; the enhancement of heat transfer coefficient was found up to about 29.7%. Naphon et al. [296] conducted an investigation using refrigerant–

nanoparticles mixtures to evaluate the efficiency enhancement of a heat pipe. Authors observed that the efficiency of a heat pipe with 0.1% nanoparticles concentration offered 1.40 times higher than that with pure refrigerant.

Cooling and heating in buildings: Varieties of nanofluids can be applied in conventional heat exchangers used for cooling and heating in buildings. Kulkarni et al. [297] investigated the performance of nanofluids in buildings heating in cold regions. In cold regions, the mixture of ethylene glycol (EG) and water or propylene glycol (PG) and water as a heat transfer fluid is commonly used in different proportions. Authors selected a conventional 60:40 EG/water (by weight) mixture and various nanofluids to study their heat transfer and flow characteristics. Authors reported that the use of nanofluids in heat exchangers could reduce volumetric flow rates as well as mass flow rates and save overall pumping power. Nanofluids also offer a smaller heating system which is capable of providing the equivalent amount of thermal energy as a larger system. Due to a reduction in power consumption, the pollutants released to the environment and the waste produced at the end of the heat transfer system lifecycle will be significantly reduced [270]. In cooling systems, the chilled water, which is commonly used in coils of air conditioning ducts can be replaced by nanofluids, This application has not been explored extensively in the technical literature [276]. Nanofluids can also be employed in the building heating systems [260].

2.2.8 Summary

Enormous exciting characteristics of nanofluids have been reported in the earlier decades. In this section, an overview of the recent developments in nanofluid investigations have been presented. The research includes synthesis, thermophysical properties, stability, evaluation techniques and potential applications of nanofluid in automotive, residential, and other industrial fields.

While nanofluids have displayed many attracting potential applications, some fundamental complications also exist before its commercialization. One of the key issues is the discrepancies between experimental results of different research groups due to variations in synthesis approaches of the nanofluid suspension, in general. Other important factors include shapes, sizes and properties of nanoparticles and additives, surfactants used in nanofluids, stability of the nanofluid suspensions, thermo-fluidic performance of nanofluid, and so. These key issues have to be taken into account. Research on nanofluids can be improved and prolonged through exploring novel nanomaterials that exhibit enriched thermal conductivity and specific heat simultaneously.

2.3 Transient Heat Transfer

Crossflow heat exchangers are being engaged in many thermal applications, such as automotive radiator, air conditioning refrigeration, and data center liquid cooling systems [18, 298]. Heat exchangers are made to work under specific steady state conditions. However, due to transient performance of heat exchanger in startup and shut down or during non-stationary function like failure, predicting of heat exchanger load under a dynamic load or operational condition became the main challenging issues [299].

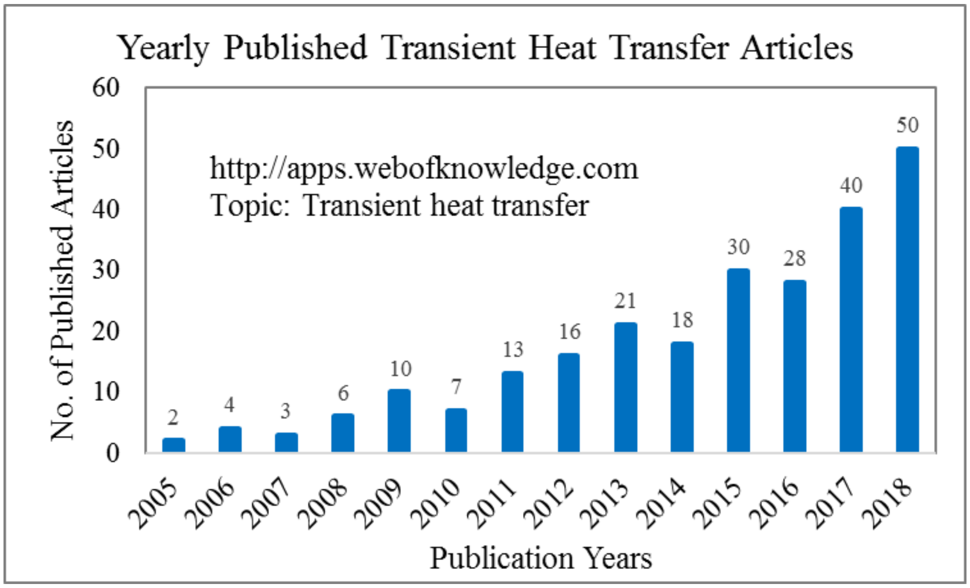

Figure 2.9: Yearly published transient heat transfer articles

Modeling and characterization of transient phenomenon has attracted the attention of many researchers for the design of improved, reliable and efficient thermal management systems. Both the mass flow and temperature variation scenarios are significant since it commonly happen in real life applications [18]. Studies predicted the impact of step variations in inlet temperature and mass flow rate of hot fluid. Pearson et al. 1974 [300] and Roetzel et al. [301] investigated the transient phenomenon of heat exchangers in step changes in mass flow rate of hot fluid. Several researchers [299, 302–304] studied dynamic responses to both temperature and mass flow variations.

London et al. [305] first suggested the transient effectiveness as a new term in studying the transient responses of a heat exchanger. Mathematical models were established for characterizing and forecasting the transient performance of a counter-flow heat exchanger under a step change in the hot fluid inlet temperature and mass flow rate. In 1954, Dusinberre accomplished the early numerical analysis for modeling and examining the dynamic behaviors in pipes and heat exchangers. After that, Turton J.S [306] studied the transient behaviour of the gas-to-gas crossflow heat exchanger. They described a general finite difference method for solving the transient response under a number of simplifications. Later on, the transient experimental characteristics of a fin-tube water-to-air crossflow heat exchanger was performed under periodic fluid inlet temperature variations by Gartner and Harrison 1965 [307].

Myers et al. [308] established an integral technique to study a gas-to-gas crossflow heat exchanger. They simplified the model by presuming one mixed fluid. They also presented a transient characteristics of the average outlet temperature of two fluids under a step change to the inlet temperature. Moreover the average outlet temperature response of gas-to-gas crossflow heat exchangers under step change to the inlet temperature of either the hot side or the cold side of fluid was predicted by Romie et al. [309] using a double Laplace transform technique.

A crossflow heat exchangers using finite difference method was examined numerically for step, ramp and exponential perturbations by Mishra et al. [310] to study the transient behavior. It was observed that the longitudinal conduction plays an important role with the increase in NTU. Authors described the dynamic performance of the crossflow heat exchanger, the effect on the dynamic performance of longitudinal conduction and axial dispersion. The dynamic performance of a crossflow heat exchanger based on a 2-D transient model was explored by Gao et al. [311]. They varied initial and final hot fluid inlet temperature by means of step, ramp and a continuous exponential function with different magnitudes and time periods to investigate the effects of transient performance on the outlet temperature.

Later on, Gao et al. [312] examined several experimental test on transient response under varying server powers and operating conditions on a data center cooling infrastructure facility to evaluate the transient response in a data center.

Bianco et al. [249] also numerically investigated the development of the laminar forced convection flow of aluminum oxide-water nanofluid a transient regime in a circular tube with a constant and uniform heat flux at the wall. They showed that heat transfer enhancement increases with the increase of particle volume concentration at the expense of an increase in wall shear stress.

The thermal conductivity of nanofluid was determined using Hamilton–Crosser model along with Brownian motion. They found that the heat transfer enhancement of nanofluids decreases with larger nanoparticle sizes due to lower movement of heavier particles. They also showed that the inlet velocity discrepancy does not have a major impact on the heat transfer enhancement mechanism for the reason that both nanofluid and base fluid heat transfer coefficient rise at the same ratio in a laminar nanofluid regime.

Sert et al. [233] carried out a numerical analysis of transient laminar forced convection of nanofluids inside a circular duct under step change in wall temperature as well as wall heat flux. Authors considered $\mathrm{Al_2O_3/water}$ nanofluid as a homogenous single-phase fluid. In the analysis, authors used Hamilton and Crosser correlation [163] for the effective thermal conductivity and a model for Brownian motion in order to take the effects of temperature and the particle diameter into account. Transient critical heat flux of water-based zinc–oxide was experimentally studied by Sharma et al. [313].

Hassan and Harmand [314] carried out a three-dimensional transient model of vapour chamber of two copper plates to investigate the effect of water based Cu, CuO and Al_2O_3 nanofluids on its performance. They reported that the nanoparticles dispersed in base fluid decrease vapour chamber temperature and liquid velocity as well as liquid pressure and increase evaporated mass. They also claimed that Cu nanofluid possessed the greatest effect on the vapour chamber temperature compared to others.

Popa et al. [225] performed a theoretical two-dimensional axisymmetric analysis of transient mixed convection flow using water based aluminum oxide (Al_2O_3) and copper oxide (CuO) nanofluids inside a vertical tube of circular cross-section. Authors found a significantly reduced recirculation zone near the wall when the volume fraction of nanoparticles was increased. This is due to the increase of viscosity with the increase of volume fraction.

Suganthi and Rajan [315] conducted an experimental study to investigate transient heat transfer performance of zinc oxide-propylene glycol (ZnO–PG) nanofluids under constant heat flux and constant bath temperature. With 2 vol.% concentration, ZnO–PG nanofluids exhibited an enhancement of 4.24% in heat transfer rate under constant heat flux and about 26% in coolant side heat transfer coefficient under constant bath temperature conditions. For both conditions, the improved heat transfer coefficient of nanofluids were found with increasing nanoparticle volume concentrations. This could be attributed to enhanced thermal conductivity as well as natural convection due to viscosity reduction.

Nasrin et al. [222] studied transient phenomena on forced convection in a fluid valve using CuO/W nanofluid. Authors used the finite element method in numerical simulation for constant Reynolds number of 100 and nanoparticles volume fraction of 5%. They found reduced heat transfer rate in the fluid valve for longer time period.

An experimental investigation on water base silicon nanofluid was carried out by Hajian et al. [316]. They investigated the effect of nanofluid on the thermal performance of cylindrical heat pipe in both transient and steady states. The authors used the suspensions of Si nanoparticles in DI-water with various concentrations. The best performance was found for the least concentration of nanofluid. The authors also reported reverse and negative effects of high concentration nanofluids.

Liu et al. [317] experimentally measured transient heat transfer coefficients of helium gas flowing over a 0.1mm thick horizontal platinum plate. The gas flow velocities, gas temperatures, and the periods of heat generation rate (τ) were varied from 4 m/s to 10 m/s, 290 K to 353 K, and 50 ms to 17 s, respectively. The authors noted that the heat transfer coefficient of helium gas approaches the quasi-steady-state for the period longer than 1s and becomes higher for the period shorter than about 1s.

Li et al. [318] conducted experimental investigation on both transient and steady state effective thermal conductivity of water based Al_2O_3 nanofluid. Authors investigated 47 nm sized normal diameter with nanoaprticles volume fractions of 0.5%, 2%, 4%, and 6%. They reported the existence of some disagreement to the validity of measured data due to diverse experimental approaches.

A significant number of numerical investigations on transient responses of heat exchangers were performed on different types of working fluids. Even though several researchers conducted their numerical transient studies to apprehend the heat transfer and flow characteristics using conventional fluids, the transient investigations using nanofluids are still very sparse in the open literatures. Majority of the numerical studies were conducted with the aid of 2D models of single tube or enclosure. They used liquid inside of the tube; however, they did not consider any fluid on the outside of the tube.

In the current study, the transient behavior of minichannel heat exchanger (MICHX) using $\mathrm{Al_2O_3/EG}$ with different volume concentration has been numerically investigated to predict the effect of step changing in the inlet mass flow rate and concentration on transient response in heat transfer performance.

2.4 Knowledge Gaps in Available Current Scientific Literature

A comprehensive review of experimental and numerical literatures have been done on heat transfer augmentation techniques and transient responses of heat exchangers. Following information gaps are found:

(i) No numerical data exist in the open scientific literature regarding simultaneous module of crossflow MICHXs, especially in automotive applications. Currently vehicles are using sequential module of heat exchangers.

(ii) No numerical data is available for 3D transient thermal performance and behaviour of serpentine air-to-liquid crossflow MICHX. Most of the researchers obtained simulations for simple geometries of 2D crossflow heat exchangers with some simplifying assumptions.

(iii) A few numerical solutions are available for 3D transient modeling of simple pipes; however, such solutions do not represent the real world scenarios. The complexities of heat transfer and fluid motion in a serpentine air-to-liquid crossflow MICHX make it challenging for the researchers to obtain 3D transient CFD simulations.

The findings of the literature survey unveiled the great necessity of further research on simultaneous module (proposed) as well as 3D transient heat transfer in the crossflow MICHX. This research is achieved with the intention of filling the current information gaps as much as possible. The established models, data, and correlations can be valuable source of improving the effective efficiency and design control strategy of MICHX.

2.5 Criteria of Model Design and Working Fluid Selection

In the current study, several models of MICHXs are used for better thermal performance. Figures 2.10(a) and (b) illustrate the slab core and channels inside the slab of the MICHXs, respectively. The basis of selecting channel diameter and cross-section, shape and geometry, materials of test specimen as well as working fluids are presented in this section.

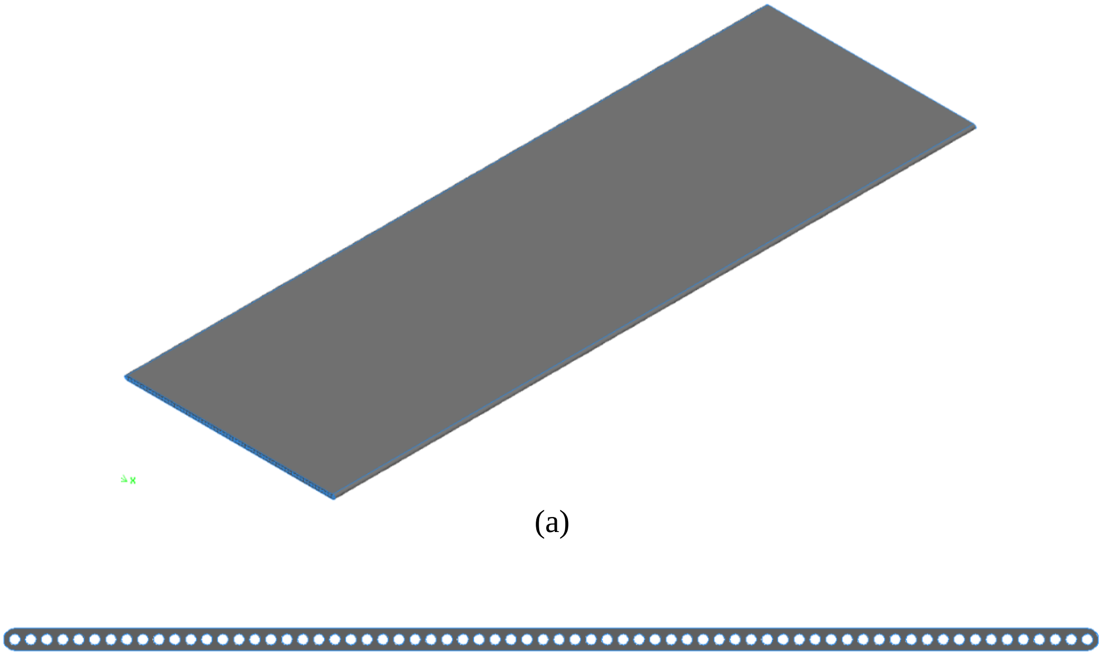

(a)

(b)

Figure 2.10: (a) Slab core, (b) channels inside the slab of the MICHX

The serpentine bend of the MICHX is shown in Figure 2.11 below.

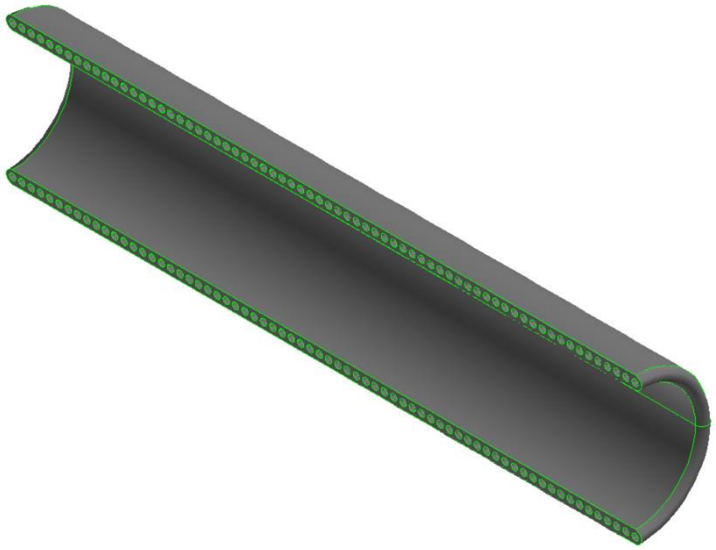

Figure 2.11: Serpentine of the MICHX

With the purpose of improving the performance of heat exchangers, many investigations have been conducted on such devices. Engineers are interested in energy efficient and environmentally friendly minichannel heat exchangers to achieve energy requirements in automotive, industrial and residential applications, in general.

Several researchers have classified heat exchangers based on channel diameter or hydraulic diameter of flow passage. Mehendale et al. [55] and Kandlinkar et al. [19] defined the classifications of heat exchangers as illustrated in Table 6.

Adams et al. [319] recommended that the hydraulic diameter of 1.2 mm could be a rational lower size limit of a flow passage that are valid for the traditional fluid flow and heat transfer correlations. Jokar et al. [27] confirmed that the conventional correlations are directly inapplicable for rectangular flow passage having hydraulic diameter within the range of 2.6 mm to 4.1 mm.

Table 6: Heat exchanger classifications based on channel size

According to Mehendale et al. [55]	According to Kandlinkar et al. [19]
Conventional: > 6 mm Compact: $1 - 6$ mm Mesochannel: $100\ \mu m - 1$ mm Microchannel: $1 - 100\ \mu m$	Conventional: > 3 mm Minichannel: $200\ \mu m < D \leq 3$ mm Microchannel: $10\ \mu m < D \leq 200\ \mu m$ Transitional Microchannel: $1\ \mu m < D \leq 10\ \mu m$ Transitional Nanochannel: $0.1\ \mu m < D \leq 1\ \mu m$ Nanochannel: $D \leq 0.1\ \mu m$

In the current study, the channel size of 1 mm is chosen as a generalized dimension of minichannel which follows the classification of Kandlikar et al. [19] as well as suggestion of Adams et al. [319]. The minichannel heat exchanger used in this study is built up by extruding flat slab of aluminum 3003.

Researchers used various cross sections of flow channels including triangular, square, rectangular, trapezoidal, elliptical, circular, and some others. Most of the work employed the rectangular cross section. The majority of the studies did not mention the particular reason of using a specific type of channel cross section. Hasan et al. [98] studied the influence of channel geometry on the performance of a counter flow microchannel heat exchanger and found that the circular channels give the best overall thermal and hydraulic performance among different shapes of channel cross sections.

The current study selects the multi-port minichannel serpentine slabs with circular cross sections as the criteria of flow passages. The test slabs are multiport extruded (MPE) tubing having smoother surfaces and more uniform diameters of channels compared to the etching tubes or ports.

Kandlikar et al. [15] studied the effect of surface roughness on heat transfer and pressure drop at the Reynolds number range of 500-2600 for 1.067 mm tube and 900-3000 for 0.62 mm tube. The authors recommended that the larger diameter (>1.067 mm) tube with $\varepsilon/D = 0.003$ may be treated as smooth tube; whereas, for the smaller diameter (<0.62 mm) tube is treated as rough tube because the Δp and Nu depend on ε/D for tube size of below 0.62 mm diameter.

The test specimens used in the present study have 1 mm channel diameter with a relative roughness, $e/D = 0.0005$; and considered as smooth channel surface. The multi-port slab has following benefits over any single or isolated bare tubes of the same diameter and numbers as the slab ports [33].

- The multi-port slab channels are separated by very thin metallic walls ensuring the unmixed liquid flow; whereas, the isolated bare tubes are separated by low conductive but high thermally resistive air media. The airside total heat transfer surface area of both the slab channels and the bare tubes are comparable. The thermal conductivity of the aluminum wall is higher than air and liquid.

- For a given operating condition, the forced convective the heat transfer in a air-to-liquid crossflow heat exchanger is slower and weaker in bare tubes than the multiport slab channels.

- The temperature distribution in multiport slab channels is more uniform compared to the isolated bare tubes due to the existence of solid walls and flatness of the slab.

- The wake region on the downstream of tube and airside fin region generally reduces the heat transfer.

- The slab having only a single wake region significantly reduces the airside pressure drop as well as the pumping cost compared to the bare tubes.

Due to the above distinguishing features, multiport slab circular microchannels have been evidently chosen in the current research.

CHAPTER 3

NUMERICAL METHODOLOGY

Details of the CFD models including, physical device, geometry, assumptions and governing equations, grid independency, computational set up and solution procedures are presented in this chapter. Simulations have been conducted through various models of air-to-liquid crossflow conventional flat tube and minichannel heat exchangers in five stages of the current study. Details of the numerical methods are described below.

3.1 Computational Fluid Dynamics (CFD) Models

CFD has undoubtedly become fully established and popular field of interest in academia research as well as industrial applications. In many modern engineering, CFD is a widely adopted approach for solving large and complex problems in fluid dynamics and heat transfer [320]. It is the fusion of the established branches of theoretical and experimental disciplines. Significant advances in CFD in various areas include computer design, simulation and engineering analysis of fluid flow and heat transfer.

The three dimensional (3D) fluid flow and heat transfer modeling described in the current study has been performed in five distinct stages and model complexity levels to accomplish the research objectives. Some level of validation is ensured at each stage.

3.1.1 Geometry Modelling

In the current research, several models are used in numerical simulations with the purpose of improving thermal performance and evaluating transient behaviour of heat exchangers. The geometric data and specifications of the models used in current research work are illustrated in Table 7.

Table 7: Summary of the specifications of the model (units are in mm)

Parameters	2-pass single loop MICHX	5-pass 3-loop MICHX	5-pass single loop MICHX	Sequential FTHX	Simultaneous FTHX	Simultaneous MICHX
Presenting Figure #	21	23	24	25	25b	26
# of channels/tube	68	68	68	1	1	68
Channel diameter Tube height	1	1	1	1	1	1
Port-to-port distance	1.463	1.463	1.463			1.463
Gap between HXs				24		
Slab width in x-direction	100	100	100	38 x 2	100	100
Slab thickness in y-direction	2	2	2	2	2	2
Slab length in z-direction	305	305	305	305	305	305
Module height				92	92	92
No. of loops/ flow circuits	1	3	1	4	2	2
No. of slabs in each loop	2	5	5	2	2	2
Fin density per 25.4mm	12	12	12	12	12	12
Fin height	16	16	16	16	16	16
Fin thickness	0.1	0.1	0.1	0.1	0.1	0.1
Inlet & exit tube diameter	4.76	4.76	4.76	4.76	4.76	4.76

First, a 3D model of 2-pass finned crossflow MICHX is developed in Stage I. Focusing on the flow and heat transfer fundamentals, the model is an equivalent representation of the actual MICHX device shown in Figures 3.1(a) and (b).

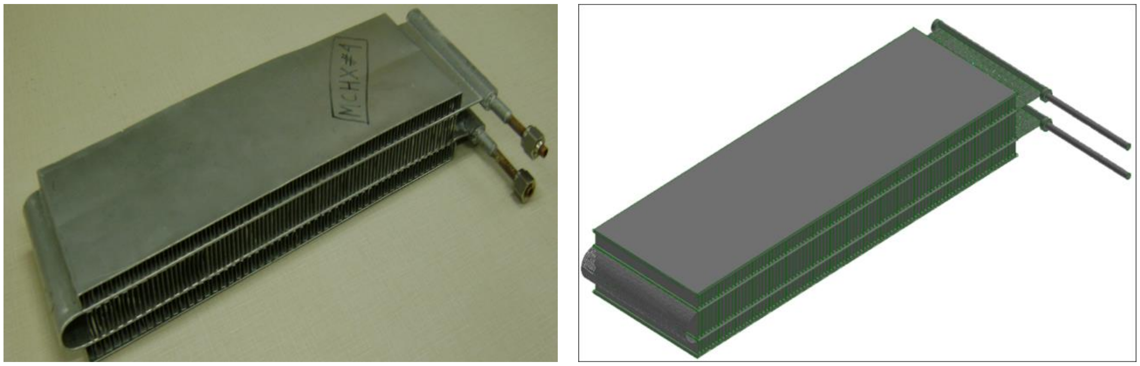

(a) (b)

Figure 3.1: (a) Photograph and (b) geometry of 2-pass single-loop crossflow MICHX

Once the geometry is modeled, the simulation results of conventional automotive fluids have been fully examined and properly validated with experimental measured data of Khan 2011 [33]. At this stage, another model of conventional flat tube heat exchanger (FTHX) having similar flow physics is also developed. Results of steady state simulations of the FTHX have been compared to those of MICHX. In this stage, nanofluids have also been included and analyzed. The respective conventional flat tube and minichannels are presented in Figure 3.2.

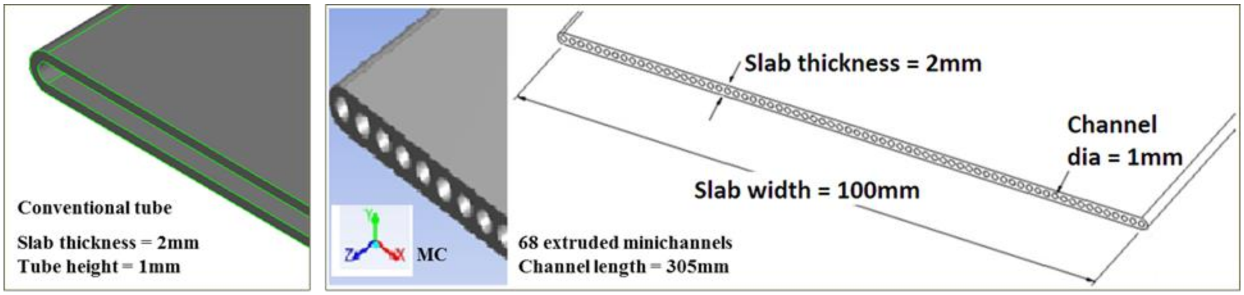

Figure 3.2: Conventional tube (left), Minichannels (middle)

In Stage II, the model is expanded to a 5-pass 3- loop MICHX, which closely represents the equivalent heat capacity of an automobile radiator. This three dimensional model is also a representative geometry of another physical device. The physical device and the geometry are shown in Figures 3.3(a) and (b), respectively.

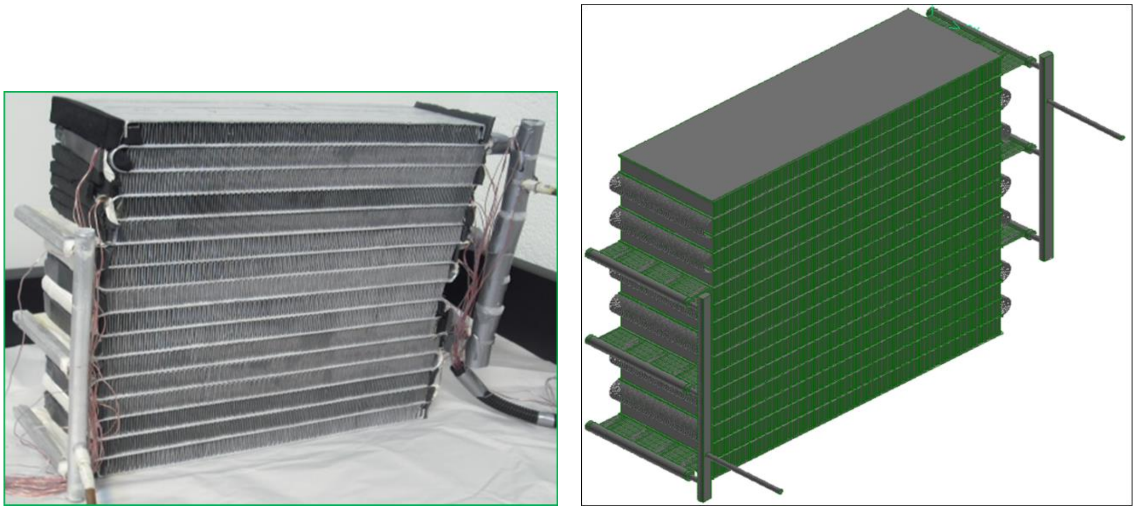
(a) (b)

Figure 3.3: (a) Photograph and (b) geometry of 5-pass 3-loop crossflow MICHX

At this stage, fluid flow and heat transfer characteristics have been modeled and validated with experimental measured data of Dasgupta 2011 [321]. Flow and heat transfer distributions in different loops as well as various channels and slabs have been evaluated in order to make a decision if only a 5-pass single-loop heat exchanger instead of 3-loop can be used for further investigation of transient heat and mass transfer, in particular.

In Stage III, Al_2O_3 nanoparticles have been incorporated with automotive fluids, such as water (W) and 50:50 ethylene glycol/water (EG) to intensify the heat transfer. Simulations have been performed in the 3D model of a 2-pass single-loop [see Figure 3.1(b)] and a 5-pass single-loop [(see Figure 3.4(b)] crossflow MICHX. Steady state model of the 2-pass single-loop MICHX is used for Al_2O_3/W nanofluid. On the other hand, transient model of the 5-pass single-loop MICHX is used for Al_2O_3/EG nanofluid.

In Stage IV, 2-pass 2-loop heat exchangers have been employed to develop two distinct modules of heat exchangers namely, sequential module and simultaneous module. At this stage, heat transfer performance is evaluated for different arrangements.

The sequential heat exchangers module, which is used in numerical simulation of two liquids having different inlet operating conditions, is illustrated in Figure 3.4. The module is consisted of two 2-pass 2-loop heat exchangers in series. In this arrangement, both heat exchangers face same mass flow rate of incoming ambient air, whereas the temperature of the air is different for each heat exchanger. The frontal heat exchanger gets the ambient air, while the rear heat exchanger receives the outlet air of the frontal heat exchanger.

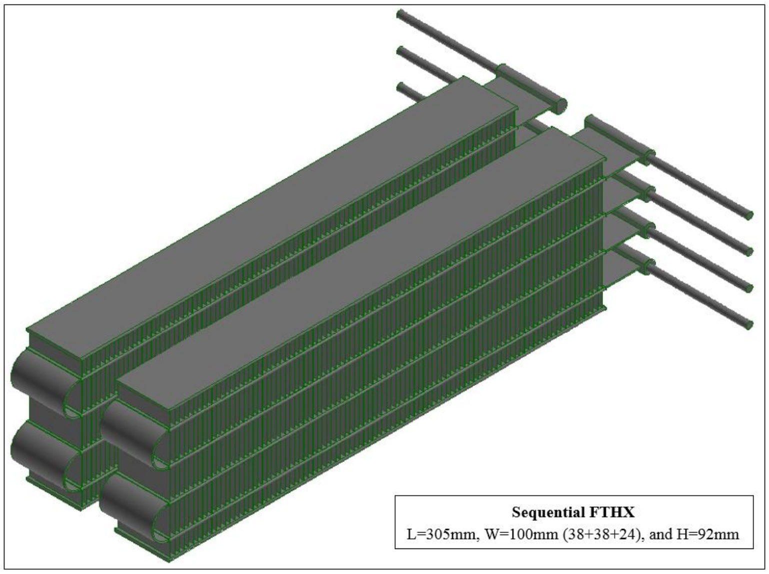

Figure 3.4: Sequential module of 2-pass 4-loop crossflow FTHX

The simultaneous heat exchangers module also uses two liquids with different operating conditions in numerical simulation. The simultaneous modules of FTHX and MICHX are illustrated in Figures 3.5(a) and (b), respectively. Each module consists of two 2-pass single-loop heat exchangers horizontally parallel to each other. Both heat exchangers get incoming air of identical ambient conditions, such as temperature, velocity, and quality.

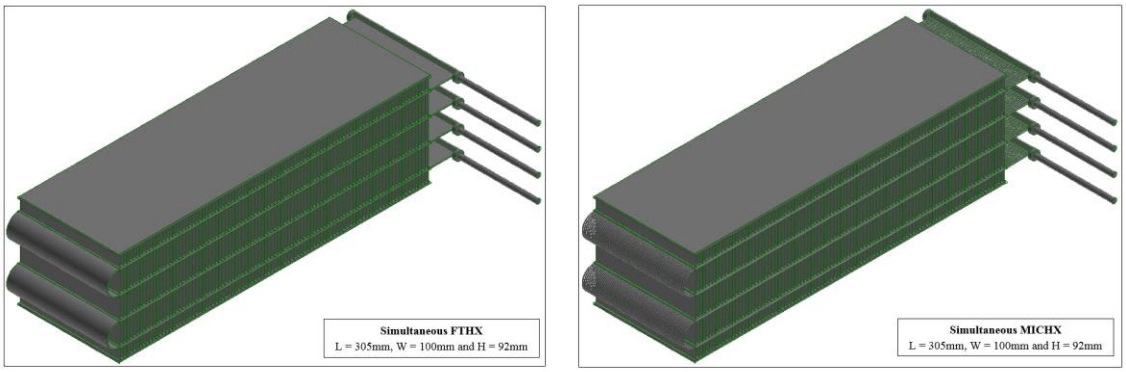

(a) (b)

Figure 3.5: Simultaneous modules of 2-pass crossflow (a) FTHX and (b) MICHX

In Stage V, 3D transient heat transfer simulation has been conducted in a 5-pass single-loop MICHX. This is also a demonstrative representation of a real heat exchanger. The photograph of the physical device and the geometry used in this stage are shown in Figures 3.6(a) and (b), respectively. The numerical results have been validated with experimental results of Fotowat et al. [322]. An extensive analysis of transient heat transfer parameters have been performed.

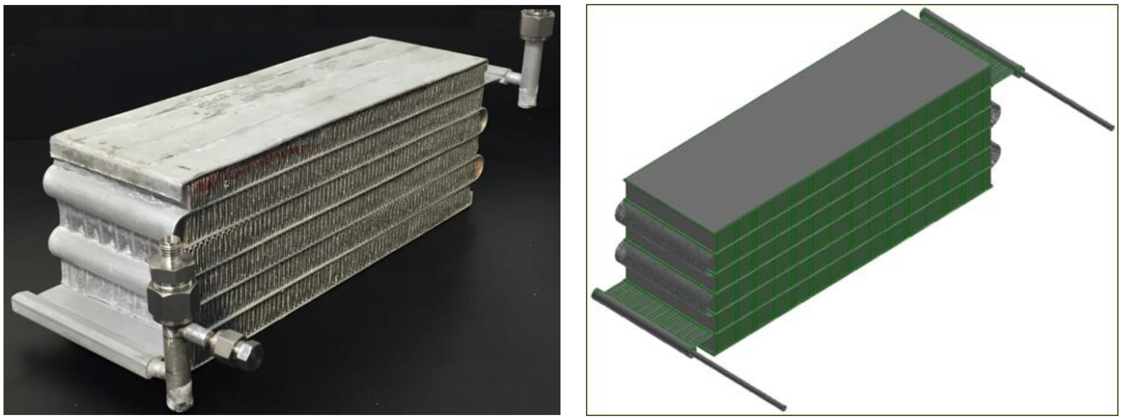

(a) (b)

Figure 3.6: (a) Photograph and (b) geometry of 5-pass single-loop crossflow MICHX

3.1.2 Computational Domain

The computational domains have been selected in consideration of the test chambers incorporating respective minichannel heat exchangers. These are equipped in the experimental setup of Vehicle Thermal Management Research Laboratory in University of Windsor. Each domain includes two continuums, the liquid and the air along with the solid heat exchanger. These domains are presented below.

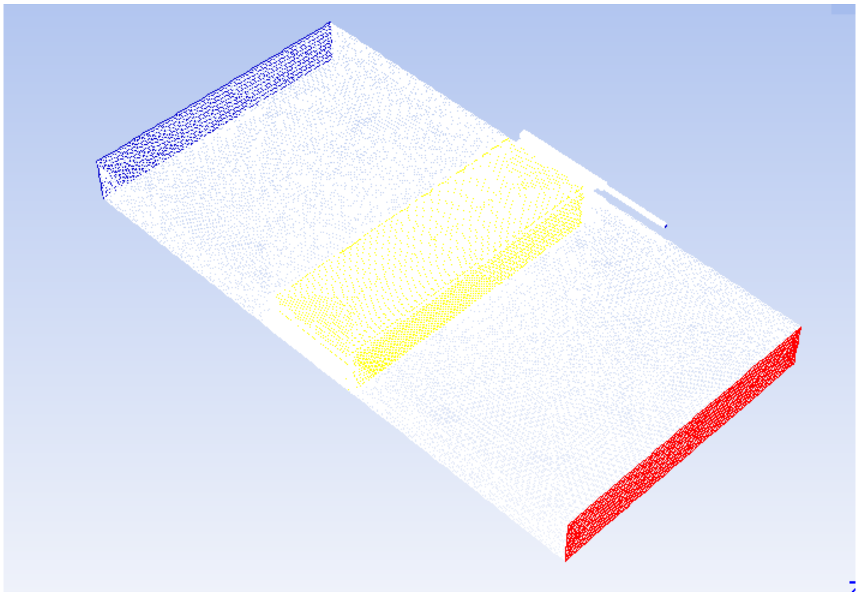

Figure 3.7: Computational domain of the 2-pass single-loop crossflow MICHX

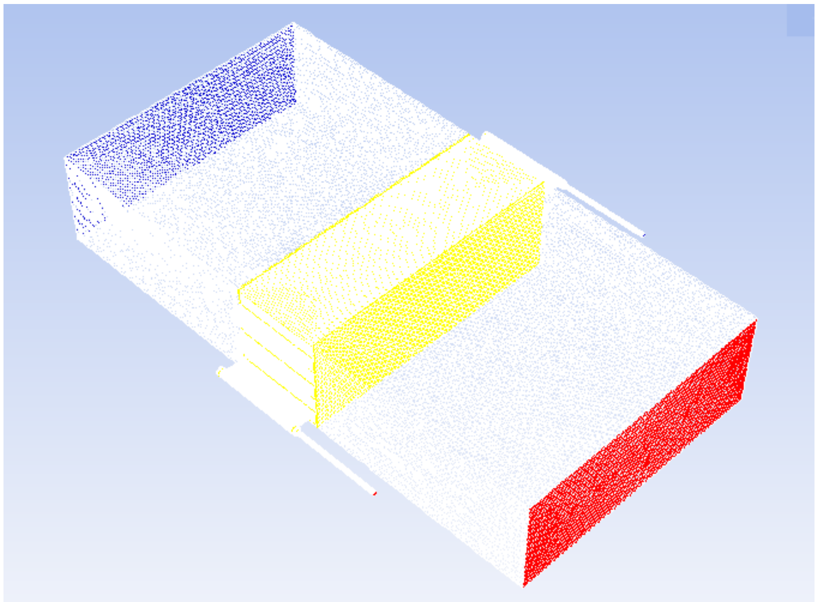

Figure 3.8: Computational domain of the 5-pass single-loop crossflow MICHX

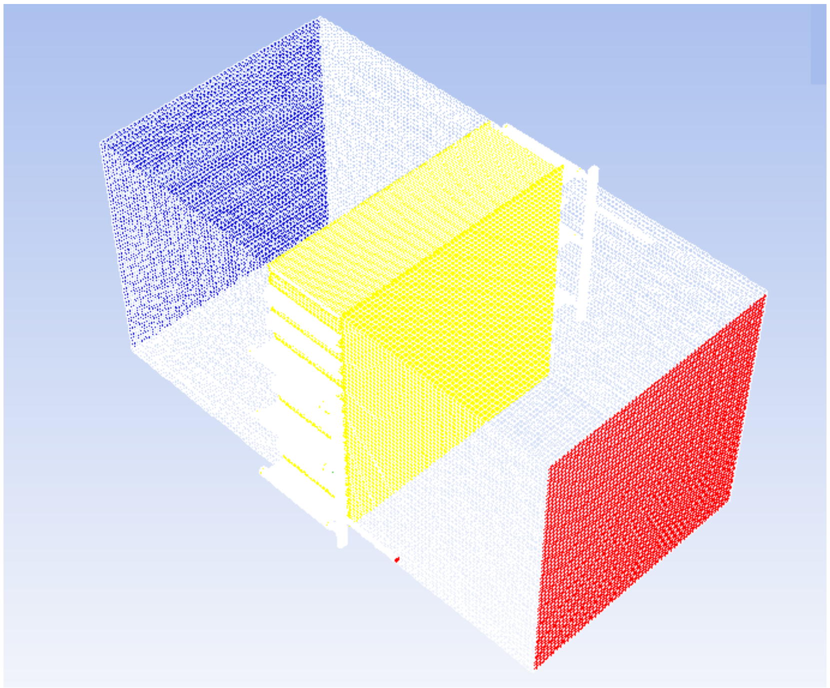

Figure 3.9: Computational domain of the 5-pass 3-loop crossflow MICHX

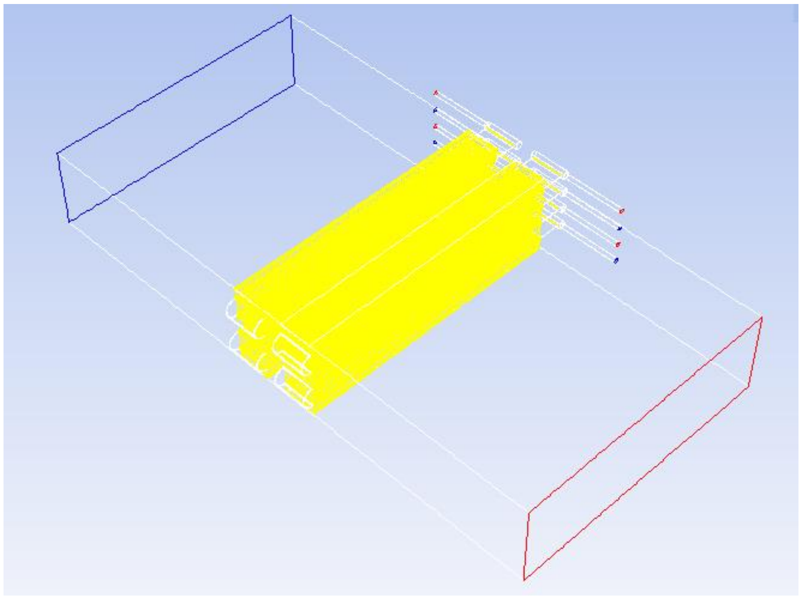

Figure 3.10: Computational domain of the crossflow MICHXs in sequential module

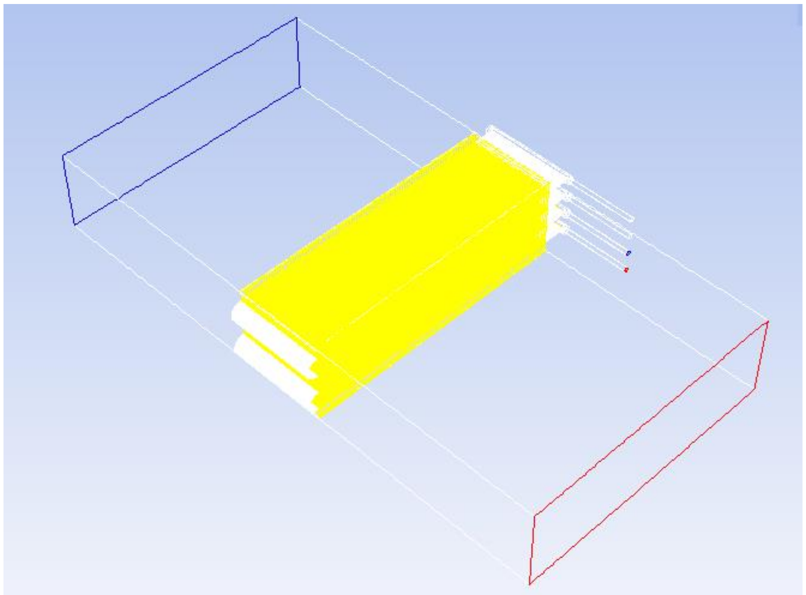

Figure 3.11: Computational domain of the crossflow MICHXs in simultaneous module

3.1.3 Mesh / Grid Generation

Meshing of the various sub-sections is discussed in this section. Various meshing approaches have been used to generate appropriate grids for each geometry in the computational domain. GAMBIT is used to create geometry and generate mesh applicable for CFD simulations using ANSYS FLUENT. Every geometry contains a huge number of surfaces and volumes because of the complex shape of the models. Due to the complexity of the geometry, it is impossible to generate a single structured mesh for the whole domain. The model is, therefore, divided into several sub-sections including air (test chamber), manifolds, headers, serpentines, channels, and solid slabs and fins. A computer with 16 parallel processors and 128GB random access memory (RAM) is used for this current study. Structured hexahedral mesh is generated for the test chamber and fins. Cooper hexahedral and wedge mesh is generated for the serpentine bends and channels, while unstructured tetrahedral, hybrid and wedge grids have been created for the rest of the model. These are shown in Figures 3.12 to 3.18.

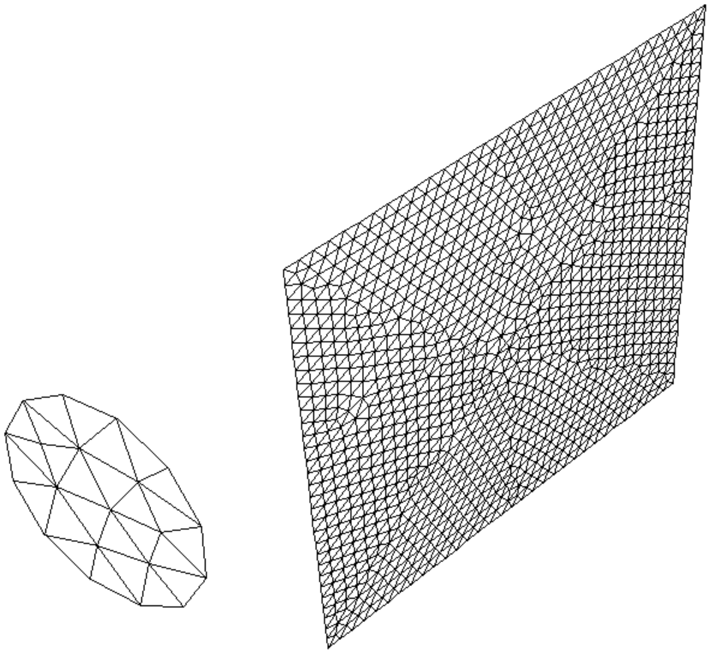

(a) (b)

Figure 3.12: (a) Channel inlet/outlet mesh (zoomed) and (b) Air inlet/outlet mesh

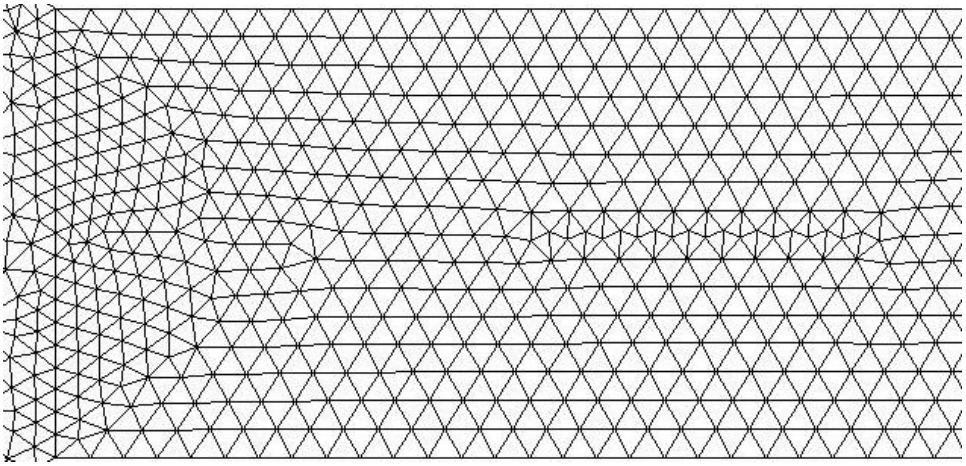

Figure 3.13: Adaptive mesh in airside wall

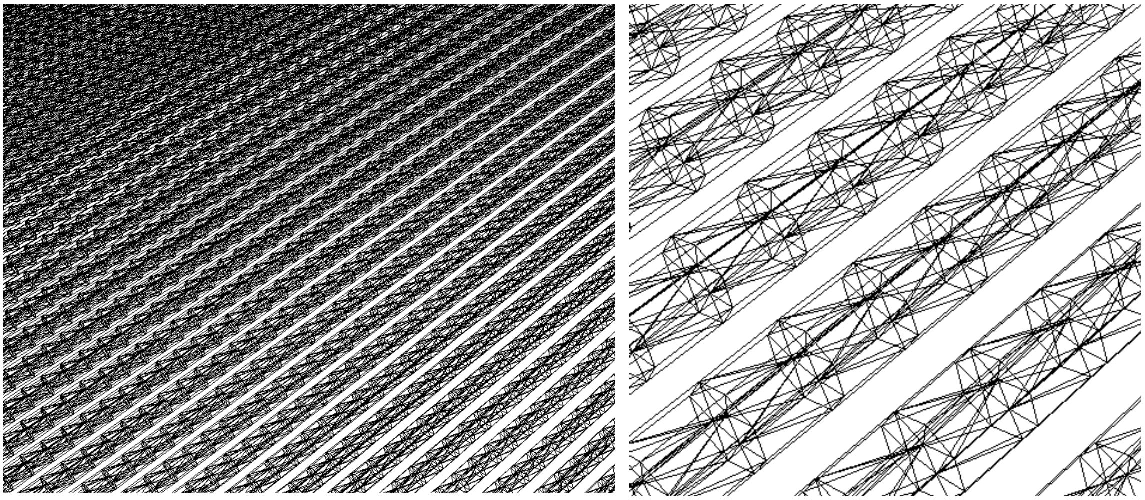

(a)

(b)

Figure 3.14: (a) Channel mesh and (b) zoomed channel mesh

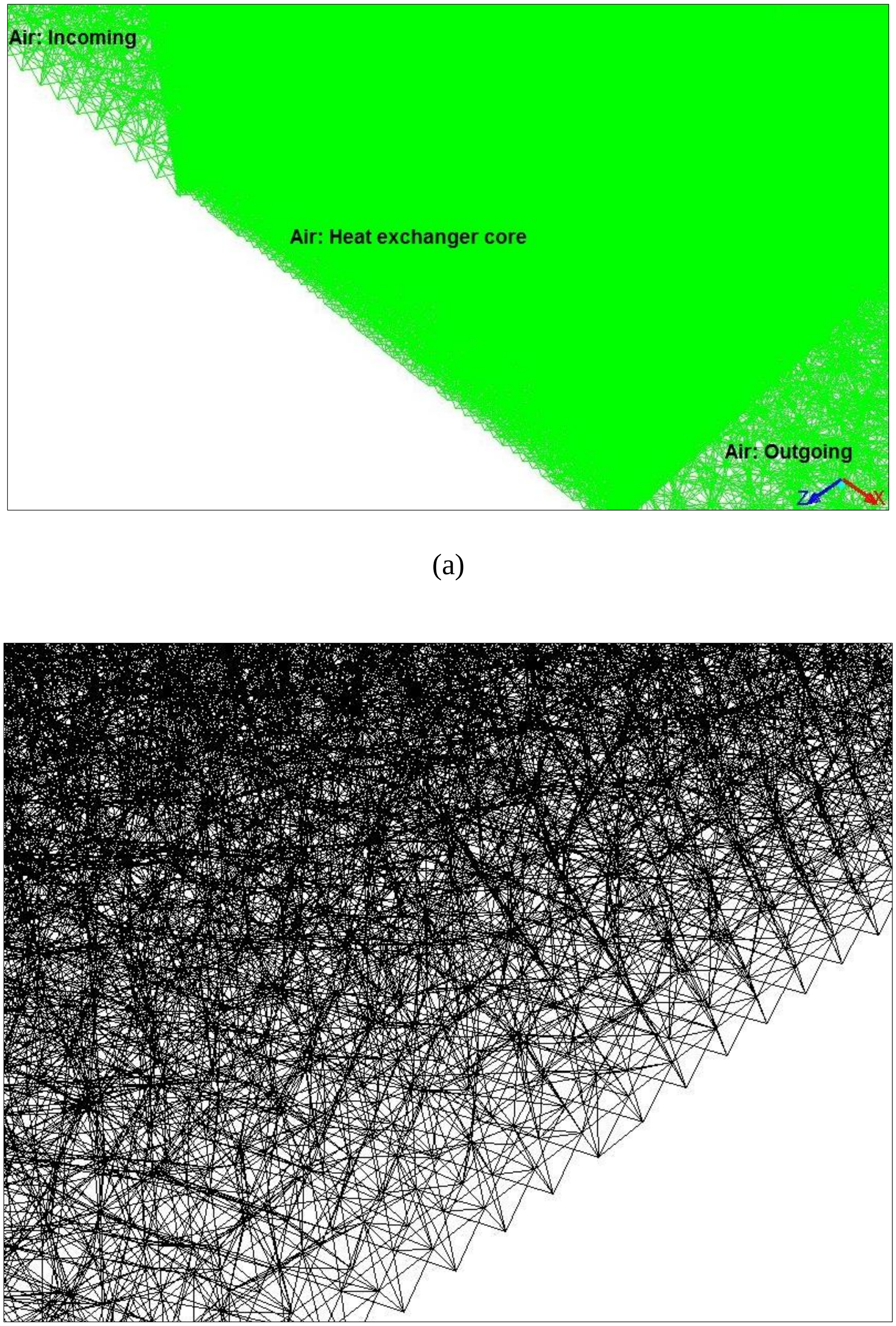

(a)

(b)

Figure 3.15: (a) Air-side mesh and (b) air-side mesh (zoomed)

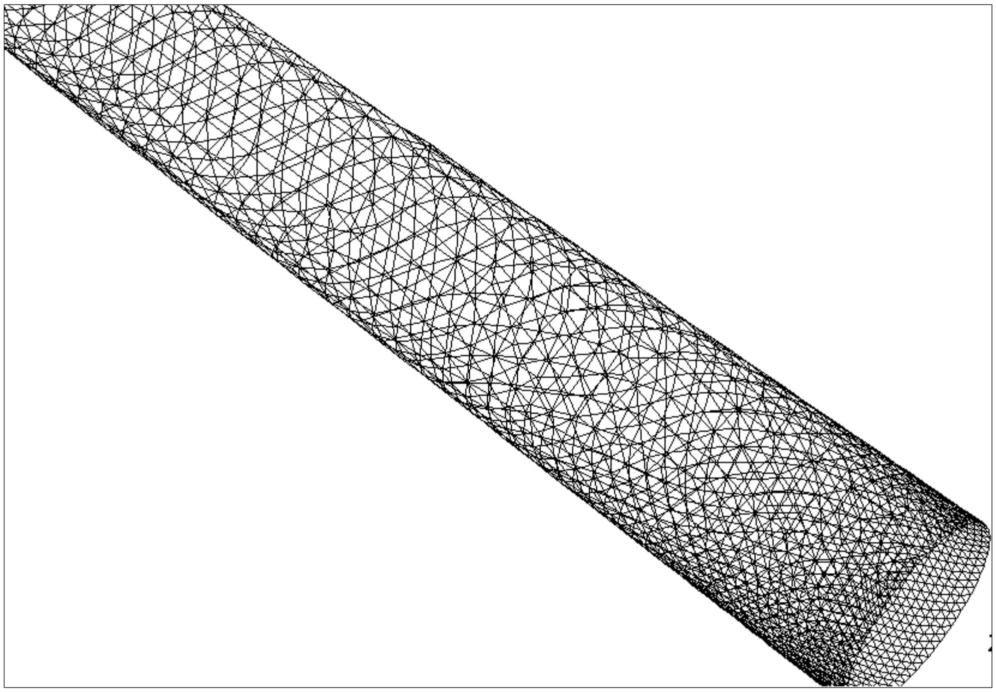

Figure 3.16: Grids of inlet and outlet tube (zoomed)

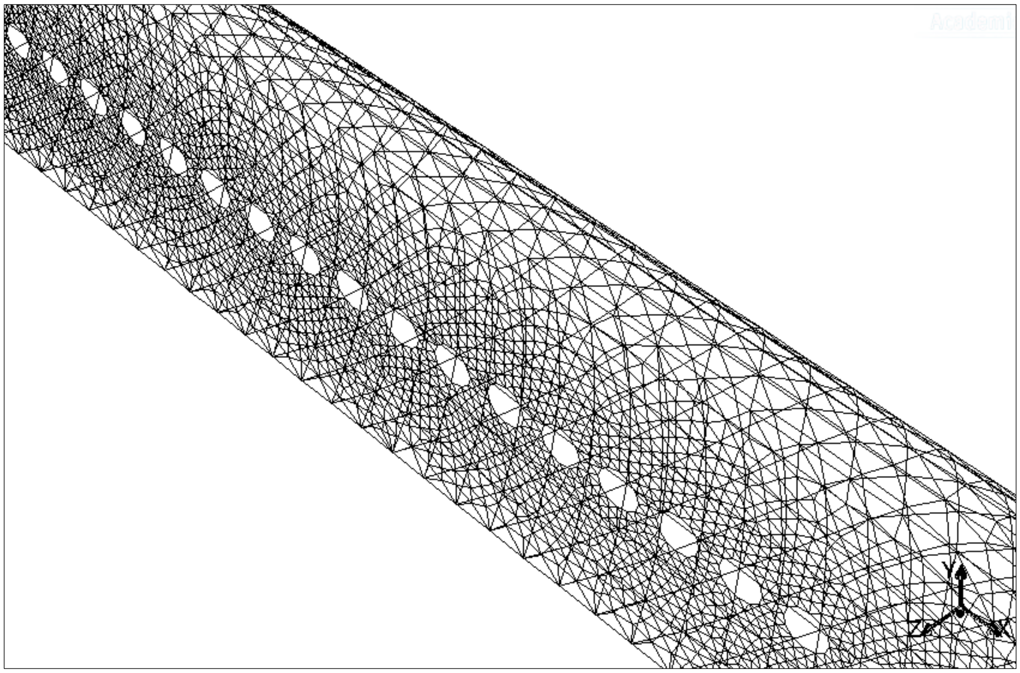

Figure 3.17: Grids of manifold (zoomed)

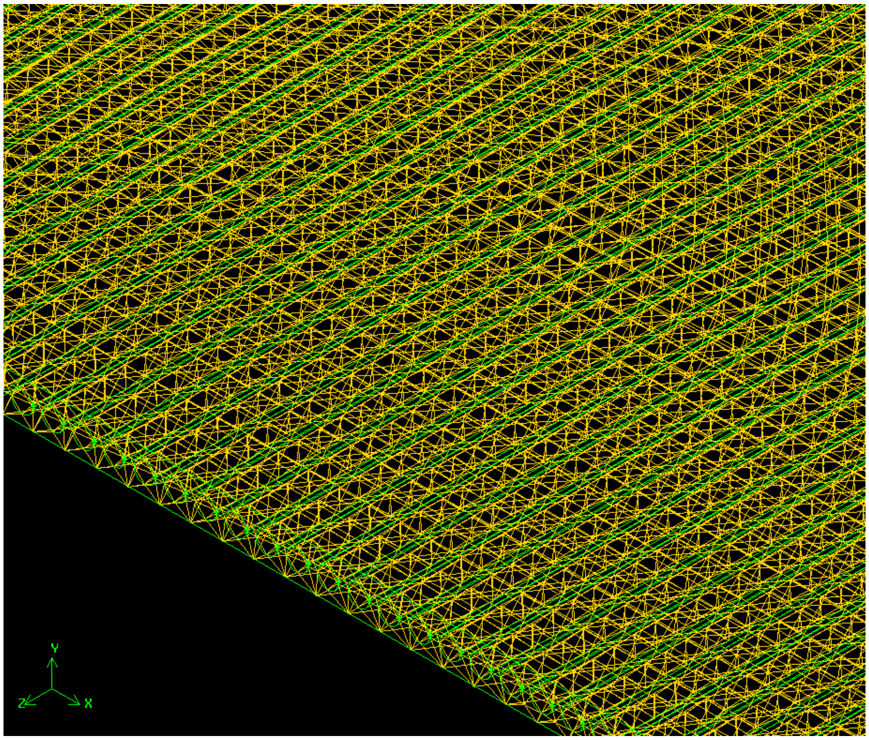

Figure 3.18: Solid slab mesh

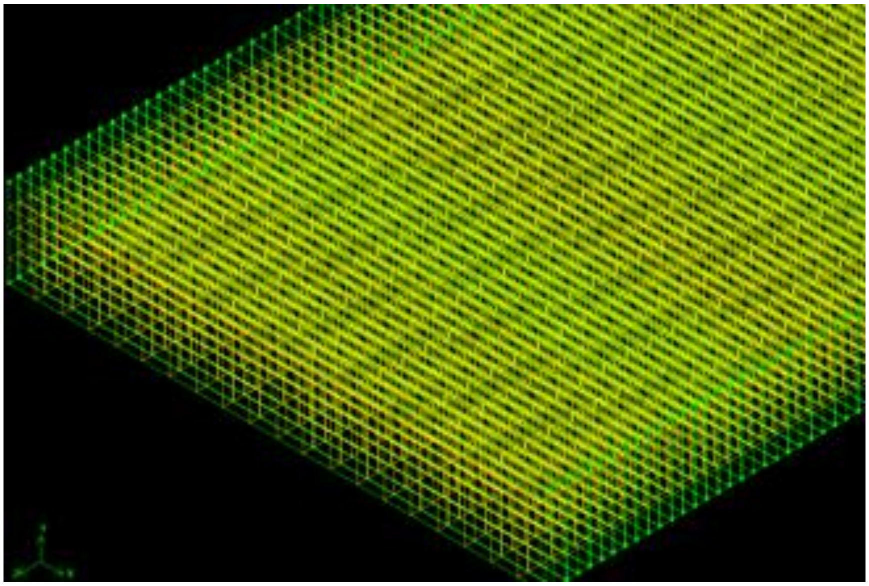

Figure 3.19: Fins mesh

3.1.4 Assumptions

The computational fluid dynamics (CFD) uses a numerical approach for solving the governing equations. Following assumptions have been made for the given flow geometry and boundary conditions in the current study.

- fluids are single phase incompressible Newtonian fluids
- thermophysical properties of liquids are the functions of temperature but independent of pressure
- thermophysical properties of air and solid (aluminium) are constant
- heat transfer takes place between liquid and air only
- walls of serpentine, manifolds, and headers are adiabatic
- there is no diffusion or radiation heat transfer in the system
- there is no heat loss or gain to or from the surroundings of the test chamber
- the standard k-ε turbulent model with standard wall function is used.

3.1.5 Governing Equations

CFD is fundamentally established on the governing equations of fluid dynamics. The physical phenomena of the boundary conditions of fluid flow and heat transfer is usually expressed in basic mathematical equations in partial differential form, in general. These equations perform a process in order to solve the particular problem and known as governing equations in CFD. The Navier–Stokes equations, which properly represent the fluid motion of an incompressible fluid have been considered as the cornerstone of CFD

[323]. One of the primary stages of the CFD modeling is to characterize the idealization of the true physical phenomena by the governing equations of the problem. These equations symbolize mathematical models of the conservation laws of physics including, mass conservation, momentum conservation and energy conservation. In the current study, based on some key assumptions, the Reynolds-averaged Navier-Stokes (RANS) equations have been solved by using ANSYS FLUENT 15.0, a finite volume method (FVM) based CFD software. In the instantaneous (exact) RANS equations, the solution variables are decomposed into the mean (ensemble-averaged or time-averaged) and fluctuating constituents [324]. A brief explanation of each governing equation used in the current study is presented in this section. The transport equations as well as turbulent viscosity computing methods and model constants for modeling fluid flow and heat transfer using standard k-ε model are also described in this section.

Continuity or mass conservation: ANSYS FLUENT [324] uses the following continuity or mass conservation equation:

$$\frac{\partial \rho}{\partial t} + \nabla.(\rho\vec{v}) = S_m \tag{3.1}$$

where, ρ, t, $\vec{v}$ and S_m respectively represent density, time, velocity and mass source i.e. the mass added due to vaporization of liquid droplets or condensation of air.

Based on the assumptions and the physics of the problem, the simplified general form of the mass conservation or continuity equation is re-written as

$$\frac{\partial}{\partial x_i}(\rho u_i) = 0 \tag{3.2}$$

Momentum conservation [324]*:* The equation of momentum conservation in an inertial (non-accelerating) reference frame is described as

$$\frac{\partial}{\partial t}(\rho\vec{u}) + \nabla.(\rho\vec{u}\vec{u}) = -\nabla P + \nabla.(\bar{\bar{\tau}}) + \rho\vec{g} + \vec{F} \tag{3.3}$$

where P, $\rho\vec{g}$, $\vec{F}$ and $\bar{\bar{\tau}}$ represent the static pressure, the gravitational body force, the external body force and the stress tensor.

The stress tensor, $\bar{\bar{\tau}}$ is defined as

$$\bar{\bar{\tau}} = \mu\left[(\nabla\vec{u} + \nabla\vec{u}^{T}) - \frac{2}{3}\nabla.\vec{u}I\right] \tag{3.4}$$

where μ = the molecular viscosity, I = the unit tensor, and the term $\left(\frac{2}{3}\nabla.\vec{u}I\right)$ = the effect of volume dilation.

In Reynolds averaging, taking a time average, the expression of the instantaneous (exact) Navier-Stoke of momentum conservation is written in Cartesian tensor form as:

$$\frac{\partial}{\partial t}(\rho u_i) + \frac{\partial}{\partial x_j}(\rho u_i u_j) = -\frac{\partial P}{\partial x_i} + \frac{\partial}{\partial x_j}\left[\mu\left(\frac{\partial u_i}{\partial x_j} + \frac{\partial u_j}{\partial x_i} - \frac{2}{3}\delta_{ij}\frac{\partial u_l}{\partial x_l}\right)\right] + \frac{\partial}{\partial x_j}(-\rho\overline{u_i' u_j'}) \tag{3.5}$$

The Reynolds stresses, $(-\rho\overline{u_i' u_j'})$ are suitably employed the Boussinesq hypothesis to the mean velocity gradients for the Reynolds-averaged approach to turbulence modeling.

$$-\rho\overline{u_i' u_j'} = \mu_t\left(\frac{\partial u_i}{\partial x_j} + \frac{\partial u_j}{\partial x_i}\right) - \frac{2}{3}\left(\rho k + \mu_t\frac{\partial u_k}{\partial x_k}\right)\delta_{ij} \tag{3.6}$$

Based on the assumptions in the current study, the equation of the momentum conservation becomes,

$$\frac{\partial}{\partial j}\left(\rho u_i u_j\right) = \frac{\partial}{\partial x_j}\left(\mu \frac{\partial u_j}{\partial x_i}\right) - \frac{\partial P}{\partial x_i} + \frac{\partial}{\partial x_j}\left(-\rho \overline{u_i' u_j'}\right) \tag{3.7}$$

Energy conservation [324]*:* The equation of energy conservation is modeled based on the Reynolds analogy concept to turbulent momentum transfer in the form of

$$\frac{\partial}{\partial t}(\rho E) + \nabla \cdot \left(\vec{u}(\rho E + P)\right) = \nabla \cdot \left(k_{eff} \nabla T - \sum_j h_j \vec{J}_j + (\overline{\overline{\tau}}_{eff} \cdot \vec{u})\right) + S_h \tag{3.8}$$

It is assumed that fluids are incompressible, there is no the diffusion flux of species (j), and there is no chemical reaction and any other volumetric heat sources (S_h); hence the simplified energy conservation equation is re-written in the Cartesian form as

$$\frac{\partial}{\partial x_i}(\rho u_i T) = \frac{\partial}{\partial x_j}\left(k_{eff} \frac{\partial T}{\partial x_j} + u_i \left(\tau_{ij}\right)_{eff}\right) \tag{3.9}$$

where k_{eff}, E and $(\tau_{ij})_{eff}$ represent the effective thermal conductivity, the total energy and the deviatoric stress tensor, respectively.

The effective thermal conductivity, k_{eff} is computed as

$$k_{eff} = k + \frac{C_p \mu_t}{Pr_t} \tag{3.10}$$

where k, μ_t and Pr_t are the thermal conductivity, turbulent viscosity and turbulent Prandtl number, respectively. The default value of the turbulent Prandtl number, Pr is 0.85.

The deviatoric stress tensor, $(\tau_{ij})_{eff}$ represents viscous heating and is defined as

$$(\tau_{ij})_{eff} = \mu_{eff}\left(\frac{\partial u_j}{\partial x_i} + \frac{\partial u_i}{\partial x_j}\right) - \frac{2}{3}\mu_{eff}\left(\frac{\partial u_k}{\partial x_k}\delta_{ij}\right) \tag{3.11}$$

Turbulence kinetic energy, k [324]*:* The following transport equation is used in the Standard k-ε Model in order to compute the turbulence kinetic energy, k;

$$\frac{\partial}{\partial \mathrm{t}}(\rho \mathrm{k})+\frac{\partial}{\partial \mathrm{x_i}}(\rho \mathrm{k u_i})=\frac{\partial}{\partial \mathrm{x_j}}\left[\left(\mu+\frac{\mu_t}{\sigma_k}\right)\frac{\partial \mathrm{k}}{\partial \mathrm{x_j}}\right]+G_k+G_b-\rho\varepsilon-Y_M+S_k \tag{3.12}$$

For incompressible fluid, there is no the turbulence kinetic energy generation (G_b) due to buoyancy, no contribution of the fluctuating dilatation in compressible turbulence to the overall dissipation rate (Y_M), and no user-defined source term (S_k). So, the equation of k can be simplified as

$$\frac{\partial}{\partial \mathrm{x_i}}(\rho \mathrm{k u_i})=\frac{\partial}{\partial \mathrm{x_j}}\left[\left(\mu+\frac{\mu_t}{\sigma_k}\right)\frac{\partial \mathrm{k}}{\partial \mathrm{x_j}}\right]+G_k-\rho\epsilon \tag{3.13}$$

where, G_k and σ_k represent the generation of k due to the mean velocity gradients and the turbulent Prandtl numbers for k, respectively.

The term, G_k may be defined from the exact equation for the transport of k as

$$G_k=-\rho\overline{u_i' u_j'}\frac{\partial u_i}{\partial x_i} \tag{3.14}$$

Turbulence energy dissipation, ε [324]*:* The following transport equation is used to calculate the turbulence kinetic energy dissipation rate, ε using Standard k-ε Model;

$$\frac{\partial}{\partial \mathrm{t}}(\rho\varepsilon)+\frac{\partial}{\partial \mathrm{x_i}}(\rho\varepsilon \mathrm{u_i})=\frac{\partial}{\partial \mathrm{x_j}}\left[\left(\mu+\frac{\mu_t}{\sigma_\varepsilon}\right)\frac{\partial\varepsilon}{\partial \mathrm{x_j}}\right]+C_{1\varepsilon}\frac{\varepsilon}{k}(G_k+C_{3\varepsilon}G_b)-C_{2\varepsilon}\rho\frac{\varepsilon^2}{k}+S_\varepsilon \tag{3.13}$$

For an incompressible fluid flow, the equation of ε can be simplified as

$$\frac{\partial}{\partial \mathrm{x_i}}(\rho\varepsilon \mathrm{u_i})=\frac{\partial}{\partial \mathrm{x_j}}\left[\left(\mu+\frac{\mu_t}{\sigma_\varepsilon}\right)\frac{\partial\varepsilon}{\partial \mathrm{x_j}}\right]+C_{1\varepsilon}\frac{\varepsilon}{k}G_k-C_{2\varepsilon}\rho\frac{\varepsilon^2}{k} \tag{3.14}$$

where, $C_{1\varepsilon}$, $C_{2\varepsilon}$, and $C_{3\varepsilon}$ are constants, and σ_ε is the turbulent Prandtl number for ε. The turbulent viscosity, μ_t is calculated from the combination of k and ε as

$$\mu_t = \rho C_\mu \frac{k^2}{\varepsilon} \tag{3.15}$$

where, C_μ is a constant.

3.1.6 Grid independency Study

It is essential to note that the mesh fineness plays a vital role in the computational fluid dynamics (CFD) simulations. In the CFD, the simulation time, cost and accuracy greatly depend on proper mesh generation in the computational domain. In order to establish the accuracy, consistency and reliability of the numerical results, and to retain the computational cost low, the grid indecency test has been performed in the current study. Several grid systems have been used to check grid independency by solving the Navier-Stokes governing equations. These are presented in Figures 3.20 and 3.21.

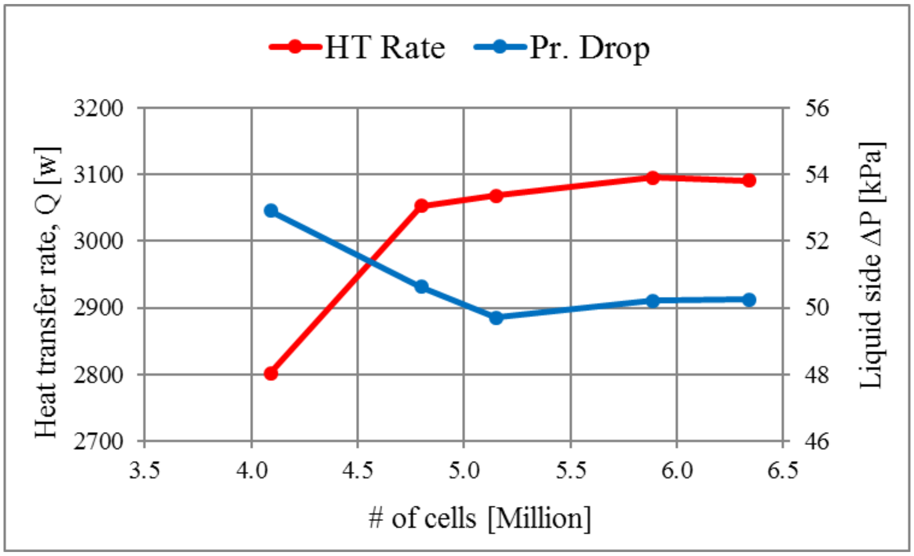

Figure 3.20: Grid independency study of 2-pass crossflow MICHX used in Stage-I

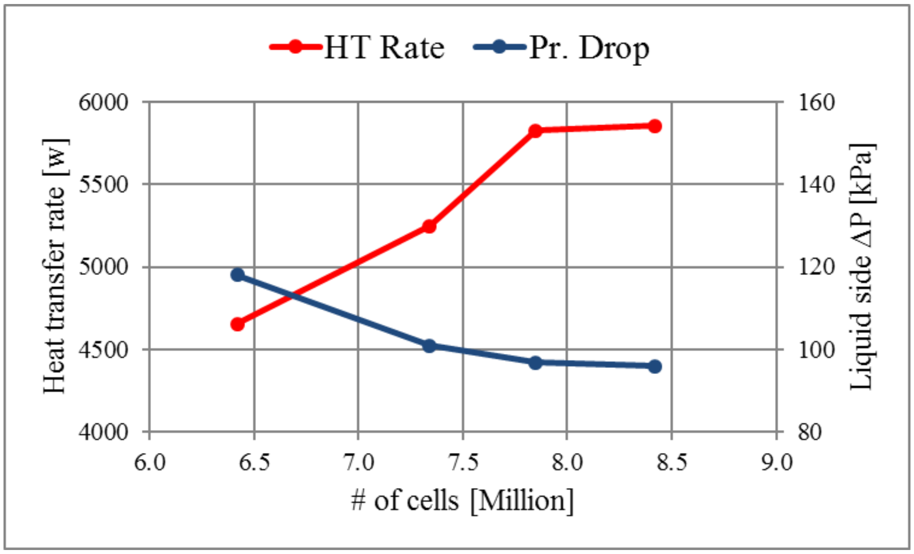

Figure 3.21: Grid independency study of 5-pass crossflow MICHX used in Stage-V

The relative deviations in the heat transfer rates ($\dot{Q}$) and the pressure drops (ΔP) in two consecutive grid systems (GS) are shown in Tables 8 and 9.

Table 8: Relative deviations in the Q and ΔP in different grid systems of 2-pass MICHX

Grid Systems (GS)	**Variations in $\dot{Q}$ [%]**	**Variations in ΔP [%]**
GS1 and GS2	8.95	4.32
GS2 and GS3	0.52	1.81
GS3 and GS4	0.88	0.99
GS4 and GS5	0.14	0.10

Table 9: Relative deviations in the Q and ΔP in different grid systems of 5-pass MICHX

Grid Systems (GS)	**Variations in $\dot{Q}$ [%]**	**Variations in ΔP [%]**
GS1 and GS2	12.70	14.41
GS2 and GS3	11.03	4.16
GS3 and GS4	0.52	0.83

The grid systems all of the numerical simulations have been chosen when the maximum variations in both the $\dot{Q}$ and the ΔP in two successive GS are observed about 1%. The selected GS for CFD simulations of the models in different Stages of the current study are presented in in Table 10.

Table 10: Selected grid systems used in the current study in different stages

Model	Stage	# Cells in the used model (Million)
2-pass single loop FTHX	Stage I	4.36
2-pass single loop MICHX	Stage I	5.89
5-pass 3-loop MICHX	Stage II	22.95
2-pass 4-loop sequential FTHX	Stage III	12.49
2-pass 2-loop simultaneous MICHX	Stage III	8.45
5-pass single loop MICHX	Stage V	7.85

3.1.7 Algorithms

Solution procedure overview:

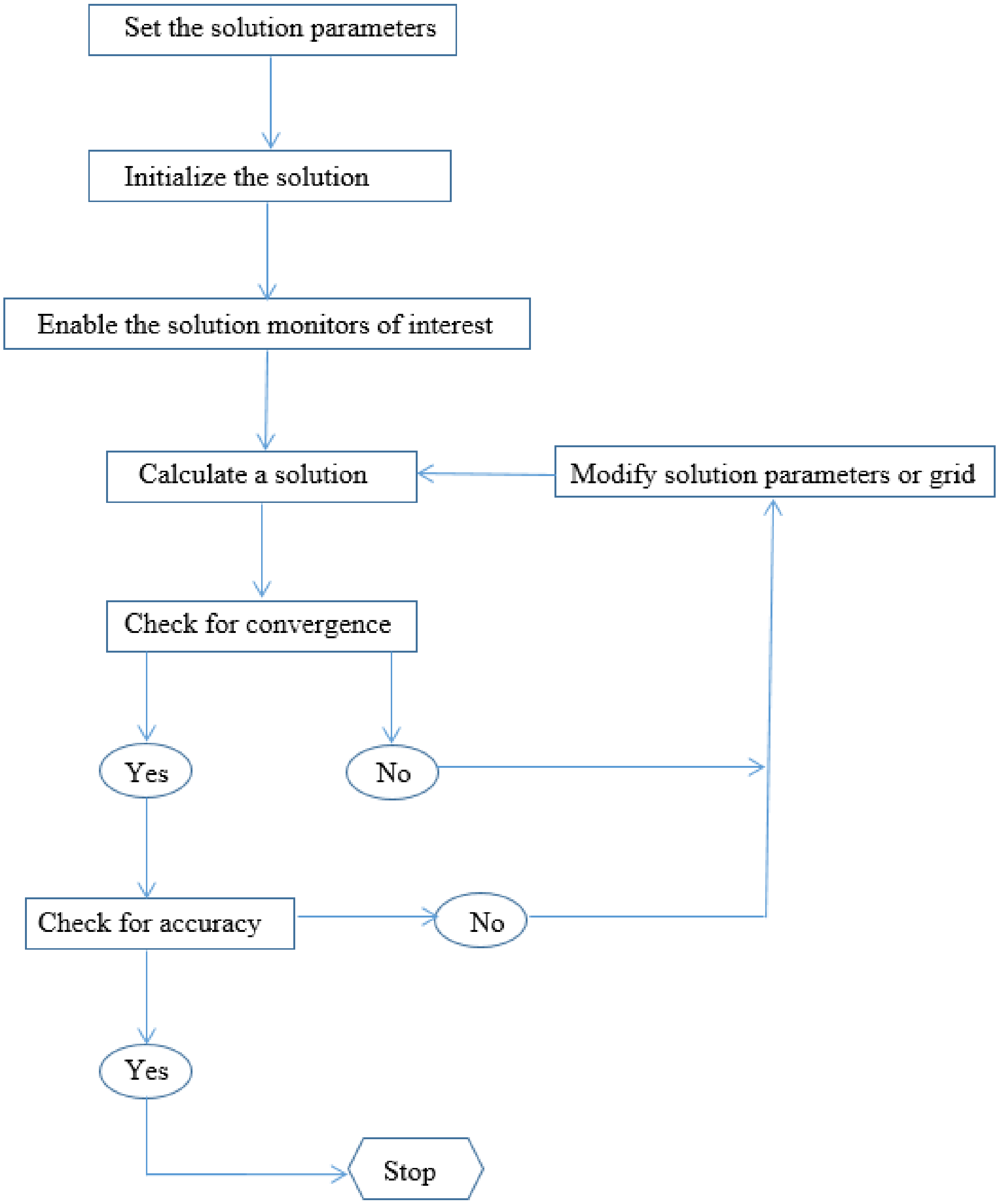

Figure 3.22: Overview of the solution approach

Pressure-based segregated algorithm: The transport equations have been solved sequentially using pressure-based segregated algorithm in which the individual governing equation for the solution variables such as $u, v, w, p, T, k,$ and ε have been solved one after another. During this solution algorithm, each iteration involves following steps.

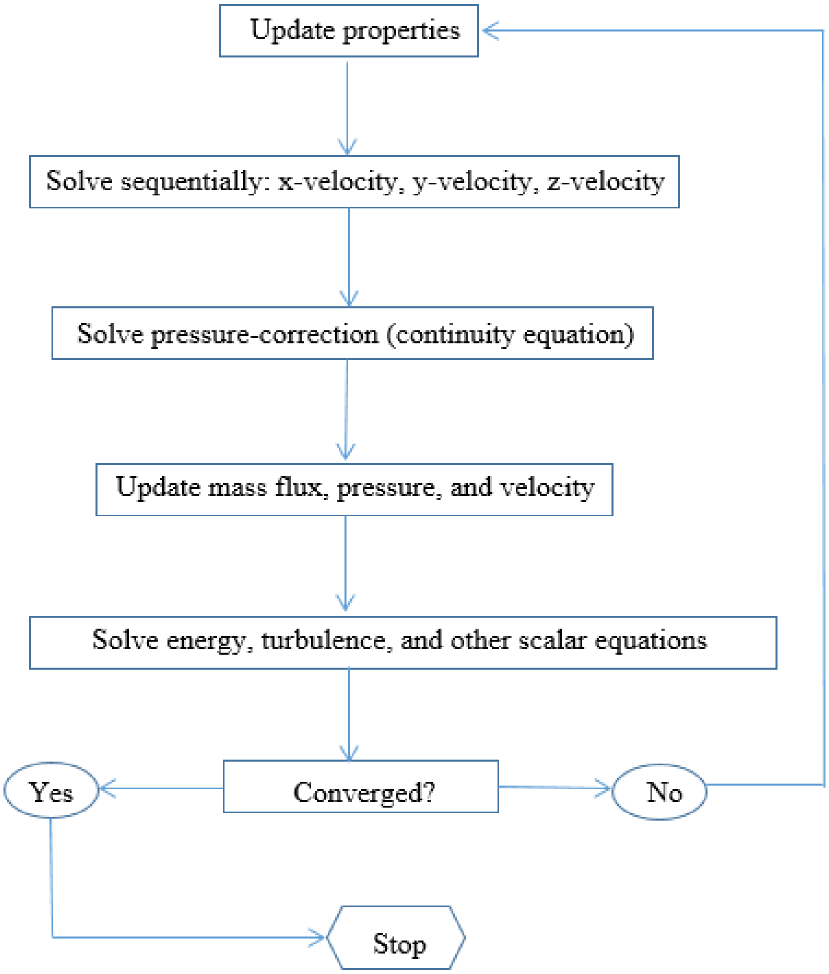

Figure 3.23: Overview of the pressure-based solution methods

The steps for every iteration of the segregated algorithm are outlined below:

1. Update fluid properties including specific heat, density, viscosity, and thermal conductivity based on the current solution.
2. Using the recently updated values of pressure and face mass fluxes, sequentially solve the momentum equations.
3. With the recently obtained mass-flux and velocity field, solve the pressure-correction equation.
4. Using the pressure-correction obtained from Step 3, update the velocity field, pressure, and mass fluxes.
5. Through the current values of the solution variables, solve the additional energy, turbulence, and other scalar equations.
6. Check for the convergence of the equations.

The above steps are continued until the convergence criteria are met.

Iterative time-advancement scheme:

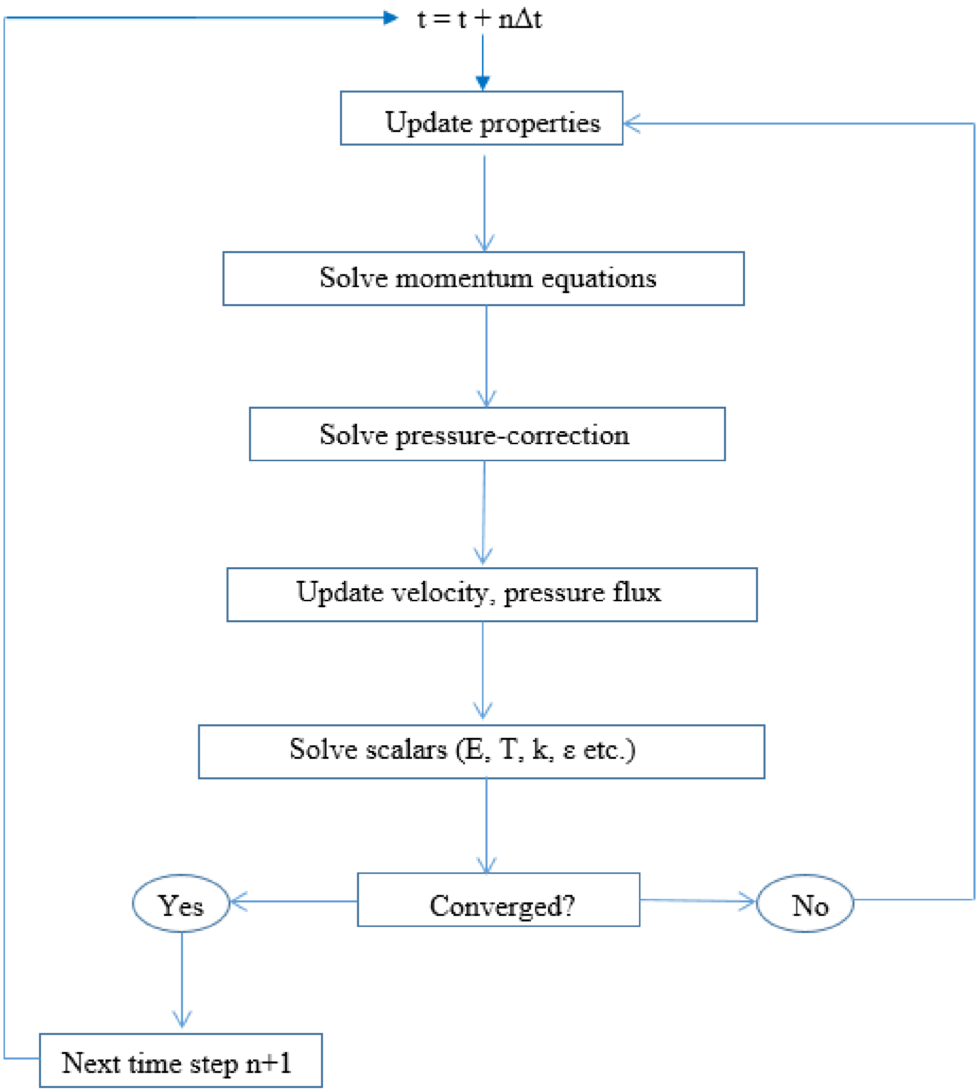

Figure 3.24: Iterative time-advancement scheme

3.1.8 Computational and Physical Setup

In CFD simulation, the setup of the physical and computational parameters is very significant. The class of model, boundary conditions and solver play the major role in the simulation process, the convergence and the accuracy of the solution. In the current study, the CFD has been carried out in three-dimensional, double precision, pressure-based, absolute velocity formulation and implicit scheme to solve the flow and heat transfer problem in complex model such as an air-to-liquid crossflow minichannel heat exchanger. Details of the structures of physical and computational fundamental parameters are described in this section.

Model selection: The quality of a numerical simulation and it's accuracy of prediction crucially depends on the selection of a model. A turbulence model is used to capture the turbulence parameters particularly in thermal and flow fields developed around the air-to-liquid crossflow heat exchanger core. This model is chosen due to the high Reynolds number of the fluids at the inlet and the outlet boundaries as well as three-dimensional unsteady random fluid motion at headers, manifolds, and heat exchanger core. In the Direct Numerical Simulation (DNS), the CPU requirements would go beyond the accessible computing power. As a result, averaging procedures have been applied to the Navier-Stokes equations.

Reynolds Averaged Navier-Stokes (RANS) turbulence models are popular in industrial CFD for fluid flow and heat transfer simulations. It is especially because of their robustness and lower computational cost with reasonable accuracy for a wide range of turbulent flows [325]. The RANS models including the k-ε or the k-ω models solve two transport equations and use turbulent viscosity or eddy viscosity approach in order to calculate the Reynolds Stresses.

The model selection depends on the flow physics, the specific problem class, the required accuracy level, the available computational resources and the available simulation time. The computational domain includes two continuums, namely liquid and air. The liquid Reynolds number is in the current study is maintained within the range of laminar regime ($26 \leq Re_{ch} \leq 2274$); however the air Reynolds number is in the turbulence flow regime ($3.4 \times 10^4 \leq Re_a \leq 2.1 \times 10^5$). In order to capture the turbulence parameters, a turbulence model is used.

Preliminary simulations have been conducted using Standard k-ε with Std Wall Function (SWF), Standard k-ε with Enhanced Wall Treatment (EWT), Realizable k-ε with EWT, and Shear Stress Transport (SST) k - ω turbulence models. Numerical predictions have been compared to the experimentally measured data. The Standard k-ε with EWT shows better results than the others do. As a result, Standard k-ε turbulence model is used in the current study.

The turbulence intensity, I is defined as

$$I = \frac{u\prime}{u_{ave}} = 0.16 {Re_{d_h}}^{-1/8} \tag{3.16}$$

where, Re_{d_h} is the Reynolds number of fluid based on hydraulic diameter, u' is the ratio of the root-mean-square of the velocity fluctuations, and u_{ave} is the mean velocity of fluid flow.

Generally, $I \leq 1\%$ for low-turbulence and $I > 10\%$ for high-turbulence. For high-turbulence having complex geometries like HXs, $5\% < I < 20\%$. For medium-turbulence or low Reynolds number with moderate devices like large pipes and ventilation, $1\% \leq I \leq 5\%$. For low-turbulence like external flow across cars, submarines, and aircrafts, $\mathrm{I} < 1\%$ [325]. In the current study, the turbulence intensity (I) is calculated using Eq. (3.16).

Viscous heating is enabled to capture the effects of viscous heating on the thermal performance of the heat exchanger. Details of the model setup is presented in Table 11.

Table 11: Model set up

Model	3D double precision (3DDP) Pressure-based velocity formulation
State	Steady, 2nd order implicit
	Transient, 2nd order implicit
RANS model	Standard k-ε with EWT turbulence model
Viscous heating	Enabled
Energy	Enabled
Radiation, Species, Pollutants, NOx, SOx, and Soot etc.	None
Model constants: Default values are considered for all constants	$C_\mu = 0.09$, $C_{1\varepsilon} = 1.44$, and $C_{2\varepsilon} = 1.92$ TKE Prandtl number = 1 TDR Prandtl Number = 1.3 Wall Prandtl number = 0.85 Energy Prandtl number = 0.85

Properties of materials: In heat transfer and fluid flow simulations, the thermophysical properties of working fluids play a significant role. With the purpose of predicting appropriate thermal and flow performance and behaviour of heat exchangers, proper thermophysical properties of each liquid have been applied in all models. Several working fluids have been used in the numerical simulations of the current study. These include water, ethylene glycol, automotive transmission fluid (ATF), aluminum oxide (Al_2O_3) based nanofluids and air. User-Defined Database has been used to create new materials including ATF and Al_2O_3 nanofluids. Thermophysical properties of all liquids have been considered temperature dependent. While the properties of air and solid (aluminum) have been assumed independent of temperature. Details are illustrated in the thermophysical properties of the working fluids section.

Boundary conditions: Appropriate boundary conditions are desired for numerical simulation in order to solve heat transfer and fluid flow problems. Following boundary conditions have been precisely followed in the current study:

- Inlet liquid: Temperature and mass flow rates are specified
- Inlet air: Temperature and mass flow rate or velocity are specified
- Outlet liquid: Pressure outlet boundary condition is specified.
- Outlet air: Pressure outlet boundary condition is specified
- Headers, manifolds and serpentines: Zero heat flux is specified.
- Walls: No slip, stationary wall and Type 1 thermal boundary conditions are specified

Residuals: When successive iteration is stopped, the sum of the normalized absolute residuals in each control volume for the flow and the energy variables have been reduced to 1e-04 and 1e-09, respectively. The intention is to maximize the accuracy of simulation results.

Initialization: Before starting calculations, the model has been initialized using Standard Initialization Method. The thermal and flow fields in the entire domain have been initialized from the inlet liquid variables.

3.2 Transient Heat Transfer Model

Heat exchanger is the key component that is widely used in engine cooling as well as automotive heating, ventilation and air conditioning (HVAC) systems. The thermal performance of the entire HVAC and cooling systems strongly depends on how well a heat exchanger responds to changes in operating conditions such as, temperature and mass flow rate, in particular. As a result, the evaluation of transient phenomenon of heat transport devices is of increasing interest in many industrial, automotive, and residential applications. In the current study, a three-dimensional transient thermal model for a air-to-liquid crossflow heat exchanger is numerically solved with the purpose of predicting the transient responses under step changes in hot fluid inlet temperature and mass flow rate. Transient responses of different heat transfer parameters, such as fluid outlet temperature, channel inner surface temperature, heat transfer rate, heat transfer coefficient, and Nusselt number have been predicted for perturbation of hot fluid mass flow rate and inlet temperature.

CHAPTER 4

THEORETICAL BACKGROUND AND DATA PROCESSING

4.1 Field Variables

The field variables have been computed by using the ANSYS FLUENT [324], a widely used commercial finite volume method based CFD software.

Evaluation of surface area: The surface area is calculated by summing the areas of the facets on the surface as

$$\int \mathrm{dA} = \sum_{\mathrm{i}=1}^{\mathrm{n}} |\mathrm{A_i}| \tag{4.1}$$

The shapes of facets that define on a surface are either triangular or quadrilateral.

Evaluation of integral of field variables: The integral of a field variable on a surface is calculated by summing the product of the facet area and the particular field variable as

$$\int \Phi \mathrm{dA} = \sum_{\mathrm{i}=1}^{\mathrm{n}} \Phi_{\mathrm{i}} |\mathrm{A_i}| \tag{4.2}$$

Evaluation of surface temperature: The area-weighted average surface temperatures of inner and outer surfaces of minichannel heat exchanger slab have been calculated as

$$\frac{1}{\mathrm{A}} \int \Phi \mathrm{dA} = \frac{1}{\mathrm{A}} \sum_{\mathrm{i}=1}^{\mathrm{n}} \Phi_{\mathrm{i}} |\mathrm{A_i}| \tag{4.3}$$

Evaluation of thermophysical properties of working fluids: The mass weighted average thermophysical properties of the working fluids used in the current study. The properties have been computed by dividing the summation of the product of the selected field variable and the absolute value of the surface mass flux by the summation of surface mass flux as

$$\frac{\int \Phi\rho|\vec{v}\cdot d\vec{A}|}{\int \rho|\vec{v}\cdot d\vec{A}|} = \frac{\sum_{i=1}^{n} \Phi_i\rho_i|\vec{v}_i\cdot\vec{A}_i|}{\sum_{i=1}^{n} \rho_i|\vec{v}_i\cdot\vec{A}_i|} \tag{4.4}$$

where,

Φ = field variable (property) of the working fluid

A = facet (surface) area associated with a cell in the domain

v = velocity vector of the working fluid

4.2 Hot Fluid Residence Time

The residence time is defined as the time occupied by the hot fluid to travel the heat exchanger core, where heat transfer takes place between the hot fluid and the cold fluid. It has been computed as

$$t_{res} = L_{ch}/\, V_{ch} = \rho_w A_{c,ch} L_{ch}/\dot{m}_{h,ch} \tag{4.5}$$

where**,** $\dot{m}_{h,ch}$, ρ_h, $A_{c,ch}$, and L_{ch} represent the mass flow rate of hot fluid though each channel, density of hot fluid, channel cross sectional area, and length of each channel, respectively.

4.3 Dimensionless Parameters

Dimensionless parameters characterize the significant reduction in the number of parameters. In order to generalize and report the simulation outcomes conveniently, parameters have been non-dimensionalized.

Nusselt number: In heat transfer at a surface boundary within a fluid, Nusselt number signifies the intensification of heat transfer by means of the convection compared to conduction normal to the boundary. It is the dimensionless form of convective heat transfer coefficient (h). It is defined as

$$\mathrm{Nu} = \frac{\text{convective heat transfer}}{\text{conductive heat transfer}} = \frac{\mathrm{h}}{\mathrm{k/d}} = \frac{\mathrm{hd}}{\mathrm{k}} \tag{4.6}$$

where d is the channel diameter and k is the thermal conductivity of the fluid.

Reynolds number: The Reynolds number symbolizes the ratio of the inertial forces to viscous forces and determines the flow regime. It is defined as

$$\mathrm{Re} = \frac{\text{inertial force}}{\text{viscous force}} = \frac{\rho \mathrm{vd}}{\mu} = \frac{\dot{\mathrm{m}}}{\mathrm{N}\pi\mu \mathrm{d}} \tag{4.7}$$

where, N is channel numbers and μ is the dynamic viscosity of the fluid.

Prandtl number: The Prandtl number is the ratio of momentum diffusivity (kinematic viscosity) to thermal diffusivity. It signifies the thermal and hydrodynamic boundary layer thickness, depending on whether it is equal to one.

$$\mathrm{Pr} = \frac{\text{viscous diffusion rate}}{\text{thermal diffusion rate}} = \frac{\mu/\rho}{\mathrm{k}/(\mathrm{c_p}\rho)} = \frac{\mu \mathrm{C_p}}{\mathrm{k}} \tag{4.8}$$

Convective heat transfer relationship is generally expressed as [12]

$$\mathrm{Nu} = \mathrm{aRe^m Pr^n} \tag{4.9}$$

Transient dimensionless outlet temperature: The time dependent dimensionless outlet temperatures of hot fluid, $\mathrm{T^*_{h,o}(t)}$ and cold fluid, $\mathrm{T^*_{c,o}(t)}$ have been defined as

$$T_{h,o}^{*}(t) = \frac{T_{h,o}(t) - T_{c,i}}{T_{h,i} - T_{c,i}} \tag{4.10}$$

$$T_{c,o}^{*} = \frac{T_{c,o}(t) - T_{c,i}}{T_{h,i} - T_{c,i}} \tag{4.11}$$

where $T_{h,o}(t)$, $T_{h,i}$and $T_{c,i}$ represent temporal hot fluid outlet temperature, hot fluid inlet temperature and cold fluid inlet temperature, respectively.

Dimensionless time (t^*): The dimensionless time is defined as

$$t^* = \frac{t}{t_{res}} \tag{4.12}$$

The residence time (t_{res}) is the time employed by the hot fluid to pass through channel, where heat exchanges between the hot and cold fluids.

4.4 Heat Transfer Performance Parameters

Following fundamental equations have been used for computations of convective heat transfer;

Heat transfer rate ($\dot{Q}$):

$$\dot{Q} = \dot{m} C_p \Delta T \tag{4.13}$$

Heat transfer coefficient (h):

$$h = \dot{Q} / \left(A_s (T_m - T_s) \right) \tag{4.14}$$

where, A_s = Heat transfer surface area in m^2

c_p = Fluid specific heat in J/kgK

$\dot{m}$ = Mass flow rate in kg/s

ΔT = Temperature difference, in ℃, between fluid enter to and exit from the heat exchanger

T_m = Fluid mean temperature in ℃, and

T_s = Channel inner surface temperature in ℃

4.5 Thermophysical Properties of Working Fluids

The thermophysical properties, such as density, specific heat, viscosity and thermal conductivity of a fluid signify the response of the fluid due to the variation in its speed or flow rate, temperature or combination of both. These properties are significant in convective heat transfer mechanism for efficient engineering design of most of the thermal systems. The temperature dependent variations of the fluid properties invalidate the constant properties, especially in case of minichannel flow. Therefore, accurate transport fluid properties are required. Numerous reliable sources, such as scientific literature, web tools, and institutions make the thermophysical properties of fluids available.

In the current study, the all working fluids have been assumed as incompressible within the operating temperature and flow regime. Therefore, the transport properties of the fluids have been considered temperature dependent only. The thermophysical properties of liquids, such as automotive fluids and nanofluids have been considered temperature dependent, while the properties of air have been assumed constant. Table 12 shows the working fluids used in the computational simulations and the source of the fluid properties composed from.

Table 12: Source of thermophysical properties of working fluids

Working fluid	Source of the properties retrieved from
Air	Assumed constant
Water (W)	National Institute of Standards and Technology (NIST), U.S.
50% Ethylene glycol (EG)	
Engine oil (EO)	Shell Nederland
Automatic transmission fluid (ATF)	CAN-AM Instruments Ltd, Canada and SAE technical paper

Aluminum oxide (Al_2O_3) based nanofluids have also been used as working fluids in the present study. Following correlations have been applied for computations of the nanofluids;

Density: Pak and Cho [126]

$$\rho_{nf} = \emptyset\rho_{np} + (1 - \emptyset)\rho_{bf} \quad (4.15)$$

where, ρ_{nf} = density of nanofluid, ρ_{np} = density of nanoparticles, ρ_{bf} = density of basefluid and $\emptyset$ = volume fraction of nanoparticles.

Specific heat: Xuan and Roetzel [130]

$$Cp_{nf} = \frac{\emptyset(\rho Cp)_{np} + (1-\emptyset)(\rho Cp)_{bf}}{\emptyset\rho_{np} + (1-\emptyset)\rho_{bf}} \quad (4.16)$$

where, Cp_{nf}, Cp_{bf} and Cp_{np} are the specific heat of nanofluid, basefluid and nanoparticles, respectively.

Dynamic viscosity: Batchelor [253]

$$\mu_{nf} = (1 + 2.5\emptyset + 6.2\emptyset^2)\mu_{bf} \tag{4.17}$$

where, μ_{nf} and μ_{bf} denote the dynamic viscosity of nanofluid and basefluid, respectively.

Thermal conductivity: Sert et al. [233]

$$k_{eff} = k_{static} + k_{dynamic} = k_{nf} + k_{brownian}$$

$$k_{eff} = \left[\frac{k_{np}+2k_{bf}+2(k_{np}-k_{bf})\emptyset}{k_{np}+2k_{bf}-(k_{np}-k_{bf})\emptyset}\right]k_{bf} + 5 \times 10^4 \beta\emptyset\rho_f c_{p,f}\sqrt{\frac{k_B T}{\rho_{np} d_{np}}}f \tag{4.18}$$

where, K_B is the Boltzmann's constant, T is the nanofluid temperature, k_{np} is the thermal conductivity of the nanoparticles, k_{bf} is the thermal conductivity of the basefluid, and β and f are the experimental constants.

For Al_2O_3/W nanofluid, $f = 1$ and $\beta = 0.0017(100\emptyset)^{-0.0841}$, for $\emptyset > 1\%$ [233]

CHAPTER 5

MODEL VERIFICATION AND VALIDATION

In the current study, different stages are aimed to fulfil the different purposes. In the initial stage, a 2-pass air-to-liquid crossflow MICHX is used to investigate basic thermal and fluid flow characteristics and compared with a conventional FTHX. Subsequently, more realistic models with different sizes and arrangements are presented.

In this chapter, aspects of accuracy and uncertainty in CFD are illustrated. The errors and the uncertainty are unavoidable features of CFD simulations [326]. It is important to develop rigorous approaches to quantify the level of confidence in the CFD results. With the purpose of addressing this issue, an organized process and rules for best practice have been followed. In that circumstance, verification and validation due to AIAA (1998) [327] and Oberkampf et al. [328] have now been commonly accepted [326].

It is essential to carry out an error analysis of numerical computation to make the results trustworthy. In order to ensure that the numerical results of the computational model are accurate and consistent, two categories of error analyses namely, verification and validation have been accomplished.

The process of verification is employed to quantify the errors. The errors in numerical results are primarily due to truncation and rounding off the numbers. The truncation or discretization error happens due to approximations used in the formulation of the numerical computation and roundoff error arises due to the use of limited number of significant digits with the computing device [12]. Some other computational matters including mesh quality and residuals are also responsible for numerical error. Since computer coding errors and user errors have been ignored, the roundoff error, the iterative convergence error, and the discretisation error have been evaluated as prescribed by AIAA (1998) [327].

With the aim of minimizing the roundoff error, CFD results have been obtained using a double precision machine with 16 significant digits. In order to quantify the iterative convergence error, the effects of residuals on mass flow rate and pressure drop have been investigated. The discretisation error is computed by mesh refinement. A grid independency study has been carried out to attain a high-quality CFD result,

Another verification has been performed by checking overall mass flow rates of both fluids and heat transfer rate of the system. Once a model is verified and displayed to be numerically reliable, a selected set of the results for each model is validated by comparing with experimental measured data. The verification and validation of different models in the current study are described in this section.

5.1 Model Verification and Validation

5.1.1 Verification of 2-pass Single-loop FTHX and MICHX

In order to ensure that the CFD results are accurate and consistent, both the conventional FTHX and MICHX have been numerically verified in a few ways. First, a grid independency study has been carried out to ensure that the grid is fine enough to capture the heat transfer and flow fields. These have been illustrated in section 3.1.6. Other verifications have been performed by analyzing the errors in the mass flow rate and the heat transfer rate for each simulation. Figure 5.1 represents the errors in the mass balance (MB) and the heat balance (HB) in numerical results in FTHX and MICHX:

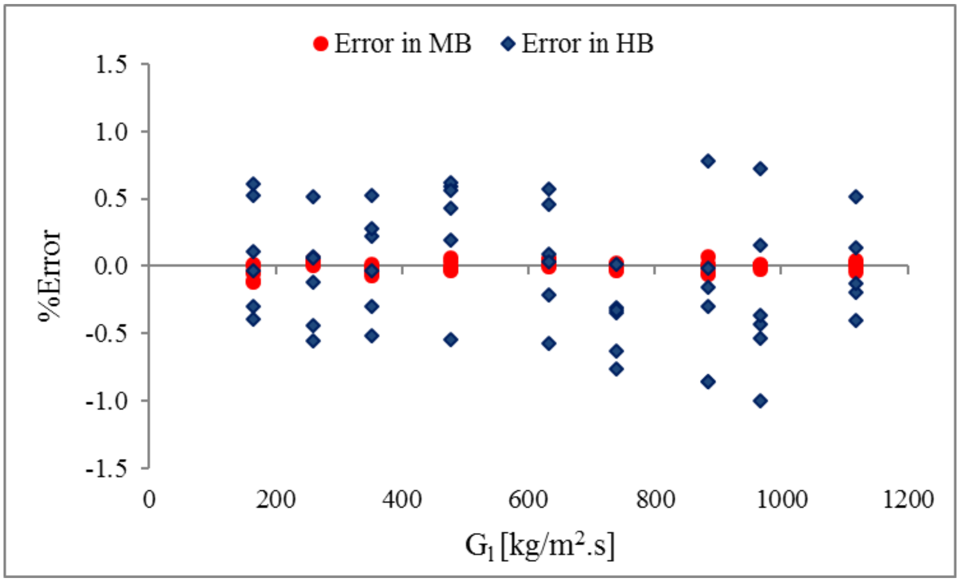

Figure 5.1: Numerical errors in mass balance (MB) and heat balance (HB) in simulation results of FTHX and MICHX

The errors in mass balance (MB) and heat balance (HB) have been found to be $\pm 0.2\%$ and $\pm 1.1\%$, respectively.

Numerical results have also been evaluated using different computing approaches. Consistent and reliable predictions have been seen. These are shown in Tables 13 and 14.

Table 13: Numerical results of 2-pass conventional FTHX at different approaches

$\dot{Q}_{o/a\_simulation}$	2194.65 w
$Q_{o/a\_calculated} = \dot{m}c_p\Delta T$	2195.37 w
$\dot{Q}_{total} = \sum_{i=1}^{61}\left(q_{i(top)} + q_{i(bottom)}\right)$	Top = 1224.95 w; Bottom = 985.82 w Total = 2210.77 w
$\bar{h}(x) = \sum_{i=1}^{122} h_i(x) \Big/ 122$	$\bar{h}(x)$_top = 5829.52 w/m^2K $\bar{h}(x)$_bottom = 5501.71 w/m^2K $\bar{h}(x)$ = 5665.38 w/m^2K
$\bar{h}(HX) = Q/A_s(T_b - T_s)$	$\bar{h}(HX)$ = 5683.971 w/m^2K

Table 14: Numerical results of 2-pass MICHX at different approaches

Computation approach	Results
$\dot{Q}_{o/a\_simulation}$	$2443.95w$
$\dot{Q}_{o/a\_calculated} = \dot{m}c_p\Delta T$	$2450.05w$
$\dot{Q}_{total} = \sum_{i=1}^{61}\sum_{j=1}^{68}\left(\dot{q}_{ij(top)} + \dot{q}_{ij(bottom)}\right)$	$Top = 1362.09w$ $Bottom = 1083.51w$ $Total = 2445.60w$
$\bar{h}(x) = \sum_{i=1}^{122} h_i(x) \Big/ 122$	$\bar{h}_{ch34\_top} = 10109.92\ w/m^2K$ $\bar{h}_{ch34_{bottom}} = 9503.55\frac{w}{m^2K}$ $\bar{h}_{ch34} = 9806.74\ w/m^2K$
$\bar{h}(HX) = \left(\sum_{n=1}^{68}\bar{h}\right)\Big/68$	$9957.27\ w/m^2K$
$\bar{h}(HX) = \frac{\dot{Q}}{A_s(T_b - T_s)}$	$10063.35\ w/m^2K$

It is obvious from the above Tables 12 and 13 that the heat transfer rates ($\dot{Q}$) and the heat transfer coefficients (h) are almost identical at different evaluation methods. The deviations in $\dot{Q}$ and h at different approaches have been found to be $\pm 0.5\%$ and $\pm 3.9\%$, respectively. These signify the consistent and reliability of the numerical predictions.

5.1.2 Validation of 2-pass Single-loop MICHX with Experimental Data

In order to ensure that the model is an accurate representation of the real world from the perspective of the indented uses, a set of simulation results has been compared with experimentally measured data [33]. The operating conditions of both the simulations and experiments are identical. Water and ethylene glycol have been cooled by air through the crossflow MICHX. The comparisons, at the laminar flow regime, are presented in Figures 5.2 to 5.9.

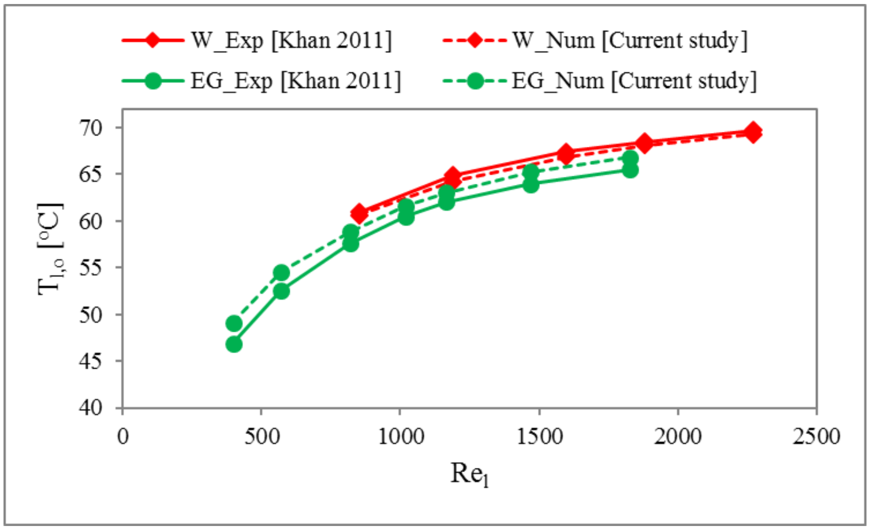

Figure 5.2: Comparison between numerical predictions and experimental data for outlet temperature of liquid

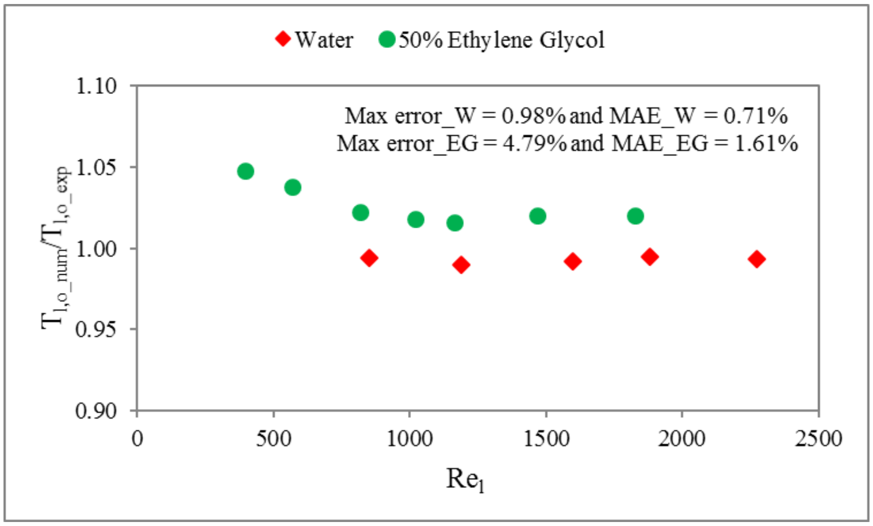

Figure 5.3: Errors in liquid outlet temperature of numerical results compared to experimental data

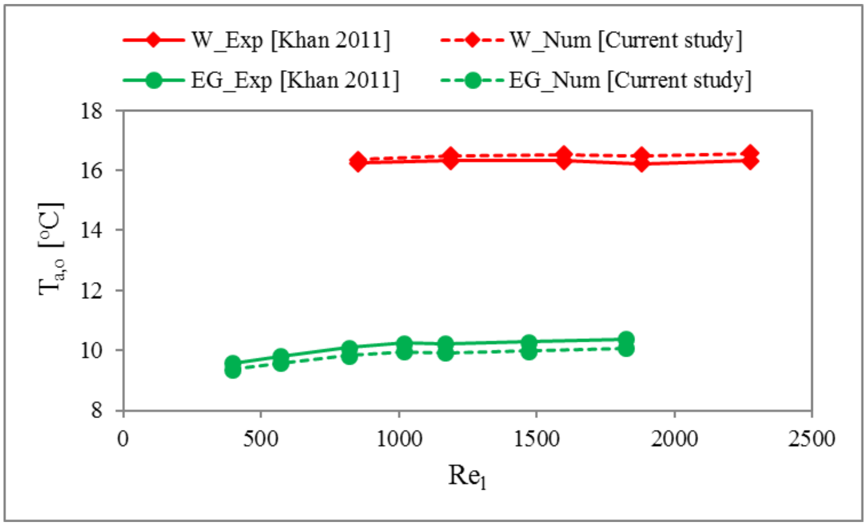

Figure 5.4: Comparison between numerical predictions and experimental data for outlet temperature of air

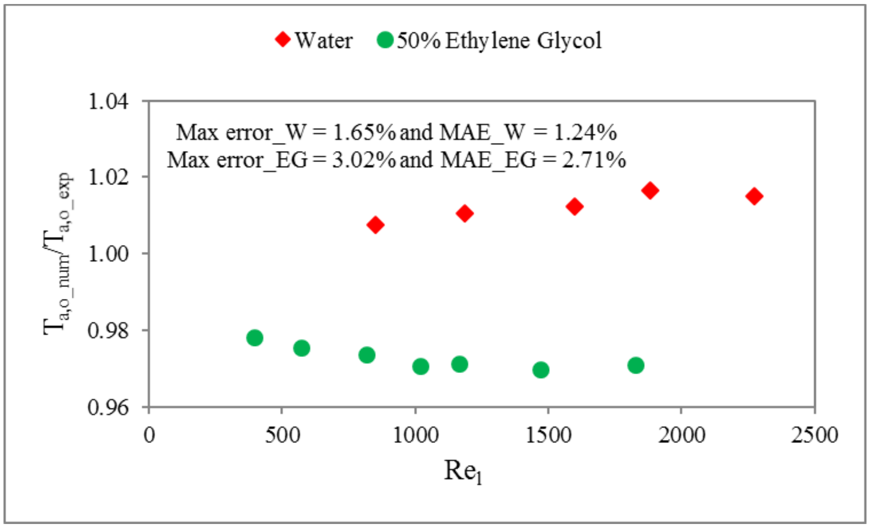

Figure 5.5: Errors in air exit temperature of numerical results compared to experimental data

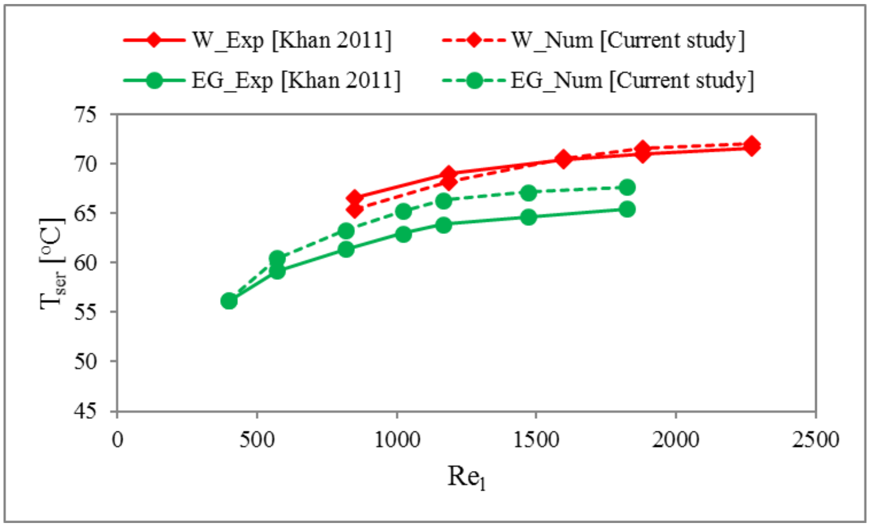

Figure 5.6: Comparison between numerical predictions with experimental data for serpentine surface temperature

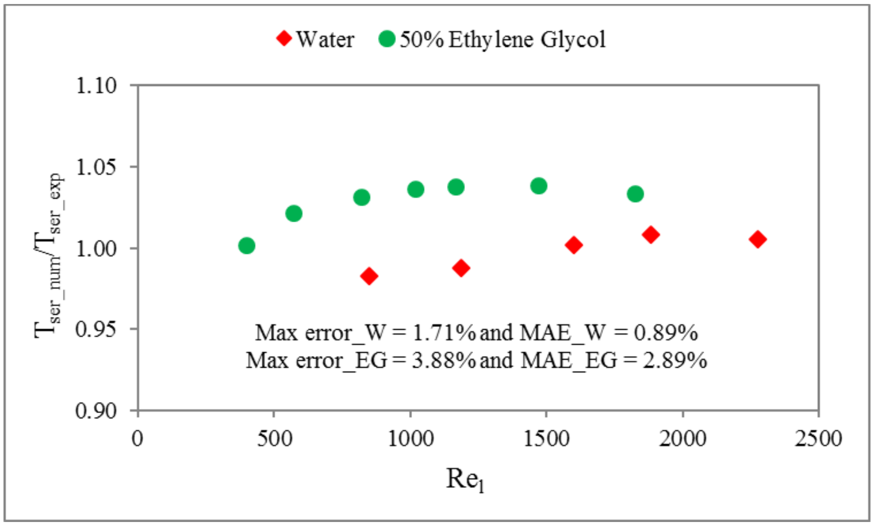

Figure 5.7: Errors in serpentine temperature of numerical results compared to experimental data

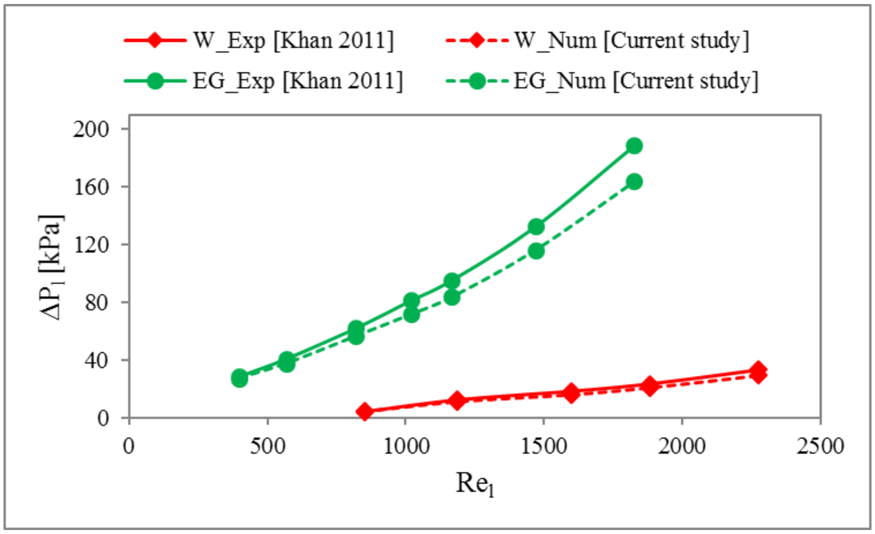

Figure 5.8: Comparison between numerical predictions and experimental data for liquid-side pressure drop

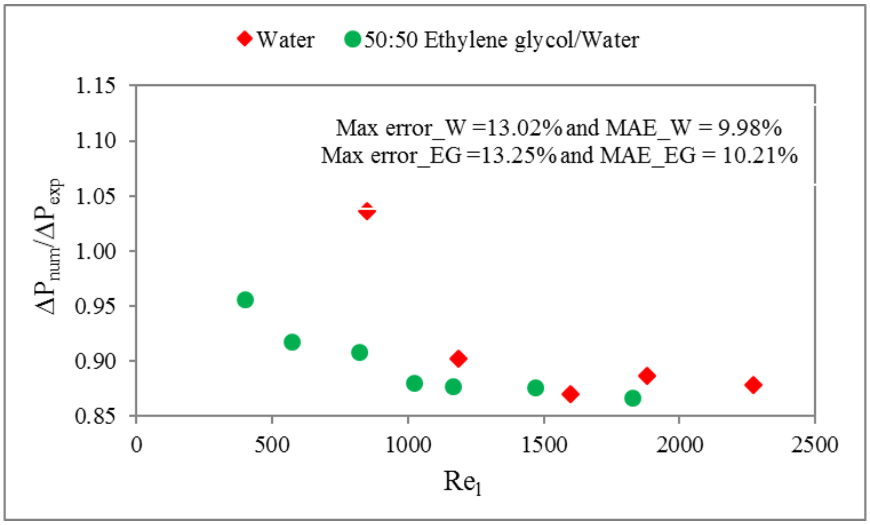

Figure 5.9: Errors in liquid-side pressure drop of numerical results compared to experimental data

Numerical predictions show a good agreement with experimentally measured data. For water, the maximum errors in liquid outlet temperature, air outlet temperature, serpentine temperature, and liquid side pressure drop have been found 0.98%, 1.65%, 1.71% and 13.02%, respectively. The corresponding maximum errors in the above parameters have been found 4.79%, 3.02%, 3.88% and 13.25% in case of ethylene glycol.

While the mean average errors have been observed between 0.71% to 9.98% for water and 1.61% to 10.21% for ethylene glycol.

5.1.3 Verification of 5-pass 3-loop MICHX

The maximum absolute errors in MB and HB have been found 1.13% and 1.21%, respectively. The respective absolute mean average errors in MB and HB have been found 0.95% and 0.85%.

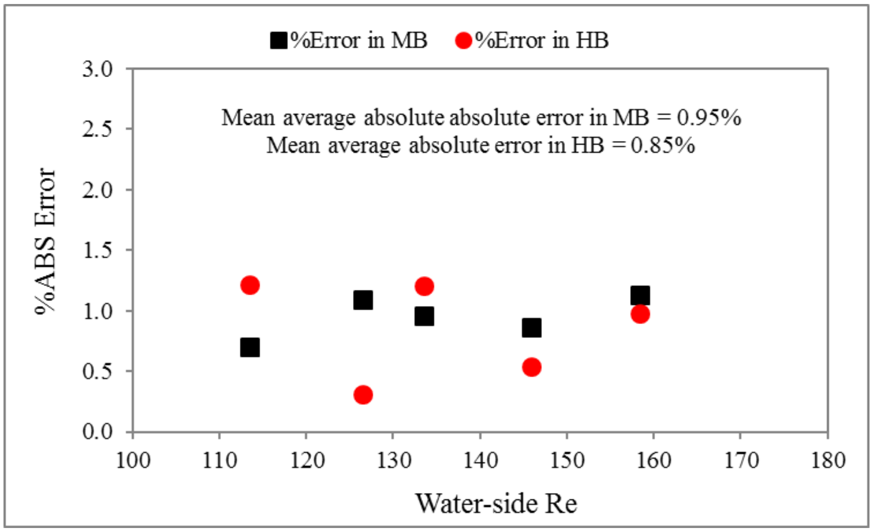

Figure 5.10: Absolute error in mass balance and heat balance

5.1.4 Validation of 5-pass 3-loop MICHX with Experimental Data

This model has been validated with experimental data [321] to confirm that the model accurately symbolize the practical applications of the physical device. In both the numerical and experimental studies, air has been cooled by water in the crossflow MICHX. The comparison between computational outcomes and actual test data is illustrated in Figures 5.11 to 5.16.

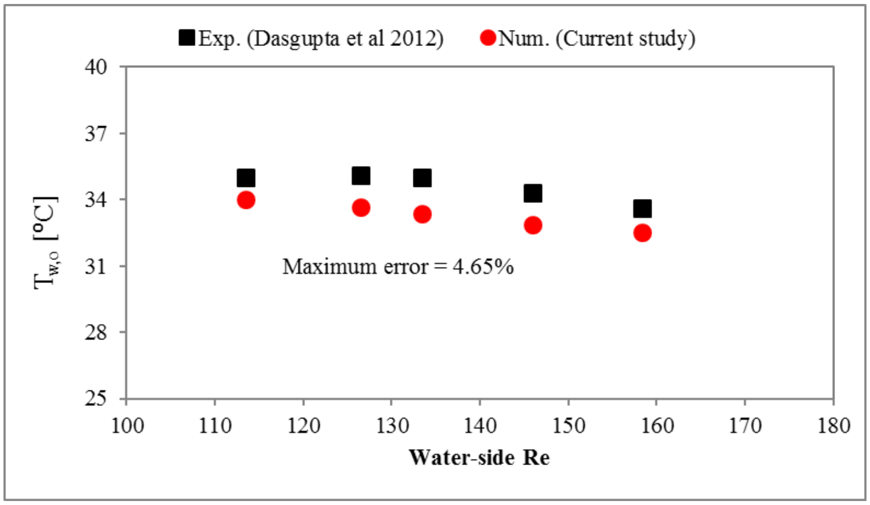

Figure 5.11: Comparison of numerical predictions and experimental data for outlet temperature of water

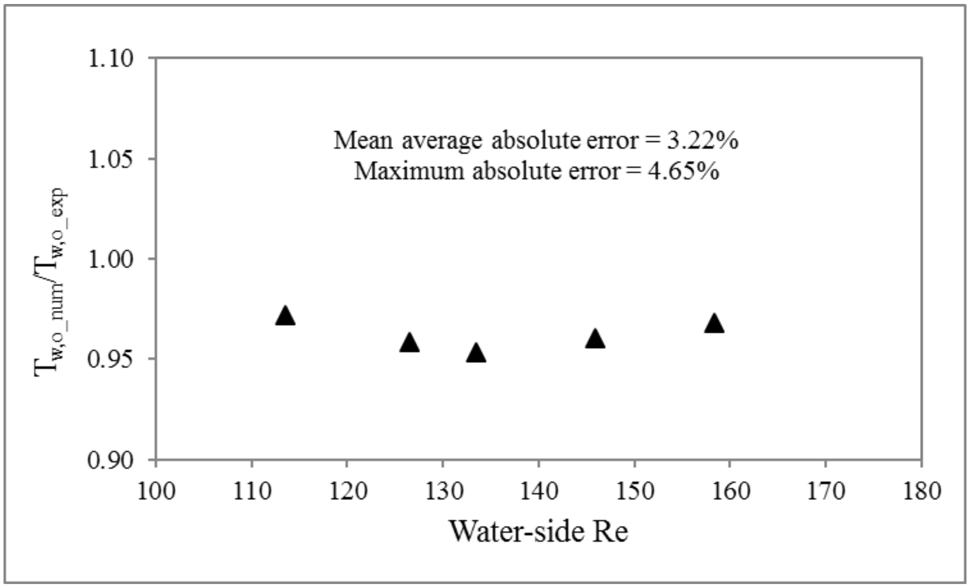

Figure 5.12: Mean average absolute error in numerical predictions of water outlet temperature compared to experimental data

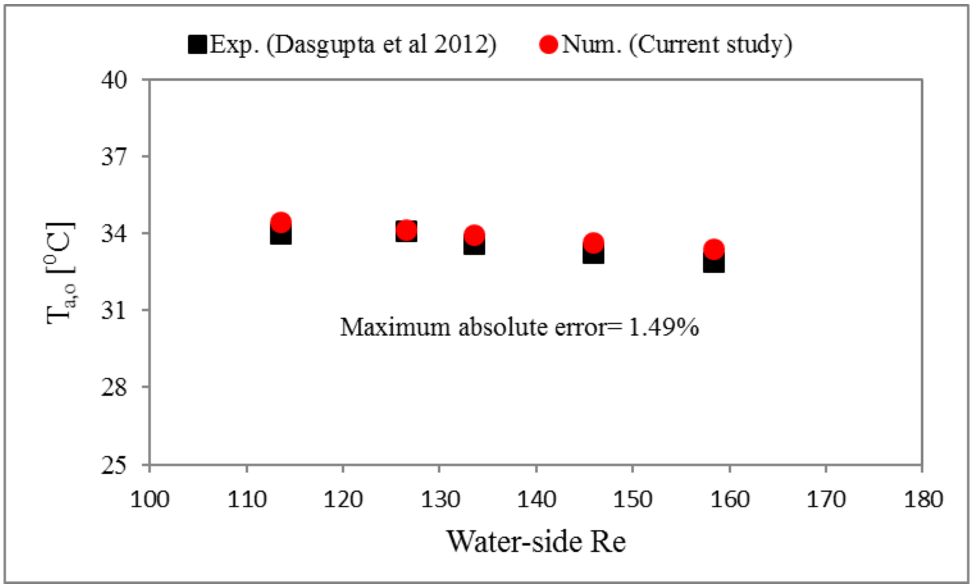

Figure 5.13: Comparison of numerical predictions and experimental data for outlet temperature of airside

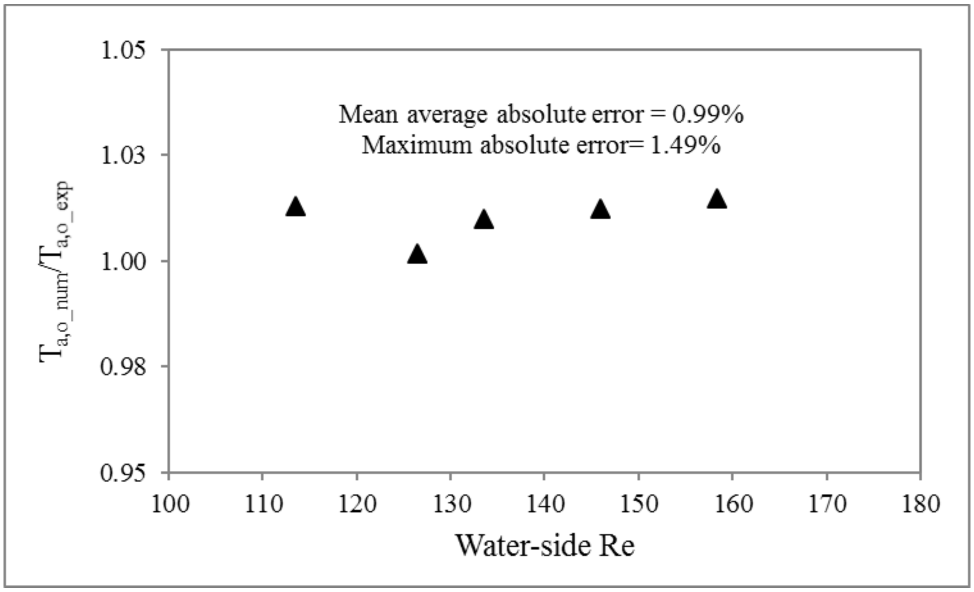

Figure 5.14: Mean average absolute error in numerical predictions of air outlet temperature to experimental data

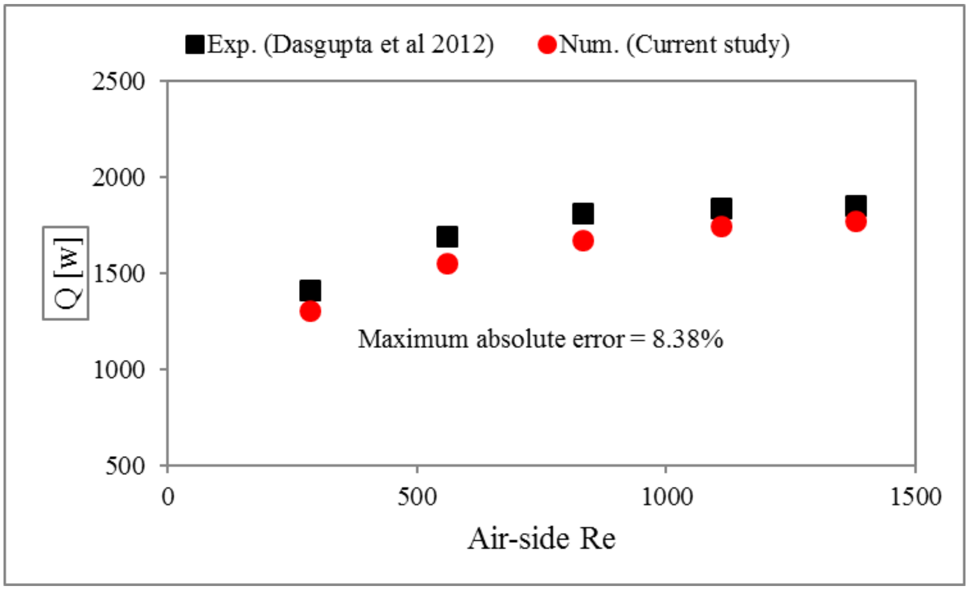

Figure 5.15: Comparison of numerical predictions with experimental results of heat transfer rate

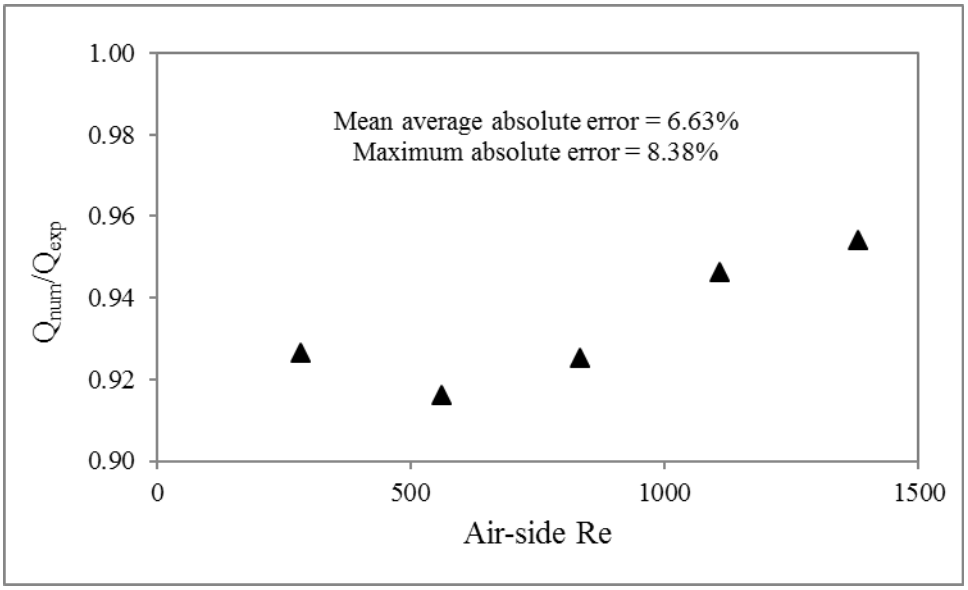

Figure 5.16: Mean average error in numerical predictions of heat transfer rate

The maximum errors of 4.65%, 1.49% and 8.38% have been found in water outlet temperature, air outlet temperature and heat transfer rate, respectively. While the mean average errors of 3.22%, 0.99% and 6.63% have been observed for the respective parameters. Numerical results predicted very good agreement with experimental results.

5.1.5 Validation of 5-pass Single-loop MICHX

With the purpose of making sure that the model precisely represents the actual applications, a set of results from transient simulations has been validated with experimental transient data [312]. In both the simulation and the experiment, water is cooled by air using the crossflow MICHX. The comparison between numerical and experimental transient results are shown in Figures 5.17 and 5.18. Figures 5.17(a) to 5.17(d) present the comparison of numerical and experimental results for the transient outlet temperature of the hot fluid due to the step change in same fluid mass flow rate. In Figure 5.17(e), outlet temperature of the hot fluid at quasi-steady state under various mass flow steps is summarized.

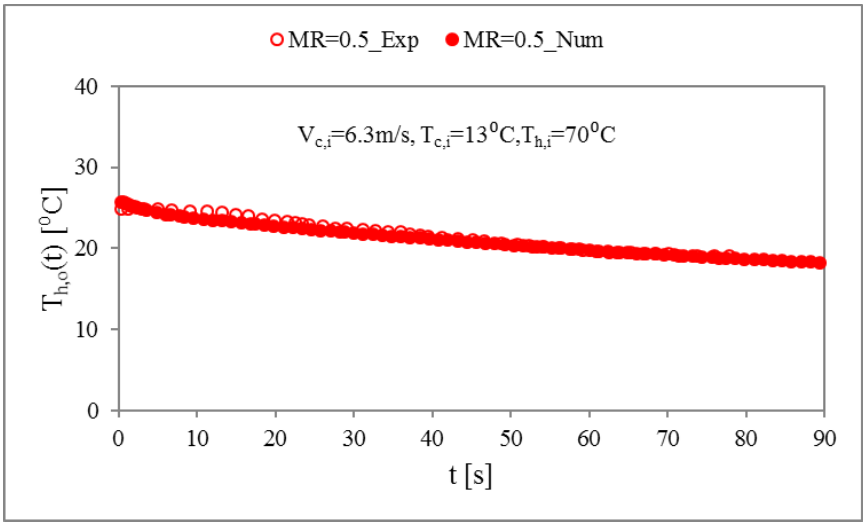

(a)

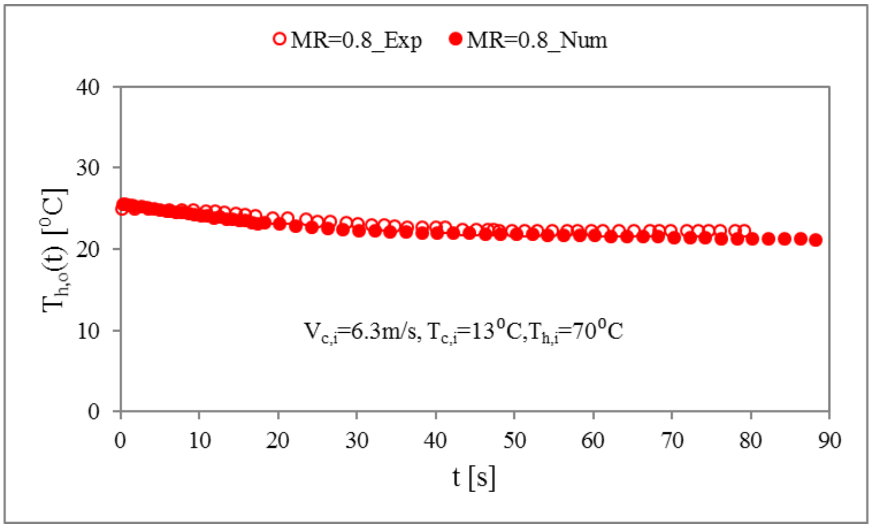
○ MR=0.8_Exp
● MR=0.8_Num
$T_{h,o}(t)$ [^oC]
40
30
20
10
0
0
10
20
30
40
50
60
70
80
90
t [s]
$V_{c,i}$=6.3m/s, $T_{c,i}$=13^{0}C,$T_{h,i}$=70^{0}C

(b)

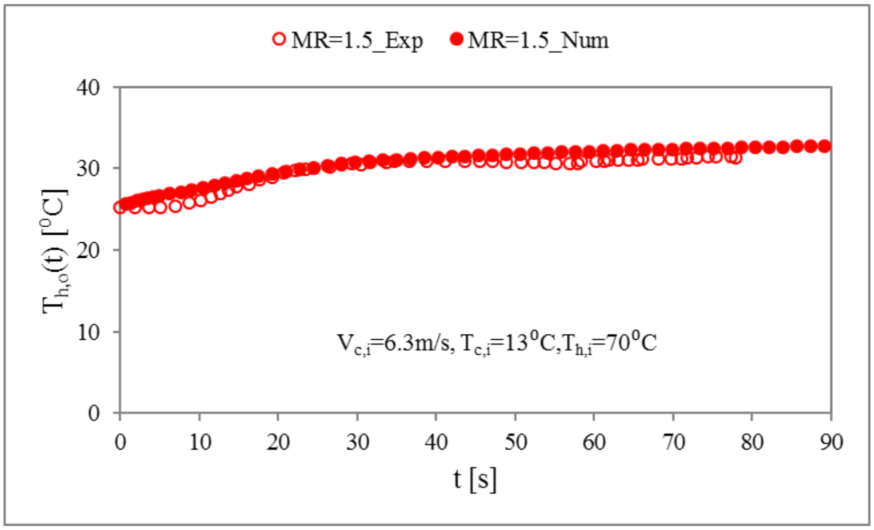
○ MR=1.5_Exp
● MR=1.5_Num
$T_{h,o}(t)$ [^oC]
40
30
20
10
0
0
10
20
30
40
50
60
70
80
90
t [s]
$V_{c,i}$=6.3m/s, $T_{c,i}$=13^{0}C,$T_{h,i}$=70^{0}C

(c)

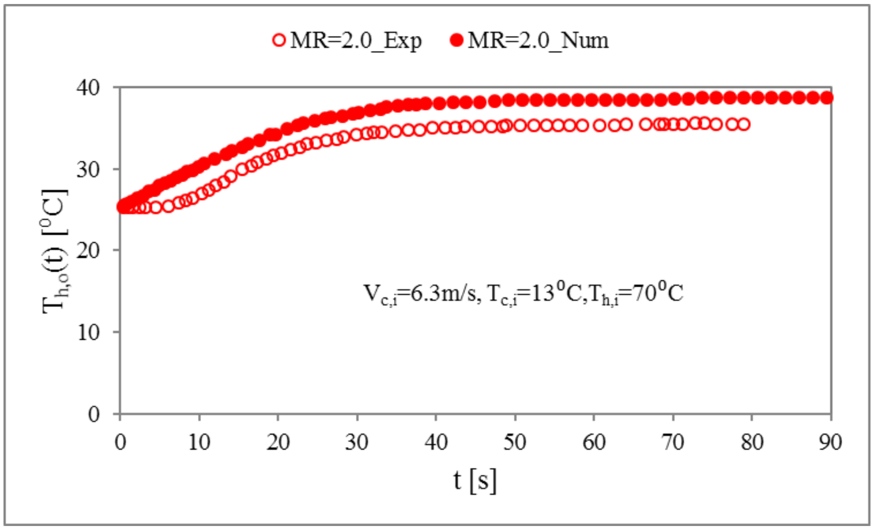

(d)

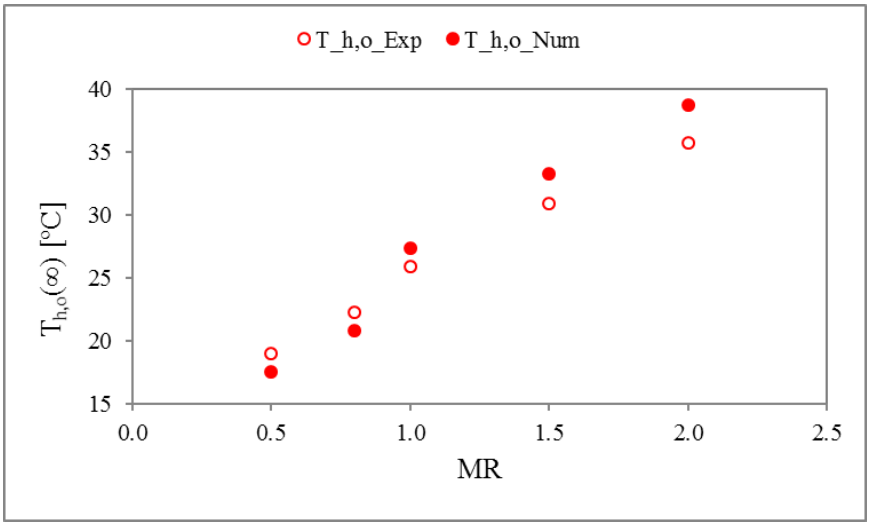

(e)

Figure 5.17: Comparison beteewn numerical and experimental data of $T_{h,o}$ for (a) MR=0.5, (b) MR=0.8, (c) MR=1.5, (d) MR=2.0 and (e) steady state

Numerical results show good agreement with the experimental data. The maximum error of 8.6% is found in the numrical results for hot fluid outlet temperature.

The numerical and experimental results for the temporal variation of cold fluid outlet temperature due to the mass flow steps have also been compared and presented in Figures 5.18(a) to 5.18(c). The Figure 5.18(d) shows the summary of cold fluid outlet temperature at quasi-steady situation under different mass flow steps.

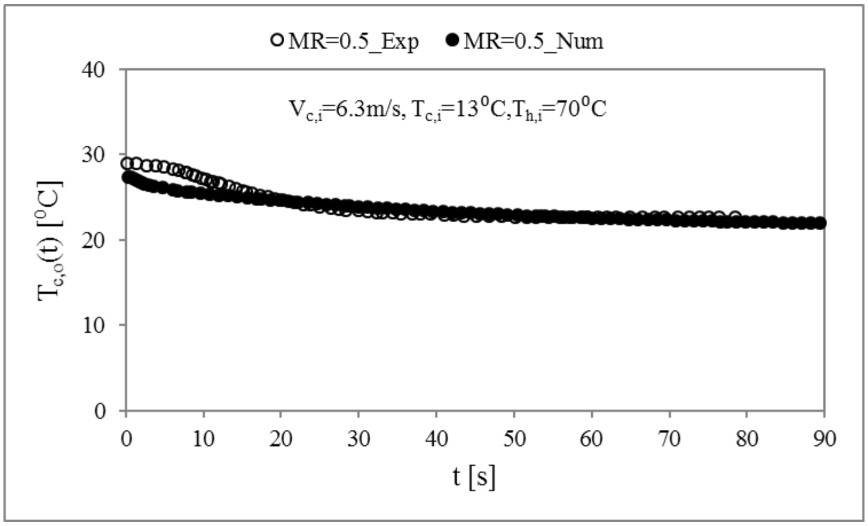

(a)

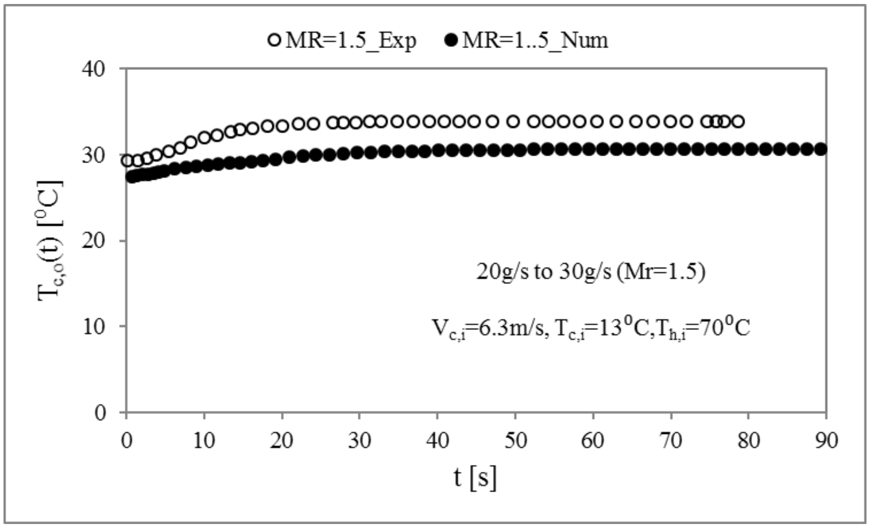

(b)

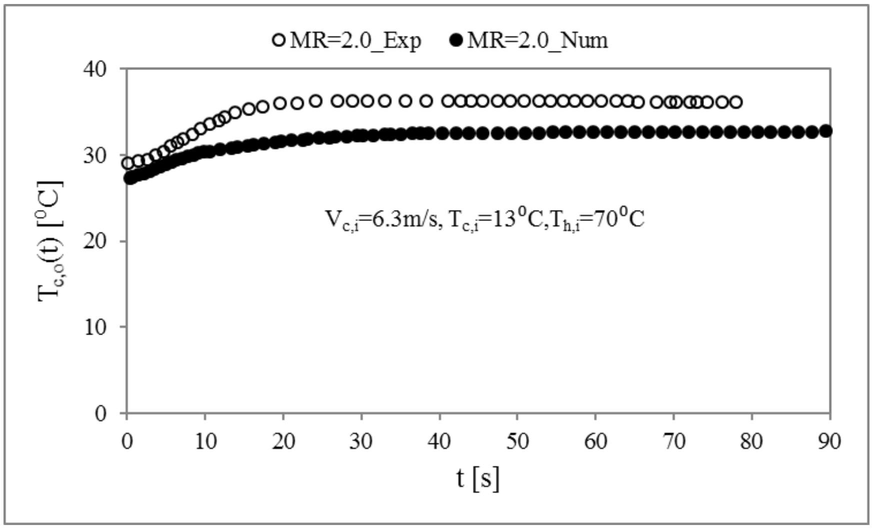

(c)

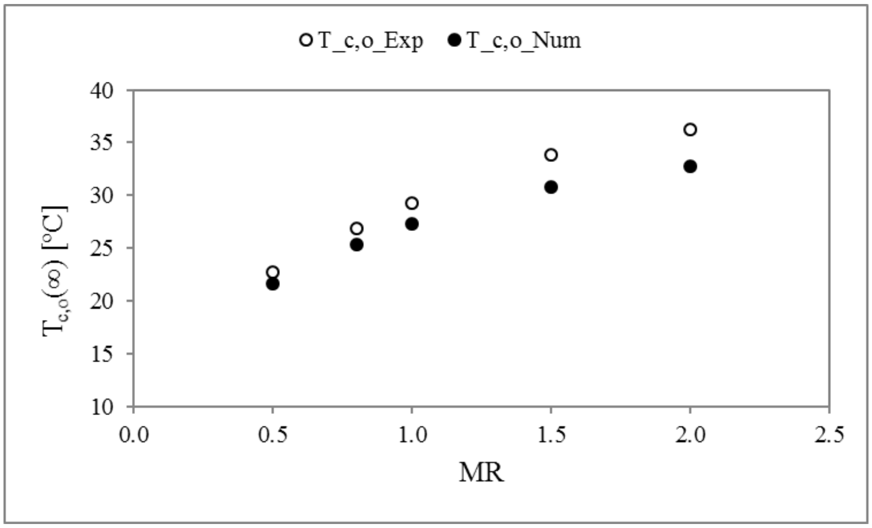

(d)

Figure 5.18: Comparison between numerical and experimental data $T_{c,o}$ for (a) MR=0.5, (b) MR=1.5, (c) MR=2.0 and (d) steady state

The maximum error of 9.7% is found in simulations for the cold fluid outlet temperature, which is within the acceptable range of error.

Figure 5.19 illustrates the absolute maximum errors in the hot and the cold fluids temperature at quasi-steady state of numerical simulations.

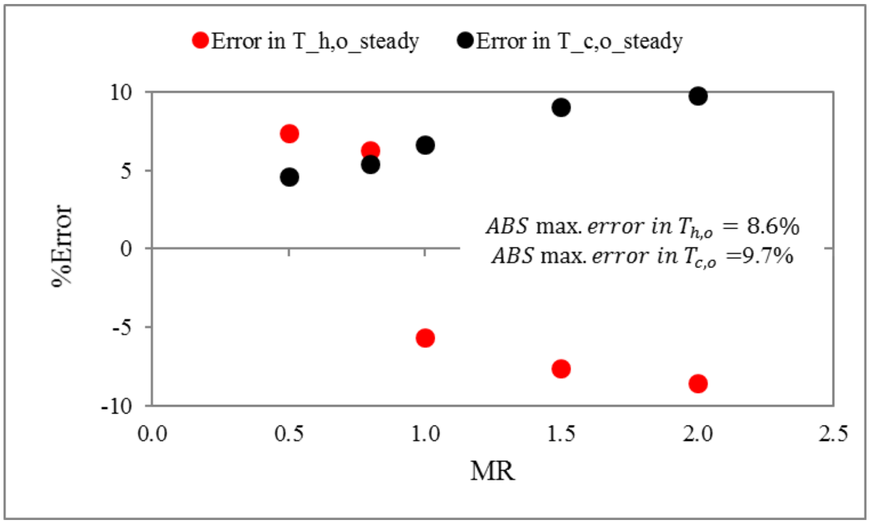

Figure 5.19: Errors in numerical predictions compared to experimental data

Figure 5.19 shows the errors in the hot fluid and the cold fluid temperatures are within ±9.7% at quasi-steady state conditions.

5.1.6 Summary:

With the intension of ensuring the accuracy and consistency of the numerical results of the computational models, two types of error analyses have been carried out. The two methods, verification and validation, have been widely acceptable as the guideline of AIAA (1998) [327] and Oberkampf et al. [328]. The key outcomes are illustrated below.

- Grid systems for the CFD simulations have been selected by means of a grid independency study.
- The errors in mass balance (MB) and heat balance (HB) in 5-pass 3-loop heat MICHX have been found to be $\pm1.13\%$ and $\pm1.21\%$,respectively.

- The heat transfer rates and the heat transfer coefficients are identical within ±3.9% deviation at different computing methods.
- The maximum errors in the CFD results among all of the computational models are presented below.
    - liquid outlet temperatures: ±8.6%
    - air outlet temperature: ±9.7%
    - serpentine temperature: ±1.71%
    - liquid pressure drop: ±13.3%
    - heat transfer rate: ±8.4%
- The above-mentioned parameters of numerical results show a very good agreement with experimental results.

The verification and validation of numerical results confirm that one can certainly depend on the accuracy and consistency of the CFD models of the current study.

CHAPTER 6

RESULTS AND DISCUSSIONS

The results of the current study are described in this chapter. The chapter is divided into four subdivisions to illustrate the results from the five distinct phases of the study. First, the results of Stage I: Conventional flat tube heat exchanger (FTHX) and minichannel heat exchanger (MICHX) is presented in Section 6.1. In this section, thermal performance of MICHX is compared to that of FTHX as preliminary study of current program. Then, the results of fluid flow and heat transfer in a 5-pass 3-loop MICHX with equivalent size of an automotive radiator are discussed in section 6.2 of Stage II. The results of Stage III: Effects of nanofluids in MICHX are illustrated in section 6.3. After that, results of Stage IV: Sequential and simultaneous heat exchanger modules are described in section 6.4. Finally, in section 6.5, results of Stage V: Transient heat transfer in MICHX are illustrated.

6.1 Stage I: Conventional and Minichannel Heat Exchanger

In this section, the simulation results for conventional FTHX and MICHX are presented. The heat transfer performance of both the heat exchangers as well as the flow and thermal distributions in the channels are also illustrated. In addition, local convective heat transfer along the channel length is discussed. It is well mentioned that both heat exchangers are identical with slab thickness, frontal area and volume. The same boundary conditions are also applied for the both heat exchangers. Hot water with temperature of 90℃ is cooled by crossflow cold air with temperature of 25℃ and velocity of 6m/s. The simulations have been conducted for different Reynolds numbers at laminar flow regime of water.

6.1.1 Water-side Temperature Drop

The water-side temperature drop for different Re in both FTHX and MICHX are presented in Figure 6.1. For both the heat exchangers, it is shown that the temperature drop and temperature gradient are higher at low Reynolds number, and they decrease with the increase of Reynolds number. This is due to the fact that the lower Reynolds number fluid takes longer residence time than that of the higher Reynolds number fluid.

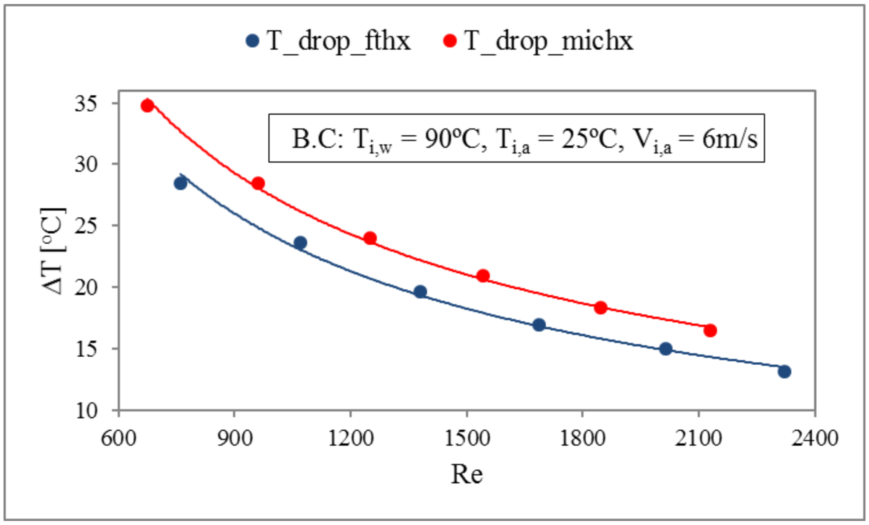

Figure 6.1: Water ΔT in FTHX and MICHX at different Reynolds numbers

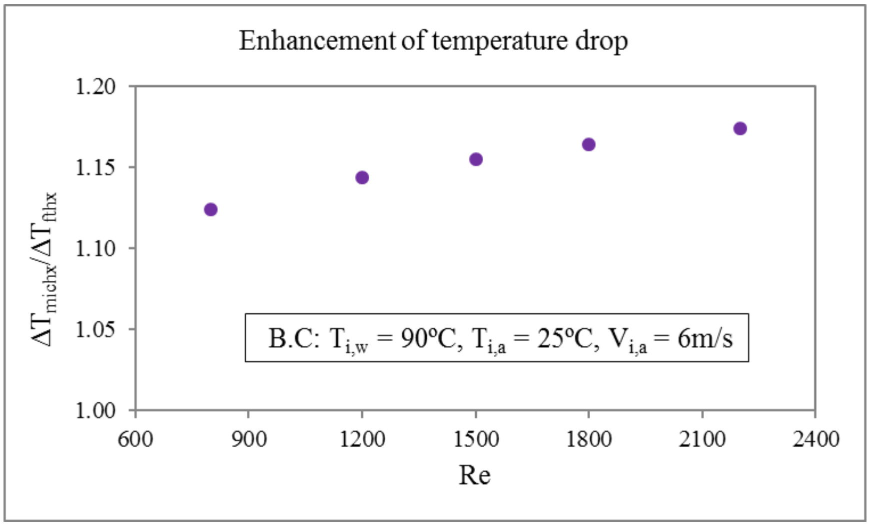

Figure 6.2: Enhancement of water ΔT in MICHX compared to FTHX for different Re

The enhancement in water temperature drop for different Reynolds numbers due to MICHX are presented in Figure 6.2. At a given Reynolds number within laminar flow regime, MICHX provides approximately 12%~18% higher temperature drop compared to FTHX. This is because of the fact that minichannels possess higher heat transfer surface area and more contact area between fluid and solid surfaces than those of flat tubes.

The higher the temperature drop, the higher the heat transfer rate is. Therefore, MICHX offers this advantage to achieve the desired low temperature faster than a given comparable conventional FTHX.

6.1.2 Heat Transfer Rate

The heat transfer rate between hot water and cold air in both the FTHX and the MICHX for different Re are illustrated in Figure 6.3. It is observed that the heat transfer rate increases with the increase of Re. This is because the heat transfer is dominated by the mass flow rate, particularly, Reynolds number of hot water inside the tube/channel.

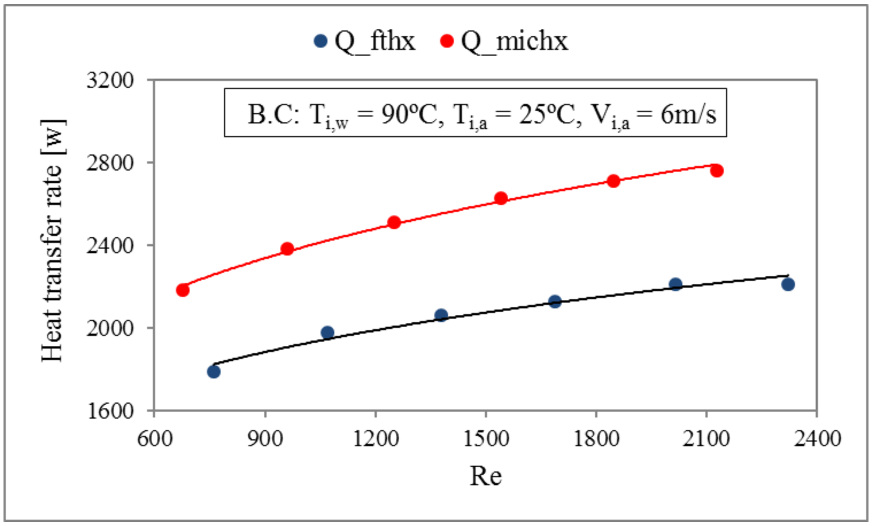

Figure 6.3: Comparison of heat transfer rate of FTHX and MICHX for different Re

The enhancement of heat transfer rate between water and air at various Reynolds numbers for the use of MICHX are shown in Figure 6.4.

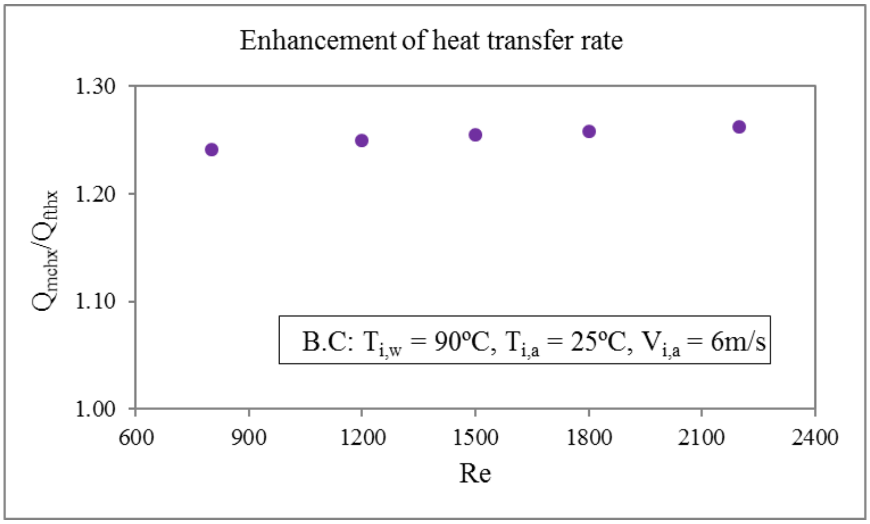

Figure 6.4: Enhancement of heat transfer rate in MICHX compared to FTHX

At a certain Reynolds number within laminar flow regime, MICHX provides about 24%~26% increased heat transfer rate compared to FTHX. This is because of the fact that minichannels possess higher heat transfer surface area and more contact between fluid and solid surfaces than that of flat tubes.

The higher heat transfer rate of the MICHX provides the higher thermal performance and meets the desired heat duty, which is gain in volume for a given duty.

6.1.3 Water-side Heat transfer Coefficient

The water-side convective transfer coefficient for both the FTHX and MICHX at different Reynolds numbers are presented in Figure 6.5. It is noticed that the heat transfer coefficient increases with the increase of Reynolds number. This is due to the fact that both the hydrodynamic and the thermal entrance lengths are function of Reynolds number.

Consequently, the convection heat transfer coefficient is strongly influenced by Reynolds number. The greater the fluid Reynolds number, the greater the molecular movement and consequently, greater the convection heat transfer coefficient.

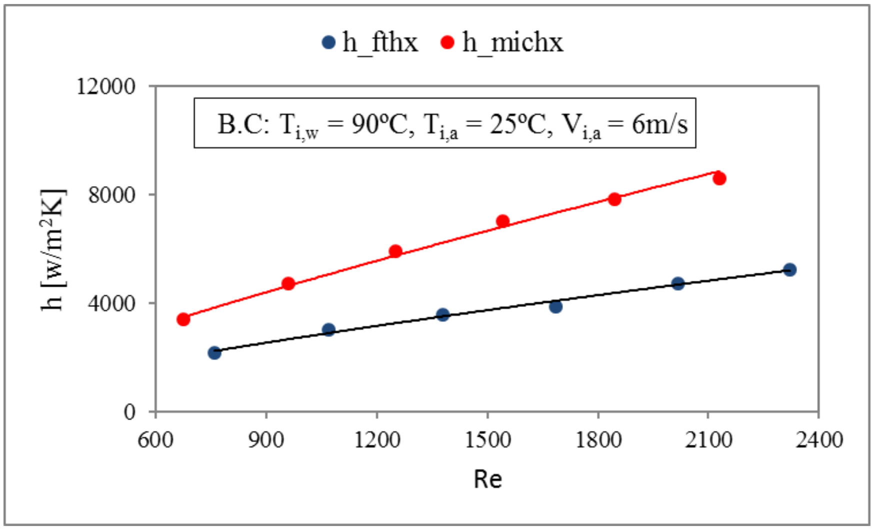

Figure 6.5: Comparison of FTHX and MICHX for heat transfer coefficient of water

The enhancement of water-side convective heat transfer coefficient at various Reynolds numbers due to the use of MICHX are presented in Figure 6.6.

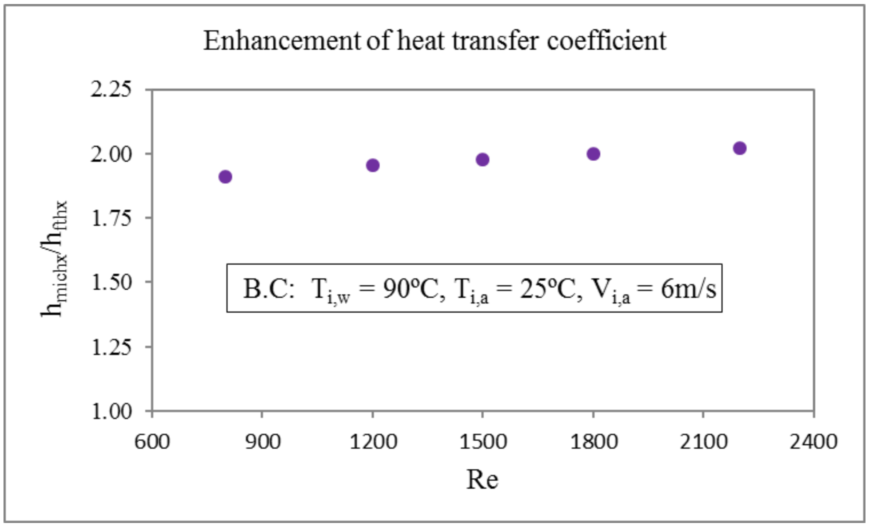

Figure 6.6: Enhancement of heat transfer coefficient in MICHX compared to FTHX

At a given Reynolds number within the laminar flow regime, for MICHX, heat transfer coefficient is increased by around 91%~102% than that of FTHX. This is because MICHX intensifies heat transfer rate due to higher heat transfer surface area and more contact area between fluid and surfaces.

6.1.4 Local Heat transfer Coefficient of Water

The water-side convective transfer coefficient for FTHX and MICHX along the length of tube/channel at a particular $G_{w,tot} = 1967\,kg/m^2s$, $T_{w,i} = 90°C$, $V_{a,i} = 6m/s$ and $T_{a,i} = 25°C$ is presented in Figure 6.7.

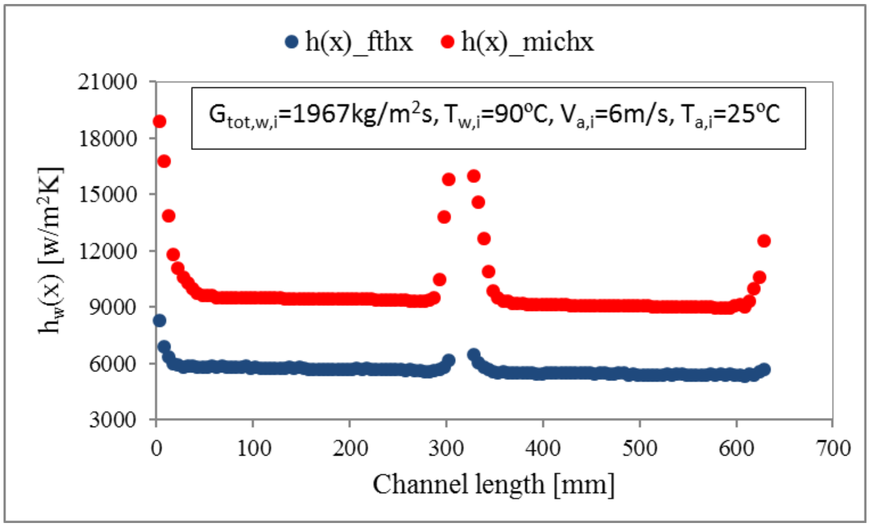

Figure 6.7: Heat transfer coefficient in MICHX and FTHX along the channel length

It is obvious that the heat transfer coefficient is the highest at the entrance. It gradually decreases along the channel length and becomes steady as the fluid reaches fully developed region. Again, the heat transfer coefficient breaks at the serpentine and reaches to a higher value. It decreases after the serpentine and becomes gradually steady along the channel length. This is due to the fact that the thermal boundary layer thickness is zero at the entrance; as boundary layer thickness increases along the channel length, the heat transfer coefficient decreases. Once the thermal boundary layer thickness becomes fully developed, the heat transfer coefficient becomes constant.

The presence of serpentine changes flow direction, creates new entrance region and the thermal boundary layer thickness becomes the least possible at the entrance of the next slab. As a result, the heat transfer coefficient increases. Since after the serpentine, thermal boundary layer develops, heat transfer coefficient gradually decreases and becomes constant at fully developed region. The entrance length is longer for the MICHX compared to the conventional FTHX, which leads to higher heat transfer coefficient for the MICHX.

6.1.5 Distribution of Mass Flow Rate in each Channel of MICHX

Channel number 1 and 68 are the first and the last channel counting from the inlet of the test chamber for air-flow. In other words, channel 68 is the first channel and channel 1 is the last channel counting from inlet pipe for water-flow, as shown in Figure 6.8.

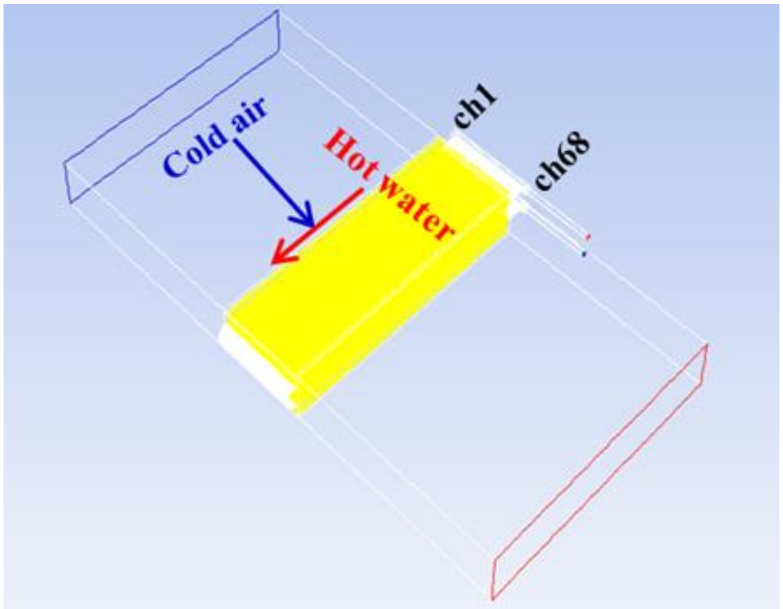

Figure 6. 8: Flow direction and channel number of air-to-water crossflow MICHX

The distributions of mass flow rate of water ($\mathrm{MFR_w}$) for a certain Reynolds number of 1888 in each of 68 channels of the MICHX are presented in Figure 6.9.

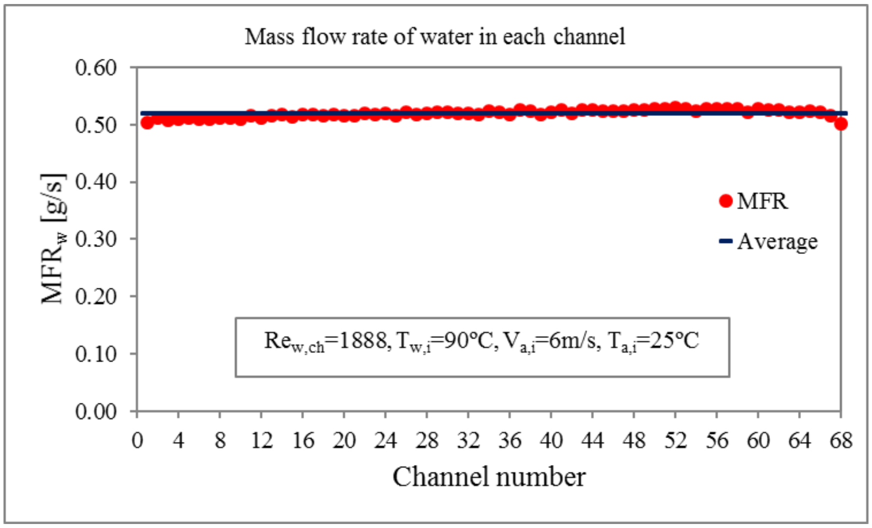

Figure 6. 9: Distribution of mass flow rate of water in each of 68 channels

As expected, slightly higher mass flow rate of water is observed in the channels nearer to the water inlet channels compared to the farther channels. Effect of entrance region in mass flow rate is also detected. This is due to the fact that the inlet tube diameter is smaller than the inlet manifold. The flow area is higher at the entrance of the manifold, which decelerates the flow rate. A small irregular mass flow rate of water is also seen. It can be due to the low viscosity of water. The mass flow distributions have been found fairly uniform with less than 3% variations.

6.1.6 Temperature Drop of Water in each Channel of MICHX

The temperature drop of water ($\Delta \mathrm{T_w}$) through all the channels for a specific $\mathrm{Re_{w,ch}} = 1888$, $\mathrm{T_{w,i}} = 90°\mathrm{C}$, $\mathrm{V_{a,i}} = 6\mathrm{m/s}$ and $\mathrm{T_{a,i}} = 25°\mathrm{C}$ is presented in Figure 6.10. It is mentioned earlier that the hot water flows inside the channels and cold air flows over the slabs in a crossflow orientation. It is also stated that channel number 1 is the first channel from the inlet of test chamber that face the cold inlet air to exchange heat between the fluids.

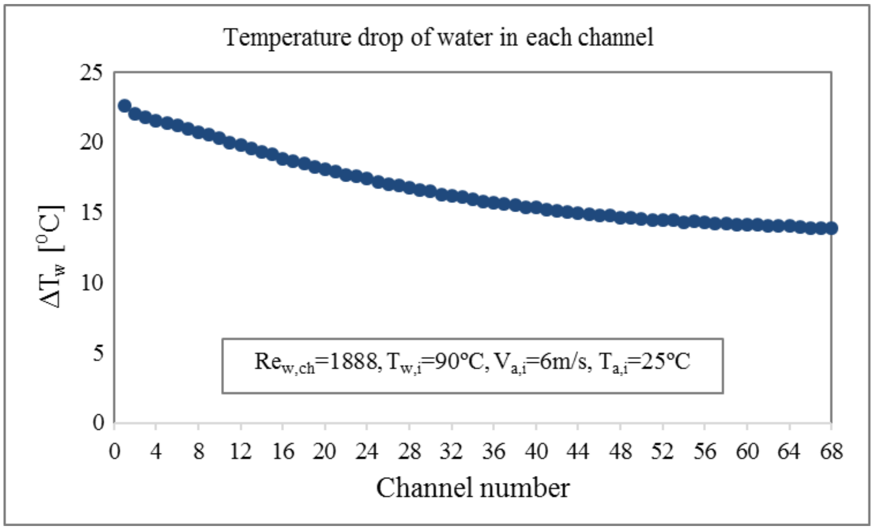

Figure 6.10: Temperature drop of water in each of 68 channels

It is evident from the Figure 6.10 that the ΔT_w gradually decreases from channel number 1 to 68 along the crossflow direction of cold air. The highest ΔT_w of 22.6ºC and the lowest ΔT_w of 13.8ºC have been computed in the first and last channel, respectively. This is because the heat transfer takes place between cold air and hot water in channel number 1 at first and 68 at the last in a crossflow orientation, as shown earlier in Figure 6.8. As air travels over the multiport slab carrying hot water inside the ports, the air temperature progressively increases starting from channel 1 to channel 68. As a result, the cooling effect of air reduces along the subsequent channels.

Figure 6.10 illustrates that the slop of the temperature drop is higher at the beginning and gradually becomes lower leading to almost flatter as number of channel increases. The figure helps to identify the required number of channels to be used depending on to the application.

6.1.7 Mean Temperatures of Water and inner surfaces of Minichannels

The mass-weighted average temperature of water ($T_{w,m}$) through all the channels for a particular $Re_{w,ch} = 1888$, $T_{w,i} = 90°C$, $V_{a,i} = 6m/s$ and $T_{a,i} = 25°C$ is presented in Figure 6.11. The area-weighted average temperature of inner surface of individual channel is also shown in the same figure. It is mentioned earlier that the hot water flows inside the channels and cold air flows over the slabs in a crossflow orientation. It is also stated that channel number 1 is the first channel from the inlet of test chamber that faces the cold inlet air to exchange heat between the fluids.

Figure 6.11 shows, both water mean temperature $T_{w,m}$ and the channel inner surface temperature T_s increase in the direction of crossflow cold air.

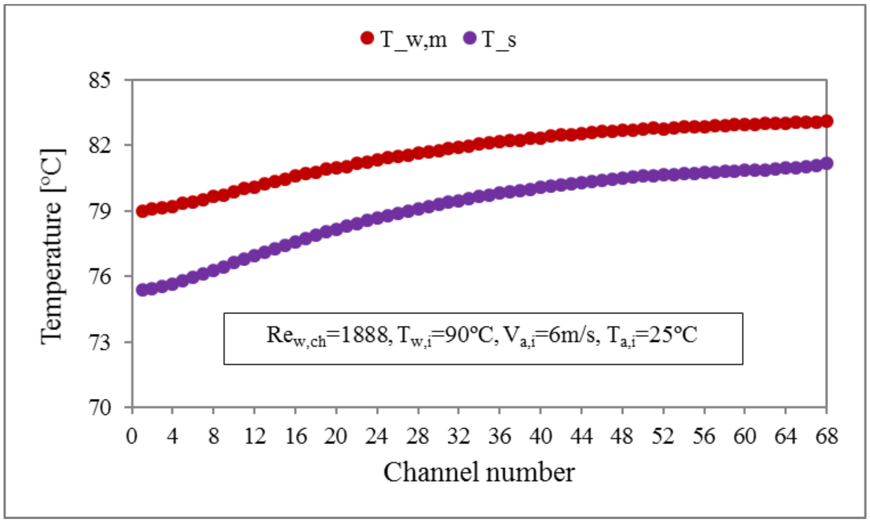

Figure 6.11: Mean temperature of water and channel inner surface

The temperature differences between water and channel wall varies from 4°C to 2°C through channels 1 to 68. The lowest $T_{w,m}$ and T_s have been evaluated in the first channel and the highest in the last channel. This is due to the fact that the most cooling effect of air happens at the channel number 1 as it faces the coldest air. In the same pattern, the least cooling effect of air occurs at channel number 68 as it gets the warmest air.

This figure signifies that the heat transfer is higher at the beginning due to the higher temperature gradient between the liquid and the channel inner surface.

6.1.8 Contribution of Heat Transfer in each Channel of MICHX

The heat transfer rate through individual channel is computed as

$$\dot{Q}_{ch} = \left[\dot{m}C_p(T_i - T_o)\right]_{ch}$$

The channel wise distribution of heat transfer rate of the air-to-water crossflow MICHX for a particular $Re_{w,ch} = 1888$, $T_{w,i} = 90℃$, $V_{a,i} = 6\,m/s$ and $T_{a,i} = 25℃$ is shown in Figure 6.12. The contribution of each channel is presented in Figure 6.13.

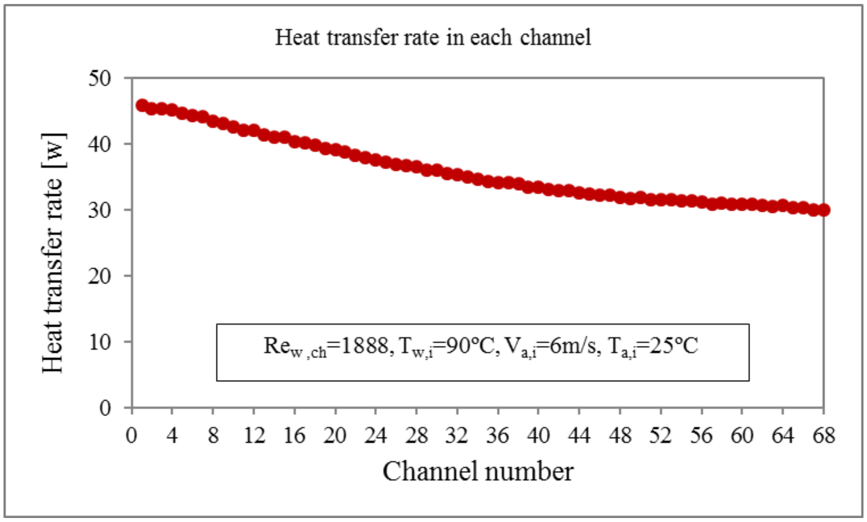

Figure 6.12: Distribution of heat transfer rate in each of the 68 channels

It is previously stated that the hot water flows internally through the channels and cold air flows externally over the channels in a crossflow manner. Channel number 1, which carries hot water is the first channel that comes in contact of the cold air. Figure 6.12 shows that the heat transfer rate is the greatest at the channel number 1, gradually decreases along the air-flow direction.

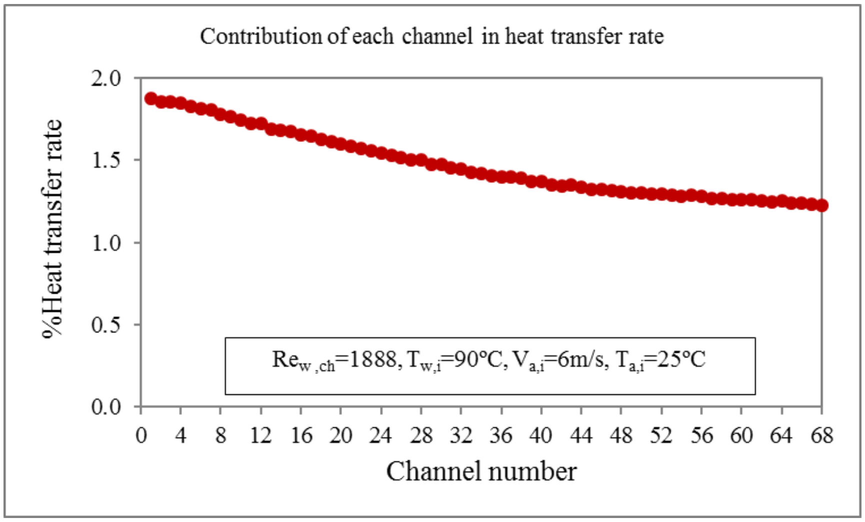

Figure 6.13: Contribution of each channel in heat transfer rate

The heat transfer rate varies from 45.83w to 29.93w starting from channel number 1 to 68. Channel 1 contributes the most (1.87%) and channel 68 contributes the least (1.2%) heat transfer rate, as shown in Figure 6.13. This is because the temperature difference is the driving force for heat transfer. Channel number 1 carrying hot water, first, comes into the contact of the cold air; then channel number 2 and so on. As air flows over the channels, the air temperature increase. Consequently, the channel wise temperature difference between water and air decreases, which is illustrated earlier in section 6.10.

Figures 6.12 and 6.13 help to recognize the number of channels to be needed for a particular heat duty depending on the system requirement.

6.1.9 Heat Transfer Coefficient of Water in each Channel of MICHX

The heat transfer coefficient of water is computed as $h_{ch} = \left[\frac{\dot{Q}}{A_s(T_{w,m} - T_s)}\right]_{ch}$.

The convective heat transfer coefficient of water in every individual channel for a certain $Re_{w,ch} = 1888$, $T_{w,i} = 90°C$, $V_{a,i} = 6m/s$ and $T_{a,i} = 25°C$ is presented in Figure 6.14. The convective heat transfer coefficient is observed to be fairly identical in every channel. The temperature contour of water of a channel is presented in Figure 6.15.

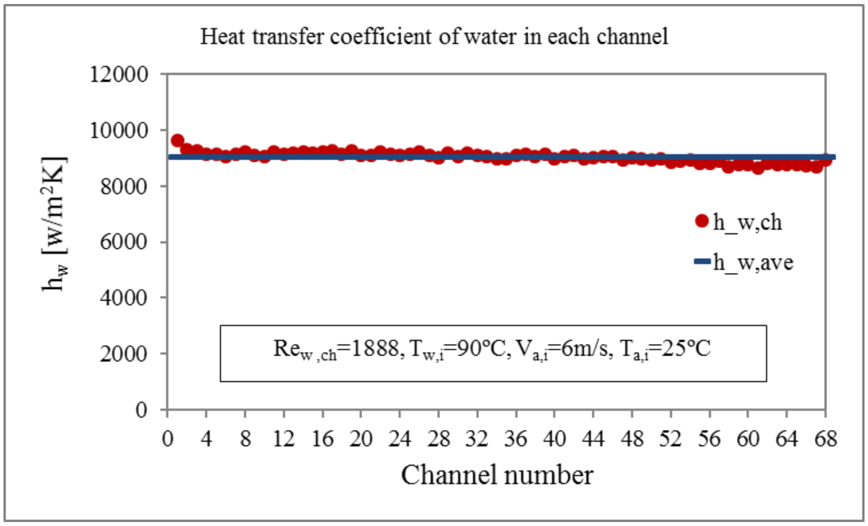

Figure 6.14: Heat transfer coefficient of water in each of 68 channels

Figure 6.14 signifies the uniform distribution of convective heat transfer coefficient of the fluid in each channel of the MICHX.

6.1.10 Contour of Water Temperature along the Length of Middle Channel

The temperature contour of the water-side along the length of a channel is illustrated in Figure 6.15. The figure shows that the temperature of the liquid is highest at the inlet and lowest at the outlet of the channel, as it is expected. The liquid temperature decreases as it flows through the channel. The change in the liquid temperature is more apparent in the top channel compared to the bottom channel. Therefore, the temperature drop in the top channel is greater than that of the bottom channel.

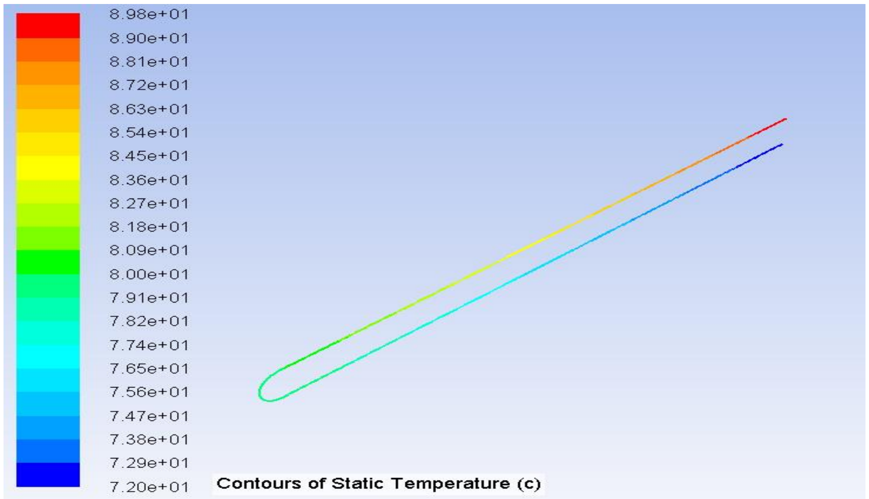

Figure 6.15: Temperature along the length of middle channel

This figure facilitates to identify the channel length for a particular application.

6.1.11 Summary

Numerical results of MICHX and conventional FTHX have been analyzed to predict their thermal and flow performance. The key findings are summarized below;

- At a given Reynolds number within laminar flow regime, MICHX offers about $24\% - 26\%$ increased heat transfer rate and $91\% - 102\%$ enhanced heat transfer coefficient compared to FTHX with the cost of higher pressure drop.
- Channel number 1 shows the maximum temperature drop, because it is the first channel in the slab that faces air to transfer heat. It shows the lowest mass flow rate because it is the last channel from the inlet header for water to flow

- Channel number 68 shows the minimum temperature drop and heat transfer rate because it is the last channel in the slab that faces air to transfer heat
- As expected, heat transfer rate gradually decreases from channel 1 to 68
- Local heat transfer coefficient decreases along the length of the channel due to the thermal boundary layer thickness
- The presence of serpentine changes the flow direction of liquid, creates new entrance region and temperature profile, and develops a new hydrodynamic and thermal boundary layers at the entrance of the bottom slab, which enhances the heat transfer coefficient of the liquid

6.2 Stage II: Multi-loop MICHX

In this section, liquid flow distributions in different loops, airside temperature in the test chamber, and liquid temperature throughout the MICHX are illustrated. In addition, temperature drop and heat transfer rate in different loops are evaluated. This heat exchanger is identical to an automotive radiator in size. The main purpose of modelling this MICHX is to predict fluid flow and temperature distribution at three different loops to make a decision for better choice whether we can use only one loop instead.

6.2.1 Contour of Liquid Flow Distribution in the Header and the Manifolds

The velocity contours at the inlet tube, the header, and the manifolds are illustrated in Figure 6.16. The headers are vertical; but the manifolds and the inlet and the outlet liquid tubes are horizontal. The inlet liquid tube is located between the top and the middle manifolds, while the outlet liquid tube is between the middle and the bottom manifolds as shown in Figure 6.16(a). It is clear from the Figure 6.16(c) that the velocity of the liquid is uniform at the inlet of the tube. The velocity is gradually increasing towards the center of the tube and becomes maximum before entering the vertical header.

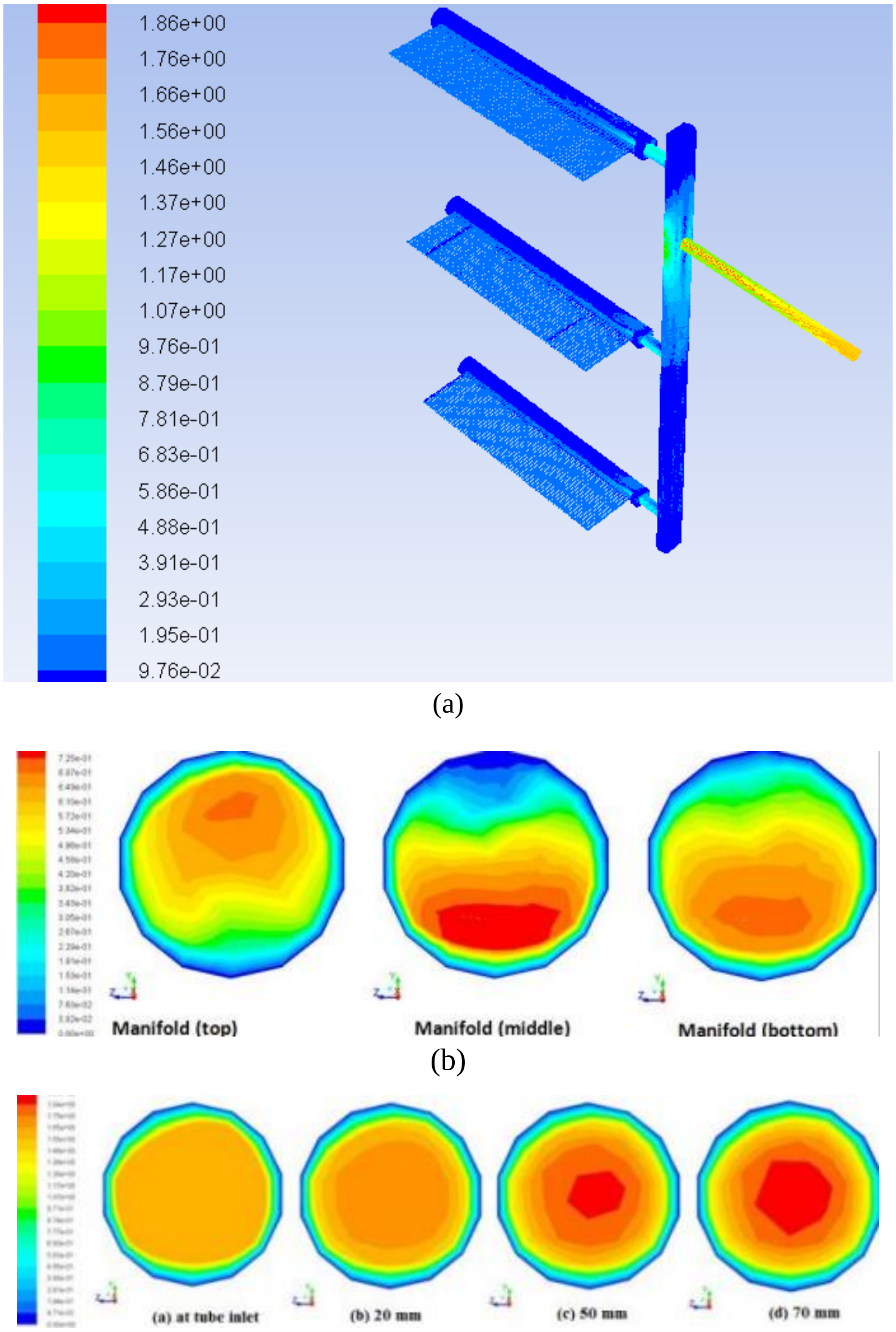

(a)

(b)

(c)

Figure 6.16: Velocity contours at (a) the inlet tube, the header, and the manifolds, (b) at the top, the middle and the bottom manifolds and (c) different cross sections of the inlet tube

6.2.2 Mass Flow Distribution of Liquid in Header and Manifolds

Due to diverse locations of manifolds, mass distribution was expected to be non-uniform. The mass flow distributions in top, middle, and bottom loops have been computed 0.475 lpm, 0.460 lpm, and 0.477 lpm, respectively.

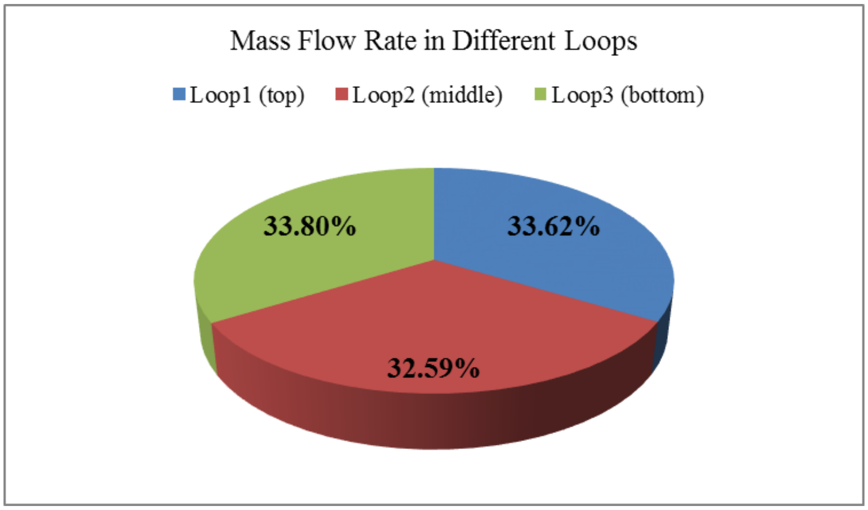

(a)

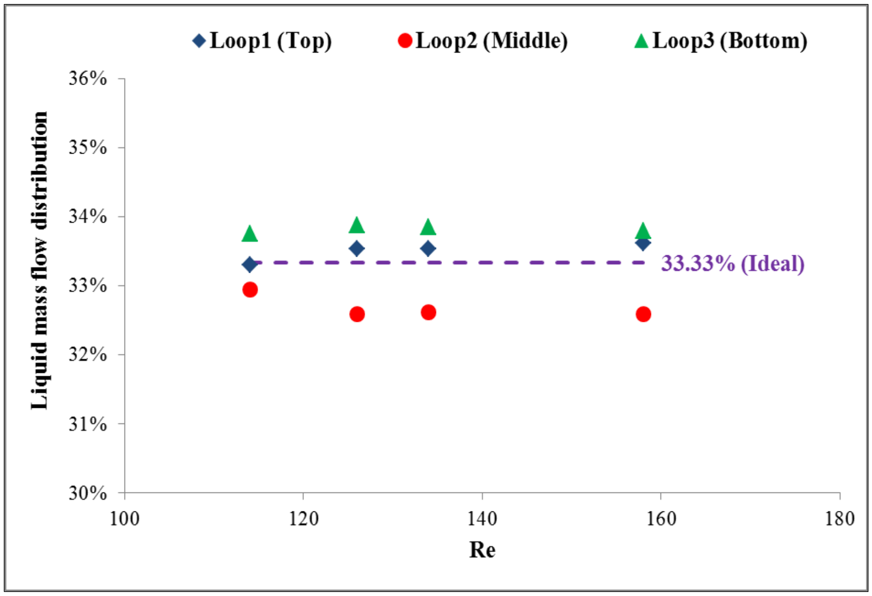

(b)

Figure 6.17: Liquid mass flow rates in the top, the middle, and the bottom loops for (a) Re=158, and (b) multiple Re.

Generally, liquid flows more easily downward. As expected, the highest mass flow rate is found in the bottom manifold. The mass distributions in the bottom, the middle, and the top loops have been found to be 33.80%, 32.59%, and 33.62%, respectively [see Figure 6.17]. The variation between the highest and the lowest mass flow rates among the loops is found to be 1.21%. The maximum difference in mass flow rate through an individual loop compared to that of the mean value is observed as 0.74%, which shows the optimum design of the inlet headers and the manifolds.

6.2.3 Air Temperature in the Test Chamber

The air temperature distribution for 15-slab 5-pass 3-loop air-to-liquid crossflow MICHX is illustrated in Figures 6.18 and 6.19. In this study, the air inlet and the liquid inlet temperatures have been kept 38℃ and 9℃, respectively.

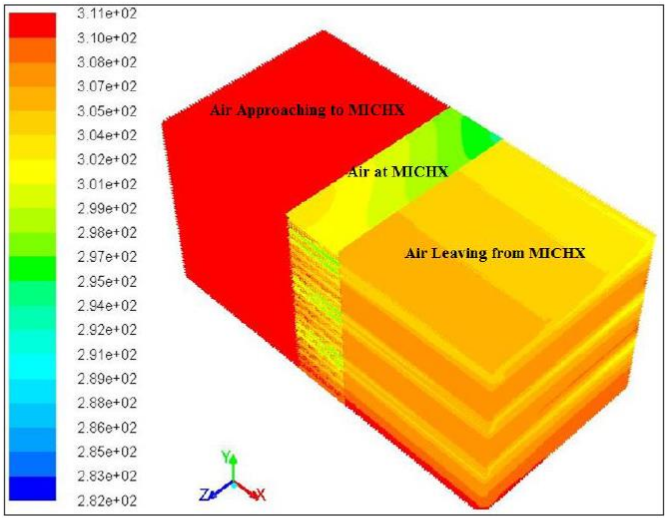

Figure 6.18: Temperature contour of the air-side

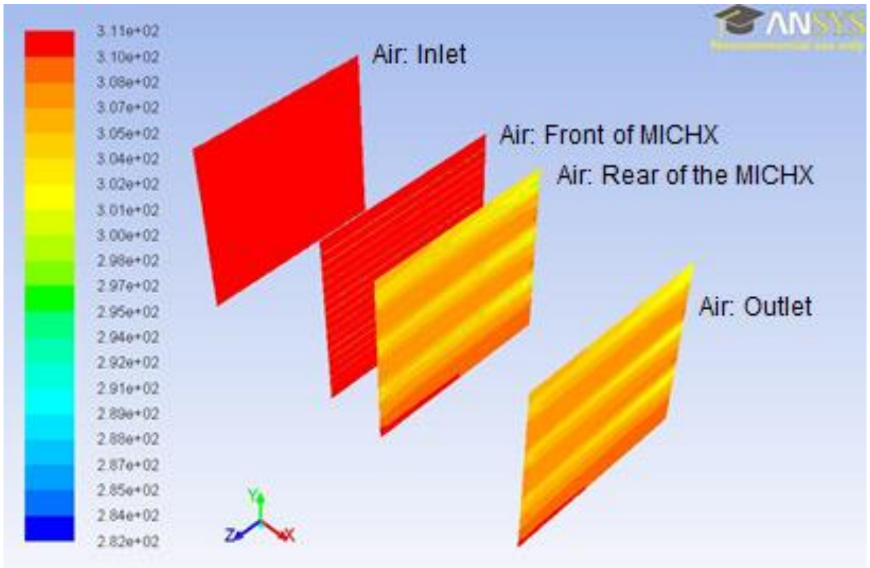

Figure 6.19: Contour of air temperature at different cross-sections of test chamber

It is obvious from the figures that the uniform inlet air possesses temperature variations for each loop after passing through the heat exchanger. For any loop, the air temperature decreases along the channel length and with the increase of slabs. In the air-side, the higher outlet temperature, i.e., the lower heat transfer rate is found for the bottom loop.

6.2.4 Liquid Temperature throughout the MICHX

The temperature distribution of liquid through the MICHX slabs are shown in Figures 6.20 and 6.21. Outlet temperature of the three loops have been found as 31.92℃, 31.86℃, and 35.10℃, i.e., the temperature rise of liquid is 22.91℃, 22.86℃, and 26.10℃ for the top, the middle and the bottom loops, respectively. This shows highest outlet temperature or the less heat transfer rate occurs at the bottom loop.

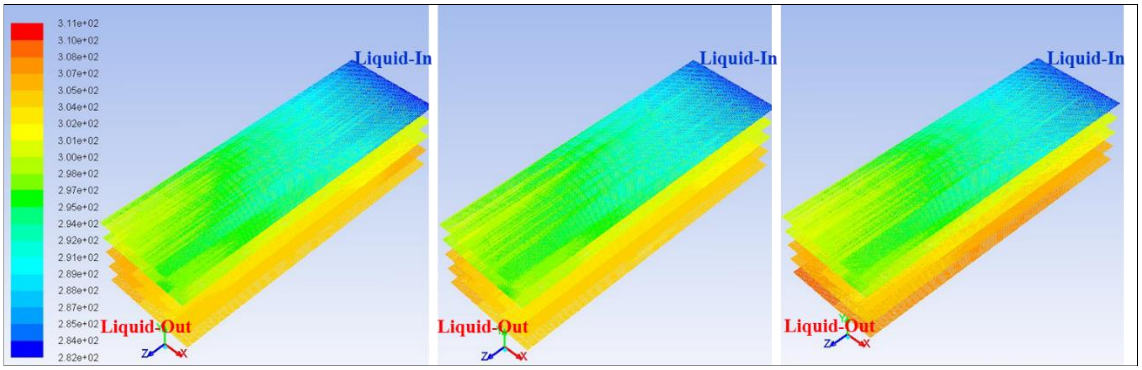

Figure 6.20: Liquid temperature contours of 3 loops in the MICHX

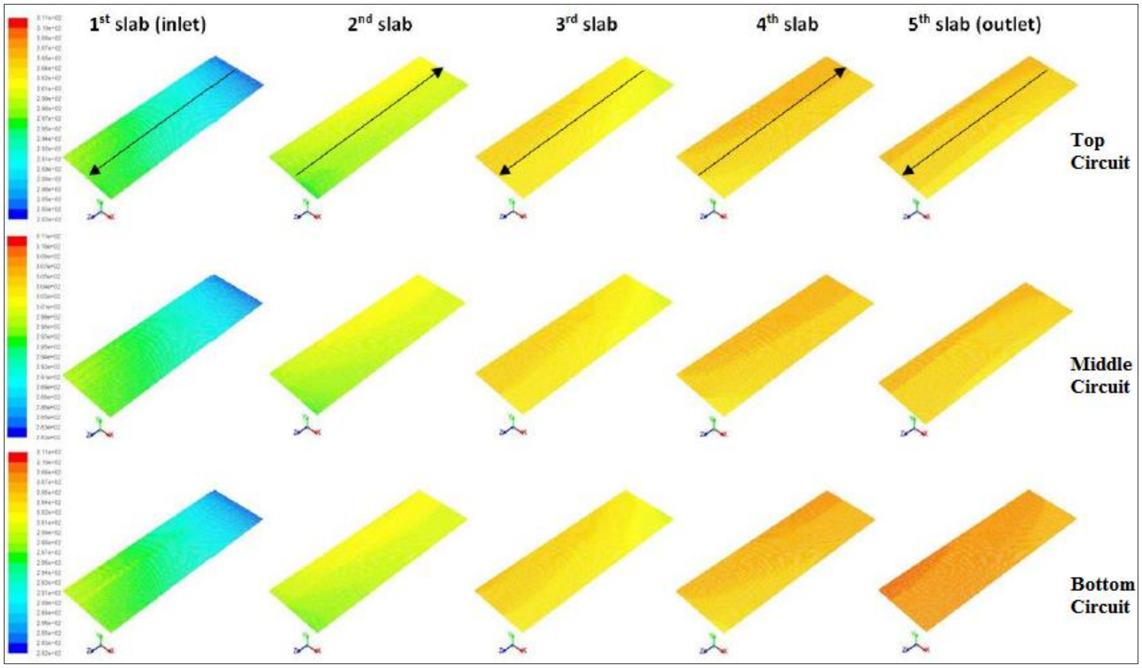

Figure 6.21: Contour of liquid temperature in channels of the MICHX slabs

This is due to the boundary conditions of the various loops; the inlet cold fluid of the bottom loop has contact with the outlet hot fluid of the middle loop, on the other hand, the outlet of the bottom loop is in contact with the dummy slab by means of fins, which is adiabatic and therefore has no heat transfer. The liquid temperature is constant or decreasing along the serpentine section due to the adiabatic boundary condition and longitudinal heat conduction along the channel wall.

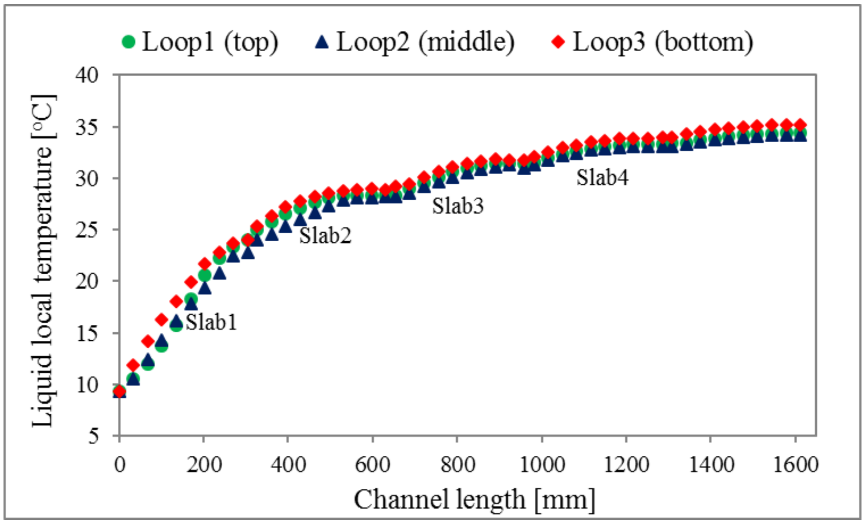

Figure 6.22: Local water temperature through the channel length of the MICHX

Figure 6.22 illustrates the local water temperature through the channel length for a mass flow rate of 1.412 lpm, which is equivalent to Re = 158. The graph shows that the local liquid temperature rises along the channels with the same trend for the first three slabs of all the three loops, as expected. The trend also displays reverse alteration for the last slab of the bottom loop due to the vicinity to the adiabatic test chamber wall. This results in the temperature rise of the bottom loop. The deviation of local temperature of the fourth slab could be explained by the serpentine effect. As the serpentine is isolated from the test chamber and thermally well insulated, and no heat is being transferred from the hot fluids, heat transfer at the serpentine area takes place along the wall by axial conduction. This phenomenon to some extent causes the temperature rise in the exit section of the fourth slab.

6.2.5 Liquid and Solid Surface Temperatures along the Length of Channel

Figure 6.23 shows the variations of inner liquid and wall surface temperature along the middle channel length of the bottom loop for the channel mass flux of $151.18 \text{ kg/m}^2\text{s}$.

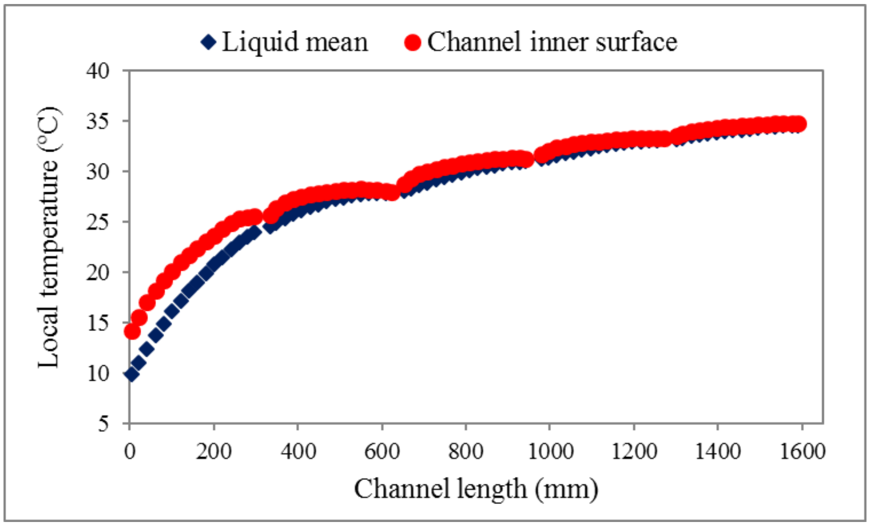

Figure 6.23: Water and channel surface temperatures along the length of the MICHX

It is clear from the figure that the surface temperature of the channel rises along the channel and the local temperature of the liquid (water) rises as it travels through the channel. The slope of the trend decreases gradually because of the mass flux is small enough to increase heat transfer rate and subsequently drop the water and wall temperature difference through the channel length. The wall surface temperature drops at both sides of the isolated serpentine due to the serpentine effect and axial heat conduction. This phenomenon decreases through the channel path because of the lower temperature difference.

6.2.6 Contributions of Different Loops and Slabs in the Heat Transfer Rate

Figure 6.24(a) demonstrates the heat transfer rates of 788w (32.90%), 768w (32.07%), and 839w (35.03%) for the top, the middle and the bottom loops, respectively.

It displays that the maximum heat transfer occurs at the bottom loop, which has the higher liquid mass flow rate and higher local water temperature. Unlike the first slab of the middle and the bottom loops, the first slab of the top loop interfaces to the adiabatic wall surface, which results in the lowest heat transfer rate for just heat transfer interaction with the flowing air.

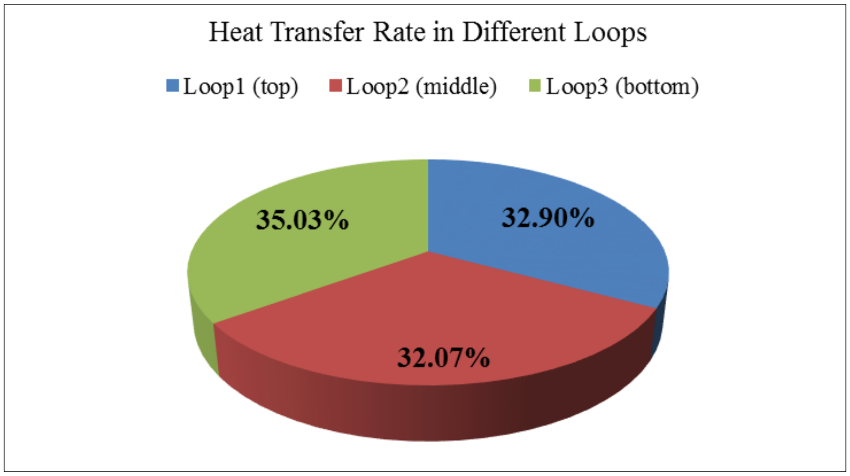

(a)

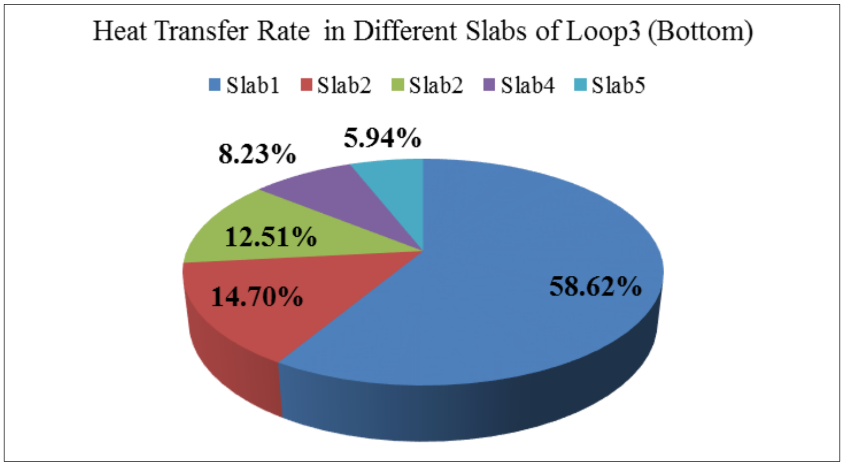

(b)

Figure 6.24: Distribution of the heat transfer rate in different (a) loops and (b) slabs

The distribution of heat transfer rate in different slabs of the bottom loop is illustrated in Figure 6.24(b). The figure shows that about 59% of the heat transfer rate occurs at the first slab, 15% at the second slab and 6% at the last slab. This indicates the effect of the latter slabs of the MICHX for the low Reynolds number of 155.

6.2.7 Effects of the Mass Flow Rates and the Thermal Boundary Conditions of Different Loops on the Heat Flux and the Heat Transfer Coefficient

Variation of streamwise wall heat flux in the top slab of the top, the middle, and the bottom loops of the MICHX is illustrated in Figure 6.25(a).

It is clear from the figure that the heat flux drops along the flow stream due to the heat transfer rate, which decreases with the channel length. This figure displays that the top slab of the bottom loop has the highest heat flux. This can be described with the results in the Figure 6.24(a) that the highest heat transfer rate among the loops belongs to the bottom one. This slab shares heat transfer interfaces not only with the flowing air but also with the bottom slab of the middle loop which increases the rate of heat flux compared with the other loops. The rate of the heat flux variation is decreasing along the flow stream which can be explained by the fact that the highest heat transfer rate happens in the first slab and rapidly drops for the other slabs.

Dissimilarity of the water (cold fluid) heat transfer coefficient along the first slab of the top, the middle, and the bottom loops of the MICHX is observed in Figure 6.25(b). This is due to the fact that there is a discrimination in mass flow of water through different loops. It is because of the elevation of the inlet manifolds. At the entrance of the channel, the heat transfer coefficient is high due to the thin thermal boundary layer thickness. It drops quickly along the length of channel as the thermal boundary layer is developing. The trend becomes almost constant as the thermal boundary layer is on the threshold of fully developed.

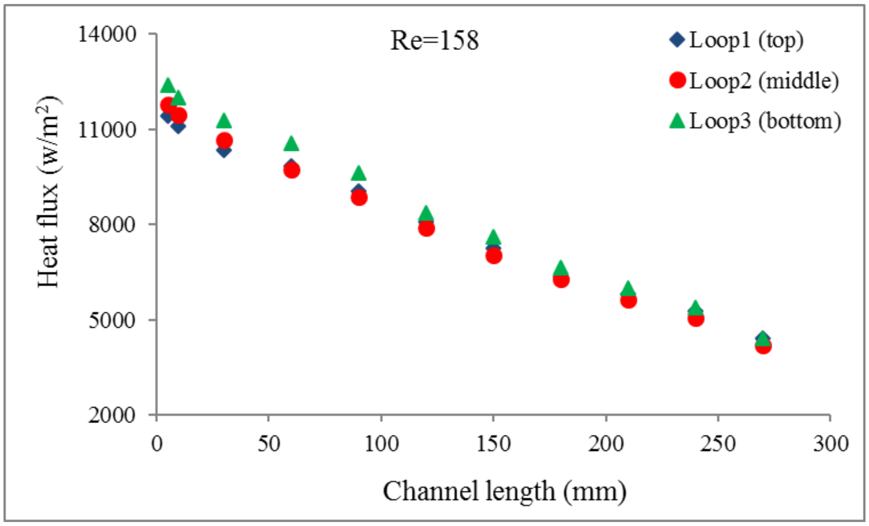

(a)

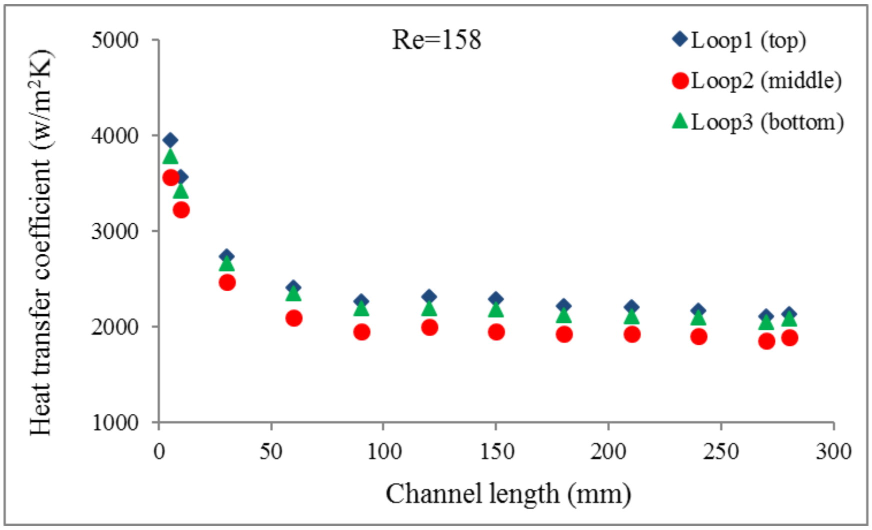

(b)

Figure 6.25: Distribution of (a) the heat flux and (b) the heat transfer coefficient in top slabs

6.2.8 Effects of Serpentine Geometry in Heat Transfer

Figure 6.26 shows the change in local heat flux with the channel length for all slabs of the bottom loop of the MICHX.

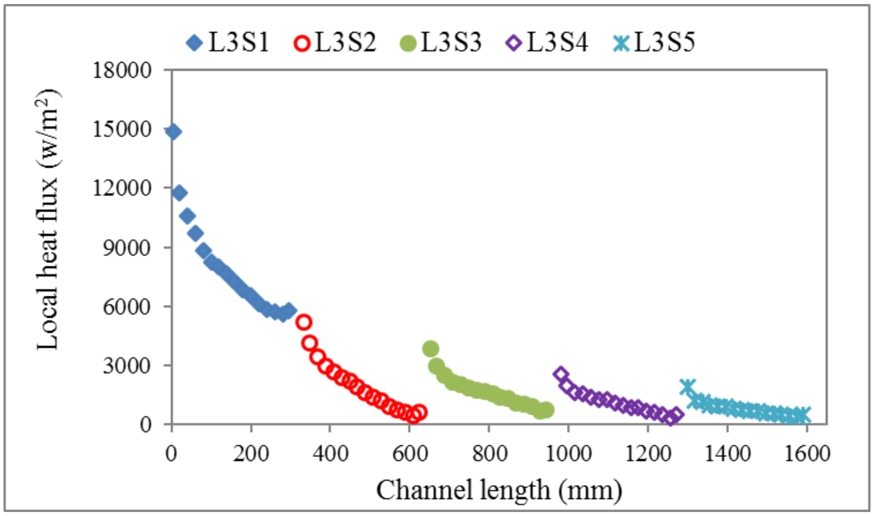

Figure 6.26: Distributions of local heat flux along the flow stream

The figure indicates that the local heat flux decreases streamwise due to the higher channel length offering lower heat transfer. The rate of reduction is higher at the beginning of each slab because of the secondary flow in the serpentine bend causing the boundary layer to diminish and start to build up again in the following slab. However, the rate of slope reduces when the boundary layer develops. There is an increase in local heat flux before the serpentine bend for all the slabs. This phenomenon can be interpreted by the serpentine effect and longitudinal heat conduction. In the region of the adiabatic serpentine, there is no heat transfer between the liquid and air; the axial heat conduction occurs along the wall. This causes the heat flux near the serpentine to increase rapidly.

Variation in local heat transfer coefficient of the bottom loop throughout the channel length is shown in Figure 6.27.

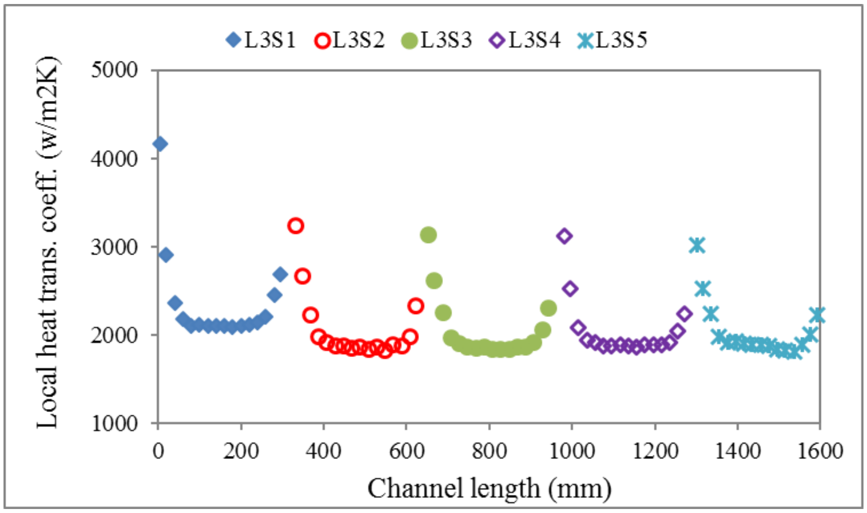

Figure 6.27: Distributions of local heat transfer coefficient along the flow stream in the bottom loop of the MICHX

It is clear from the figure that the local heat transfer coefficient drops rapidly at the beginning of each slab. This could be clarified by the effect of the boundary layer. At the entrance of the channel, thermal boundary layer thickness is very small. As fluid moves forward, the thermal boundary layer is developing. Once the boundary layer becomes fully developed, the heat transfer coefficient becomes constant along the channel length. This can be also be explained by the fact that the local heat transfer coefficient has a direct proportion to the heat transfer rate and inverse proportion to the temperature drop. Both the heat transfer rate and the temperature drop are decreasing along the channel and resulting in the constant local heat transfer coefficient. The local heat transfer coefficient rises rapidly at the end of each slab. This is because of (i) the existence of serpentine, (ii) secondary flow of the fluid and (iii) the effect of longitudinal heat conduction as explained earlier.

6.2.9 Heat Transfer in Different Loops and Slabs in the MICHX

The heat transfer rate of water in different loops and slabs for Re = 134 are shown in Figure 6.28. It is well mentioned that this multi-loop MICHX is validated with the experimental measured data for $110 \leq \mathrm{Re} \leq 158$. Among this flow regime, one Reynolds number (Re = 134) is chosen for in-depth investigation.

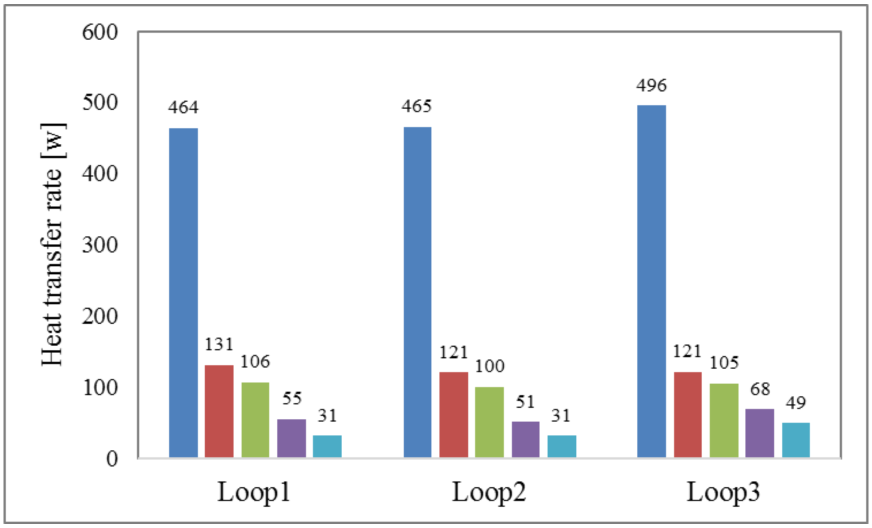

Figure 6.28: Heat transfer rate of water in different loops and slabs

Loop1, Loop2, and Loop3 represent the top, the middle and the bottom loops, respectively. Slab1 to slab5 denote the top to the bottom slabs for all 3 loops. The figure shows that the most of the heat transfer rate occurs at the top slab of each loop. It also illustrates that slab4 and slab5, i.e. last 2 slabs have insignificant heat transfer rate of water for the low Reynolds number of 134, as expected. The figure also shows that there is no significant difference in heat transfer rate between slab2 and slab3.

The results of the current study using a MICHX have also been compared with those of a conventional in-line elliptical tube array [28]. For the same frontal area, same mass flow rate and similar operating conditions, both the heat transfer rate and the heat transfer coefficient of water in a MICHX have been found higher than those of conventional elliptical tube array. However, the Nusselt number of water in a MICHX is observed to be lower than that of the conventional tube. This is due to the low Reynolds number ($\mathrm{Re} = 134$) of water in the current study compared to $\mathrm{Re} = 1079$ in conventional one [28].

6.2.10 Summary

A comprehensive analysis of the numerical predictions of flow and heat transfer in the 5-pass 3-loop MICHX has been carried out. The main outcomes of this Stage II of the current study are summarized in Table 15.

Table 15: Quantitative heat transfer rate in different loops and slabs

	Heat transfer rate, Q (w)		
	Loop1 (top)	Loop2 (middle)	Loop3 (bottom)
Slab1 (top)	464	465	496
Slab2	131	121	121
Slab3	106	100	105
Slab4	55	51	68
Slab5 (last)	31	31	49
Overall	788	768	839
Net deviation	1.31%	3.78%	-5.09%

- The liquid velocity at the inlet of the pipe is uniform, which becomes fully developed before entering the vertical header. Liquid flow rates have been found moderately uniform through the manifolds for the three distinct loops of the MICHX.

  The deviations in massflow rate is about ±2.2% due to the elevation of the manifolds. Heat transfer rate in each loop is also considerably similar. The deviations in heat transfer rate among the loops have been predicted to be ±5.1% because of the effects of mass flow rate and thermal boundary conditions of the loops.

  A single-loop can be used instead of a 3-loop in CFD simulations for further research on similar type of crossflow MICHX. This can reduce the computational complexity, time and cost.

- For the low Reynolds number of 134, the first slab contributes the most (about 59%) heat transfer rate, while the contribution of the fifth slab is the least (about 6%). The significant contribution of heat transfer is also found for the second and the third slabs; however, the heat transfer in the fourth and the fifth slabs are insignificant. Number of slabs can be preferred depending on the demand of the thermal systems.

6.3 Stage III: Effects of Nanofluids in the Heat Transfer and the Pressure Drop

The use of nanofluids has recently become the core interest of many researchers due to its elevated heat transfer performance. In the present study, heat transfer and flow characteristics of $\mathrm{Al_2O_3/W}$, $\mathrm{Al_2O_3/ATF}$ and $\mathrm{Al_2O_3/EG}$ nanofluids have been numerically investigated. A steady state model of a 2-pass MICHX is used for $\mathrm{Al_2O_3/W}$ and $\mathrm{Al_2O_3/ATF}$ while a transient model of a 5-pass MICHX is used for $\mathrm{Al_2O_3/EG}$. Nanofluids have been considered as homogeneous single-phase fluids. With the intention of cooling the $\mathrm{Al_2O_3/W}$ and $\mathrm{Al_2O_3/ATF}$ nanofluid, cold air at a constant mass flow rate of $0.507\mathrm{kg/s}$ and temperature of $14℃$, is passed through the finned heat exchanger in a crossflow orientation. The liquid in a laminar regime of $300 \leq \mathrm{Re}_{\mathrm{Al_2O_3/W}} \leq 1850$ and $50 \leq \mathrm{Re}_{\mathrm{Al_2O_3/atf}} \leq 210$ is forced to flow through the channels of the MICHX. The volumetric concentration of the nanofluid is varied from 1.0% to 4.0%, while the inlet temperature of liquid is kept constant at $76℃$.

For $\mathrm{Al_2O_3/EG}$ nanofluid, the constant liquid inlet temperature and mass flow rate have been maintained at $10\mathrm{kg/s}$ and $70℃$, respectively. For the air side, the constant inlet velocity and temperature have been kept constant at $10\mathrm{m/s}$ and $20℃$, respectively. Transient simulations have been carried out for step change in the volume concentrations $(\emptyset)$ of $\mathrm{Al_2O_3/EG}$. The $\emptyset$ of $\mathrm{Al_2O_3/EG}$ have been varied from 2% to 3% in order to evaluate its effects on thermal performance. The numerical predictions are illustrated in this section.

The boundary conditions have been chosen in light of the ambient air and the automotive coolant conditions within the laminar flow regime, particularly seen in the fall weather. The particular concentrations of nanofluids have been chosen as the dynamic viscosity of nanofluids are usually applicable for $\leq 5.0\%$ [123, 251, 252].

6.3.1 Centreline Velocity of Al_2O_3/W Nanofluids

For a given mass flux of $1117 \mathrm{kg/m^2s}$, the variations of centreline velocity of fluid streams at the top and the bottom slabs along the channel length are shown in Figure 6.29.

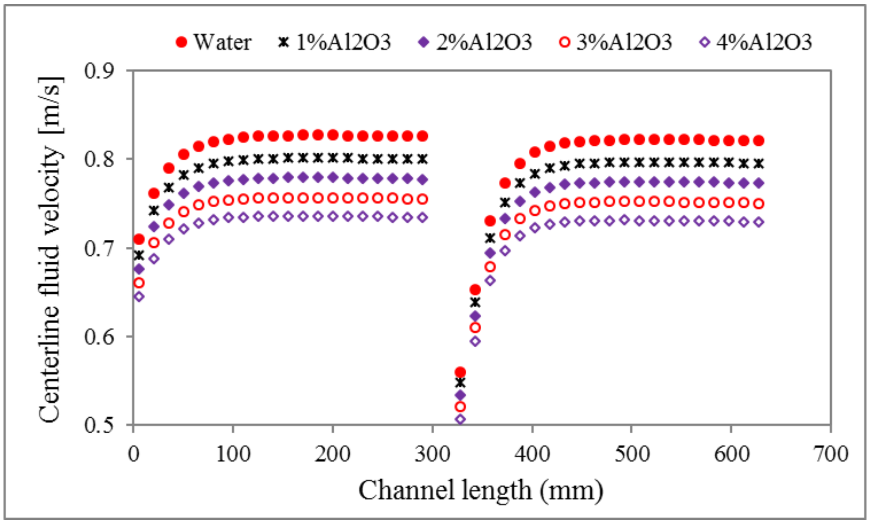

Figure 6.29: Local centerline fluid velocity along the channel length for different volume concentration of a nanofluid for a given mass flux of 1117 $\mathrm{kg/m^2s}$

Fluid enters each circular channel at a uniform mass flux. The fluid particles in the layer in contact with the channel surface come to a complete stop. This layer gradually slows down the fluid particles in the adjacent layers due to friction. The fluid velocity at the channel centre needs to increase to make up for this velocity reduction and retain the mass flow rate constant through the channels. As a result, a hydrodynamic boundary layer develops along the channel. The boundary layer thickness increases in the direction of fluid flow until it reaches the channel center.

The figure shows that the flow in the entrance region develops a hydrodynamic boundary layer along the length of channel and becomes hydrodynamically fully developed beyond the entrance region of the first slab. This boundary layer breaks when the fluid enters to the serpentine. A new boundary layer develops after leaving the serpentine and becomes fully developed beyond the entrance region of the next slab. The centreline velocity of the fluid is lower for higher volume fraction.

6.3.2 Convective Heat Transfer Coefficient of Al_2O_3/W Nanofluid

The variations of liquid-side convective heat transfer coefficient (h) of Al_2O_3/W nanofluid with different concentration ($\emptyset$) and Re are shown in Figure 6.30. The figure shows that h increases nonlinearly with the increase of Re as well as increase of $\emptyset$. The effect of Brownian motion is not taken into account in the calculation of effective thermal conductivity of a nanofluid used in the numerical simulation at this stage.

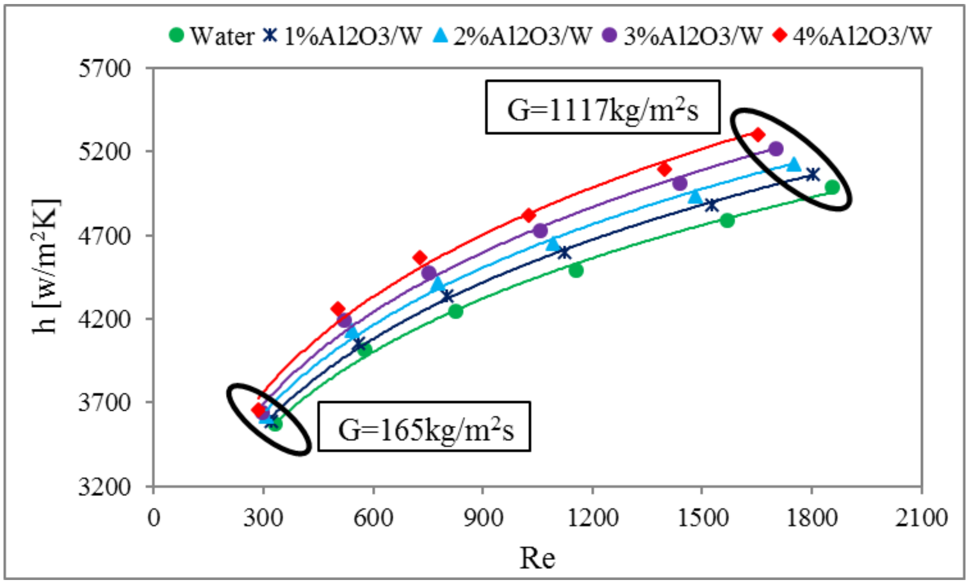

Figure 6.30: Effect of Al_2O_3/W nanofluids on heat transfer coefficient

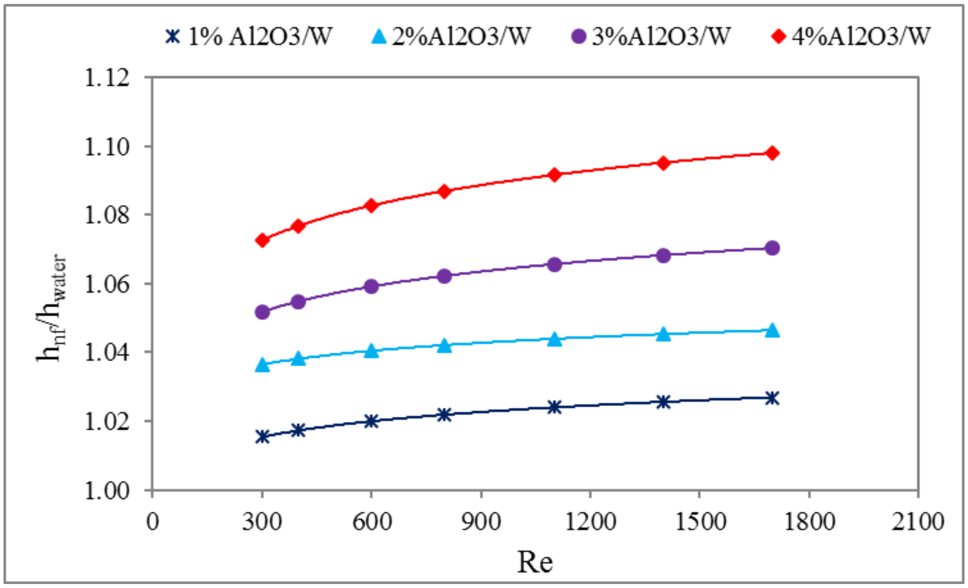

Figure 6.31: Effect of Al_2O_3/W nanofluids on heat transfer coefficient enhancement

The enhancement of heat transfer coefficient due to insertion of Al_2O_3 nanoparticles in the water is found to be higher than that of the base fluid at both the higher Ø and the higher Re. The heat transfer coefficient is increased by up to 10% for Ø=4%vol., as shown in Figure 6.31. This is because of the fact that the greater the volume concentration, the higher the thermal conductivity and the temperature gradient between the wall surface and the fluid. These result the higher heat transfer coefficient of the fluid.

6.3.3 Convective Heat Transfer Coefficient of Al_2O_3/ATF Nanofluids

The heat transfer coefficient of Al_2O_3/ATF nanofluid for various Ø under different Re is illustrated in Figure 6.32. The figure shows that h increases with the increase of Re, as expected. For a particular Re, heat transfer coefficient of nanofluid becomes slightly higher at a higher concentration for the range of 1%≤Ø≤3%. The enhancement of heat transfer coefficient of Al_2O_3/ATF nanofluid is observed up to 7.1% to 8.5% for Ø=3% under Re=50, as shown in Figure 6.33.

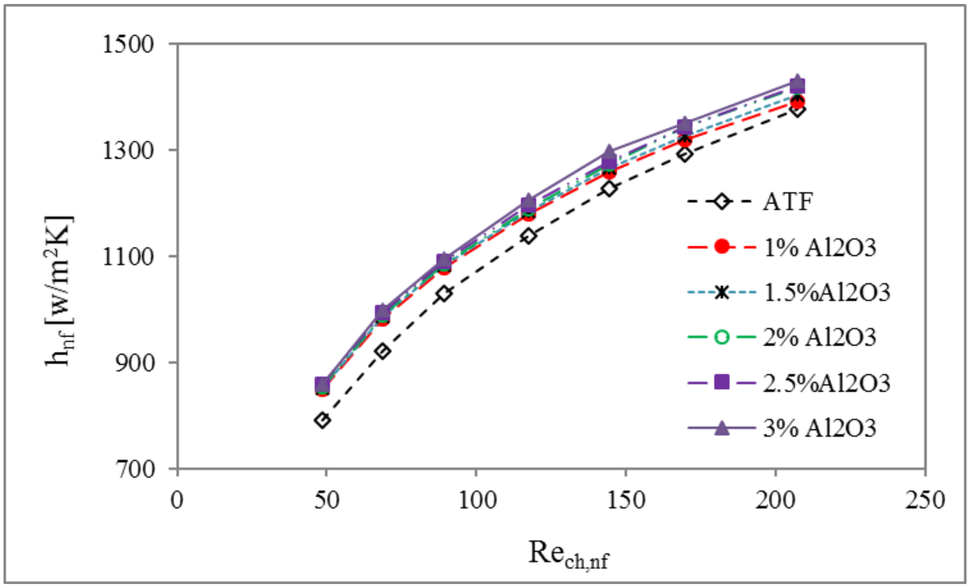

Figure 6.32: Effect of Al_2O_3/ATF nanofluids on heat transfer coefficient

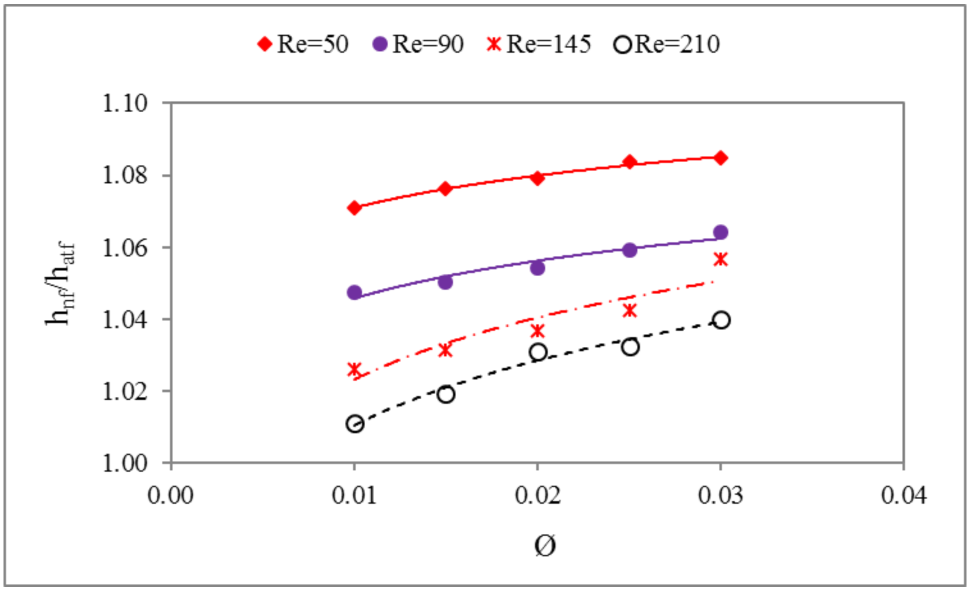

Figure 6.33: Effect of Al_2O_3/ATF nanofluids on heat transfer coefficient enhancement

6.3.4 Nu-Re-Pr correlation of Al_2O_3/ATF nanofluid

The convective heat transfer coefficient for forced convection is generally stated in terms of Nu as a function of Re and Pr. Figure 6.34 shows the effect of liquid-side Re on Nu for Al_2O_3/ATF nanofluid concentration from 1% to 3% at constant inlet liquid temperature of 76℃ and air temperature 14℃. The Nu of the nanofluid is found higher for lower concentration. It is due to the fact that thermal conductivity of nanofluid dominates the Nu compared to its heat transfer coefficient. For Re≤100, Nusselt number of nanofluid is observed higher than that of the base fluid ATF. This is because the heat transfer coefficient of nanofluid dominates the Nu. However, for Re>100, Nu_{nf} is lower than Nu_{atf} because the thermal conductivity of nanofluid dominates the Nu.

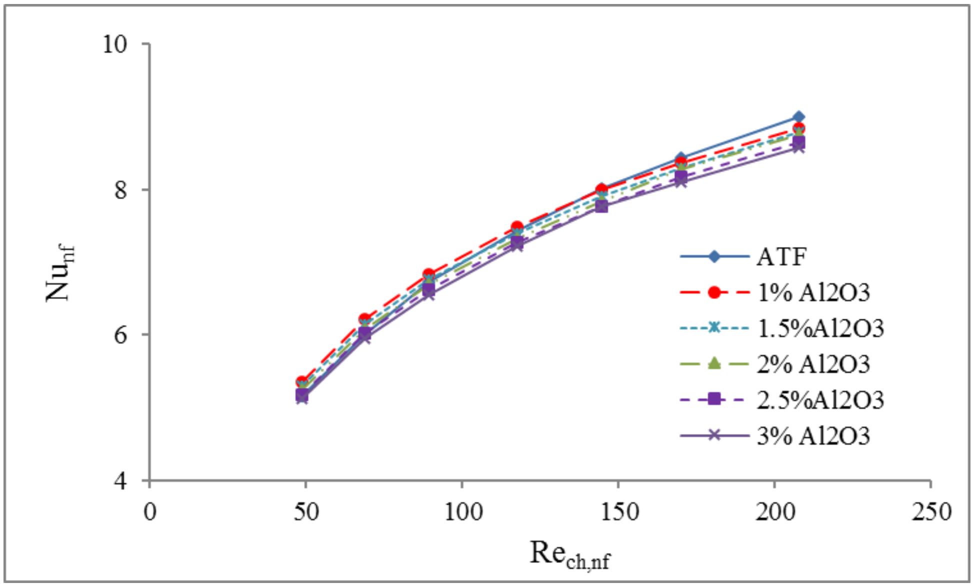

Figure 6.34: Effects of Reynolds number on Nusselt number of Al_2O_3/ATF

Figure 6.35 shows the Nu-Re-Pr correlation of Al_2O_3/ATF nanofluid. From a nonlinear regression analysis (NLREG), an overall correlation is obtained for 50≤Re≤210 and 1%≤∅≤3%, as $\mathrm{Nu} = 0.23\mathrm{Re}^{0.37}\mathrm{Pr}^{1/3}$.

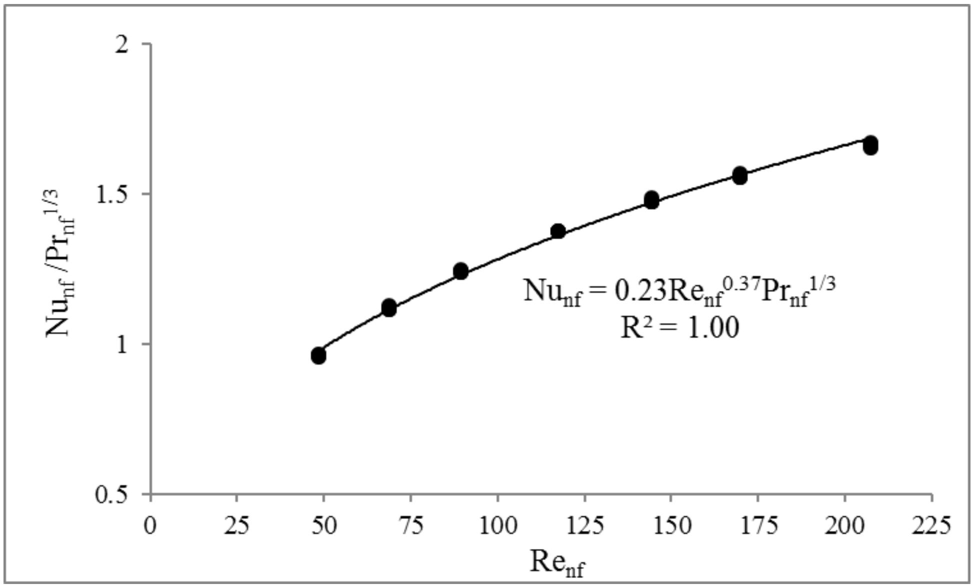

Figure 6.35: Nu-Re-Pr correlation of Al_2O_3/ATF nanofluid

6.3.5 Thermal performance of Al_2O_3/EG nanofluid using dispersion method

The results of single-phase homogenous modeling can be improved by using the dispersion approach. In this approach, the Brownian motion or the random motion of nanoparticles in the base fluid is taken into account for thermal dispersion. The size (diameter) and the shape of the nanoparticles as well as the volume concentration and thermophysical properties of nanofluids influence the thermal dispersion. In dispersion approach, effective thermal conductivity of nanofluids is illustrated by the following equations [233].

$$k_{eff} = k_{static} + k_{dynamic} = k_{nf} + k_{brownian}$$

$$k_{eff} = \left[\frac{k_{np}+2k_{bf}+2(k_{np}-k_{bf})\emptyset}{k_{np}+2k_{bf}-(k_{np}-k_{bf})\emptyset}\right]k_{bf} + 5\times10^4\beta\emptyset\rho_f c_{p,f}\sqrt{\frac{k_B T}{\rho_{np} d_{np}}}f$$

where, K_B is the Boltzmann's constant, T is the nanofluid temperature and k_{nf}, k_{np} and k_{bf} are the thermal conductivity of nanofluid, nanoparticle and basefluid, respectively.

The thermal performance of 3%vol. Al_2O_3/EG nanofluid for $220 \leq Re \leq 1380$ has been numerically predicted by using single-phase homogenous and dispersion approaches. The results are illustrated in Figures 6.36 and 6.37.

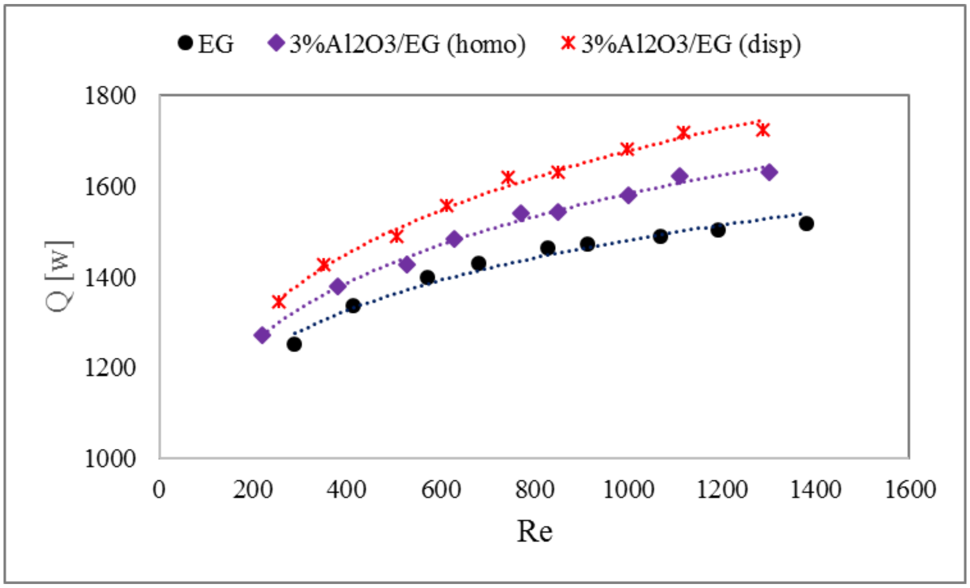

Figure 6.36: Heat transfer rate of Al_2O_3/EG nanofluid

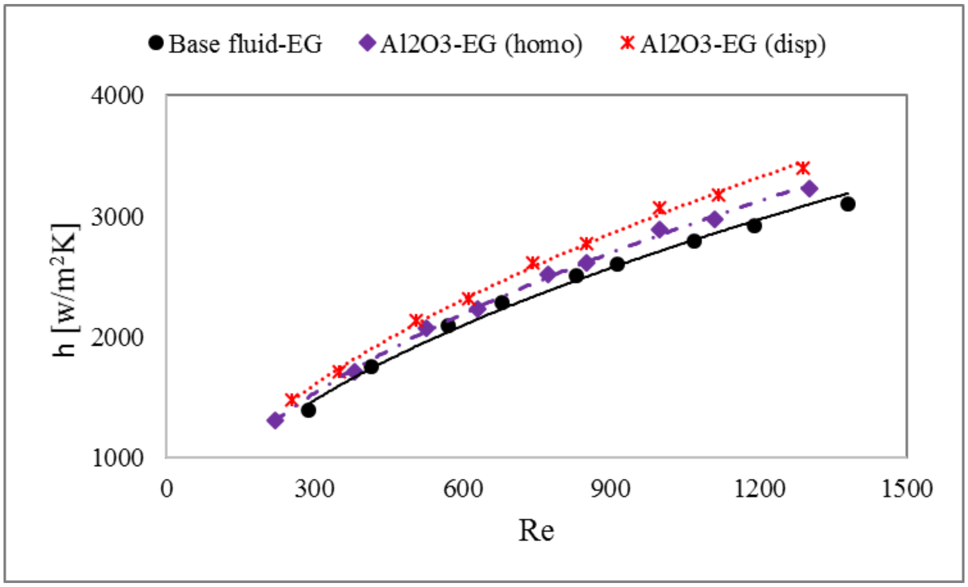

Figure 6.37: Heat transfer coefficient of Al_2O_3/EG nanofluid

It is observed that both the heat transfer rate and the heat transfer coefficient of the fluid are increased due to the inclusion of Al_2O_3 nanoparticles into the basefluid. It is also found that the dispersion approach provide better thermal performance than the single-phase homogeneous approach. The single-phase homogeneous model predicted about 4.5% - 8.9% higher heat transfer rate and 2.9% - 9.6% higher heat transfer coefficient than those of the basefluid. While, the dispersion approach predicted approximately 9.2% - 16.5% higher heat transfer rate and 7.2% - 15.1% higher heat transfer coefficient compared to those of the basefluid.

6.3.6 Comparison of Nusselt numbers of Al2O3/EG nanofluids between homogeneous and dispersion approaches

The variation of Nusselt number for two distinct approaches, homogeneous and dispersion, is presented in Figure 6.38.

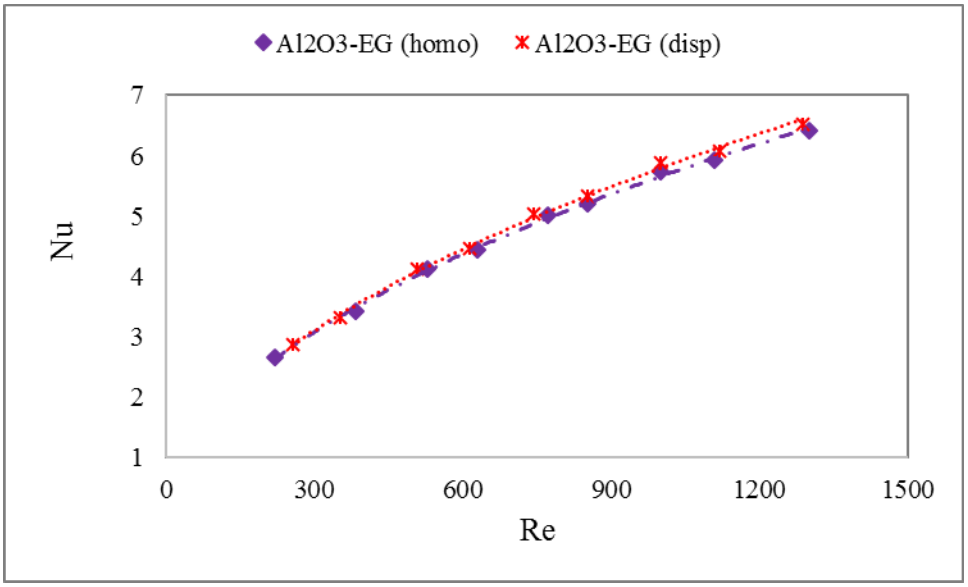

Figure 6.38: Comparison of Nusselt numbers of Al_2O_3/EG nanofluids

It is clear from the figure that Nusselt number of Al_2O_3/EG increases with the increase of Reynolds number. It follows a power law relationship with a positive exponent. The numerical results also shows that the Nusselt number is slightly higher for dispersion model than that of single-phase homogeneous model. The insignificant difference in Nu is due to the fact that the conductivity and the heat transfer coefficients rise approximately at similar proportion.

6.3.7 Effects of Al_2O_3 nanoparticles on liquid-side pressure drop

The effects of Al_2O_3 nanoparticles on the liquid-side pressure drop is illustrated in Figure 6.39.

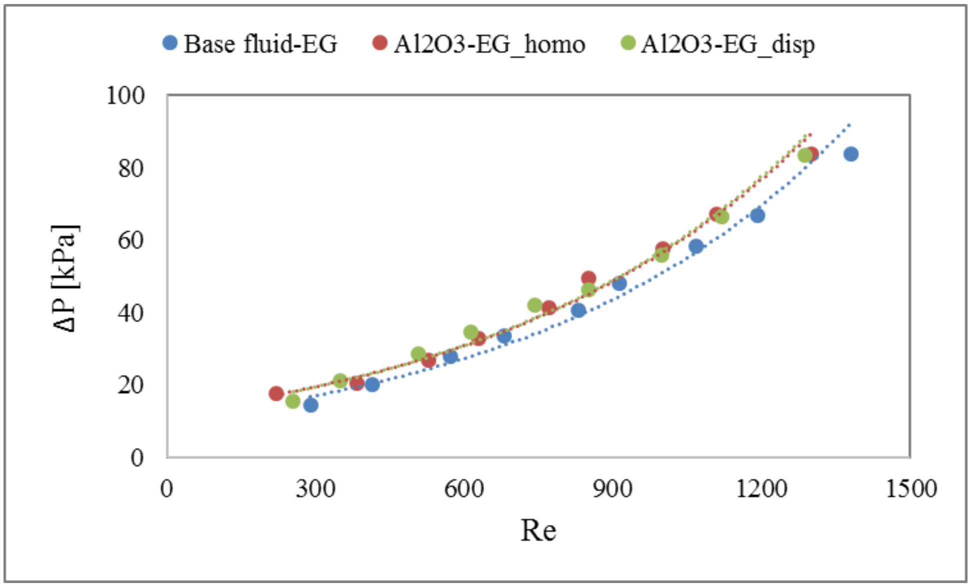

Figure 6.39: Effects of nanoparticles on liquid-side pressure drop

The figure shows that the liquid-side pressure drop, ΔP exponentially increases with the increase of fluid Reynolds number. For $220 \le Re \le 1380$, the ΔP increases by 10.0% to 17.5% due to dispersion of 3%vol. fraction of Al_2O_3 nanoparticles in the base fluid. This is because of the greater viscosity of nanofluids. The higher the dynamic viscosity of a fluid, the higher the pressure drop. The liquid-side pressure drop is identical for both the homogeneous and dispersion models. This is because of the fact that the same viscosity correlation is employed for both the models.

6.3.8 Variation of dimensionless temperature (T*) of Al_2O_3/EG nanofluid with dimensionless time (t*)

In order to evaluate the transient responses of nanofluid, a time-dependent model is used for numerical simulations of Al_2O_3/EG nanofluids. The variation of dimensionless temperature (T*) of Al_2O_3/EG nanofluid with dimensionless time (t*) is presented in Figure 6.40.

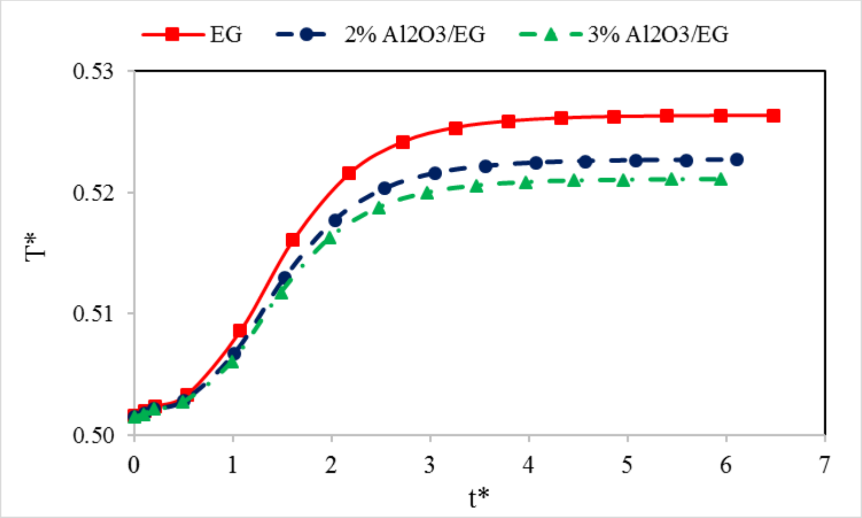

Figure 6.40: Variation of dimensionless liquid temperature with dimensionless time

The T* and t* have been defined as

$$T^* = \frac{T(t) - T_{c,in}}{T_{h,i} - T_{c,in}} \tag{6.3.1}$$

$$t^* = \frac{t}{t_{res}} \tag{6.3.2}$$

where, $T(t)$ is temperature of liquid at time (t), and t_{res} is the residence time, which is occupied by the fluid to go through the serpentine channel starting from the inlet to reach the outlet of the boundary.

Figure 6.40 demonstrates the comparison between the base fluid (EG) and nanofluid (Al_2O_3/EG) with 2%vol. and 3%vol. fraction as a function of dimensionless temperature and time.

The dimensionless liquid temperature (T*) and the dimensionless time (t*) have been used to have a better understanding of the response time of the liquid. The T* represents the liquid outlet temperature. The higher temperature drop is found in nanofluids compared to that of the base fluid EG. This is because of the influences of Brownian motion and the thermophysical properties of nanofluids. It is also evaluated that the time taken by the fluids to reach from one steady state to the another steady state is sooner for nanofluids with the higher volume fraction with respect to the base fluid.

6.3.9 Summary

The effects of Al_2O_3/W, Al_2O_3/ATF and Al_2O_3/EG nanofluids on thermal performance of a MICHX have been evaluated. The key outcomes are

- Enhanced convective heat transfer coefficient is predicted due to the dispersion of Al_2O_3 nanoparticles in the base fluids with the cost of higher pressure drop.
- Dispersion approach predicts better thermal performance than the single-phase homogeneous approach

- Nusselt number of Al_2O_3 based nanofluids increases with the increase of Re and follows the power law relationship with a positive exponent. For Re≤100, Nusselt number of Al_2O_3/ATF nanofluid is observed higher than that of the base fluid ATF. This is because the heat transfer coefficient of nanofluid dominates the Nu. However, for Re>100, Nu_{nf} is lower than Nu_{atf} because the thermal conductivity of nanofluid dominates the Nu.

- Nusselt number of Al2O3/EG nanofluid is slightly higher for dispersion model than that of single-phase homogeneous model. The insignificant difference in Nu is due to the fact that the conductivity and the heat transfer coefficients rise approximately at similar proportion.

- The response time for Al_2O_3/EG nanofluids is shorter than the base fluid EG; it decreases with the increase of nanofluid concentration due to higher heat transfer coefficient.

6.4 Stage IV. Sequential vs Simultaneous Heat Exchanger Modules

In this section, the simulation results for sequential and simultaneous modules of conventional FTHX and MICHX are presented. Both the sequential and the simultaneous modules of FTHX and MICHX are identical with slab thickness, frontal area and volume. The same boundary conditions have also been applied for both the heat exchanger modules. Water with two distinct temperatures of $65℃$ and $95℃$ is cooled by crossflow cold air temperature of $25℃$ and velocity of $6 \mathrm{m/s}$. Water mass flow rates have been varied within the Reynolds number range of $350 \leq \mathrm{Re} \leq 2250$. The heat exchangers associated with the water inlet temperatures of $65℃$ and $90℃$ are denoted as MT-HX and HT-HX, respectively. The simulations have been conducted for different Reynolds numbers at laminar flow regime. With the purpose of improving the thermal performance, each module of both the FTHX and the MICHX in various combinations have been simulated and evaluated. For sequential module, the HT-HX is employed in the forward-facing with regard to the incoming cold air, while the MT-HX is placed in the rear of the HT-HX. For simultaneous module, the HT-HX is positioned on the top of the MT-HX. Simulations for simultaneous arrangement have also been carried out using the reverse placement of HT-HX and MT-HX and illustrated below. The particular boundary conditions of the models been chosen in consideration of the operating conditions of an automotive condenser and radiator when the vehicle runs in the city during the fall.

6.4.1 Simultaneous FTHX vs Sequential FTHX

Figures 6.41(a) to 6.41(c) illustrate the heat transfer rate of simultaneous and sequential modules of FTHX. For sequential module, the MT-HX is placed in front of the HT-HX regarding the incoming cold air. For simultaneous module, the HT-HX is positioned on the top of the MT-HX.

The figures display that the heat transfer rate increases with increase of Reynolds number for all the cases within the laminar flow regime, as expected. Significant improvement in thermal performance of the HT-HX is observed in simultaneous module than the conventional sequential orientation. Figure 6.41(a) shows about 10.6%−17.3% enhancement in heat transfer rate in the HT-HX of the simultaneous module. This is because the heat exchanger faces the incoming ambient air in this module, while it receives the outlet warmer air of the MT-HX in sequential module.

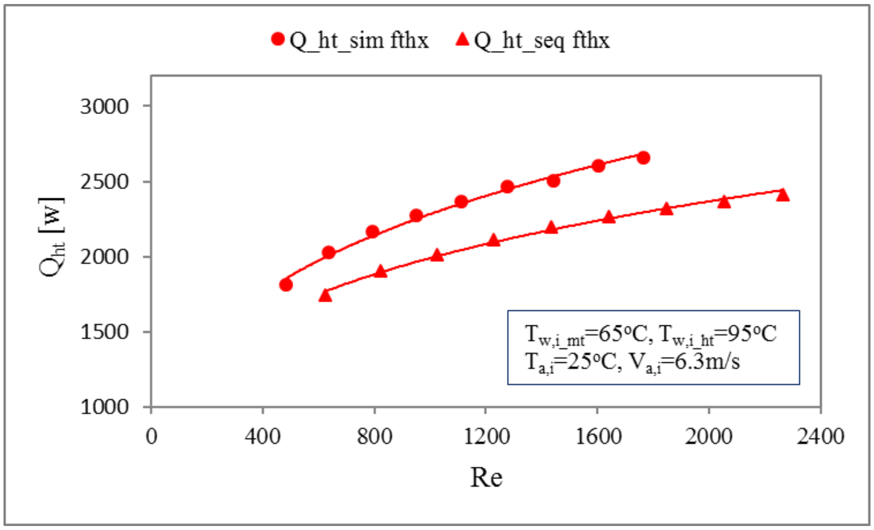
● Q_ht_sim fthx
▲ Q_ht_seq fthx
Q_{ht} [W]
3000
2500
2000
1500
1000
0
400
800
1200
1600
2000
2400
Re
T_{w,i_mt}=65°C, T_{w,i_ht}=95°C
$T_{a,i}$=25°C, $V_{a,i}$=6.3m/s

(a)

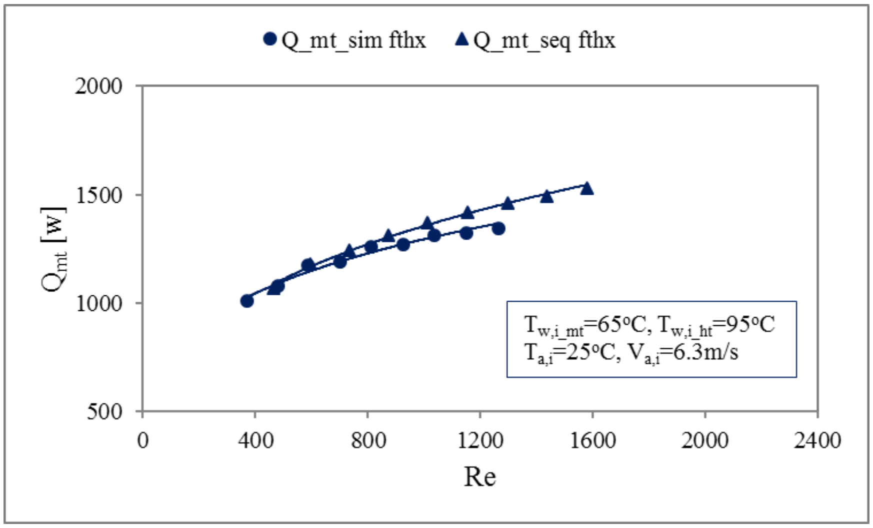
● Q_mt_sim fthx
▲ Q_mt_seq fthx
Q_{mt} [W]
2000
1500
1000
500
0
400
800
1200
1600
2000
2400
Re
T_{w,i_mt}=65°C, T_{w,i_ht}=95°C
$T_{a,i}$=25°C, $V_{a,i}$=6.3m/s

(b)

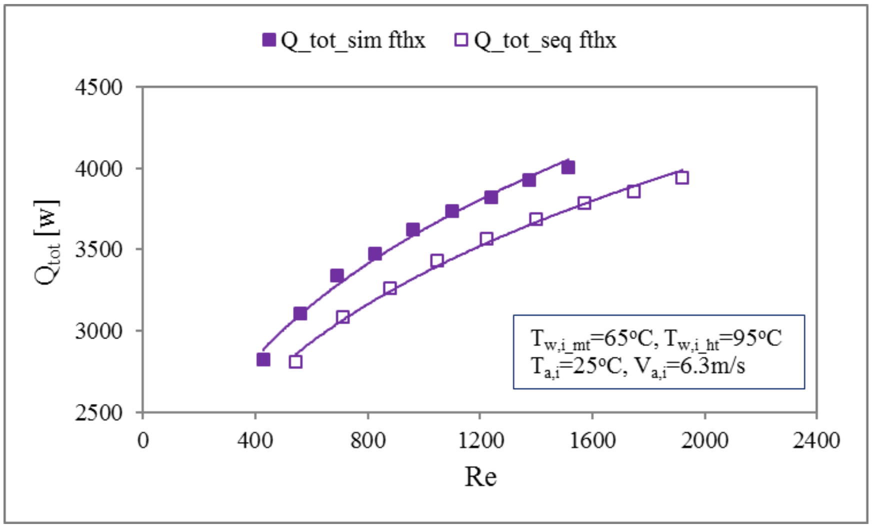

(c)

Figure 6.41: Heat transfer rate of simultaneous and sequential FTHXs: (a) HT-HX, (b) MT-HX and (c) overall module

The MT-HX displays insignificant improvement or somewhat reduced thermal performance in simultaneous than sequential arrangement, as shown in Figure 6.41(b). This is because, for both the simultaneous and the sequential arrangement, MT-HX faces identical air of ambient condition, such as quality, velocity, and temperature. However, the MT-HX receives heat from the neighboring HT-HX by means of thermal interaction. For a given Reynolds number, the overall heat transfer rate of simultaneous FTHX is greater than that of sequential FTHX, as shown in Figure 6.41(c). Numerical simulations predict about 7.5% to 8.1% increased heat transfer rate for $350 \leq \mathrm{Re} \leq 2250$.

6.4.2 Simultaneous MICHX vs Sequential FTHX

Figures 6.42(a) to 6.42(c) illustrate the heat transfer rates of simultaneous MICHX and sequential FTHX modules. Both modules possess same frontal area, volume and operating conditions. Figures 6.42(a) and 6.42(b) represent the numerical predictions of the heat transfer rates through HT-HX and MT-HX, respectively. The overall heat transfer rates of both the modules are presented in Figure 6.42(c).

Figure 6.42(a) displays higher transfer rate in HT-HX of simultaneous MICHX than that of sequential FTHX within the laminar flow regime. The simultaneous module predicts nearly 22.4% to 27.7% higher heat transfer rate over the sequential module, as shown in Figure 6.42(a). This is because, in simultaneous module, HT-HX faces the incoming air with ambient conditions; whereas, in sequential module, it receives the outlet warmer air of the MT-HX.

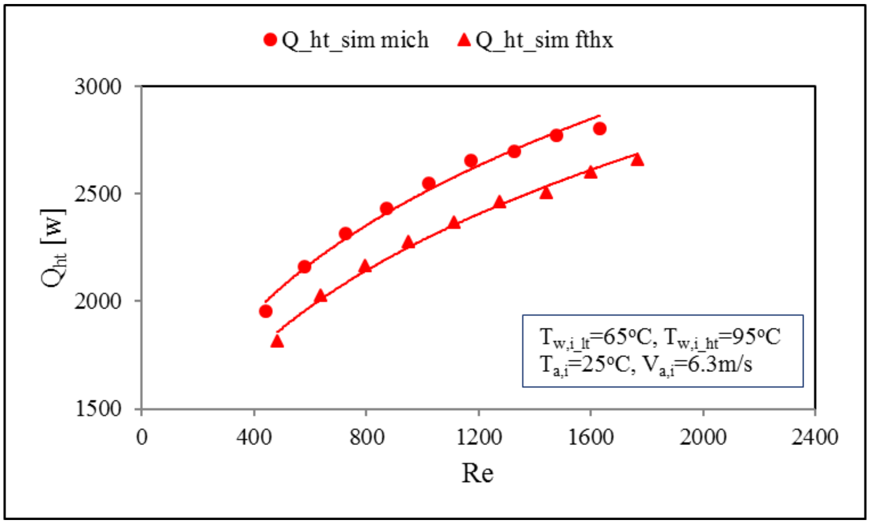

(a)

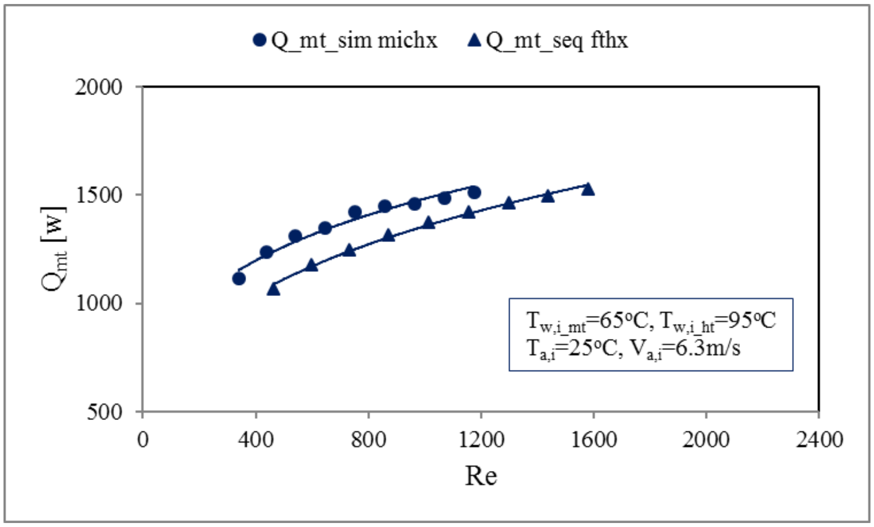

(b)

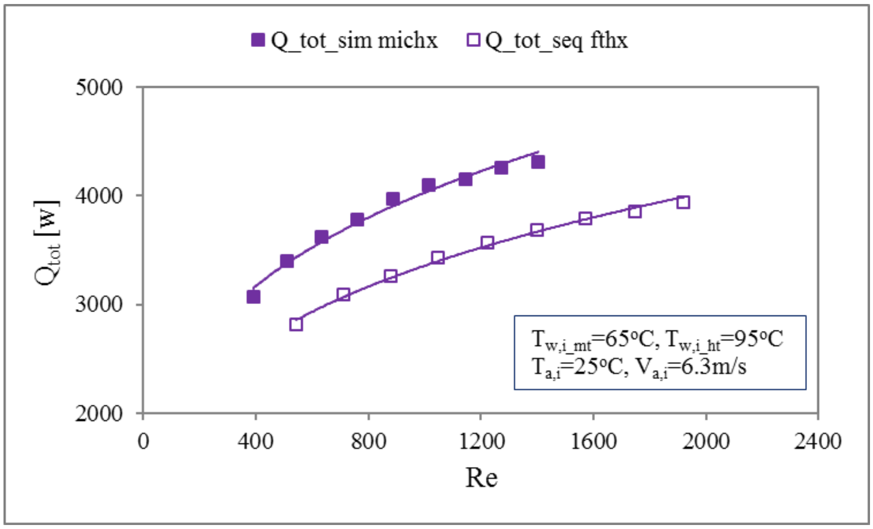

(c)

Figure 6.42: Heat transfer rate of simultaneous MICHX and sequential FTHX: (a) HT-HX, (b) MT-HX and (c) overall

In case of MT-HX, as shown in Figure 6.42(b), heat transfer rate increases approximately 11.34% in the simultaneous module at low Reynolds, particularly at Re ≈ 400. As Reynolds number increases, the heat transfer rate in the simultaneous module gradually becomes identical to, or somewhat lower than that of the sequential module. This is because, for both the simultaneous and the sequential arrangements, MT-HX faces ambient air with identical quality, velocity, and temperature. However, in simultaneous orientation, the MT-HX receives heat from the neighboring HT-HX by means of thermal interaction. At a particular Reynolds number, the overall thermal performance of simultaneous MICHX is superior to that of conventional sequential FTHX. The overall heat transfer rate in simultaneous MICHX is observed to be about 19.8%~20.4% higher compared to that of the sequential FTHX.

Figures 6.43(a) and 6.43(b) characterize the numerical predictions of h for HT-HX and MT-HX, respectively. The enhancement of h due to employment of simultaneous MICHX for both the HT-HX and the MT-HX is quantified and shown in Figure 6.43(c).

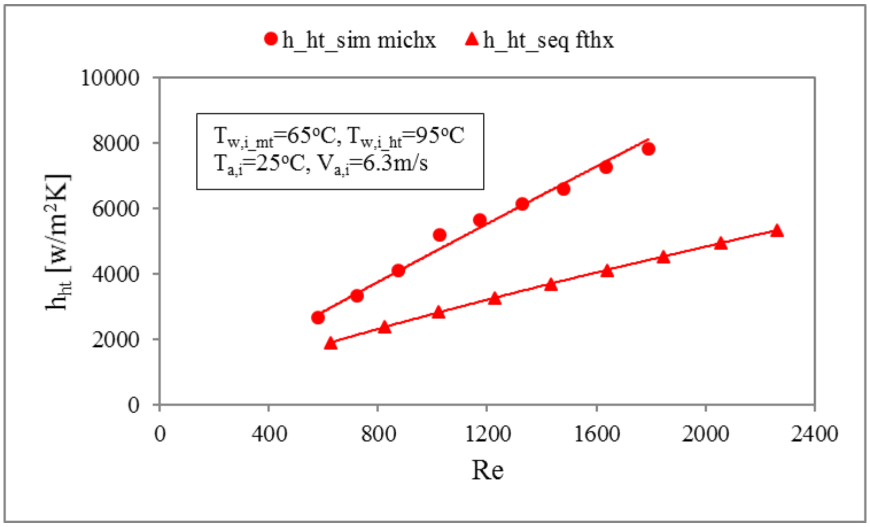

(a)

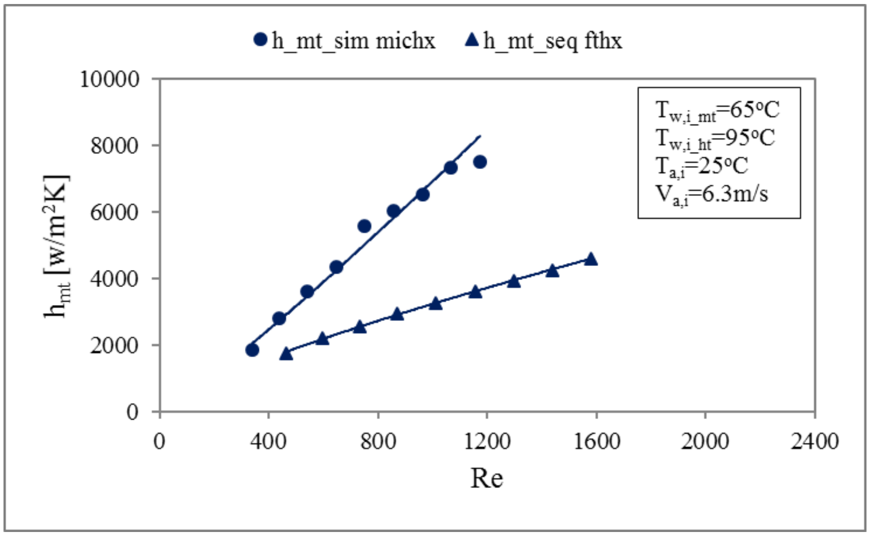

(b)

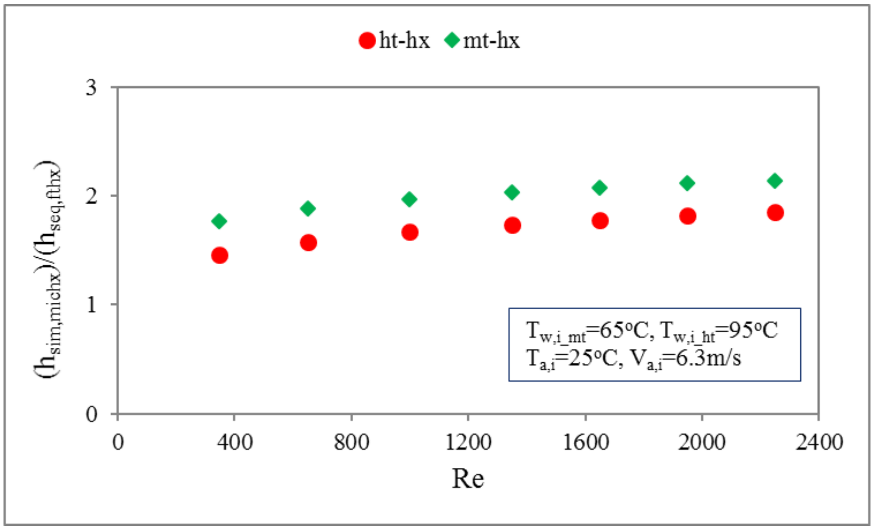

(c)

Figure 6.43: Heat transfer coefficient: (a) HT-HX, (b) MT-HX and (c) enhancement

Within the laminar flow regime, for the HT-HX, the h of simultaneous MICHX module is predicted a 45.9% to 85.4% higher than that of the sequential FTHX module. For the MT-HX, the h of simultaneous MICHX module is found to be about 77%−114.4% higher than that of the sequential FTHX module.

New Nu correlations by means of Re and Pr for both the HT and the LT of each module have been obtained. The correlations are in the form of $\mathrm{Nu} = \mathrm{ARe^m Pr^n}$. The developed correlations are illustrated in Figures 6.44(a) and 6.44(b).

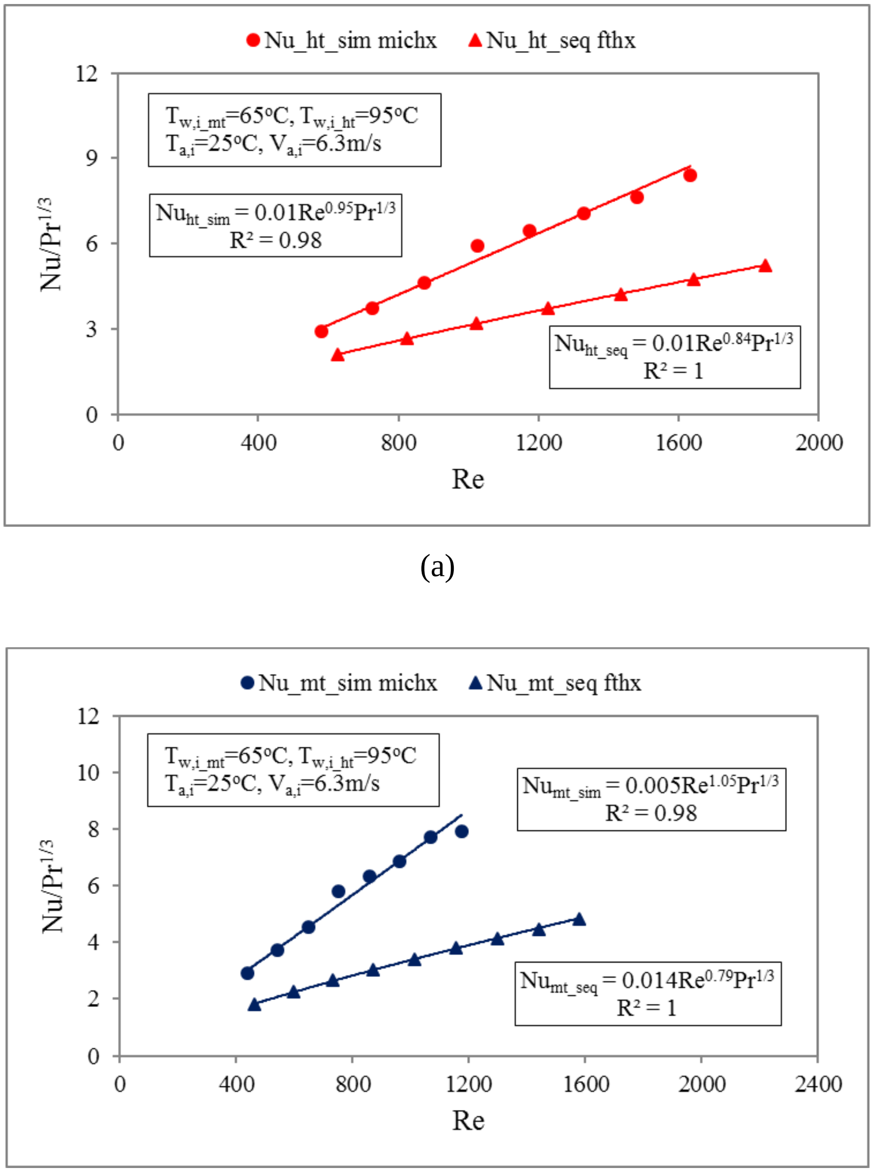

(a)

(b)

Figure 6.44: Nusselt number correlations: (a) MT-HXs and (b) HT-HXs

6.4.3 Simultaneous MICHX and Simultaneous FTHX

The thermal performance of simultaneous modules of the MICHX and the FTHX have been evaluated with intention of making the most effective use of the modules. The numerical predictions of heat transfer rates in both the modules are presented in Figures 6.45(a) to 6.45(c).

It is seen in Figures 6.45(a) and 6.45(b) that the heat transfer rates in both the HT-HX and the MT-HX are higher in simultaneous MICHX than that of the FTHX. Consequently, the overall heat transfer rate is also greater in the MICHX module, as shown in Figure 6.45(c).

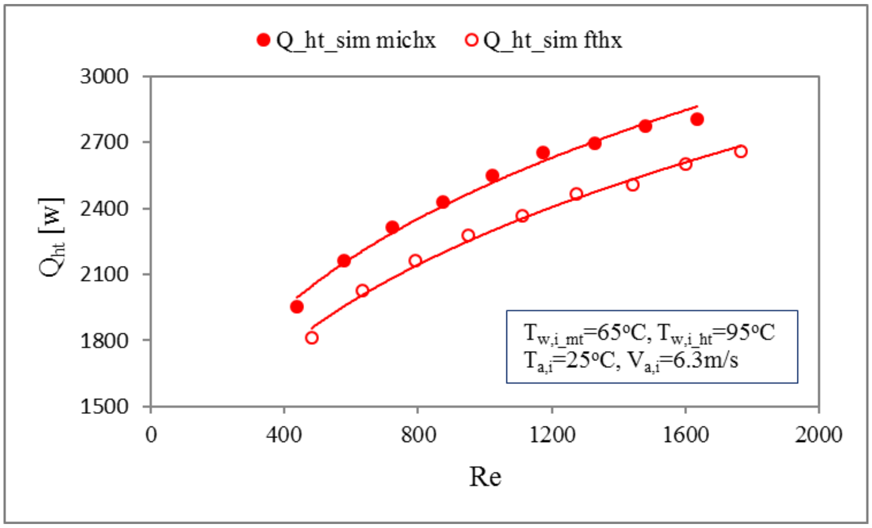

(a)

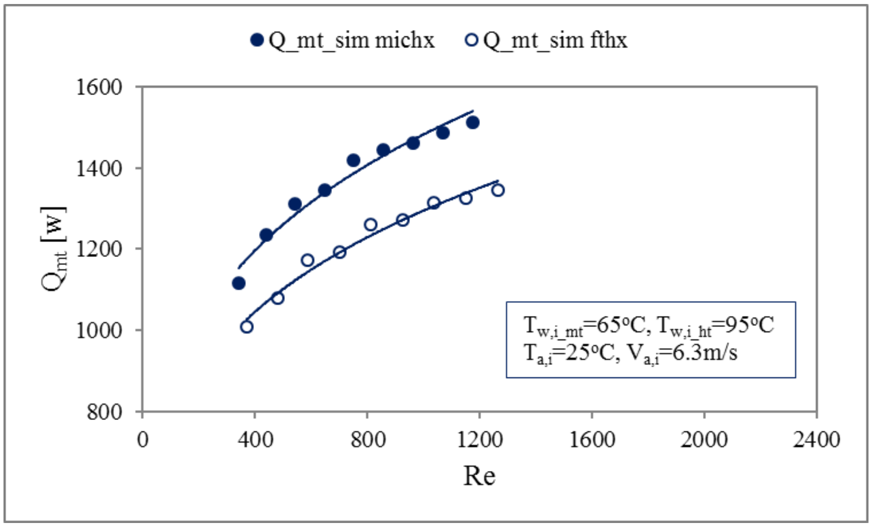

(b)

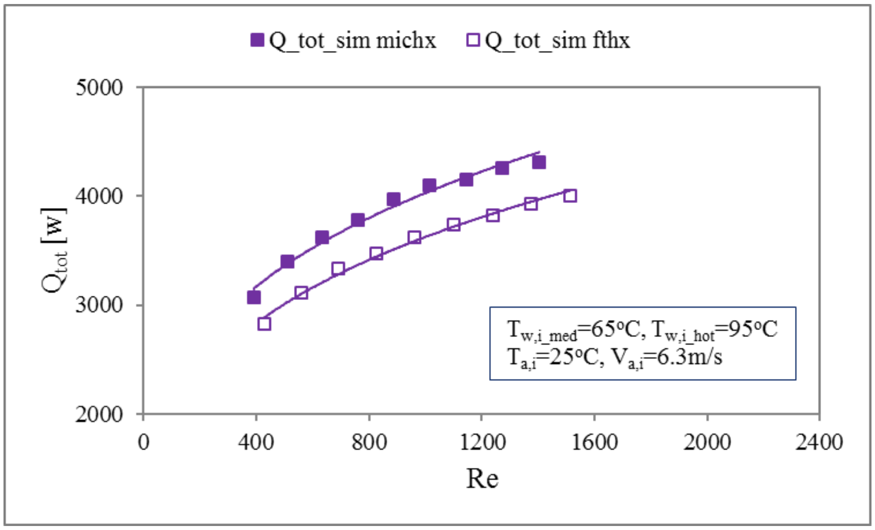

(c)

Figure 6.45: Heat transfer rate: (a) HT-HXs, (b) MT-HXs and (c) Overall

The enhancement of heat transfer rate ($Q_{enh.}$) in simultaneous MICHX is compared to that of the FTHX in Figure 6.46.

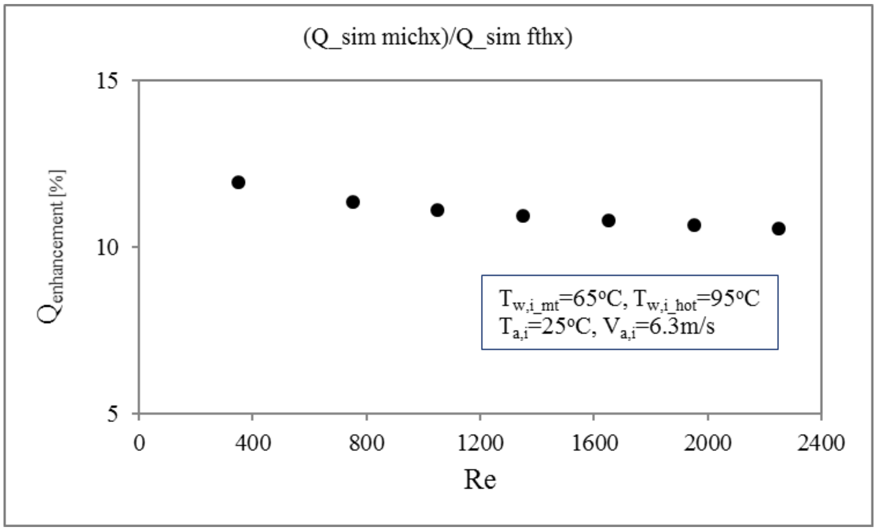

Figure 6.46: Comparison between simultaneous modules of MICHX and FTHX

The $Q_{enh.}$ of both simultaneous modules have been assessed with reference to an identical sequential FTHX module as a benchmark. They provide greater heat transfer rates than the sequential module. Between the two simultaneous modules, MICHX provides belter thermal performance than FTHX. The numerical results predict approximately 10.6% and 11% higher heat transfer rate for the HT-HX and MT-HX, respectively at the simultaneous MICHX module than that of the FTHX module.

6.4.4 Simultaneous MICHX: Effect of the Positions of HT-HX and MT-HX

The effect of the placement sequence of the HT-HX and MT-HX in simultaneous MICHX module is also predicted for building the best operational use of the resource. Two options are available for the positioning of the heat exchangers in the simultaneous module. Option-1: HT-HX on the top and MT-HX in the bottom and Option-2: MT-HX on the top and HT-HX in the bottom

The heat transfer rates for the both options are illustrated in Figures 6.47(a) and 6.47(b).

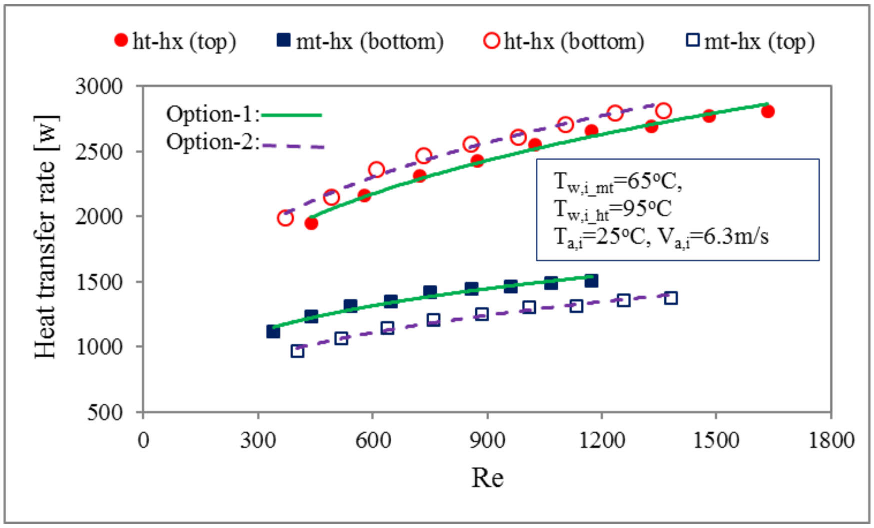

(a)

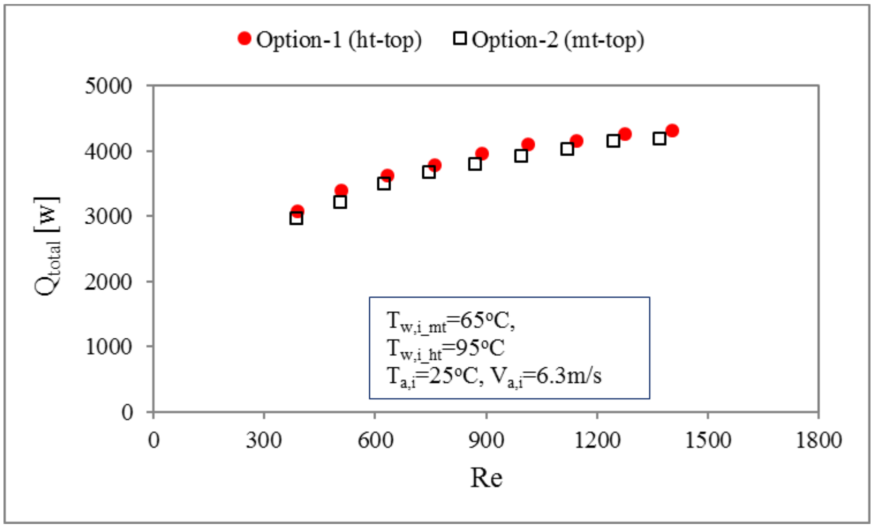

(b)

Figure 6.47: Comparison of heat transfer rate of HT-HX and MT-HX between two discrete options

In Figures 6.47(a) and 6.47(b), the solid and dashed lines represent the heat transfer rate for Option-1 and Option-2, respectively. It is obvious from Figure 6.47(a) that the position of the heat exchangers significantly effects on the thermal performance of individual heat exchanger. The figure shows that both the HT and MT heat exchangers provide higher heat transfer rate when they have been placed in the bottom. This is due to the thermal boundary conditions and thermal interactions between HT-HX and MT-HX. The inlet slab of the top heat exchanger and the outlet slab the bottom heat exchanger are with the contact of adiabatic wall surfaces. On the other hand, the outlet slab of the top heat exchanger makes contact with the inlet slab of the bottom heat exchanger. Consequently, the thermal interaction takes place between two the heat exchangers. This phenomenon significantly effects the heat transfer rate. The intensity of the thermal interaction depends on the position of HT-HX and MT-HX. In fact, it is not feasible to place both the heat exchangers at the same position in a module. Depending on the thermal system requirements, decision needs to be taken for positioning the order of HT-HX and MT-HX.

Figure 6.47(b) shows that the overall heat transfer rates for both Option-1 and Option-2 are identical. This is because of the fact that both the heat exchangers work as a single unit. They have been cooled by crossflow air within a single domain of adiabatic wall. The heat transfer occurs between air and water by means of solid slabs and fins.

6.4.5 Summary

With the aim of improving the thermal performance of heat exchangers and making the most effective use of heat exchangers, simultaneous and sequential modules have been numerically investigated. The numerical predictions of the simultaneous MICHX have been compared with the sequential FTHX as a benchmark. The major findings of the performance analysis of these two heat exchanger modules are shortlisted as follows:

- Heat transfer performance of the simultaneous module is superior to that of the sequential module. Simultaneous FTHX provides nearly 7.5% to 8.1% increased heat transfer rate compared to the sequential FTHX module as a benchmark.

- The thermal performance of the simultaneous MICHX is even better than that of the simultaneous FTHX. The simultaneous MICHX delivers about 19.8%~20.4% increased heat transfer rate than that of the benchmark module.

- Significant improvement in thermal performance of the HT-HX is observed in the simultaneous module than the conventional sequential orientation. This is because the heat exchanger faces the incoming ambient air in this module, while it receives the outlet warmer air of the MT-HX in the sequential module.

- The MT-HX displays insignificant improvement or somewhat reduced thermal performance in the simultaneous than the sequential arrangement. This is because, for both the simultaneous and the sequential arrangement, MT-HX faces identical air of ambient condition, such as quality, velocity, and temperature. However, in the simultaneous orientation, the MT-HX receives heat from the neighboring HT-HX by means of thermal interaction.

- The position of heat exchangers possess significant influence on the thermal performance of each heat exchanger in the simultaneous module. Both the HT-HX and the MT-HX provide higher heat transfer rate if these have been positioned in the bottom. In reality, it is not feasible to place both the heat exchangers in the same location in a module. Therefore, the decision for placement of each heat exchanger needs to be taken based on the requirements of the thermal systems.

6.5 Stage V. Transient Heat Transfer in the MICHX

Transient thermal performance and behaviors of MICHX for perturbation of hot fluid mass flow rate and inlet temperature are illustrated in this section.

6.5.1 Step Change in Hot Fluid Mass Flow Rate (MR)

Step variation scenario of hot fluid mass flow rate is important, as it frequently occurs in real-world applications of heat exchangers. The transient response of an air-to-water crossflow heat exchanger under particular changes in the hot water mass flow rate has been numerically studied. Different variations in the mass flow rate starting from an original value of $20\mathrm{g/s}$ to the subsequent steps of 0.5, 0.8, 1.5, 2.0, 2.5 and 3.0 have been solved. The water (hot fluid) inlet temperature of $70\mathrm{℃}$ and air (cold fluid) inlet temperature of $13\mathrm{℃}$ and velocity of $6\mathrm{m/s}$ have been kept constant throughout all the simulations for all the mass flow steps. Numerical results are presented in this section.

6.5.1.1 Transient Effect of MR on Hot Fluid Residence Time

The effect of hot fluid (water) MR on the residence time ($\mathrm{t_{res}}$) is shown in Figure 6.48. The MR is defined as the ratio of new mass flow rate $\left(\dot{\mathrm{m}}_{\mathrm{h,new}}\right)$ to the original (reference) mass flow rate $\left(\dot{\mathrm{m}}_{\mathrm{h,ref}}\right)$. It is calculated as

$$\mathrm{MR} = \dot{\mathrm{m}}_{\mathrm{h,new}}/\dot{\mathrm{m}}_{\mathrm{h,ref}} \tag{6.5.1}$$

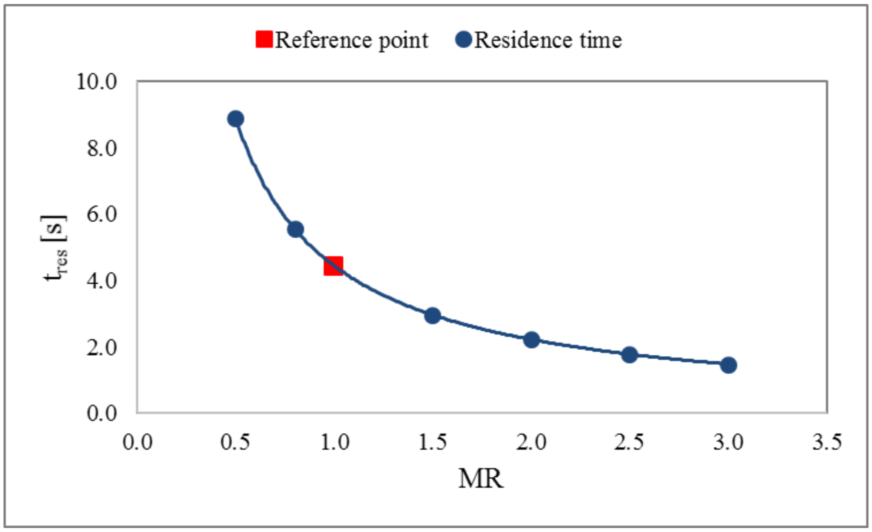

Figure 6.48: Variations of residence time under various mass flow step ratio

The magnitude of MR for original mass flow rate, stepping up (fold-increase) and stepping down (fold-decrease) are $MR = 1$, $MR > 1$ and $MR < 1$, respectively.

It is observed that the residence time decreases with increase of mass flow step variation in a nonlinear pattern of geometric sequence. The gradient of the residence time is greater for step down scenarios than the step up scenarios, and approaches toward the smaller magnitude. The residence time becomes double for half-fold decrease and turns into half for 2-fold increase of mass flow rate. This is due to the fact that the smaller the step ratio, the lower the fluid velocity and Reynolds number of the fluid.

6.5.1.2 Transient Effect of MR on Response Time

The effects of hot fluid mass flow rate step variations on the transient response time for fold-increase and fold-decrease are shown in Figure 6.49(a) and 6.49(b), respectively. The response time is defined as the time taken by the hot fluid to reach the steady state condition.

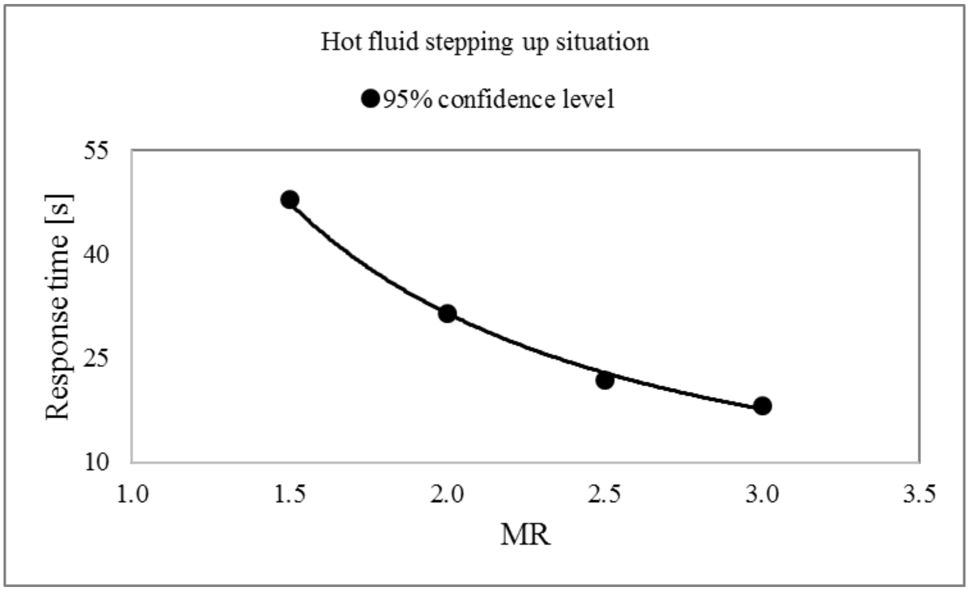

(a)

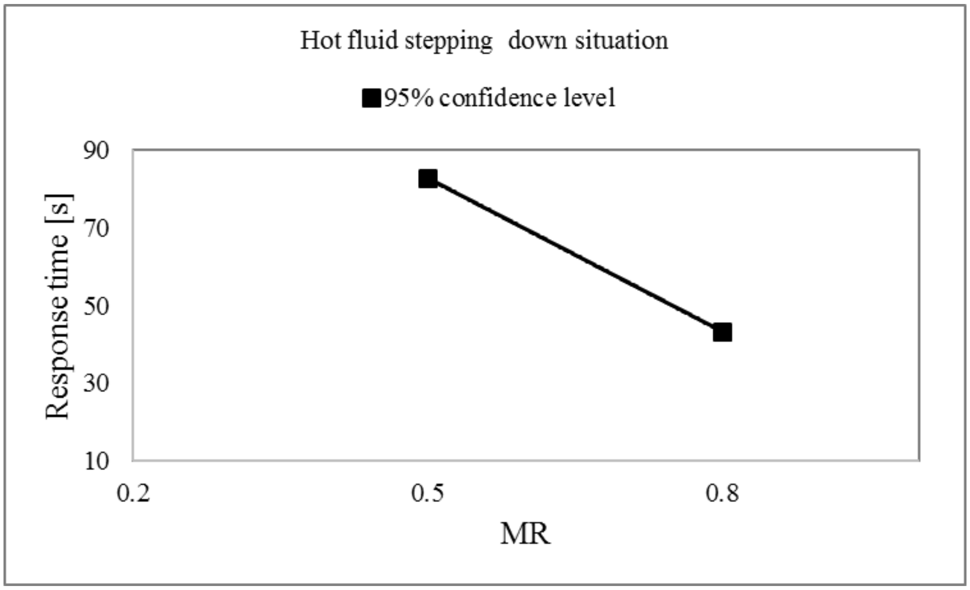

(b)

Figure 6.49: Effects of hot fluid mass flow step variation on response time for (a) stepping up and (b) stepping down

It is observed from Figures 6.49(a) and 6.49(b) that the transient response time is shorter for greater MR, while it is longer for smaller MR. The gradient is much more steeper for MR $<$ 1 compared to the gradient for MR $>$ 1. At 95% confidence level of steady state, the numerical prediction shows that the response time taken by the MICHX is about 30s and 110s for 2-fold increase and half-fold decrease of mass flow rate. This can be interpreted as the fact that the fluid transportation velocity, molecular movement and the heat transfer coefficient increase with the increase of the mass flow rate.

6.5.1.3 Transient Effects of MR on Outlet Temperatures of Fluids

The transient variations of hot (water) and cold (air) fluids outlet temperature due to step changes in hot fluid mass flow rate are presented in Figures 6.50(a) and 6.50(b), respectively. The hot fluid mass flow rate step ratio, MR $=$ 1 defines the original or reference value. For both the hot fluid and the cold fluid, the time occupied to approach the steady state decreases with the increase of MR value. At higher MR value, greater steady state (final) outlet temperature is observed for both the fluids. This is because the working condition of the heat exchanger is "heats the cold fluid". The higher the mass flow rate, the higher the Reynolds number and the heat transfer coefficient.

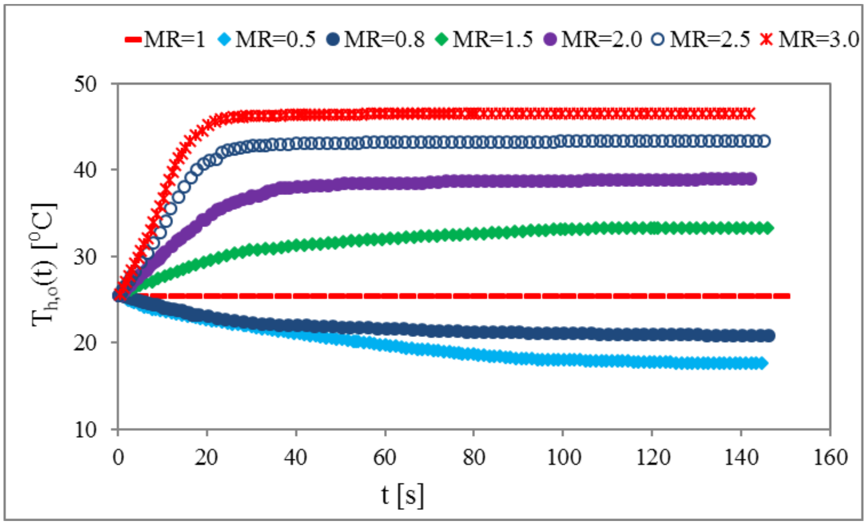

(a)

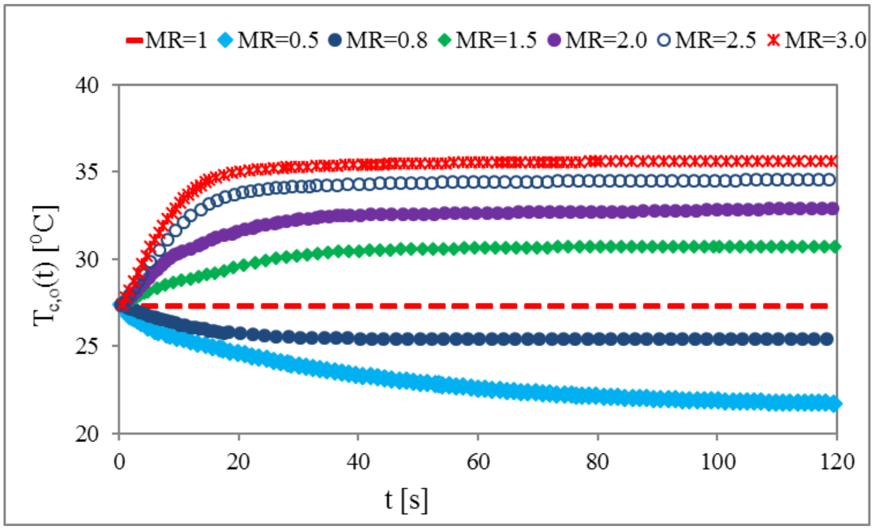

(b)

Figure 6.50: Transient responses of the outlet temperature of (a) the hot fluid and (b) the cold fluid under MR

Results from numerical simulations also show that the trend for transient and quasi-steady state outlet temperatures are not symmetrical for step up and step down mass flow variations. This can be interpreted as the time dependent outlet temperatures of both the hot fluid and the cold fluid for 2-fold step up (MR = 2) and half-fold step down (MR = 0.5) are asymmetrical. For 2-fold step up mass flow rate, the outlet temperature of the hot fluid and the cold fluids at steady state condition are increased by 42% and 20%, respectively. Whereas, the corresponding outlet temperature are decreased by 36% and 21% for half-fold step down mass flow rate.

6.5.1.4 Transient Effect of MR on the Hot Fluid and the Channel Inner Surface Temperatures

The transient variations of hot fluid and channel inner surface temperatures under hot fluid mass flow steps are presented in Figures 6.51(a) and 6.51(b), respectively.

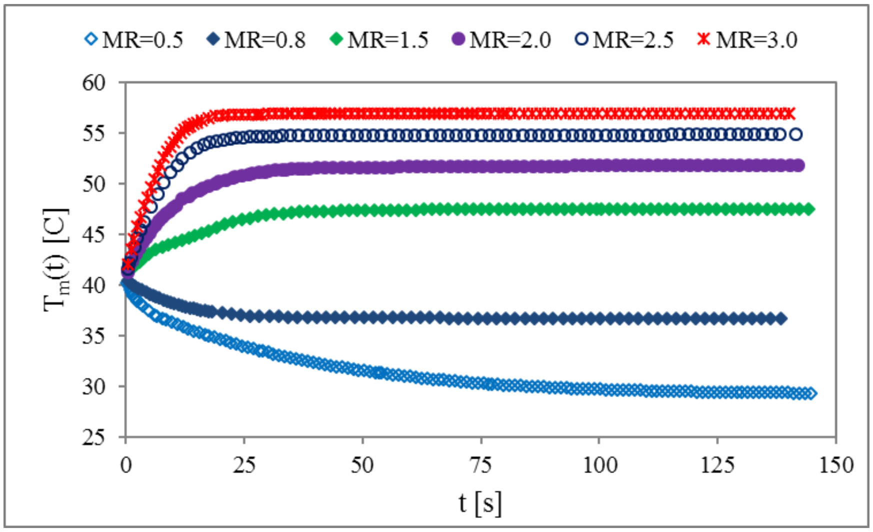

(a)

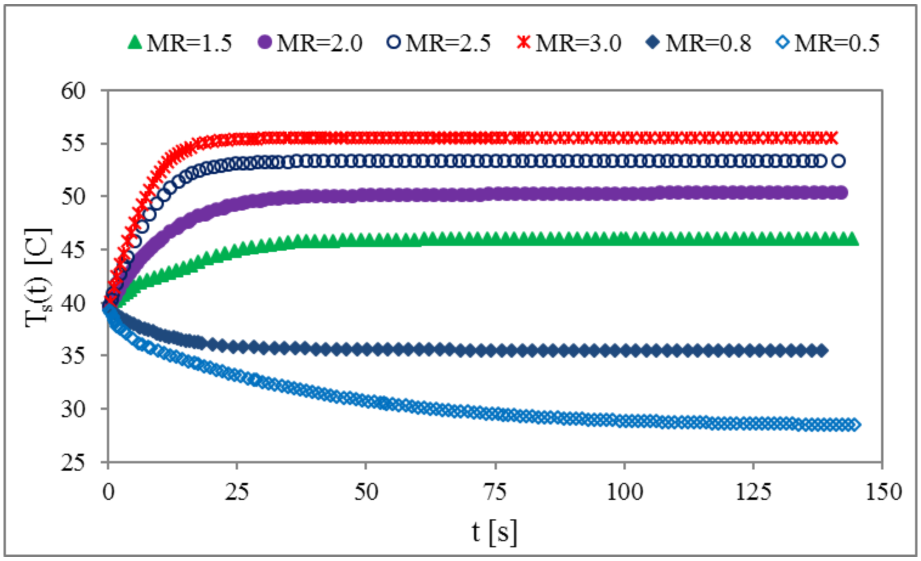

(b)

Figure 6.51: Transient effect of MR on (a) the hot fluid mean temperature and (b) the channel inner surface temperature

The mass-weighted average temperature of the hot fluid is computed as

$$\sum_{j=1}^{n}(T_{l,j}m_{l,j})\Big/\sum_{j=1}^{n}m_{l,j} \tag{6.5.2}$$

where, T_l denotes the temperature of the liquid (hot fluid) associated with a cell in the domain and m_l represents the mass of the liquid associated with the cell

The area-weighted average temperature of channel inner surface is computed as

$$\sum_{j=1}^{n}\left(T_{s,j}A_j\right)\Big/\sum_{j=1}^{n}A_j \tag{6.5.3}$$

where, T_s is the channel inner surface temperature associated with a cell in the domain and A is the facet (surface) area associated with the cell

6.5.1.5 Correlation for Transient Dimensionless Outlet Temperature of the Hot Fluid at Various MR

Figure 6.52 shows the variations of the dimensionless hot fluid temporal outlet temperature to the quasi-steady outlet temperature at various dimensionless time and hot fluid mass flow steps. It is shown in the figure that at transient region, hot fluid outlet temperatures are influenced by both the time and the mass flow rate. They approach asymptotic value of 1 in the quasi-steady state. The effect of mass flow step variations on transient response of temperatures is stronger at the beginning and becomes gradually weaker with decreasing gradient.

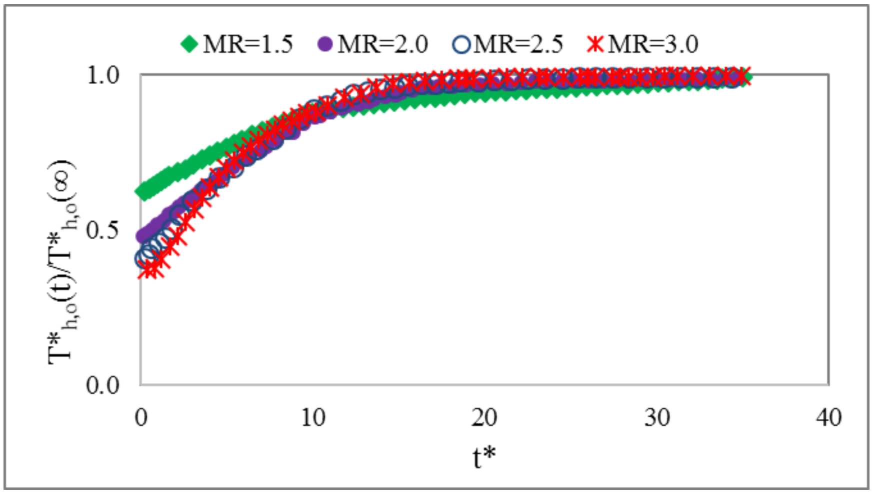

Figure 6.52: Transient responses of dimensionless outlet temperature of the hot fluid under MR

A general correlation for $T^*_{h,o}(t)$ in terms of $T^*_{h,o}(\infty)$ under various mass flow steps is developed. First, the correlation for $T^*_{h,o}(\infty)$ with regard to MR is obtained and presented in Figure 6.53.

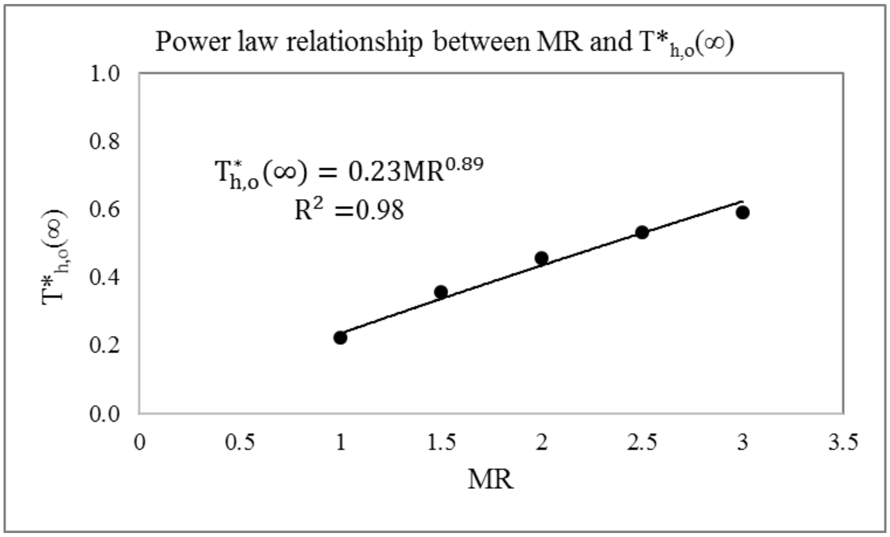

Figure 6.53: Relationship between $T^*_{h,o}(\infty)$ and MR

Expectedly, the $T^*_{h,o}(\infty)$ increases with the increase of MR. The variations follow a power relationship with positive exponent as

$$T^*_{h,o}(\infty) = 0.23\mathrm{MR}^{0.89} \tag{6.5.4}$$

Then, the correlation for each MR is obtained and presented in Figures 6.54 to 6.57.

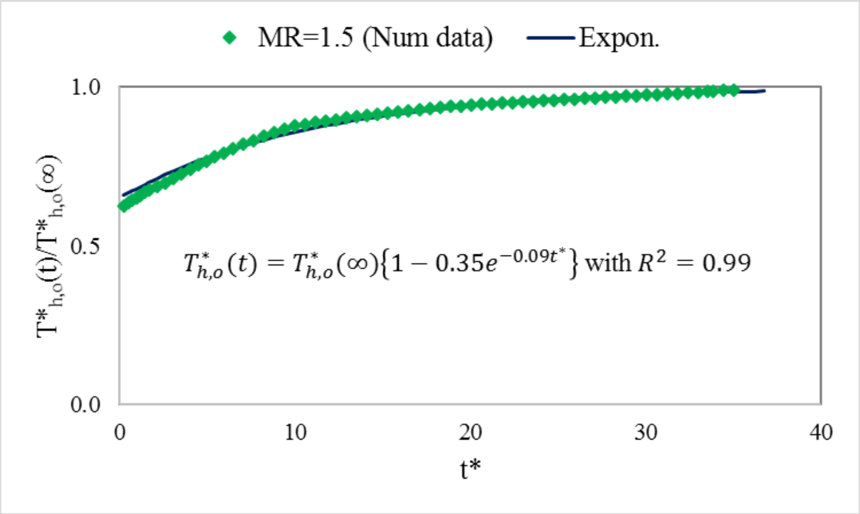

Figure 6.54: Correlation for dimensionless transient outlet temperature of hot fluid at MR=1.5

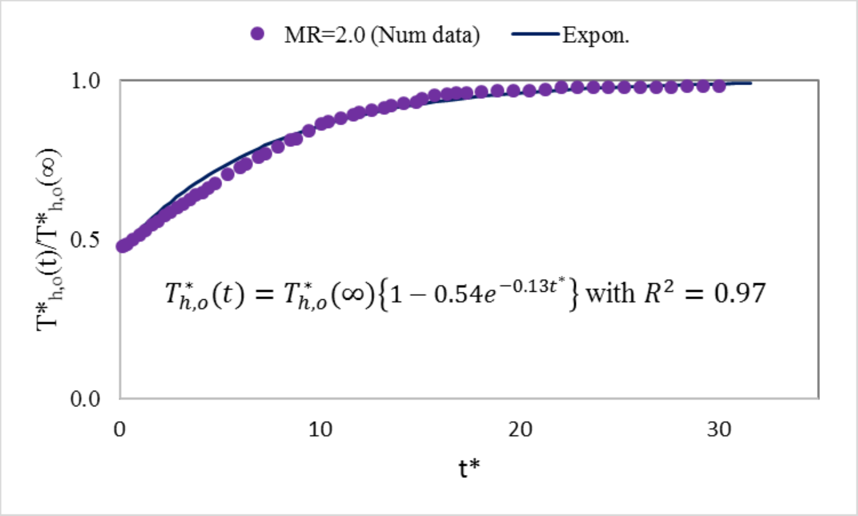

Figure 6.55: Correlation for dimensionless transient outlet temperature of hot fluid at MR=2.0

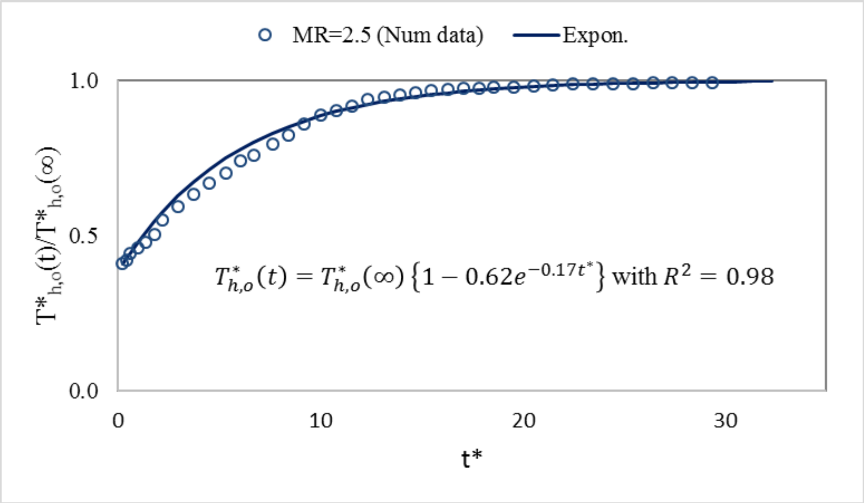

Figure 6.56: Correlation for dimensionless transient outlet temperature of hot fluid at MR=2.5

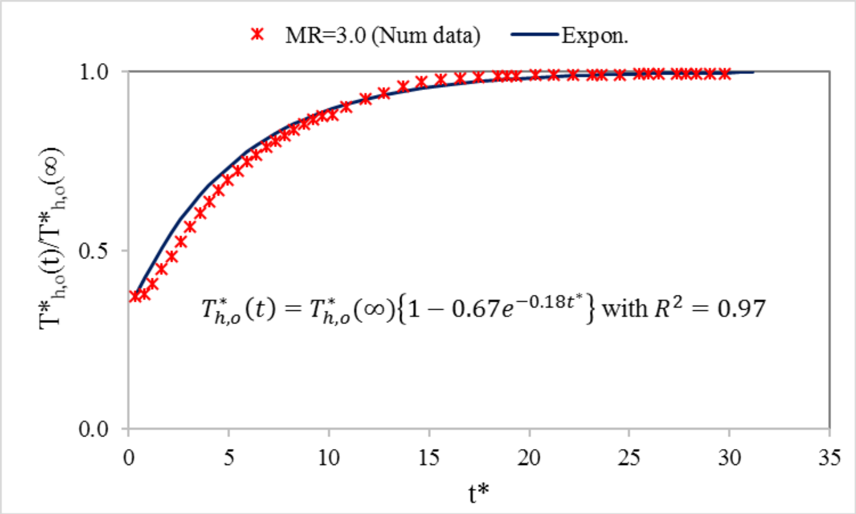

Figure 6.57: Correlation for dimensionless transient outlet temperature of hot fluid at MR=3.0

The correlations for the $\mathrm{T}^*_{\mathrm{h,o}}(\mathrm{t})$ with regard to $\mathrm{T}^*_{\mathrm{h,o}}(\infty)$ corresponding to each mass flow step change are presented below;

$$\mathrm{T}^*_{\mathrm{h,o}}(\mathrm{t}) = \mathrm{T}^*_{\mathrm{h,o}}(\infty)\{1 - 0.35\mathrm{e}^{-0.09\mathrm{t}^*}\} \text{ with } \mathrm{R}^2 = 0.99, \text{ for MR=1.5} \tag{6.5.5}$$

$$\mathrm{T}^*_{\mathrm{h,o}}(\mathrm{t}) = \mathrm{T}^*_{\mathrm{h,o}}(\infty)\{1 - 0.54\mathrm{e}^{-0.13\mathrm{t}^*}\} \text{ with } \mathrm{R}^2 = 0.97, \text{ for MR=2.0} \tag{6.5.6}$$

$$T^*_{h,o}(t) = T^*_{h,o}(\infty)\left\{1 - 0.62e^{-0.17t^*}\right\} \text{ with } R^2 = 0.98, \text{ for MR=2.5} \qquad (6.5.7)$$

$$T^*_{h,o}(t) = T^*_{h,o}(\infty)\left\{1 - 0.67e^{-0.18t^*}\right\} \text{ with } R^2 = 0.97, \text{ for MR=3.0} \qquad (6.5.8)$$

The above relations from (6.5.5) to (6.5.8) have been correlated to obtain a generalized correlation for the $T^*_{h,o}(t)$ as a function of $T^*_{h,o}(\infty)$, $t^*$and MR. These Equations can be expressed in the following generalized form;

$$T^*_{h,o}(t) = T^*_{h,o}(\infty)\left\{1 - C_1e^{-D_1t^*}\right\} \qquad (6.5.9)$$

where,

$T^*_{h,o}(\infty) = 0.23MR^{0.89}$, as shown before in Equation (6.5.4).

$$C_1 = 0.25MR^{0.93} \qquad (6.5.10)$$

$$D_1 = 0.06MR^{1.05} \qquad (6.5.11)$$

where, $T^*_{h,o}(\infty)$, C_1 and D_1 are dependent on the mass flow step variations. The regression analyses have been done with the purpose of obtaining C_1 and D_1, which are presented in Appendix C.

The developed generalized correlation (6.5.9) for transient dimensionless temperature of the hot fluid is compared with the numerical data for each mass flow step variations. This correlation fits all data in the transient schemes with maximum deviation of 10.39% as shown in Figure 6.58.

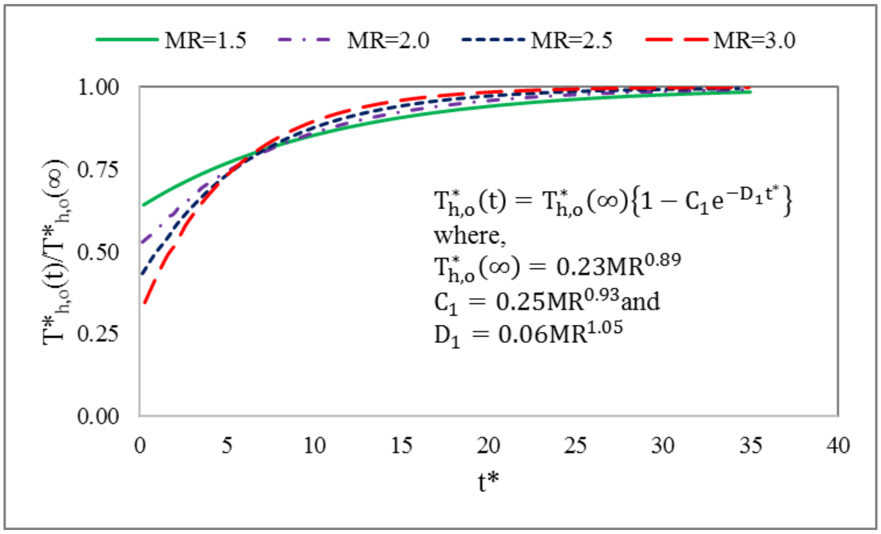

Figure 6.58: Correlation for dimensionless transient outlet temperature of the hot fluid under mass flow step changes

6.5.1.6 Transient Effect of MR on the Heat Transfer Rate

The transient effects of step change in hot fluid mass flow rate on the heat transfer rate are shown in Figures 6.59(a) and 6.59(b). The figures present the heat transfer rate for stepping up or fold-increase scenarios.

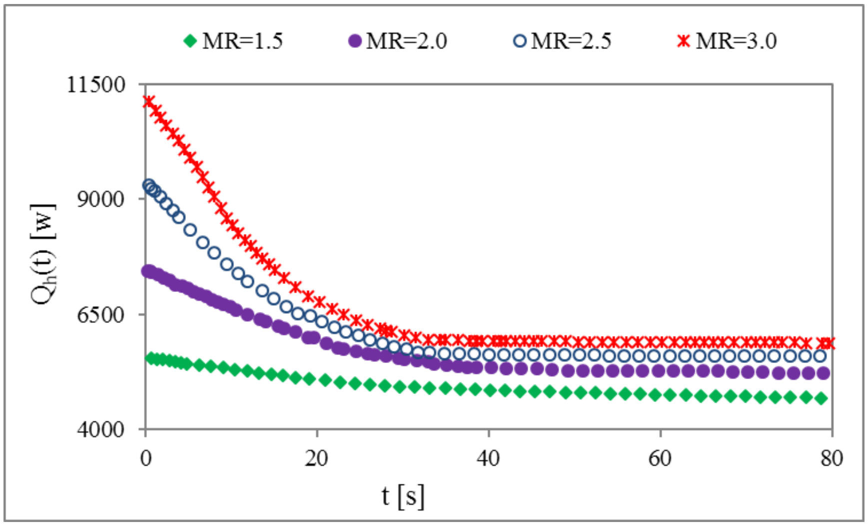

(a)

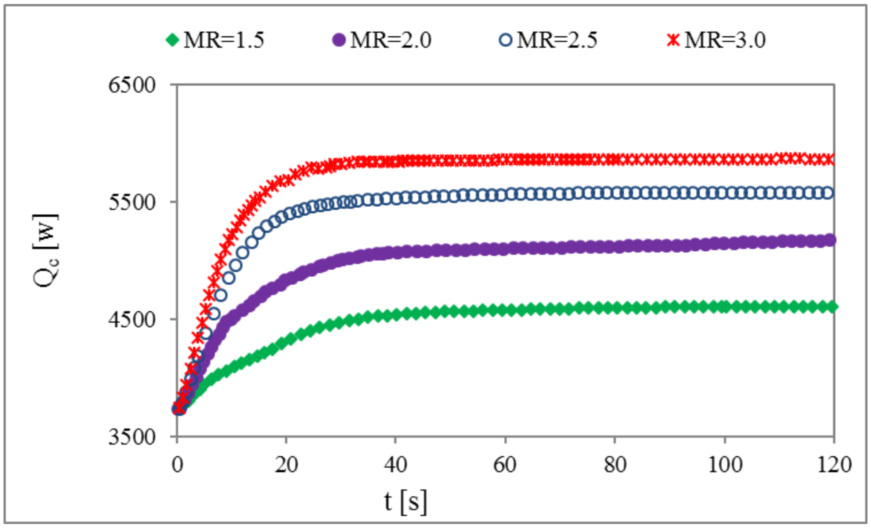

(b)

Figure 6.59: Transient effect of mass flow steps on heat transfer rate in (a) the hot fluid side and (b) the cold fluid side

As fold-increases, heat transfer rate in the hot fluid-side, as shown in Figure 6.59(a), starts from a higher magnitude. On the other hand, the start-up magnitude of heat transfer in cold fluid-side, as shown in Figure 6.59(b), is constant for all steps. This is because of the fact that the steps have been obtained in hot fluid mass flow rate from a reference steady state condition. It can be interpreted as cooling and heating modes in the heat transfer based fluid flow.

The heat transfer rate in the hot fluid drops down and cold fluid rises up from their start-up values until it reaches to the thermal equilibrium condition and becomes steady state. For both the hot fluid and the cold fluid, increasing mass flow steps results faster and higher heat transfer rate. For any particular step, the response time is larger for the hot fluid than the cold fluid. This is because of the fact that that the hot fluid residence time is greater than the cold fluid. Another reason is that the step change has been attained in the hot fluid-side.

6.5.1.7 Transient Effect of MR on the Heat Transfer Coefficient of Hot Fluid

The transient effects of hot fluid MR on hot fluid's heat transfer coefficient fluid is illustrated in Figures 6.60(a) and 6.60(b) below. The Figure 6.60(a) represents stepping up, while Figure 6.60(b) represents stepping down situations.

The transient response of the air-to-liquid crossflow heat exchanger has been considered for mass flow steps of 0.5, 0.8, 1.5, 2.0, 2.5 and 3.0. At the start-up, it is seen that the heat transfer coefficient of the hot fluid (h_h) for fold-increase (MR = 1.5, 2.0, 2.5 and 3.0) is higher than that of the original value. However, the h_h is lower than the original value for fold-decrease (MR = 0.08 and 0.05). This is because of the fact that the fluid mass flow rate dictates the Reynolds number, which strongly influences the heat transfer coefficient. It is well mentioned that the steps have been obtained from a steady state condition of the original MR of 1.

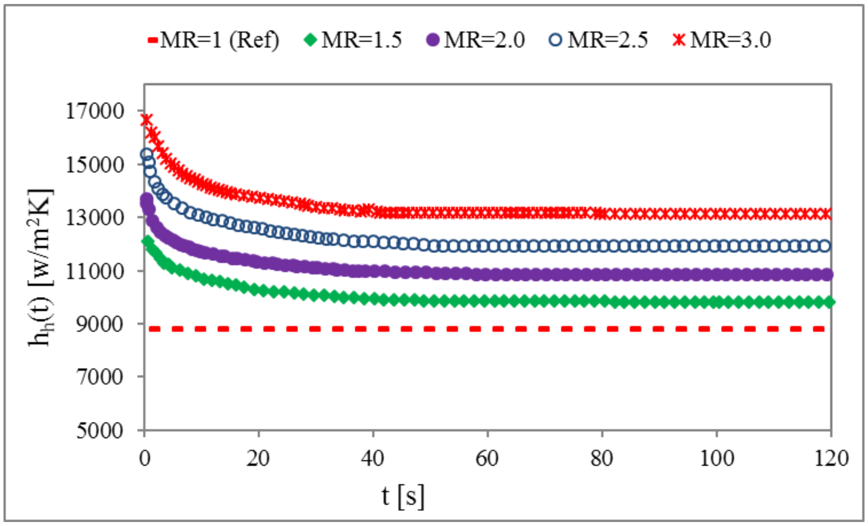

(a)

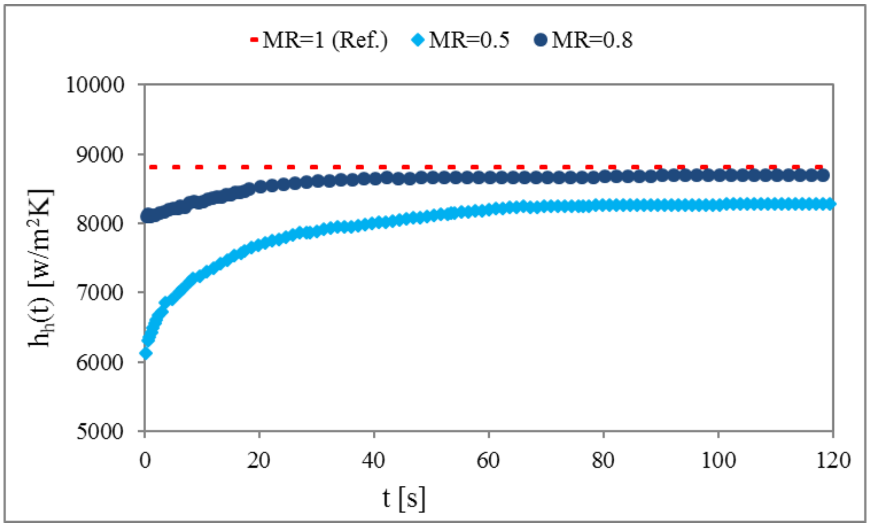

(b)

Figure 6.60: Transient heat transfer coefficient of hot fluid for (a) stepping up of MR and (b) stepping down of MR

The heat transfer coefficient gradually decreases with time for stepping up, becomes constant at the fully developed region and reaches a steady state. On the other hand, the heat transfer coefficient gradually increases with time for stepping down and becomes constant at steady state. The opposite trend of the heat transfer coefficient for stepping up and stepping down can be interpreted by the fact that the heat exchanger works in heating and cooling modes.

The heat transfer coefficient of hot fluid at quasi-steady state under perturbation of the hot fluid mass flow rate is illustrated in Figure 6.61(a). Increasing heat transfer coefficient is found with the increase of MR. This is because of the fact that the higher MR causes the higher temperature gradient between the wall surface and the fluid, which results in higher heat transfer coefficient.

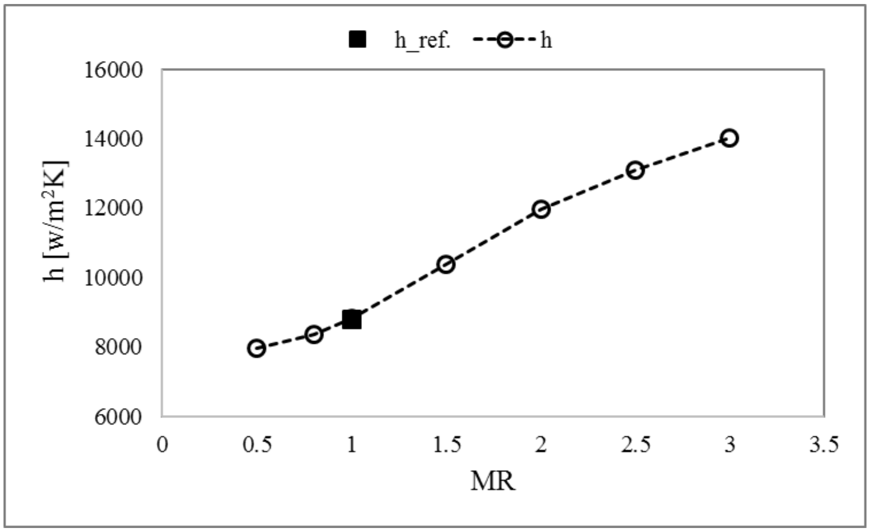

(a)

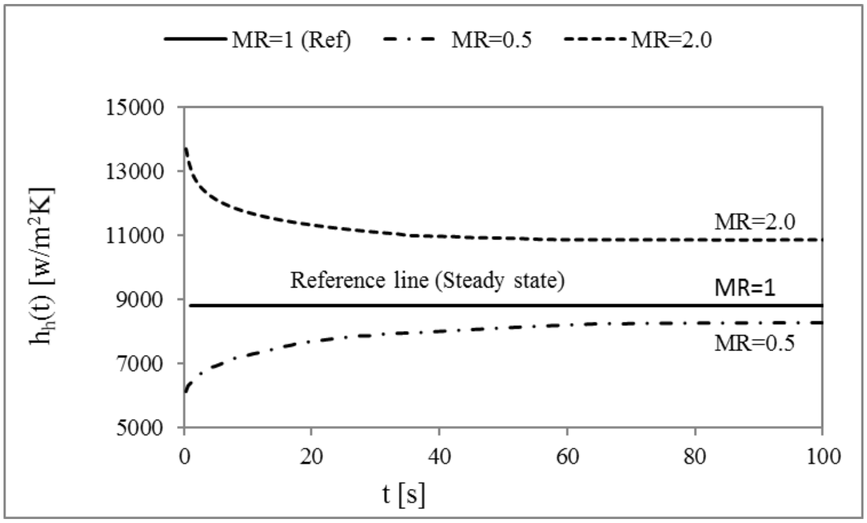

(b)

Figure 6.61: (a) Heat transfer coefficient of the hot fluid at steady state and (b) comparison of the $h_h(t)$ between a 2-fold increase and a half-fold decrease of MR

A relative heat transfer coefficient of hot fluid due a 2-fold increase and a half-fold decrease of MR is shown in Figure 6.61(b). Asymmetric h_h have been predicted for stepping up and stepping down situations. This can be compared with the effect of the heating mode over the cooling mode in heat transfer. This is because of the fact that the formation of thermal and hydrodynamic boundary layers in heat transfer based fluid flow is different due to affected fluid density and hence the Prandtl number [12].

6.5.1.8 Correlation for Transient Nu at Various Re under MR

Figure 6.62 illustrates the hot fluid transient Nusselt number, $\mathrm{Nu_h(t)}$ to quasi-steady Nusselt number, $\mathrm{Nu_h(\infty)}$ with dimensionless time,t^* and hot fluid MR. The figure shows that at transient state, the ratio of $\mathrm{Nu_h(t)}$ to $\mathrm{Nu_h(\infty)}$ is influenced by both the time and the mass flow rate. The value of $\mathrm{Nu_h(t)/Nu_h(\infty)}$ approaches to asymptotic value of 1 in the quasi-steady state. The effect of mass flow steps on transient responses of Nusselt number is initially stronger with higher gradient. The effect gradually reduces with smaller gradient and approaches to the quasi-steady state.

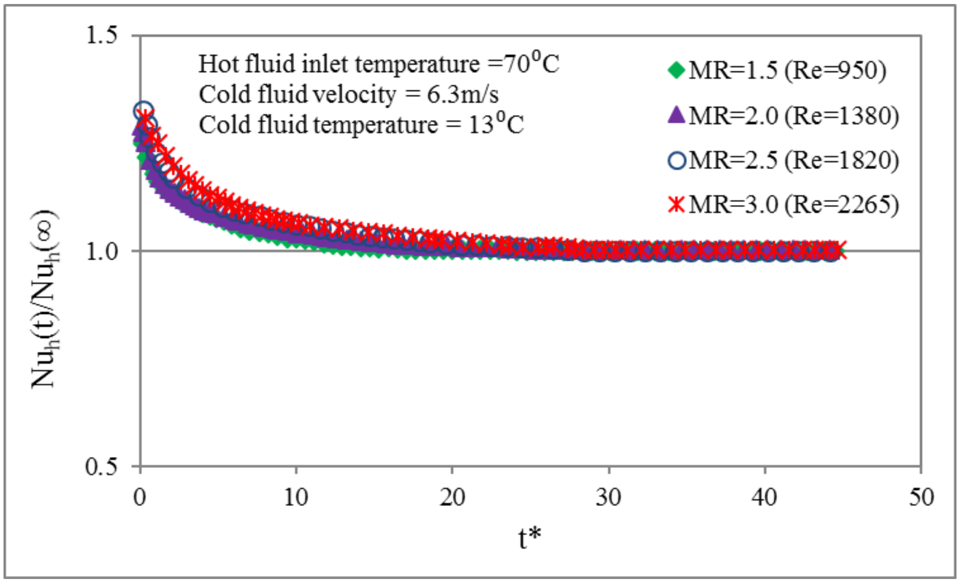

Figure 6.62: Transient Nusselt number at various Reynolds number

A general correlation for $\mathrm{Nu_h(t)}$ in terms of $\mathrm{Nu_h(\infty)}$ at mass flow step variations is developed. The correlation for $\mathrm{Nu}_h(\infty) - \mathrm{Re} - \mathrm{Pr}$ is obtained from the best curve fit as illustrated in Figure 6.63.

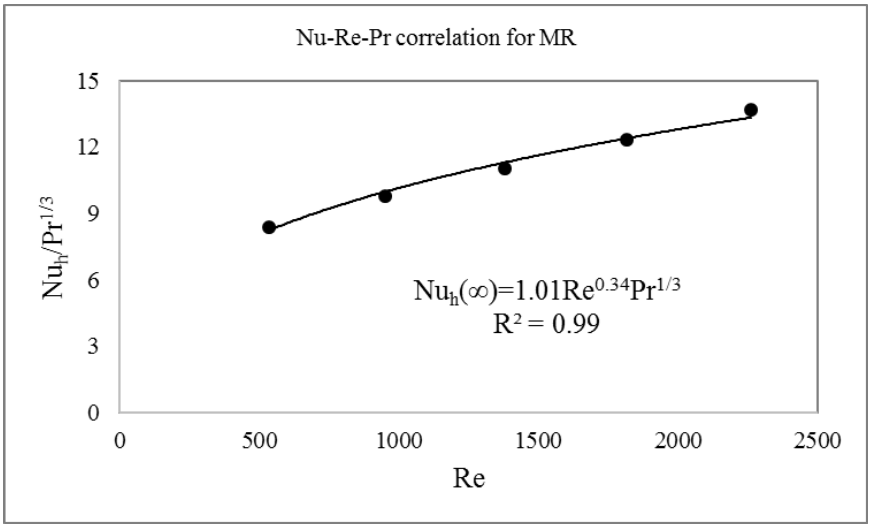

Figure 6.63: Nu-Re-Pr correlation for mass flow step variations

It is obvious from the figure that the $\mathrm{Nu_h}(\infty)$ increases with the increase of Re, which is subjected to MR. The variation of $\mathrm{Nu_h}(\infty)$ with regard to Re and Pr follows the power-law relationship with positive exponent as

$$\mathrm{Nu_h}(\infty) = 1.01\mathrm{Re}^{0.34}\mathrm{Pr}^{1/3} \tag{6.5.12}$$

Then, the correlation of $\mathrm{Nu_h}(\mathrm{t})$ for each MR is attained and presented in Figures 6.64 to 6.67.

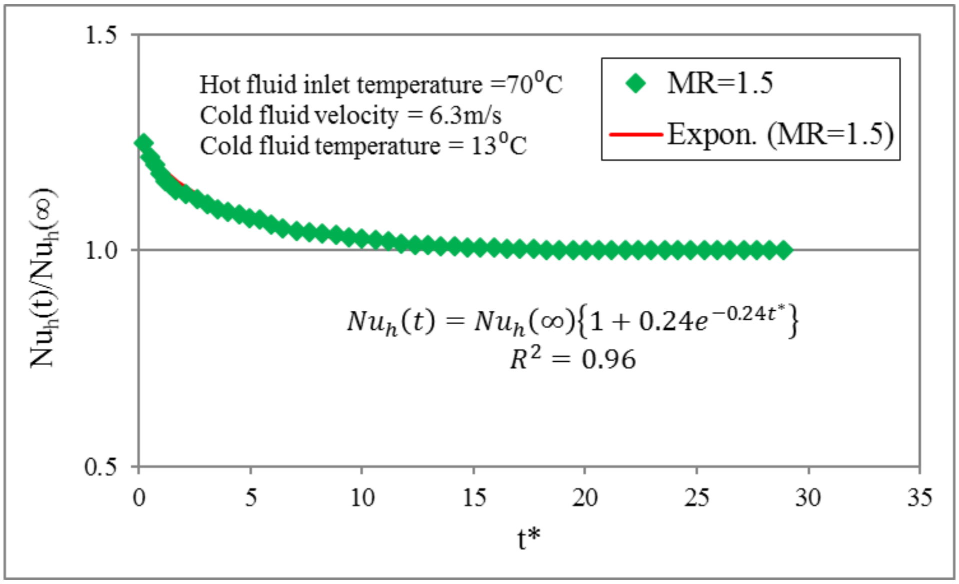

Figure 6.64: Correlation for transient Nusselt number at MR=1.5

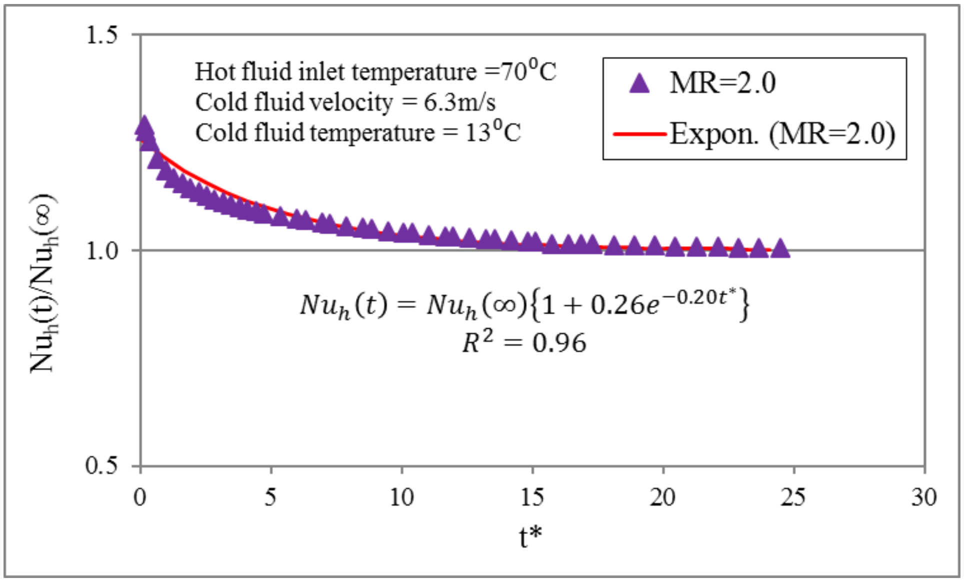

Figure 6.65: Correlation for transient Nusselt number at MR=2.0

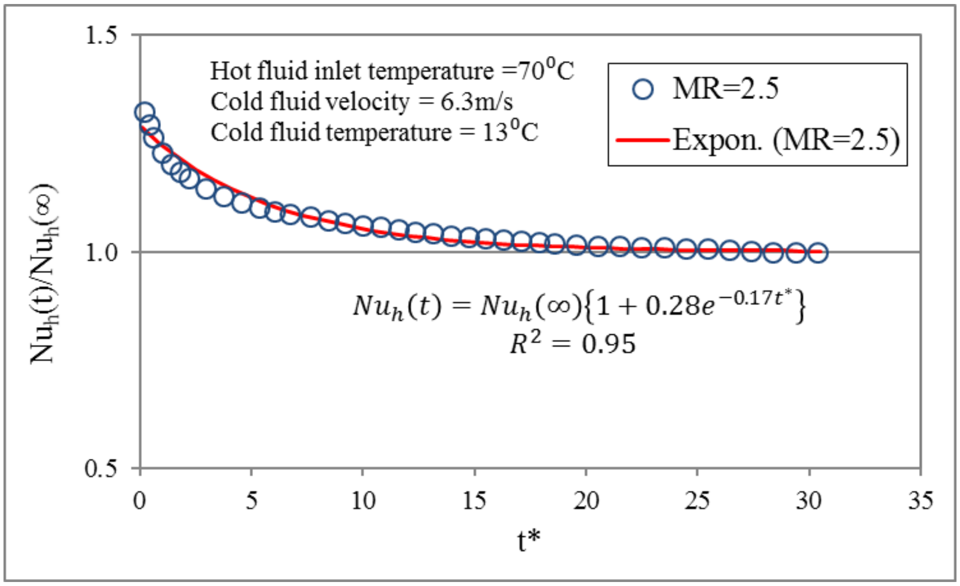

Figure 6.66: Correlation for transient Nusselt number at MR=2.5

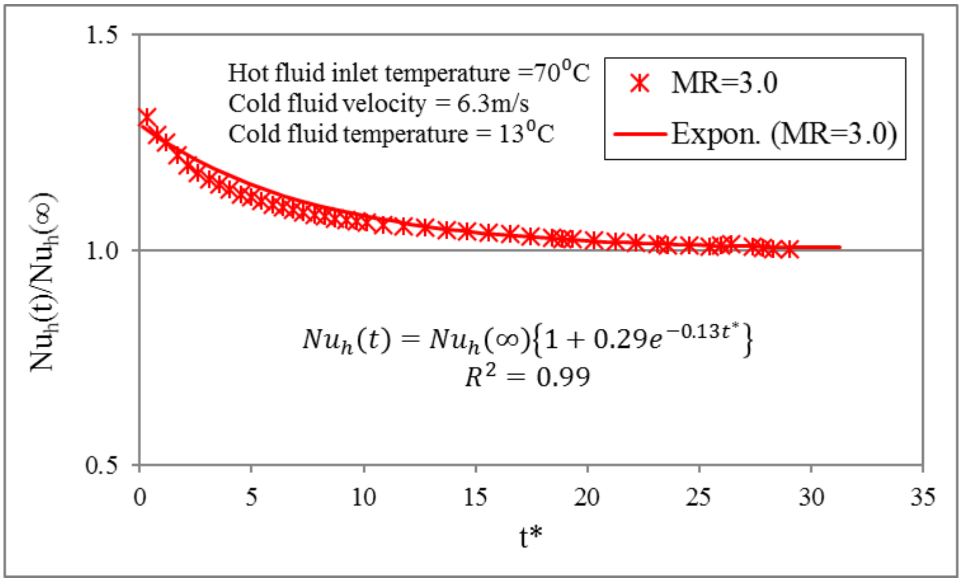

Figure 6.67: Correlation for transient Nusselt number at MR=3.0

The correlations for the $\mathrm{Nu_h(t)}$ in terms of $\mathrm{Nu_h(\infty)}$ and $\mathrm{t^*}$ corresponding to each mass flow step are stated below:

$$\mathrm{Nu_h(t)} = \mathrm{Nu_h(\infty)}\{1 + 0.24\mathrm{e}^{-0.24\mathrm{t}^*}\} \text{ with } \mathrm{R}^2 = 0.96, \text{ for } \mathrm{MR} = 1.5 \qquad (6.5.13)$$

$$\mathrm{Nu_h(t) = Nu_h(\infty)\{1 + 0.26e^{-0.20t^*}\}} \text{ with } \mathrm{R^2 = 0.96}, \text{ for } \mathrm{MR = 2.0} \qquad (6.5.14)$$

$$\mathrm{Nu_h(t) = Nu_h(\infty)\{1 + 0.28e^{-0.17t^*}\}} \text{ with } \mathrm{R^2 = 0.95}, \text{ for } \mathrm{MR = 2.5} \qquad (6.5.15)$$

$$\mathrm{Nu_h(t) = Nu_h(\infty)\{1 + 0.29e^{-0.13t^*}\}} \text{ with } \mathrm{R^2 = 0.99}, \text{ for } \mathrm{MR = 3.0} \qquad (6.5.16)$$

The above Equations from (6.5.13) to (6.5.16) have been correlated to develop a generalized correlation for the $\mathrm{Nu_h(t)}$as a function of $\mathrm{Nu_h(\infty)}$, $\mathrm{t^*}$ and MR. These can be illustrated in the following generalized form;

$$\mathrm{Nu_h(t) = Nu_h(\infty)\{1 + C_2e^{-D_2t^*}\}} \qquad (6.5.17)$$

where,

$\mathrm{Nu_h(\infty) = 1.01Re^{0.34}Pr^{1/3}}$, derived earlier, see Equation (6.5.12)

$$\mathrm{C_2 = 0.21MR^{0.28}} \qquad (6.5.18)$$

$$\mathrm{D_2 = -0.07MR + 0.35} \qquad (6.5.19)$$

The coefficient $\mathrm{C_2}$ and exponent $\mathrm{D_2}$, both depend on the mass flow steps. A regression analysis has been carried out with the aim of attaining $\mathrm{C_2}$ and $\mathrm{D_2}$; it is illustrated in Appendix C.

The developed correlation (6.5.17) for transient Nusselt number of the hot fluid is compared with the numerical data for each mass flow step. This generalized correlation fits all data in the transient schemes within 4.7% deviation as shown in Figure 6.68.

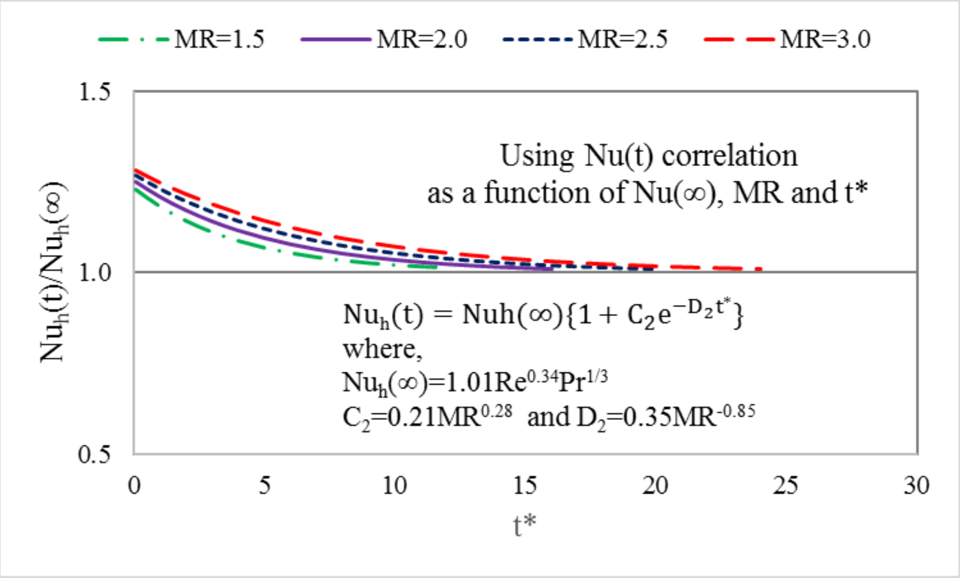

Figure 6.68: Correlation for transient Nusselt number of hot fluid under MR

6.5.2 Step Change in Hot Fluid Inlet Temperature (TR)

Step variations of hot fluid inlet temperatures are common in actual applications of heat exchangers. In the current study, the transient response of an air-to-water crossflow minichannel heat exchanger at certain changes in the hot water inlet temperature has been numerically obtained. Different steps in the hot fluid inlet temperature starting from an original value 22℃ to the subsequent steps of 1.5, 2.0, 2.5, 3.0 and 3.5 have been solved.

The hot fluid (water) inlet temperature of 70℃, cold fluid (air) inlet temperature of 13℃ and air velocity of 6m/s have been kept constant throughout all simulations of hot fluid mass flow steps. Numerical results are presented in this section.

6.5.2.1 Transient Response of Outlet Temperatures of Fluids under TR

The transient responses of water (hot fluid) and air (cold fluid) outlet temperatures due to TR are illustrated in Figures 6.69(a) and 6.69(b), respectively.

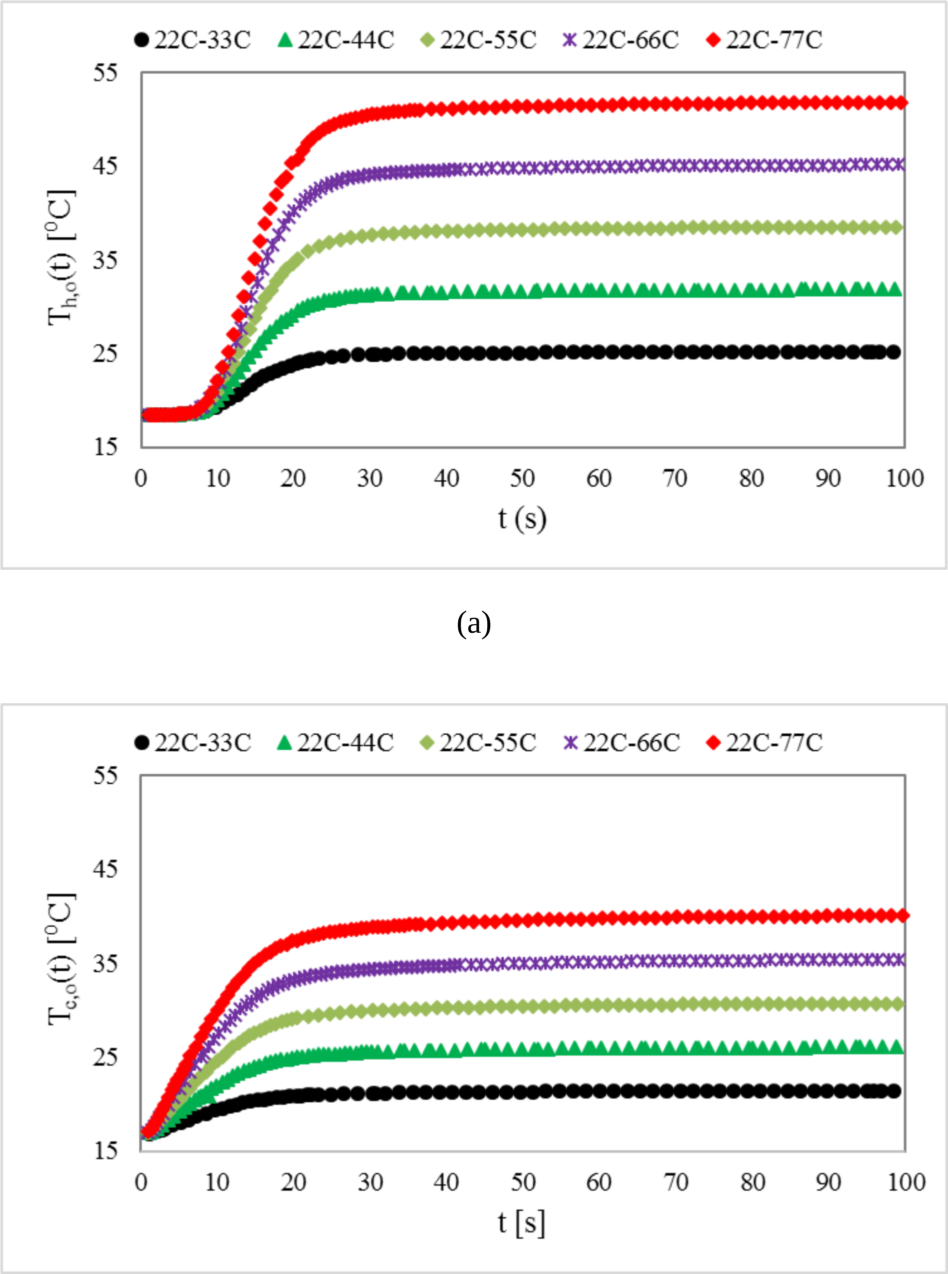

(a)

(b)

Figure 6.69: Transient response of (a) the $T_{h,o}$ and (b) the $T_{c,o}$ under TR

The hot fluid inlet temperature has been changed into 5 steps (TR), while other operating conditions of both fluids have been kept constant. It is found that both the hot fluid and the cold fluid outlet temperatures do not respond instantaneously with the step variations, TR due to the residence time of the fluids. This is because of the energy stored in the wall and the finite propagation time related to the inlet perturbations.

Figure 6.69(a) shows that there is an obvious delay time to initiate any change in the hot fluid outlet temperature. This is because, for a single mass flow rate of 0.06kg/s, the hot fluid (water) takes about 3s to go through the serpentine minichannels. On the other hand, Figure 6.69(b) displays invisible delay time for initiating any change in the cold fluid outlet temperature. This can be interpreted as the cold fluid (air) needs less than 0.02s only to pass over the MICHX core. In addition, the cold fluid nearby the hot fluid inlet comes to the contact of the hot fluid by means of solid walls and fins immediately after any step change.

It is clear from the figures that both the hot fluid and the cold fluid obtained higher transient outlet temperature with higher gradient for the higher step change. It is also observed that the response time decreases with the increase of hot fluid inlet temperature step, TR. The response time is the time required for the heat exchanger, when subjected to any step change, to reach the fluid outlet temperature from one steady state to another steady state.

The faster responses of the MICHX for higher temperature step (TR) can be interpreted as the higher heat transfer coefficient of fluid with the higher temperature steps. The higher temperature steps provides higher Reynolds number, as shown in Figure 6.70. The higher Re leads the higher heat transfer coefficient of fluid.

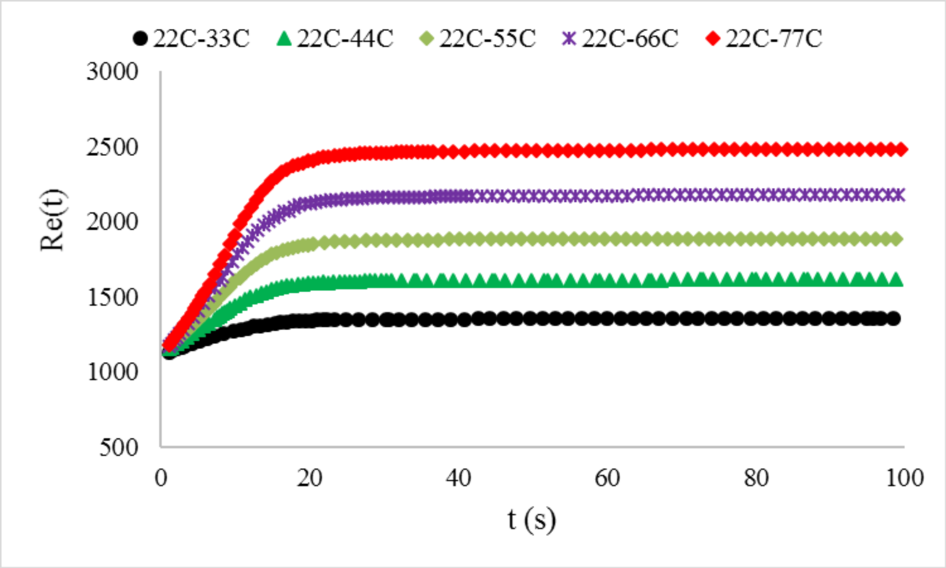

Figure 6.70: Effect of temperature steps (TR) on hot fluid Reynolds number

6.5.2.2 Correlation for $T^*_{h,o}(t)$ of Hot Fluid under TR

The transient response of dimensionless hot fluid outlet temperature for perturbation of same fluid inlet temperature is illustrated in Figure 6.71.

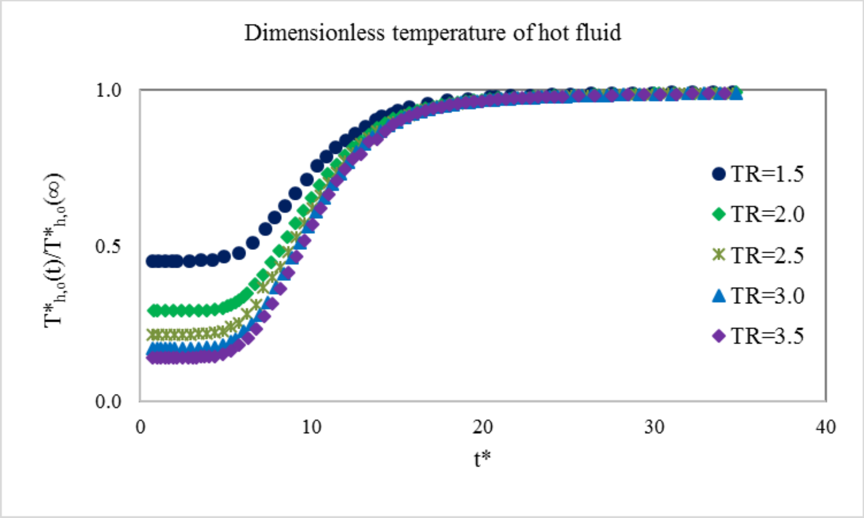

Figure 6.71: Transient effect of TR on the dimensionless hot fluid outlet temperature

The transient (t) and steady state (∞) dimensionless temperature of hot fluid have been defined as $T^*_{h,o}(t) = \frac{T_{h,o}(t) - T_{c,i}}{T_{h,i} - T_{c,i}}$ and $T^*_{h,o}(\infty) = \frac{T_{h,o}(\infty) - T_{c,i}}{T_{h,i} - T_{c,i}}$, respectively. For all the TR, the figure shows that the ratio $T^*_{h,o}(t)$ to $T^*_{h,o}(\infty)$ exponentially increases with time, but decreases with temperature steps. It is obvious from the figure that there are two distinct trends of variations in the transient dimensionless temperature of hot fluid. The ratio $T^*_{h,o}(t)$ to $T^*_{h,o}(\infty)$ increases very slowly for nearly $t^* \leq 5$. This is because of the propagation time of hot fluid inlet temperature steps. On the other hand, the ratio of $T^*_{h,o}(t)$ to $T^*_{h,o}(\infty)$ increases exponentially with a higher gradient for about $t^* > 5$ and gradually approaches to the quasi-steady state, which is $\frac{T^*_{h,o}(t)}{T^*_{h,o}(\infty)} \simeq 1$. This is because of the fact that each step starts from a lower steady state temperature and steps up to a higher temperature in the inlet of the hot fluid. After end of propagation time, the fluid outlet temperature initially increases rapidly in the beginning. Then, as the temperature difference between the hot fluid and the cold fluid gradually decreases, subsequently, the $T^*_{h,o}(t)$ to $T^*_{h,o}(\infty)$ ratio decreases. The values of $\frac{T^*_{h,o}(t)}{T^*_{h,o}(\infty)}$ for all steps become approximately equal to 1.

With the aim of obtaining a general correlation for the transient dimensionless temperature of the hot fluid, first, the correlation for $T^*_{h,o}(\infty)$ in connection with TR is developed from the best curve fit as shown in Figure 6.72.

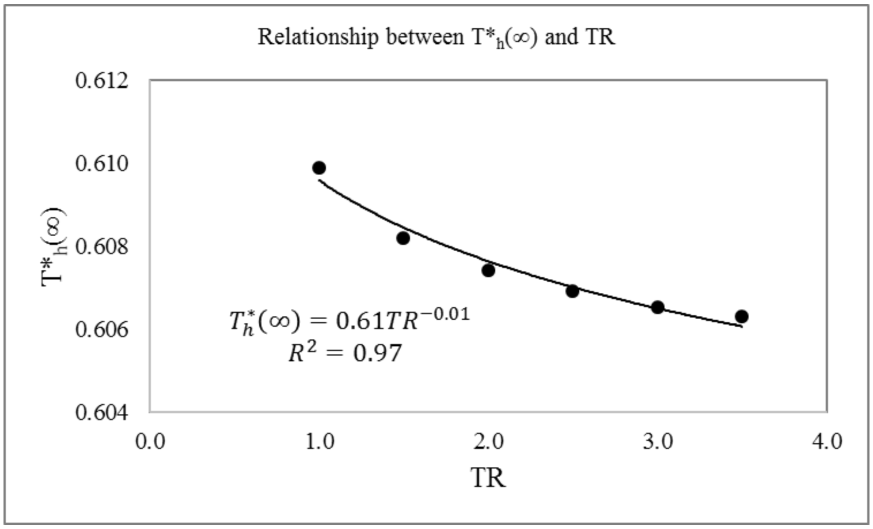

Figure 6.72: Correlation for $T^*_{h,o}$ (∞) with regard to TR

The Figure 6.72 shows that the $T^*_{h,o}(\infty)$ decreases with the increase of TR. The trend follows a power relationship with negative exponent as expected. The relationship of $T^*_{h,o}$ (∞) with TR is shown in Equation (6.5.20) as

$$T^*_{h,o}(\infty) = 0.61\mathrm{TR}^{-0.01} \tag{6.5.20}$$

Then, the Figure 6.71 is divided into two parts for better illustration and understanding. These are shown in Figures 6.73(a) and 6.73(b).

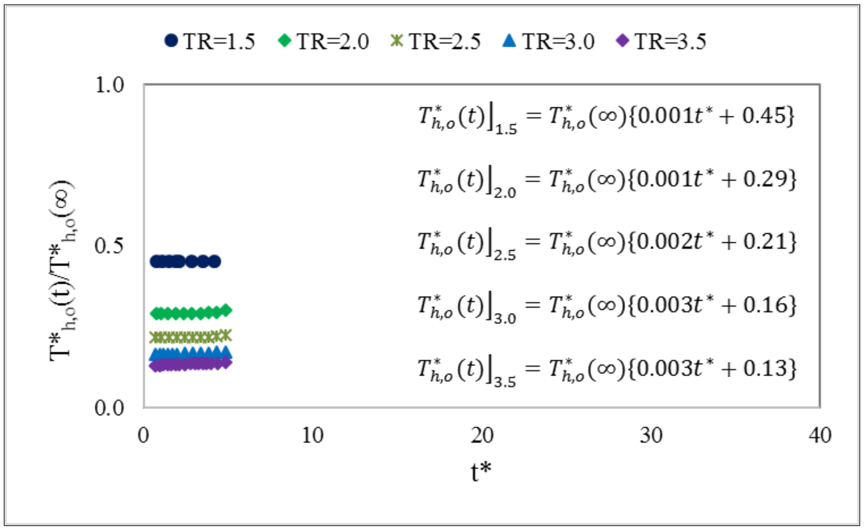

(a)

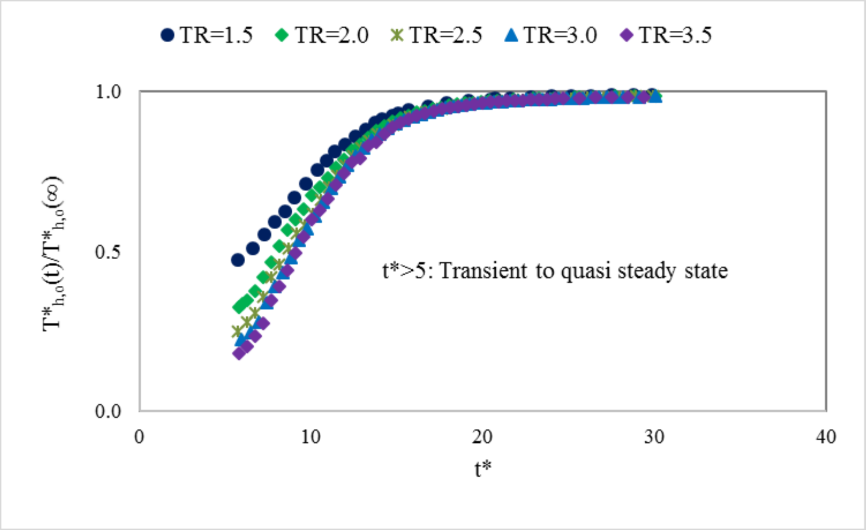

(b)

Figure 6.73: Transient effect of TR on the dimensionless hot fluid outlet temperature for (a) t*≤5 and (b) t*>5

There is a little deviation in the t* values from 5, where linear trends of the curves changes to exponential patterns in the t* versus $\frac{T^*_{h,o}(t)}{T^*_{h,o}(\infty)}$ plots. The average rounding value 5 is chosen to avoid the complexity of developing one general correlation of $T^*_{h,o}(t)$. One correlation is developed for $t^* \leq 5$ from the best data fit in Figure 6.73(a). Another correlation is obtained for $t^* > 5$ from the best curve fit as presented in the Figure 6.73(b). In order to develop general correlations for each section, the individual best curve fit equations, with R^2-values ranging from 0.96 to 1, have been produced for each temperature step. The correlation of each transient temperature for $t^* \leq 5$ is obtained from the best curve fit as shown in Figure 6.73(a). These are illustrated below:

$$\text{For TR} = 1.5: \qquad T^*_{h,o}(t) = T^*_{h,o}(\infty)\,\{0.001t^* + 0.45\} \tag{6.5.21}$$

$$\text{For TR} = 2.0: \qquad T^*_{h,o}(t) = T^*_{h,o}(\infty)\,\{0.001t^* + 0.29\} \tag{6.5.22}$$

For TR = 2.5: $T_{h,o}^{*}(t) = T_{h,o}^{*}(\infty)\{0.002t^{*} + 0.21\}$ (6.5.23)

For TR = 3.0: $T_{h,o}^{*}(t) = T_{h,o}^{*}(\infty)\{0.003t^{*} + 0.16\}$ (6.5.24)

For TR = 3.5: $T_{h,o}^{*}(t) = T_{h,o}^{*}(\infty)\{0.003t^{*} + 0.13\}$ (6.5.25)

The Equations from 6.5.21 to 6.5.25 have been correlated in order to develop a generalized correlation for the $T_{h,o}^{*}(t)$ as a function of $T_{h,o}^{*}(\infty)$, t^{*} and TR. The generalized correlation of $T_{h,o}^{*}(t)$ for $t^{*} \leq 5$ is presented below:

$$T_{h,o}^{*}(t) = T_{h,o}^{*}(\infty)\{C_3 t^{*} + D_3\} \tag{6.5.26}$$

where,

$$C_3 = 0.002 \tag{6.5.27}$$

$$D_3 = 0.81\mathrm{TR}^{-1.47} \tag{6.5.28}$$

Since the magnitudes of coefficient C_3 in each of the equations from 6.5.21 to 6.5.25 are very small, an average of all coefficients is considered for C_3 in Equation 6.5.26. However, the values of D_3 is strongly dependent on the TR. The value of D_3 decreases with the increase of TR and follows the power law relationship. The analysis for calculating C_3 and D_3 have been carried out and appended in Appendix C.

The correlation of each temperature for $t^{*} > 5$ is obtained from the best data fit in Figure 6.73(b). Individual steps are presented in Figures 6.74 to 6.78.

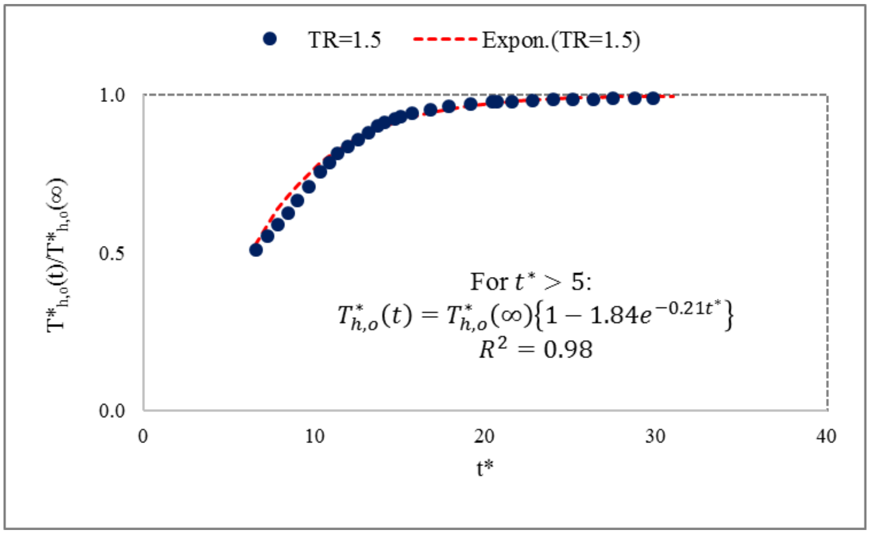

Figure 6.74: Correlation for dimensionless transient outlet temperature of hot fluid under TR=1.5, for t*>5

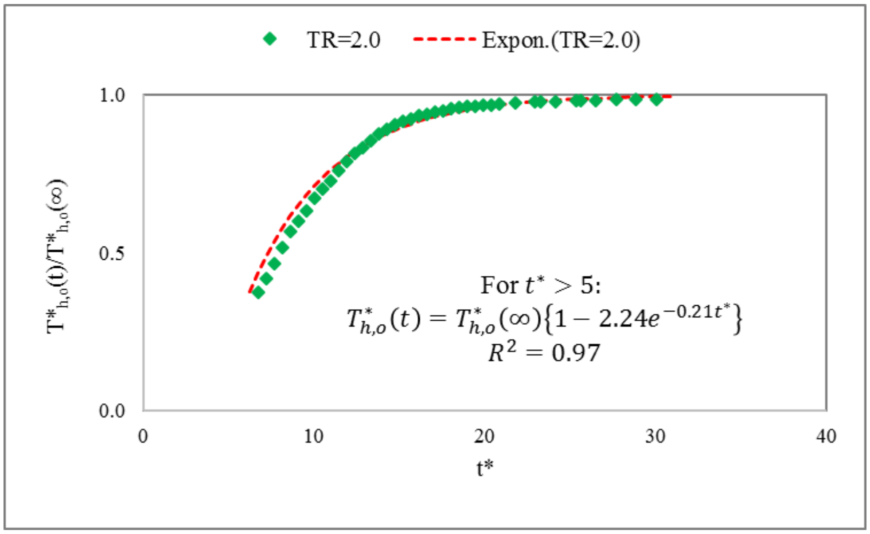

Figure 6.75: Correlation for dimensionless transient outlet temperature of hot fluid under TR=2.0, for t*>5

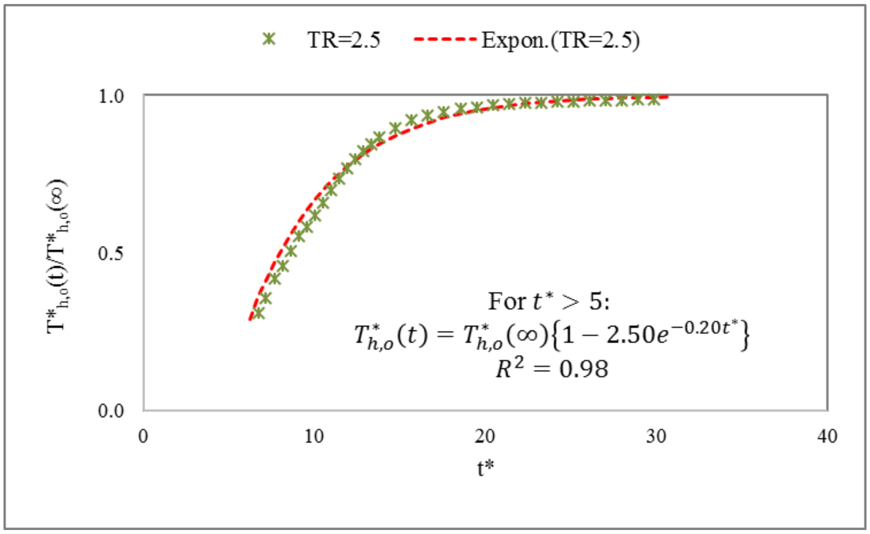

Figure 6.76: Correlation for dimensionless transient outlet temperature of hot fluid under TR=2.5, for t*>5

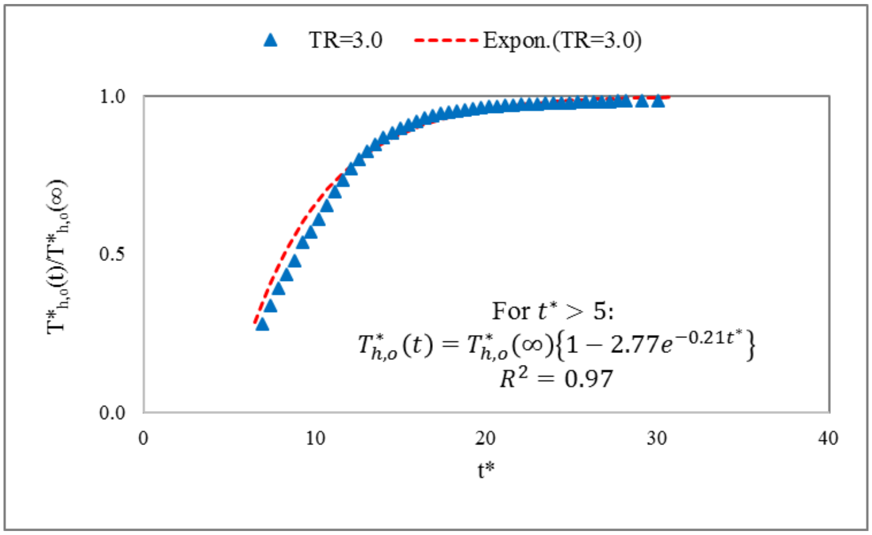

Figure 6.77: Correlation for dimensionless transient outlet temperature of hot fluid under TR=3.0, for t*>5

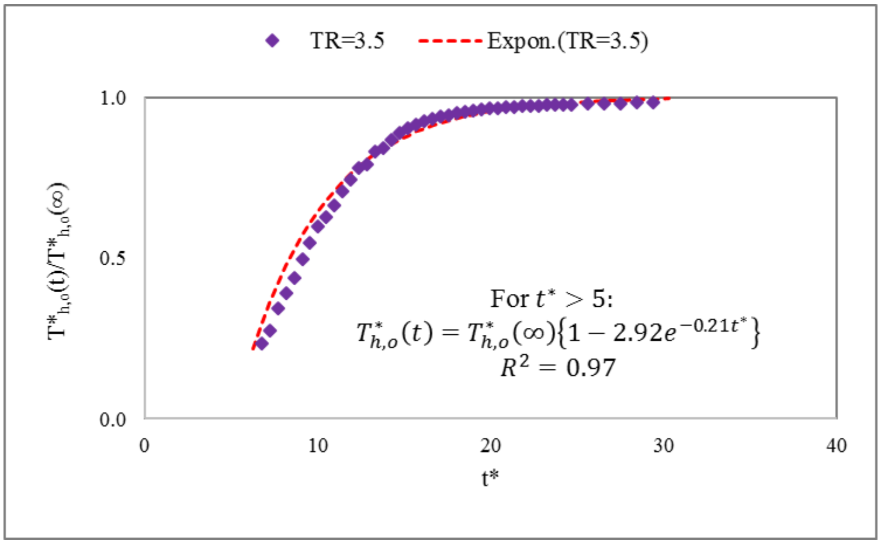

Figure 6.78: Correlation for dimensionless transient outlet temperature of hot fluid under TR=3.5, for t*>5

The correlation for each transient temperature for $t^* > 5$ is obtained from the best curve fit as illustrated in Figures 6.74 to 6.78 and illustrated below:

$$\text{For TR} = 1.5: \quad T^*_{h,o}(t) = T^*_{h,o}(\infty)\{1 - 1.84e^{-0.21t^*}\} \text{ with } R^2 = 0.98 \qquad (6.5.29)$$

$$\text{For TR} = 2.0: \quad T^*_{h,o}(t) = T^*_{h,o}(\infty)\{1 - 2.24e^{-0.21t^*}\} \text{ with } R^2 = 0.97 \qquad (6.5.30)$$

$$\text{For TR} = 2.5: \quad T^*_{h,o}(t) = T^*_{h,o}(\infty)\{1 - 2.50e^{-0.20t^*}\} \text{ with } R^2 = 0.98 \qquad (6.5.31)$$

$$\text{For TR} = 3.0: \quad T^*_{h,o}(t) = T^*_{h,o}(\infty)\{1 - 2.77e^{-0.21t^*}\} \text{ with } R^2 = 0.97 \qquad (6.5.32)$$

$$\text{For TR} = 3.5: \quad T^*_{h,o}(t) = T^*_{h,o}(\infty)\{1 - 2.92e^{-0.21t^*}\} \text{ with } R^2 = 0.97 \qquad (6.5.33)$$

The Equations from 6.5.29 to 6.5.33 have been solved to develop a generalized correlation for the $T^*_{h,o}(t)$ as a function of $T^*_{h,o}(\infty)$, t^* and TR for t*>5. The generalized correlation of $T^*_{h,o}(t)$ for $t^* > 5$ is obtained and illustrated below:

$$\mathrm{T}^{*}_{\mathrm{h,o}}(\mathrm{t}) \;= \mathrm{T}^{*}_{\mathrm{h,o}}(\infty)\left\{1 - \mathrm{C}_4 \mathrm{e}^{-\mathrm{D}_4 \mathrm{t}^{*}}\right\} \tag{6.5.34}$$

where,

$$\mathrm{C}_4 = 1.50\mathrm{TR}^{0.55} \tag{6.5.35}$$

$$\mathrm{D}_4 = 0.21 \tag{6.5.36}$$

The coefficient C_4 is strongly dependent on temperature steps and follows the power law relationship. Whereas, the value of exponent D_4 is approximately a constant. The analysis of evaluating C_4 and D_4 have been performed and included in Appendix C.

The new correlations for transient Nusselt number are summarized and illustrated in Figures 6.79 to 6.81.

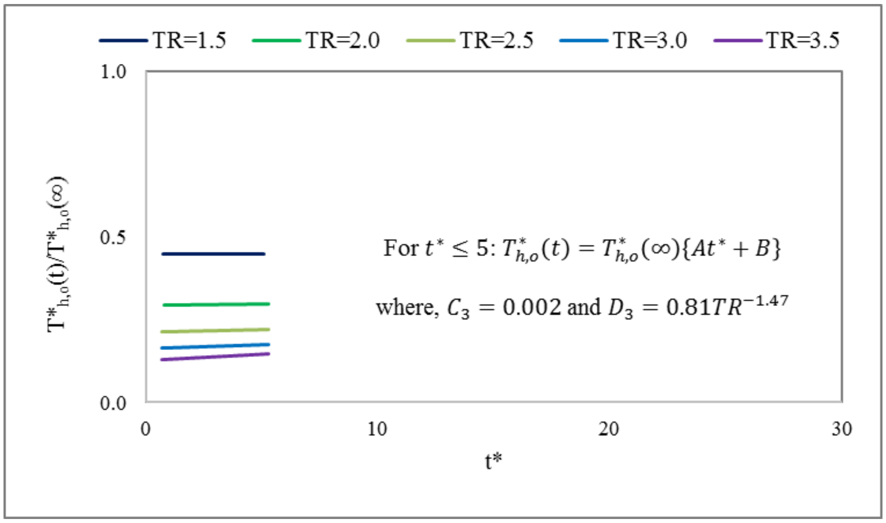

Figure 6.79: The correlation for dimensionless transient outlet temperature of hot fluid under temperature steps for t*≤5

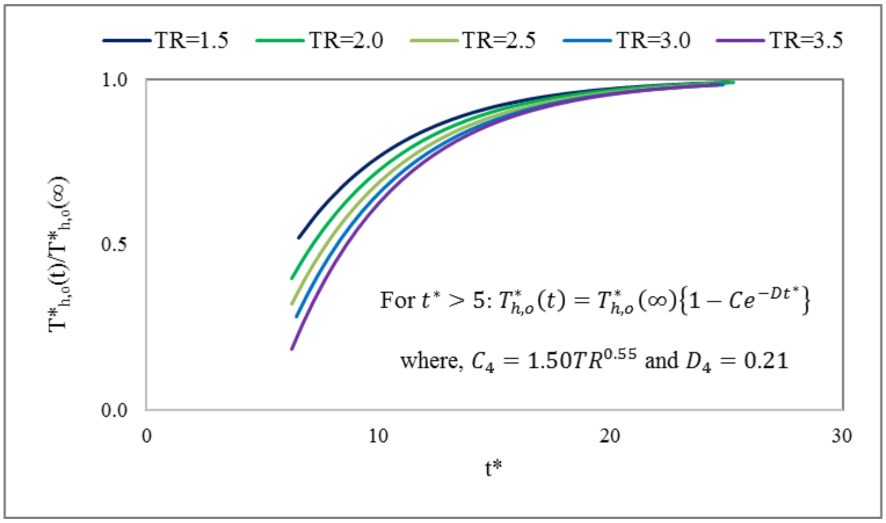

Figure 6.80: The correlation for dimensionless transient outlet temperature of hot fluid under temperature steps for t*>5

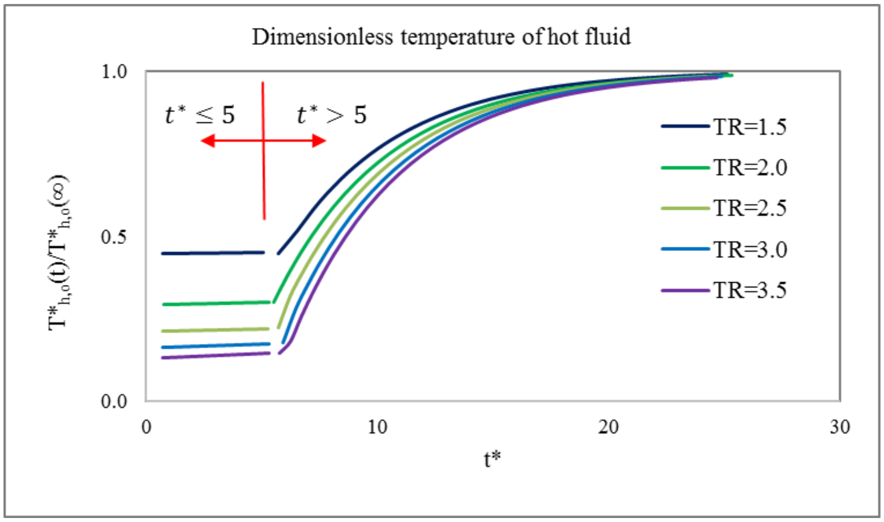

Figure 6.81: The correlation of transient Nusselt number for step change in hot fluid inlet temperature

6.5.2.3 Transient Effect of TR on the Heat Transfer Coefficient of Hot Fluid

The transient heat transfer coefficient of the hot fluid, $h_h(t)$ for perturbation of the hot fluid inlet temperature, TR is illustrated in Figure 6.82.

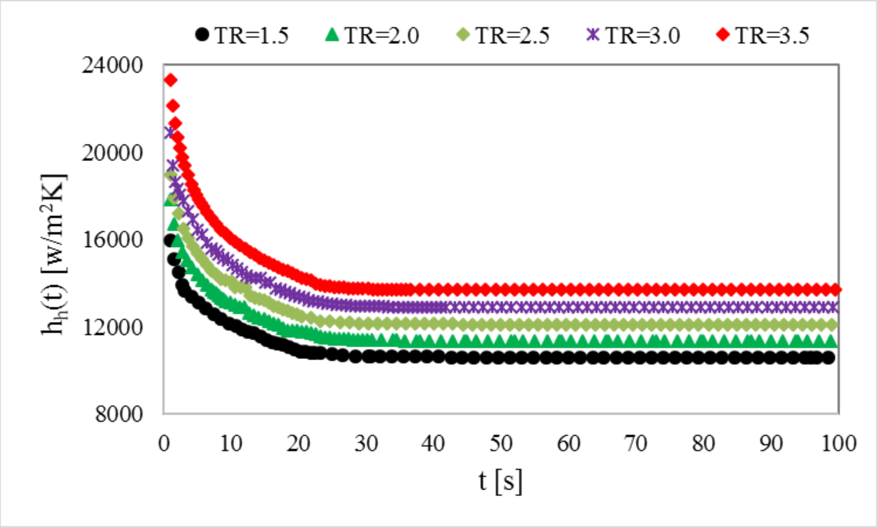

Figure 6. 82: The transient heat transfer coefficient of the hot fluid for temperature steps

Transient response of the air-to-liquid crossflow MICHX is obtained for the hot fluid inlet temperature steps of 1.5, 2.0, 2.5, 3.0 and 3.5. It is obvious from Figure 6.82 that heat transfer coefficient of hot fluid (h_h) is maximum at the starting of each temperature step. This is because of the minimum thermal boundary layer thickness of the hot fluid at the beginning. Then h_h starts decreasing with time and gradually becomes constant when the fluid reaches to the steady state. At smaller time values, the temperature gradients between the channel surface and fluid is high, the heat transfer coefficient is, therefore, higher than that of the steady state.

It is also seen that the heat transfer coefficient of the hot fluid is higher for higher temperature step. This is due to the fact that the higher temperature builds higher Reynolds number, which dominates the heat transfer coefficient. The average h_h of each TR is quantified for the transient situation and presented in Figure 6.83.

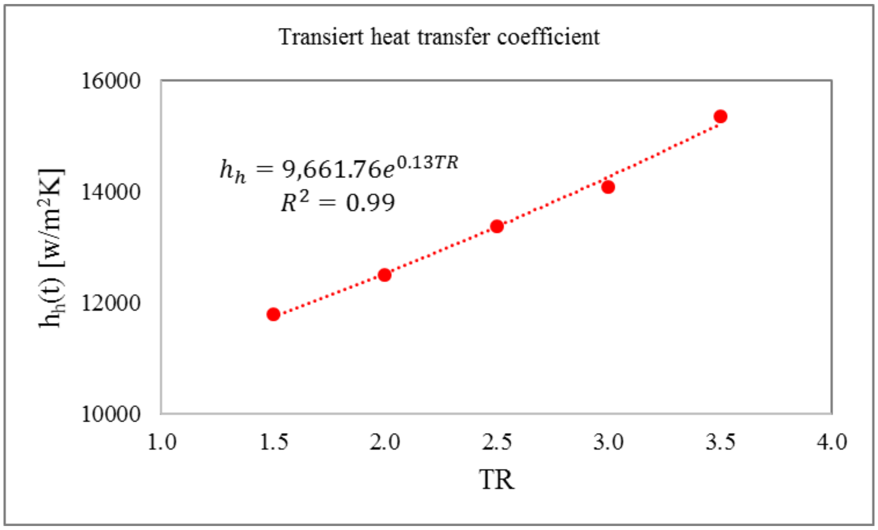

Figure 6.83: The heat transfer coefficient of the hot fluid at steady state under TR

A correlation for average $\mathrm{h_h}$ with temperature step is presented below;

$$\mathrm{h_h} = 9661.76\mathrm{e}^{0.13\mathrm{TR}} \tag{6.5.37}$$

The heat transfer coefficient of hot fluid exponentially increases with the increase of the temperature step.

6.5.2.4 Correlation for Transient Nusselt Number under TR

Figure 6.84 illustrations the hot fluid $\mathrm{Nu_h(t)}$ to $\mathrm{Nu_h(\infty)}$ with t^* and TR. The figure shows that at transient state, both the time and the temperature step effect the $\mathrm{Nu_h(t)}$. The value of $\mathrm{Nu_h(t)/Nu_h(\infty)}$ reaches an asymptotic value of 1 in the quasi-steady state. At the beginning, the effect of temperature steps on transient responses of Nusselt number is stronger with the higher gradient. The effect gradually reduces with smaller gradient and becomes steady state.

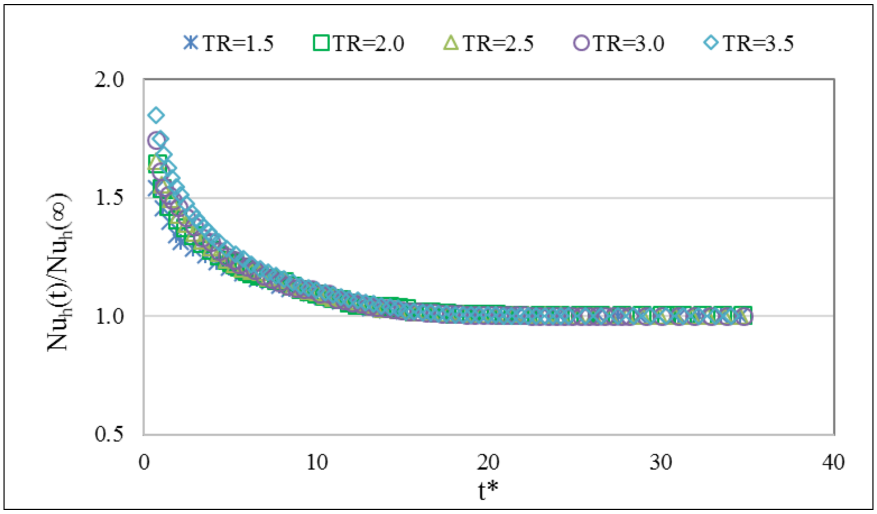

Figure 6.84: Transient Nusselt number at various temperature steps (TR)

A general correlation for $\mathrm{Nu_h(t)}$ in terms of $\mathrm{Nu_h(\infty)}$ for step changes in the hot fluid inlet temperature is obtained. The correlation for $\mathrm{Nu}_h(\infty) - \mathrm{Re} - \mathrm{Pr}$ is developed from the best curve fit as shown in Figure 6.85.

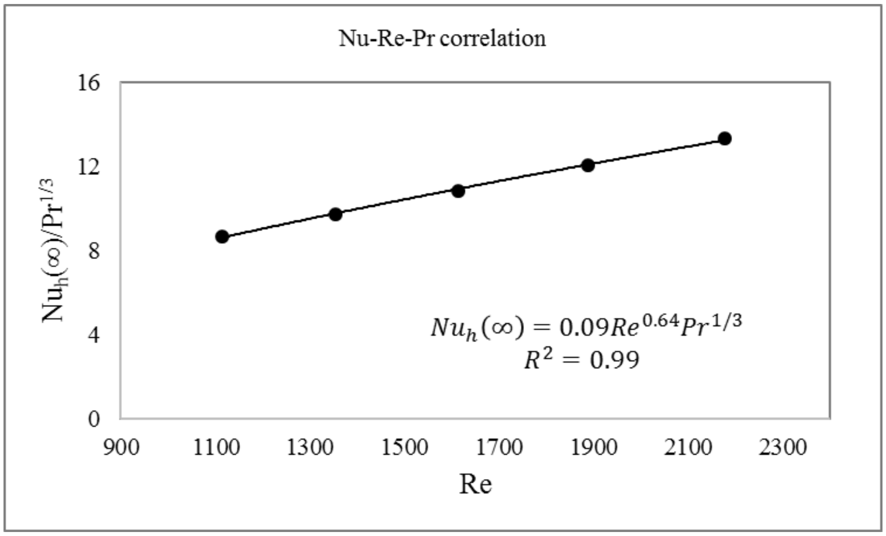

Figure 6.85: Nu-Re-Pr correlation for step changes in hot fluid inlet temperature

The figure shows that the $\mathrm{Nu_h}(\infty)$ increases with the increase of Re, which is a function of fluid inlet temperature. The variation of $\mathrm{Nu_h}(\infty)$ relating to Re and Pr follows the power-law relationship with positive exponent as

$\mathrm{Nu_h}(\infty) = 0.09\mathrm{Re}^{0.64}\mathrm{Pr}^{1/3}$ (6.5.38)The correlation of $\mathrm{Nu_h}(\mathrm{t})$ for each TR is obtained from the best curve fit as illustrated in Figures 6.86 to 6.90.

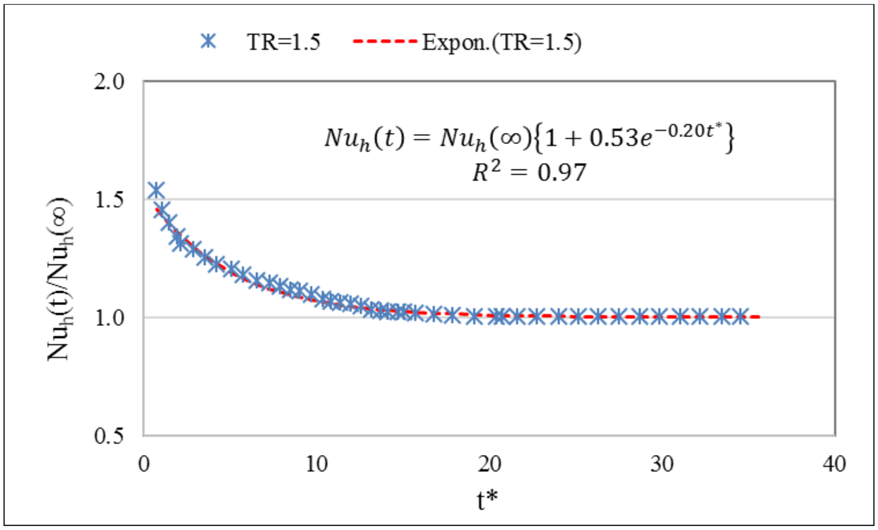

Figure 6.86: Variations of the transient Nusselt number at TR=1.5

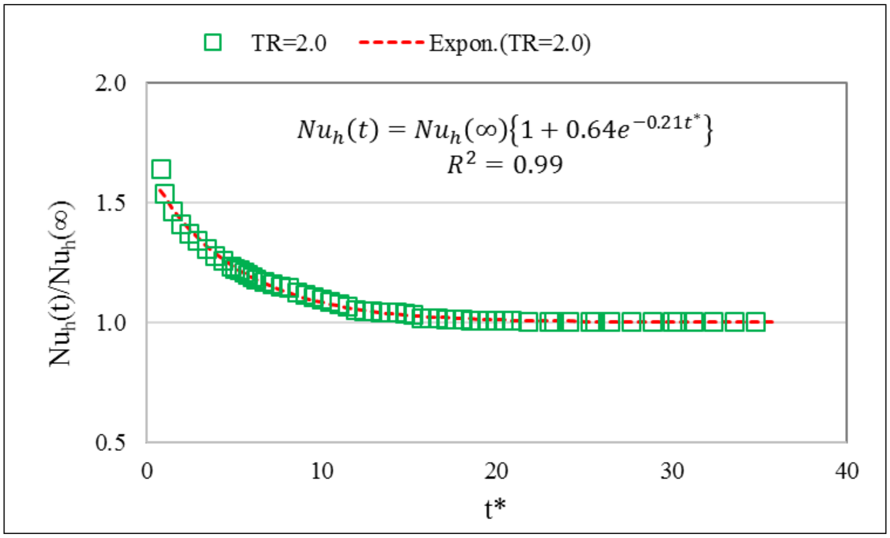

Figure 6.87: Variations of the transient Nusselt number at TR=2.0

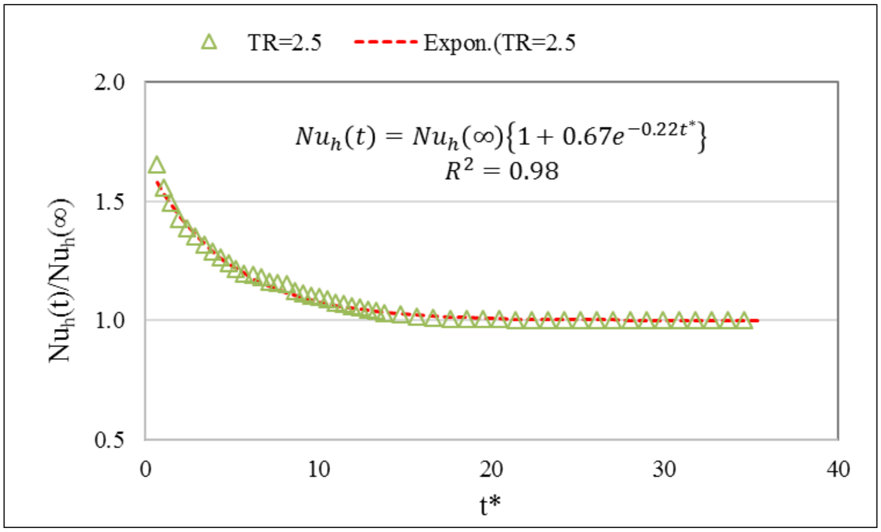

Figure 6.88: Variations of the transient Nusselt number at TR=2.5

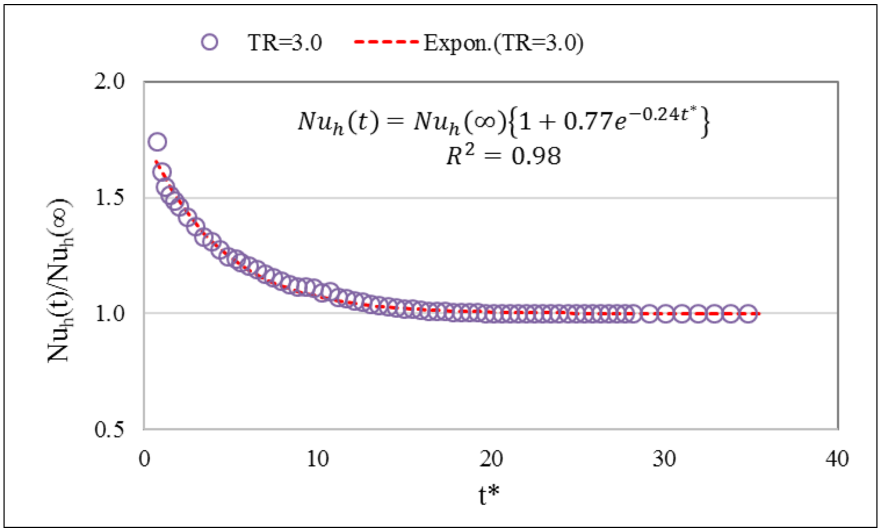

Figure 6.89: Variations of the transient Nusselt number at TR=3.0

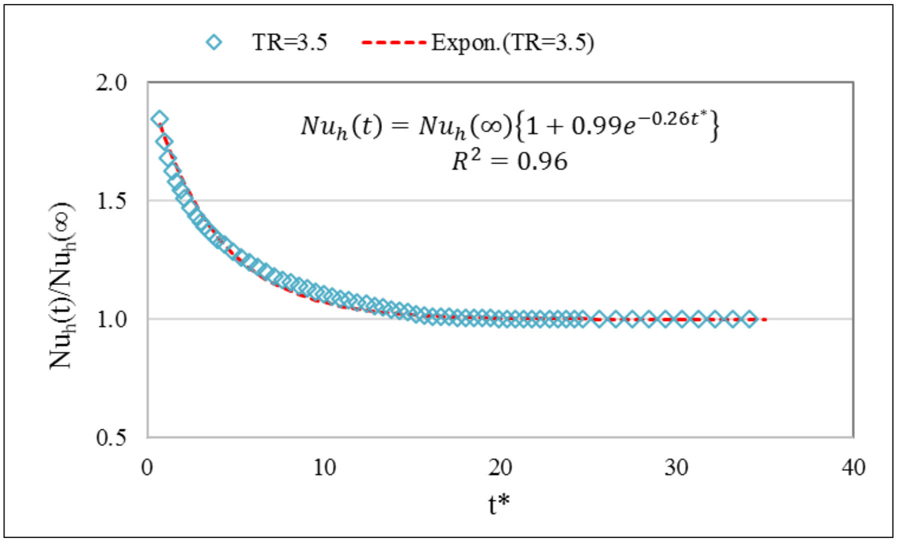

Figure 6.90: Variations of the transient Nusselt number at TR=3.5

The correlations for the ratio of $\mathrm{Nu_h(t)}$ to $\mathrm{Nu_h(\infty)}$ corresponding to each temperature step are as follows:

$$\mathrm{Nu_h(t) = Nu_h(\infty)\{1 + 0.53e^{-0.20t^*}\}\ with\ R^2 = 0.97,\ for\ TR = 1.5} \tag{6.5.39}$$

$$\mathrm{Nu_h(t) = Nu_h(\infty)\{1 + 0.64e^{-0.21t^*}\}\ with\ R^2 = 0.99,\ for\ TR = 2.0} \tag{6.5.40}$$

$$\mathrm{Nu_h(t) = Nu_h(\infty)\{1 + 0.67e^{-0.22t^*}\}\ with\ R^2 = 0.98,\ for\ TR = 2.5} \tag{6.5.41}$$

$$\mathrm{Nu_h(t) = Nu_h(\infty)\{1 + 0.77e^{-0.24t^*}\}\ with\ R^2 = 0.98,\ for\ TR = 3.0} \tag{6.5.42}$$

$$\mathrm{Nu_h(t) = Nu_h(\infty)\{1 + 0.99e^{-0.26t^*}\}\ with\ R^2 = 0.96,\ for\ TR = 3.0} \tag{6.5.43}$$

The above Equations from 6.5.39 to 6.5.43 have been correlated to develop a generalized correlation for $\mathrm{Nu_h(t)}$as a function of $\mathrm{Nu_h(\infty)}$, $\mathrm{t^*}$ and TR. The generalized correlation for $\mathrm{Nu_h(t)}$ is

$$\mathrm{Nu_h(t) = Nu_h(\infty)\{1 + C_5e^{D_5t^*}\}} \tag{6.5.44}$$

where,

$\mathrm{Nu_h}(\infty) = 0.09\mathrm{Re}^{0.64}\mathrm{Pr}^{1/3}$, derived earlier, see Equation (6.5.38)

$$\mathrm{C_5} = 0.34\mathrm{TR}^{0.29} \tag{6.5.45}$$

$$\mathrm{D_5} = 0.16\mathrm{TR}^{0.13} \tag{6.5.46}$$

Both the coefficient $\mathrm{C_5}$ and the exponent $\mathrm{D_5}$ change exponentially with the increase of temperature step. In order to obtain $\mathrm{C_5}$ and $\mathrm{D_5}$, a regression analysis has been performed and appended in Appendix C.

The developed correlation for transient Nusselt number of the hot fluid with the temperature steps has been compared with the numerical data for individual step change. The correlation fits all data in the numerical predictions of transient Nusselt number with maximum deviation of 5.28%, 7.51%, 3.29%, 4.61% and 3.16% for temperature steps of 1.5, 2.0, 2.5, 3.0, and 3.5, respectively.

6.5.2.5 Comparison of Transient Responses between MR and TR

With the purpose of finding which step provides faster response, the variations of Reynolds number for step change in the MR is compared to that of the inlet temperature step (TR). This is illustrated in Figure 6.91.

It is clear from Figure 6.91 that the enhancement of Reynolds number is higher and steeper for the mass flow steps compared with the temperature steps. It shows that if the mass flow rate is increased by 2-fold from a given steady state condition, the Reynolds number is increased by ≃2.58-fold when it reaches another steady state condition. However, for the same fold-change in temperature, Reynolds number is increased by ≃1.45-fold. This is because of the fact that the sudden jump in mass flow rate has more influence on fluid motion and Reynolds number than temperature. The Reynolds numbers dictates the heat transfer coefficient of fluid, and subsequently, mass flow steps provides quicker responses. As a result, faster response with higher gradient is observed for the perturbation of hot fluid mass flow rate.

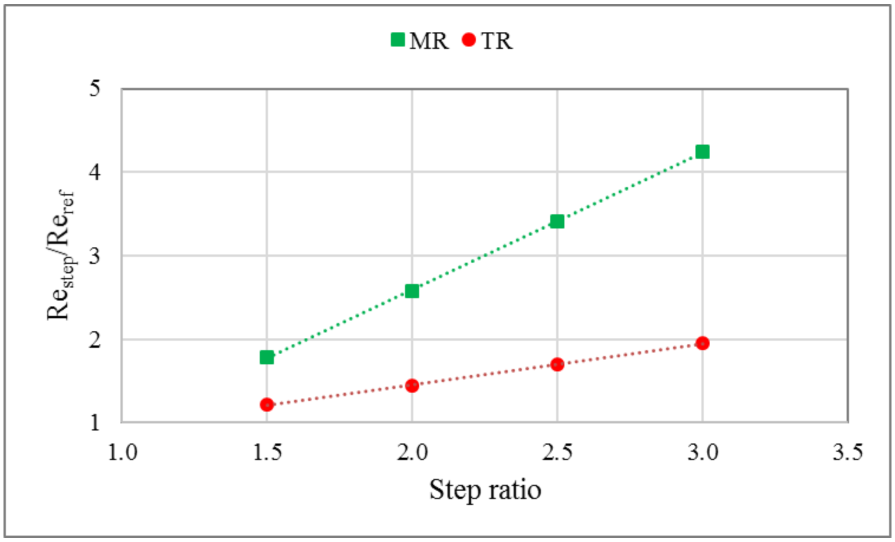

Figure 6.91: The effects of MR and TR on Reynolds number

6.5.3 Summary

The computational results for transient responses of the MICHX have been extensively analyzed for both the MR and the TR. New correlations for transient temperature and Nusselt number have been developed for both the MR and the TR.

- Transient response is faster for greater steps and lower for smaller steps.
- MR provides faster transient response than the TR

- Heat transfer coefficient of the hot fluid is maximum at the beginning of each step due to the minimum thermal boundary layer thickness of the fluid.

- Heat transfer coefficient gradually decreases with time and becomes constant when the fluid approaches to the steady state.

- Heat transfer coefficient is higher for higher step ratio due to the higher fluid transportation speed and Reynolds number, which dictates the heat transfer coefficient.

- The general forms of the new correlations of dimensionless temperature and Nusselt number for hot fluid mass flow step, MR and same fluid inlet temperature step, TR are as follows:

For hot fluid mass flow step, MR:

$$T^*_{h,o}(t) = T^*_{h,o}(\infty)\left\{1 - C_1 e^{-D_1 t^*}\right\} \tag{6.5.9}$$

where, $T^*_{h,o}(\infty) = 0.23\text{MR}^{0.89}$, $C_1 = 0.25\text{MR}^{0.93}$ and $D_1 = 0.06\text{MR}^{1.05}$

$$\text{Nu}_h(t) = \text{Nu}_h(\infty)\left\{1 + C_2 e^{-D_2 t^*}\right\} \tag{6.5.17}$$

where, $\text{Nu}_h(\infty) = 1.01\text{Re}^{0.34}\text{Pr}^{1/3}$, $C_2 = 0.21\text{MR}^{0.28}$ and $D_2 = 0.35\text{MR}^{-0.85}$

For hot fluid inlet temperature step, TR:

For $t^* \leq 5$: $$T^*_{h,o}(t) = T^*_{h,o}(\infty)\left\{C_3 t^* + D_3\right\} \tag{6.5.23}$$

For $t^* > 5$: $$T^*_{h,o}(t) = T^*_{h,o}(\infty)\left\{1 - C_4 e^{-D_4 t^*}\right\} \tag{6.5.29}$$

where, $T^*_{h,o}(\infty) = 0.61TR^{-0.01}$, $C_3 = 0.002$, $D_3 = 0.81TR^{-1.47}$, $C_4 = 1.5TR^{0.55}$ and $D_4 = 0.21$

$$Nu_h(t) = Nu_h(\infty)\left\{1 + C_5 e^{D_5 t^*}\right\} \tag{6.5.44}$$

where, $Nu_h(\infty) = 0.09Re^{0.64}Pr^{1/3}$, $C_5 = 0.34TR^{0.29}$ and $D_5 = 0.16TR^{0.13}$

CHAPTER 7

CONCLUSIONS AND RECOMMENDATIONS

7.1 Conclusions

The current research has been intended to achieve detailed numerical investigative analyses with heat exchangers to improve thermal performance and characterize transient behavior. In this section, conclusions have been drawn based on the research findings in this current work as illustrated in the preceding chapters.

Conventional FTHX and MICHX:

- MICHX outperformed FTHX. MICHX predicted about 91% to102% enhanced heat transfer coefficient compared to that of FTHX. It is, however, with the expense of higher pressure drop at a given Reynolds number within laminar flow regime.
- Local heat transfer coefficient is maximum at the entrance region due to lower thermal boundary layer thickness. It gradually decreases along the channel length becomes constant at fully developed region.
- Presence of the serpentine in the flow channel changes the flow direction, breaks boundary layer, creates secondary flow, and develops new entrance region and temperature profile. All of these together elevate the heat transfer coefficient.

Multi-loop MICHX:

- The massflow rate distributions in each of the three loops are identical with ±2.2% variations due to the elevation of the manifolds. Heat transfer rate is also considerably similar in each loop with ±5.1% deviations. This is because of the differences in mass flow rate among the loops. Also, due to the effects of the thermal interactions between two neighbouring loops caused by their inconsistent wall surface temperatures.

- Numerical results predicted that a single-loop can be used in CFD simulations instead of multi-loop crossflow MICHX of similar kind. This will significantly decrease the computational complexity, time and cost.
- The most (about 59%) heat transfer takes place in the first slab, while the least (about 6%) heat transfer occurs in the fifth slab due to the long travel of the fluid flow.
- The significant contributions of heat transfer have also been predicted for the second and the third slabs; however, the fourth and fifth slabs played insignificant roles.
- Number of slabs can be chosen based on the thermal demand of the systems.

Effects of Aluminum oxide (Al_2O_3) based nanofluid:

- Enhanced convective heat transfer coefficient is predicted due to the dispersion of Al_2O_3 nanoparticles in base fluids with the expense of higher pressure drop.
- Dispersion approach predicts better thermal performance than the single-phase homogeneous approach
- Nusselt number of Al_2O_3 based nanofluids increases with the increase of Reynolds number and follows the power law relationship with a positive exponent. For

Re≤100, Nusselt number of Al_2O_3/ATF nanofluid is observed higher than that of the base fluid ATF. This is because heat transfer coefficient of nanofluid dominates the Nusselt number. However, for Re>100, Nu_{nf} is lower than Nu_{atf} because thermal conductivity of nanofluid dominates the Nusselt number.

- Nusselt number of Al2O3/EG nanofluid is slightly higher for dispersion model than that of the single-phase homogeneous model. The insignificant difference in Nu is due to the fact that the thermal conductivity and heat transfer coefficient of the nanofluid increase with fairly identical proportion.
- The response time for Al_2O_3/EG nanofluids is shorter than the base fluid EG; it decreases with the increase of nanofluid concentration due to higher heat transfer coefficient.

Simultaneous and sequential heat exchanger modules:

- Simultaneous MICHX offers nearly 20%−25% increased heat transfer rate than that of the sequential FTHX as a benchmark. Whereas, the FTHX if oriented to simultaneous arrangement, offers nearly 10%−12% increased heat transfer rate compared to its previous sequential orientation.
- The intensification of heat transfer coefficient in simultaneous MICHX have been predicted about 46% to 85% for HT-HX and 77% to 114% for MT-HX.
- The position of heat exchangers significantly influences the thermal performance of the heat exchangers in simultaneous module. Both the HT-HX and the MT-HX provide higher heat transfer rate if these have been positioned in the bottom.

Unluckily, it is not feasible to place both heat exchangers at the same location in a module. The placement of heat exchanger, therefore, depends on the requirements of the thermal systems.

Transient heat transfer:

- Transient response is faster for higher steps and slower for lower steps.
- MR provides faster transient response than the TR.
- Heat transfer coefficient of hot fluid is higher at the small time values due to the minimum thermal boundary layer thickness. The longer entrance length decreases the thermal boundary layer thickness, and hence increases the heat transfer coefficient. The heat transfer coefficient starts decreasing with time and gradually becomes constant when the fluid approaches to the steady state.
- Heat transfer coefficient (h) is higher for higher step ratio due to the higher fluid transportation speed and Reynolds number, which dictate the h.
- The general forms of the new correlations of dimensionless temperature and Nusselt number for MR and TR are as follows:

For MR: $$\mathrm{T}^*_{\mathrm{h,o}}(\mathrm{t}) = \mathrm{T}^*_{\mathrm{h,o}}(\infty)\left\{1 - \mathrm{C}_1 \mathrm{e}^{-D_1 \mathrm{t}^*}\right\} \quad (6.5.9)$$

where, $\mathrm{T}^*_{\mathrm{h,o}}(\infty) = 0.23\mathrm{MR}^{0.89}$, $\mathrm{C}_1 = 0.25\mathrm{MR}^{0.93}$ and $\mathrm{D}_1 = 0.06\mathrm{MR}^{1.05}$

$$\mathrm{Nu_h}(\mathrm{t}) = \mathrm{Nu_h}(\infty)\left\{1 + \mathrm{C}_2 \mathrm{e}^{-\mathrm{D}_2 \mathrm{t}^*}\right\} \quad (6.5.17)$$

where, $\mathrm{Nu_h}(\infty) = 1.01\mathrm{Re}^{0.34}\mathrm{Pr}^{1/3}$ $\mathrm{C}_2 = 0.21\mathrm{MR}^{0.28}$ and $\mathrm{D}_2 = 0.35\mathrm{MR}^{-0.85}$

For TR:

$$T^*_{h,o}(t) = T^*_{h,o}(\infty)\,\{C_3t^* + D_3\}, \text{ for } t^* \le 5 \tag{6.5.26}$$

$$T^*_{h,o}(t) = T^*_{h,o}(\infty)\,\left\{1 - C_4e^{-D_4t^*}\right\}, \text{ for } t^* > 5 \tag{6.5.32}$$

where, $T^*_{h,o}(\infty) = 0.61TR^{-0.01}$, $C_3 = 0.002$, $D_3 = 0.81TR^{-1.47}$, $C_4 = 1.5TR^{0.55}$ and $D_4 = 0.21$

$$Nu_h(t) = Nu_h(\infty)\left\{1 + C_5e^{D_5t^*}\right\} \tag{6.5.41}$$

where, $Nu_h(\infty) = 0.09Re^{0.64}Pr^{1/3}$, $C_5 = 0.34TR^{0.29}$ and $D_5 = 0.16TR^{0.13}$

7.2 Recommendations

Some recommendations are proposed for the future work to progress the current research topic. It is expected to terminate or minimize the shortcomings of the current research work.

- The research can be extended to investigate the transient effects of heat exchangers due to perturbations of airside operating conditions.
- Transient performance can be carried out to investigate the effectiveness of PCM incorporating in heat exchangers
- Transient response of heat exchangers can be performed in the turbulence flow regime.

REFERENCES / BIBLIOGRAPHY

[1] Enerdata 2018, “Global energy statistical yearbook 2018,” *Enerdata*, 2018. [Online]. Available: https://yearbook.enerdata.net/.

[2] EPA U.S., “Inventory of U.S. Greenhouse Gas Emissions and Sinks: 1990-2015,” 2017.

[3] BPstats, *BP Statistical Review of World Energy*, 67th ed., vol. June. UK: BP p.l.c., 2018.

[4] Environment and Climate Change Canada, “National inventory report 1990-2015: Greenhouse gas sources and sinks in Canada,” *United Nations Framework Convention on Climate Change*, 2017. .

[5] IOCA, “International Organization of Motor Vehicle Manufacturers (OICA) production statistics,” 2017. [Online]. Available: http://www.oica.net/category/production-statistics/2017-statistics/. [Accessed: 17-Dec-2018].

[6] A. E. Hershey and R. F. Paton, “Flame temperatures in an internal combustion engine,” vol. XXXI, no. 9, pp. 1–55, 1933.

[7] R. Rundle, *Automotive Cooling System Basics*. Iola, WI, USA: Krause Publications, 1999.

[8] R. K. Shah and D. P. Sekulic, *Fundamentals of heat technology*, 2003rd ed. Hoboken, New Jersey, U.S.A: John Wiley & Sons, Inc., 2003.

[9] J. Eitel, W. Kramer, and E. Pantow, “Charge air cooling: New systems and components,” *ATZ Worldw.*, vol. 105, pp. 27–28, 2003.

[10] GM e-bodies, “Basic air conditioning,” 2018. [Online]. Available: http://www.79-85gm-ebodies.org/articles/a/basicairconditioning.html. [Accessed: 14-Dec-2018].

[11] T. L. Bergman, A. S. Lavine, F. P. Incorpera, and D. P. Dewitt, *Fundamentals of heat and mass transfer*, 7th ed. The United States of America: John Wiley & Sons, Inc, 2011.

[12] Y. A. Cengel, *Heat and Mass Transfer (SI Units): A Practical Approach*, 3rd ed. McGraw Hill, 2006.

[13] H. Herwig, “What exactly is the Nusselt number in convective heat transfer problems and are there alternatives?,” *Entropy*, vol. 18, no. 5, pp. 1–15, 2016.

[14] F. M. White, *Heat and mass transfer*, 1 edition. Reading, Mass. : Addison-Wesley, 1988.

[15] S. G. Kandlikar, S. Joshi, and S. Tian, “Effect of surface roughness on heat transfer and fluid flow characteristics at low Reynolds numbers in small diameter tubes,” *Heat Transf. Eng.*, vol. 24, no. 3, pp. 4–16, 2003.

[16] D. Wen, G. Lin, S. Vafaei, and K. Zhang, “Review of nanofluids for heat transfer applications,” *Particuology*, vol. 7, no. 2, pp. 141–150, 2009.

[17] S. U. S. Choi and J. A. Eastman, “Enhancing thermal conductivity of fluids with nanoparticles,” *Argonne National Laboratory, ANL/MSD/CP-84938*, vol. 66, no.

January 1995. The U.S. Department of Energ, Argonne, Illinois, pp. 99–105, 1995.

[18] T. Gao, J. Geer, and B. Sammakia, “Review and analysis of cross flow heat exchanger transient modeling for flow rate and temperature variations,” *J. Therm. Sci. Eng. Appl.*, vol. 7, no. 4, pp. 041017, 1–10, 2015.

[19] S. Kandlikar, “Effect of liquid-vapor phase distribution on the heat transfer mechanisms during flow boiling in minichannels and microchannels,” *Heat Transf. Eng.*, vol. 27, no. 1, pp. 4–13, 2006.

[20] M. Ismail, S. Fotowat, and A. Fartaj, “Uniformity of flow and heat transfer distribution in minichannel heat exchanger slab: A numerical approach,” *Proc. IASTED Int. Conf. Model. Simul.*, no. Ms, pp. 296–301, 2013.

[21] H. Liu, P. Li, and J. Van Lew, “CFD study on flow distribution uniformity in fuel distributors having multiple structural bifurcations of flow channels,” *Int. J. Hydrogen Energy*, vol. 35, no. 17, pp. 9186–9198, 2010.

[22] M. G. Khan and A. Fartaj, “A review on microchannel heat exchangers and potential applications,” *Int. J. Energy Res.*, vol. 35, pp. 553–582, 2011.

[23] J. Liu, S. Hussain, W. Wang, L. Wang, G. Xie, and B. Sundén, “Heat transfer enhancement and turbulent flow in a rectangular channel using perforated ribs with inclined holes,” *J. Heat Transfer*, vol. 141, no. April, pp. 041702, 1–15, 2019.

[24] Z. Li, W. Q. Tao, and Y. L. He, “A numerical study of laminar convective heat transfer in microchannel with non-circular cross-section,” *Int. J. Therm. Sci.*, vol. 45, pp. 1140–1148, 2006.

[25] E. S. Dasgupta, F. A. Siddiqui, and A. Fartaj, “Experimental study on air side heat transfer and fluid flow characteristics of microchannel heat exchanger,” *SAE Int. J. Mater. Manuf*, vol. 4, no. 1, pp. 1198–1210, 2012.

[26] M. Ismail, S. Fotowat, and A. Fartaj, “Effect of channel size on heat transfer and pressure drop in thin slabs minichannel heat exchanger,” *Int. J. Mech. Eng. Mechatronics*, vol. 2, no. 1, pp. 32–41, 2014.

[27] A. Jokar, S. J. Eckels, and M. H. Hosni, “Single-phase flow in meso-channel compact heat exchangers for air conditioning applications,” *Heat Transf. Eng.*, vol. 31, no. 1, pp. 3–16, 2010.

[28] S. G. Kandlikar, “Fundamental issues related to flow boiling in minichannels and microchannels,” *Exp. Therm. Fluid Sci.*, vol. 26, no. 2–4, pp. 389–407, 2002.

[29] S. G. Kandlikar, “A roadmap for implementing minichannels in refrigeration and air-conditioning systems - Current status and future directions,” *Heat Transf. Eng.*, vol. 28, no. 12, pp. 973–985, 2007.

[30] M. S. Saadi, M. Ismail, S. Fotowat, M. A. Quaiyum, and A. Fartaj, “Study of motor oil cooling at low Reynolds number in multi-port narrow channels,” *SAE Int. J. Engines*, vol. 6, no. 2, pp. 1287–1298, 2013.

[31] M. A. Quaiyum, A. Fartaj, and S. Askar, “An experimental characterization of automatic transmission fluid flowing through air cooled microchannel heat exchanger,” *SAE Int. J. Mater. Manf.*, vol. 5, no. 2, pp. 503–516, 2012.

[32] Y. Fan and L. Luo, “Recent applications of advances in microchannel heat

exchangers and multi-scale design optimization," *Heat Transf. Eng.*, vol. 29, no. 5, pp. 461–474, 2008.

[33] M. G. Khan, "Experimental investigation of heat transfer and pressure drop characteristics of water and glycol-water mixture in multi-port serpentine microchannel slab heat exchangers," University of Windsor, 2011.

[34] E. S. Dasgupta, S. Askar, M. Ismail, A. Fartaj, and M. A. Quaiyum, "Air cooling by multiport slabs heat exchanger: An experimental approach," *Exp. Therm. Fluid Sci.*, vol. 42, pp. 46–54, 2012.

[35] N. B. Chien, P. Q. Vu, N. Mohd-Ghazali, and O. Jong-Taek, "Convective heat transfer characteristics of single phase liquid in multiport minichannel tube: Experiment and CFD simulation," *Energy Procedia*, vol. 75, pp. 3180–3185, 2015.

[36] M. E. Steinke and S. G. Kandlikar, "Single-phase heat transfer enhancement techniques in microchannel and minichannel flows," in *The 2nd International Conference on Microchannels and Minichannels*, 2004, pp. 1–8.

[37] M. Ismail, A. Fartaj, and M. Karimi, "Numerical investigation on heat transfer and fluid flow behaviors of viscous fluids in a minichannel heat exchanger," *Numer. Heat Transf. Part A Appl.*, vol. 64, no. 1, pp. 1–29, 2013.

[38] S. Fotowat, A. Fartaj, M. Ismail, M. A. Quaiyum, and S. Askar, "Experimental study on air-heating through a cross-flow minichannel heat exchanger," *CSME Bienn. Int. Conf.*, pp. 1–6, 2012.

[39] M. A. Quaiyum, M. Ismail, and A. Fartaj, "Study of automatic transmission fluid

in a serpentine minichannel heat exchanger: An experimental approach," *Exp. Heat Transf.*, vol. 28, no. 3, pp. 244–266, 2015.

[40] W. Wang and X. Wang, "Experiments of condensation heat transfer in micro channel heat exchanger," in *International Refrigeration and Air Conditioning Conference at Purdue*, 2010, pp. 2290, 1–6.

[41] A. Arteconi, G. Giuliani, M. Tartuferi, and F. Polonara, "Characterization of a mini-channel heat exchanger for a heat pump system," *J. Phys. Conf. Ser.*, vol. 501, no. 1, pp. 0–10, 2014.

[42] M. Asadi, G. Xie, and B. Sunden, "A review of heat transfer and pressure drop characteristics of single and two-phase microchannels," *Int. J. Heat Mass Transf.*, vol. 79, pp. 34–53, 2014.

[43] Y. Zhai, G. Xia, Z. Li, and H. Wang, "Experimental investigation and empirical correlations of single and laminar convective heat transfer in microchannel heat sinks," *Exp. Therm. Fluid Sci.*, vol. 83, pp. 207–214, 2017.

[44] S. M. Hoi, A. L. Teh, E. H. Ooi, I. M. L. Chew, and J. J. Foo, "Plate-fin heat sink forced convective heat transfer augmentation with a fractal insert," *Int. J. Therm. Sci.*, vol. 142, pp. 392–406, 2019.

[45] S. Isaev, A. Leontiev, Y. Chudnovsky, D. Nikushchenko, I. Popov, and A. Sudakov, "Simulation of vortex heat transfer enhancement in the turbulent water flow in the narrow plane-parallel channel with an inclined oval-trench dimple of fixed depth and spot area," *Energies*, vol. 12, no. 7, pp. 1–24, 2019.

[46] A. E. Bergles, “Heat transfer enhancement - The encouragement and accommodation of high heat fluxes,” in *Tansactions of the ASME*, 1997, vol. 119, no. February, pp. 8–19.

[47] Heat transfer enhancement, “Web of Science.” [Online]. Available: http://apps.webofknowledge.com/. [Accessed: 26-Dec-2018].

[48] C. A. Balaras, “A review of augmentation techniques for heat transfer surfaces in single-phase heat exchangers,” *Energy*, vol. 15, no. 10, pp. 899–906, 1990.

[49] A. E. Bergles, *Enhanced heat transfer: Endless frontier, or mature and routine?* Applied Optical Measurements, Springer-Verlag Berlin Heidelberg, 1999.

[50] A. E. Bergles, “ExHFT for fourth generation heat transfer technology,” *Exp. Therm. Fluid Sci.*, vol. 26, pp. 335–344, 2002.

[51] A. E. Bergles, M. K. Jensen, and B. Shome, “The literature on enhancement of convective heat and mass transfer,” *J. Enhanc. Heat Transf.*, vol. 4, no. 1, pp. 1–6, 1996.

[52] I. Papautsky, T. Ameel, and a B. Frazier, “A review of laminar single-phase flow in microchannels,” in *2001 ASME International Mechanical Enginnering Congress and Exposition*, 2001, pp. 1–9.

[53] W. Q. Tao, Y. L. He, Q. W. Wang, Z. G. Qu, and F. Q. Song, “A unified analysis on enhancing single phase convective heat transfer with field synergy principle,” *Int. J. Heat Mass Transf.*, vol. 45, no. 24, pp. 4871–4879, 2002.

[54] H. Togun, T. Abdulrazzaq, S. N. Kazi, A. Badarudin, A. A. H. Kadhum, and E. Sadeghinezhad, “A review of studies on forced, natural and mixed heat transfer to fluid and nanofluid flow in an annular passage,” *Renew. Sustain. Energy Rev.*, vol. 39, pp. 835–856, 2014.

[55] S. S. Mehendale, A. M. Jacobi, and R. K. Shah, “Fluid flow and heat transfer at micro- and meso-scales with application to heat exchanger design,” *Appl. Mech. Rev.*, vol. 53, no. 7, p. 175, 2000.

[56] A. Cavallini, D. Del Col, and L. Rossetto, “Heat transfer and pressure drop of natural refrigerants in minichannels (low charge equipment),” *Int. J. Refrig.*, vol. 36, no. 2, pp. 287–300, 2013.

[57] C. S. Jwo, L. Y. Jeng, T. P. Teng, and C. C. Chen, “Performance of overall heat transfer in multi-channel heat exchanger by alumina nanofluid,” *J. Alloys Compd.*, vol. 504, no. SUPPL. 1, pp. S385–S388, 2010.

[58] S. G. Kandlikar and W. J. Grande, “Evolution of microchannel flow passages-thermohydraulic performance and fabrication technology,” *Heat Transf. Eng.*, vol. 24, no. 1, pp. 3–17, 2003.

[59] W. M. Kays and A. L. London, *Compact heat exchangers*, 2nd ed. New York: McGraw-Hill Book Co., 1964.

[60] K. J. Bell, “Heat exchanger design for the process industries,” *J. Heat Transfer*, vol. 126, no. December, pp. 877–885, 2004.

[61] W. Zhang, T. Hibiki, and K. Mishima, “Correlation for flow boiling heat transfer

in mini-channels," *Int. J. Heat Mass Transf.*, vol. 47, no. 26, pp. 5749–5763, 2004.

[62] R. L. Webb and M. Zhang, "Heat transfer and friction in small diameter channels," *Microscale Thermophys. Eng.*, vol. 2, no. 3, pp. 189–202, 1998.

[63] B. X. Wang and X. F. Peng, "Experimental investigation on liquid forced-convection heat transfer through microchannels," *Int. J. Heat Mass Transf.*, vol. 37, no. SUPPL. 1, pp. 73–82, 1994.

[64] L. Sun and K. Mishima, "Evaluation analysis of prediction methods for two-phase flow pressure drop in mini-channels," *Int. J. Multiph. Flow*, vol. 35, no. 1, pp. 47–54, 2009.

[65] S. M. Kim and I. Mudawar, "Universal approach to predicting saturated flow boiling heat transfer in mini/micro-channels – Part II. Two-phase heat transfer coefficient," *Int. J. Heat Mass Transf.*, vol. 64, pp. 1239–1256, 2013.

[66] L. Cheng and D. Mewes, "Review of two-phase flow and flow boiling of mixtures in small and mini channels," *Int. J. Multiph. Flow*, vol. 32, no. 2, pp. 183–207, 2006.

[67] V. Alagesan, "Flow boiling heat transfer in mini and micro channels - A state of the art review," *Int. J. ChemTech Res.*, vol. 4, no. 4, pp. 1247–1259, 2012.

[68] F. W. Dittus and L. M. K. Boelter, "Heat transfer in automobile radiators," *Int. Comm. Heat Mass Transf.*, vol. 12, pp. 3–22, 1985.

[69] P. Wu and W. A. Little, "Measurement of the heat transfer characteristics of gas

flow in fine channel heat exchangers used for microminiature refrigerators," *Cryogenics (Guildf).*, vol. 24, no. 8, pp. 415–420, 1984.

[70] I. Papautsky, B. K. Gale, S. K. Mohanty, T. A. Ameel, and A. B. Frazier, "Effects of rectangular microchannel aspect ratio on laminar friction constant."

[71] B. Agostini, A. Bontemps, and B. Thonon, "Effects of geometrical and thermophysical parameters on heat transfer measurements in small-diameter channels," *Heat Transf. Eng.*, vol. 27, no. 1, pp. 14–24, 2006.

[72] V. Gnielinski, "New equations for heat and mass transfer in turbulent pipe and channel flow," *Int. Chem. Eng.*, vol. 16, no. 2, pp. 359–368, 1976.

[73] X. Li, R. Wang, R. Huang, and Y. Shi, "Numerical and experimental investigation of pressure drop characteristics during upward boiling two-phase flow of nitrogen," *Int. J. Heat Mass Transf.*, vol. 50, no. 9–10, pp. 1971–1981, 2007.

[74] T. Harirchian and S. V. Garimella, "Microchannel size effects on local flow boiling heat transfer to a dielectric fluid," *Int. J. Heat Mass Transf.*, vol. 51, no. 15–16, pp. 3724–3735, 2008.

[75] Z. Y. Guo and Z. X. Li, "Size effect on single-phase channel flow and heat transfer at microscale," *Int. J. Heat Fluid Flow*, vol. 24, no. 3, pp. 284–298, 2003.

[76] G. Mohiuddin Mala, D. Li, C. Werner, H.-J. Jacobasch, and Y. B. Ning, "Flow characteristics of water through a microchannel between two parallel plates with electrokinetic effects," *Int. J. Heat Fluid Flow*, vol. 18, no. 5, pp. 489–496, 1997.

[77] D. Lelea, S. Nishio, and K. Takano, “The experimental research on microtube heat transfer and fluid flow of distilled water,” *Int. J. Heat Mass Transf.*, vol. 47, no. 12–13, pp. 2817–2830, 2004.

[78] M. Venkatesan, S. K. Das, and A. R. Balakrishnan, “Effect of diameter on two-phase pressure drop in narrow tubes,” *Exp. Therm. Fluid Sci.*, vol. 35, no. 3, pp. 531–541, 2011.

[79] S. G. Kandlikar, “Two-phase flow patterns, pressure drop, and heat transfer during boiling in minichannel flow passages of compact evaporators,” *Heat Transf. Eng.*, vol. 23, no. 1, pp. 5–23, 2002.

[80] S. Kim, E. Choi, and Y. I. Cho, “The effect of header shapes on the flow distribution in a manifold for electronic packaging applications,” *Int. Commun. Heat Mass Transf.*, vol. 22, no. 3, pp. 329–341, 1995.

[81] B. Mathew, T. J. John, and H. Hegab, “Effect of manifold design on flow distribution in multichanneled microfluidic devices,” in *Proceedings of FEDSM2009 2009 ASME Fluids Engineering Division Summer Meeting FEDSM2009*, 2009, vol. 2, pp. 543–548.

[82] G. Griffini and A. Gavriilidis, “Effect of microchannel plate design on fluid flow uniformity at low flow rates,” *Chem. Eng. Technol.*, vol. 30, no. 3, pp. 395–406, 2007.

[83] S. A. Solovitz and J. Mainka, “Manifold design for micro-channel cooling with uniform flow distribution,” *J. Fluids Eng.*, vol. 133, pp. 051103, 1–11, 2011.

[84] O. Tonomura, S. Tanaka, M. Noda, M. Kano, S. Hasebe, and I. Hashimoto, "CFD-based optimal design of manifold in plate-fin microdevices," *Chem. Eng. J.*, vol. 101, no. 1–3, pp. 397–402, 2004.

[85] M. Pan, X. Wei, D. Zeng, and Y. Tang, "Trend prediction in velocity distribution among microchannels based on the analysis of frictional resistances," *Chem. Eng. J.*, vol. 164, no. 1, pp. 238–245, 2010.

[86] M. Pan, Y. Tang, W. Zhou, and L. Lu, "Flow distribution among microchannels with asymmetrical manifolds," *2007 IEEE Int. Conf. Control Autom. ICCA*, vol. 00, no. 2, pp. 193–197, 2008.

[87] M. Pan, Y. Tang, L. Pan, and L. Lu, "Optimal design of complex manifold geometries for uniform flow distribution between microchannels," *Chem. Eng. J.*, vol. 137, no. 2, pp. 339–346, 2008.

[88] D. B. Tuckerman and R. F. W. Pease, "High-performance heat sinking for VLSI," *IEEE Electron Device Lett.*, vol. EDL-2, no. 5, pp. 126–129, 1981.

[89] M. Mohammadi, G. N. Jovanovic, and K. V. Sharp, "Numerical study of flow uniformity and pressure characteristics within a microchannel array with triangular manifolds," *Comput. Chem. Eng.*, vol. 52, pp. 134–144, 2013.

[90] R. L. Webb and K. Chung, "Two-phase flow distribution to tubes of parallel flow air-cooled heat exchangers," *Heat Transf. Eng.*, vol. 26, no. 4, pp. 3–18, 2005.

[91] T. Kulkarni, C. W. Bullard, and K. Cho, "Header design tradeoffs in microchannel evaporators," *Appl. Therm. Eng.*, vol. 24, no. 5–6, pp. 759–776, 2004.

[92] R. W. Knight, J. S. Goodling, and D. J. Hall, “Optimal thermal design of forced convection heat sinks-analytical,” *J. Electron. Packag.*, vol. 113, no. September 1991, pp. 313–321, 2007.

[93] N. Zakhia, “Effect of the hydraulic diameter on pressure drop across restrictions of a tube supoort plate used in heat exchanger,” in *1995 National Heat Transfer Conference, ASME 1995*, 1995, no. August, p. HTD-Vol. 308.

[94] F. Jiang and X. Deng, “Deep heat transfer performance and ratio of length to diameter in shell and tube heat exchangers,” *Commun. Comput. Inf. Sci.*, vol. 232 CCIS, no. PART 2, pp. 396–404, 2011.

[95] P. Gao, S. Le Person, and M. Favre-Marinet, “Scale effects on hydrodynamics and heat transfer in two-dimensional mini and microchannels,” *Int. J. Therm. Sci.*, vol. 41, no. 11, pp. 1017–1027, 2002.

[96] M.-H. Kim and C. W. Bullard, “Performance evaluation of a window room air conditioner with microchannel condensers,” *J. Energy Resour. Technol.*, vol. 124, no. 1, pp. 47–55, 2002.

[97] J. H. Kim and E. A. Groll, “Performance comparisons of a unitary split system using microchannel and fin-tube outdoor coils, Part I: Cooling tests,” *Int. Refrig. Air Cond. Conf.*, no. Paper 557, pp. 219–229, 2002.

[98] M. I. Hasan, A. A. Rageb, M. Yaghoubi, and H. Homayoni, “Influence of channel geometry on the performance of a counter flow microchannel heat exchanger,” *Int. J. Therm. Sci.*, vol. 48, no. 8, pp. 1607–1618, 2009.

[99] J. Buongiorno, “Convective transport in nanofluids,” *J. Heat Transfer*, vol. 128, no. 3, pp. 240–250, 2006.

[100] R. Taylor *et al.*, “Small particles, big impacts: A review of the diverse applications of nanofluids,” *J. Appl. Phys.*, vol. 113, no. 1, 2013.

[101] Y. Xuan and Q. Li, “Heat transfer enhancement of nanofluids,” *Int. J. Heat Fluid Flow*, vol. 21, pp. 58–64, 2000.

[102] S. A. Angayarkanni and J. Philip, “Review on thermal properties of nanofluids: Recent developments,” *Adv. Colloid Interface Sci.*, vol. 225, pp. 146–176, 2015.

[103] S. Pathak and A. Kaimkuriya, “Heat transfer augmentation in heat exchanger using nanofluid: A review,” *Int. J. Trend Sci. Res. Dev.*, vol. 2, no. 3, pp. 1939–1944, 2018.

[104] S. U. S. Choi and J. A. Eastman, “Enhancing thermal conductivity of fluids with nanoparticles,” *Argonne National Laboratory*. The U.S. Department of Energ, Argonne, Illinois, 1995.

[105] EPA U.S., “Module 3 : Characteristics of particles - Particle size categories,” 2017.

[106] C. G. Granqvist and R. A. Buhrman, “Ultrafine metal particles,” *J. Appl. Phys.*, vol. 47, no. 5, pp. 2200–2219, 1976.

[107] S. K. Das *et al.*, *Nanofluids : Science and technology*. John Wiley & Sons, Inc, 2007.

[108] J. C. Maxwell, *A Treatise on electricity and magnetism*, 2nd ed., vol. I. London,

UK: Oxford at the Clarendon Press, 1881.

[109] S. Lee, S. U.-S. Choi, S. Li, and J. A. Eastman, "Measuring thermal conductivity of fluids containing oxide nanoparticles," *J. Heat Transfer*, vol. 121, no. May, pp. 280–289, 1999.

[110] S. K. Das, S. U. S. Choi, and H. E. Patel, "Heat transfer in nanofluids - A review," *Heat Transf. Eng.*, vol. 27, no. 10, pp. 3–19, 2006.

[111] Nanofluid, "Web of science." [Online]. Available: http://apps.webofknowledge.com/. [Accessed: 02-May-2019].

[112] W. J. Danziger, "Heat transfer to fluidized gas-solids mixtures in vertical transport," *Ind. Eng. Chem. Process Des. Dev.*, vol. 2, no. 4, pp. 269–276, 1963.

[113] L. Farbar and C. A. Depew, "Heat transfer effects to gas-solids mixtures using solid spherical particles of uniform size," *Ind. Eng. Chem. Fundam.*, vol. 2, no. 2, pp. 130–135, 1963.

[114] Final Report, *Evaluation of gas-graphite suspensions as nuclear reactor coolants.* U.S. Atomic Energy Commission. Division of Technical Information., 1961.

[115] S. U. S. Choi, Z. G. Zhang, W. Yu, F. E. Lockwood, and E. A. Grulke, "Anomalous thermal conductivity enhancement in nanotube suspensions," *Appl. Phys. Lett.*, vol. 79, no. 14, pp. 2252–2254, 2001.

[116] E. Abu-Nada, Z. Masoud, and A. Hijazi, "Natural convection heat transfer enhancement in horizontal concentric annuli using nanofluids," *Int. Commun. Heat*

Mass Transf., vol. 35, no. 5, pp. 657–665, 2008.

[117] E. Abu-Nada, “Effects of variable viscosity and thermal conductivity of Al2O3-water nanofluid on heat transfer enhancement in natural convection,” *Int. J. Heat Fluid Flow*, vol. 30, no. 4, pp. 679–690, 2009.

[118] A. Akbarinia and R. Laur, “Investigating the diameter of solid particles effects on a laminar nanofluid flow in a curved tube using a two phase approach,” *Int. J. Heat Fluid Flow*, vol. 30, no. 4, pp. 706–714, 2009.

[119] E. B. Elcioglu, “Experimental and theoretical investigations on alumina–water nanofluid viscosity with statistical analysis,” MIDDLE EAST TECHNICAL UNIVERSITY, 2013.

[120] S. Göktepe, K. Atalik, and H. Ertürk, “Comparison of single and two-phase models for nanofluid convection at the entrance of a uniformly heated tube,” *Int. J. Therm. Sci.*, vol. 80, no. 1, pp. 83–92, 2014.

[121] M. Akhtari, M. Haghshenasfard, and M. R. Talaie, “Numerical and experimental investigation of heat transfer of α-Al2O3/water nanofluid in double pipe and shell and tube heat exchangers,” *Numer. Heat Transf. Part A Appl.*, vol. 63, no. 12, pp. 941–958, 2013.

[122] J. Albadr, S. Tayal, and M. Alasadi, “Heat transfer through heat exchanger using Al2O3nanofluid at different concentrations,” *Case Stud. Therm. Eng.*, vol. 1, no. 1, pp. 38–44, 2013.

[123] W. H. Azmi, K. V. Sharma, R. Mamat, A. B. S. Alias, and I. Izwan Misnon,

"Correlations for thermal conductivity and viscosity of water based nanofluids," *IOP Conf. Ser. Mater. Sci. Eng.*, vol. 36, no. 1, 2012.

[124] P. C. M. Kumar, J. Kumar, S. Suresh, and K. P. Babu, "Heat transfer enhancement in a helically coiled tube with Al2O3/ater nanofluid under laminar flow condition," *Int. J. Nanosci.*, vol. 11, no. 05, pp. 1250029-1–9, 2012.

[125] P. Kumar and K. M. Pandey, "Effect on heat transfer characteristics of nanofluids flowing under laminar and turbulent flow regime - A review," *IOP Conf. Ser. Mater. Sci. Eng.*, vol. 225, no. 1, 2017.

[126] B. C. Pak and Y. I. Cho, "Hydrodynamic and heat transfer study of dispersed fluids with submicron metallic oxide particles," *Exp. Heat Transf.*, vol. 11, no. 2, pp. 151–170, 1998.

[127] H. O'Hanley, J. Buongiorno, T. McKrell, and L. W. Hu, "Measurement and model validation of nanofluid specific heat capacity with differential scanning calorimetry," *Adv. Mech. Eng.*, vol. 2012, 2012.

[128] K. Khanafer, K. Vafai, and M. Lightstone, "Buoyancy-driven heat transfer enhancement in a two-dimensional enclosure utilizing nanofluids," *Int. J. Heat Mass Transf.*, vol. 46, pp. 3639–3653, 2003.

[129] E. E. Michaelides, "Transport properties of nanofluids. A critical review," *J. Non-Equilibrium Thermodyn.*, vol. 38, no. 1, pp. 1–79, 2013.

[130] Y. Xuan and W. Roetzel, "Conceptions for heat transfer correlation of nanofluids," *Int. J. Heat Mass Transf.*, vol. 43, no. 19, pp. 3701–3707, 2000.

[131] D. Shin and D. Banerjee, "Specific heat of nanofluids synthesized by dispersing alumina nanoparticles in alkali salt eutectic," *Int. J. Heat Mass Transf.*, vol. 74, pp. 210–214, 2014.

[132] B. Barbés, R. Páramo, E. Blanco, and C. Casanova, "Thermal conductivity and specific heat capacity measurements of Al2O3 nanofluids," *J. Therm. Anal. Calorim.*, vol. 111, pp. 1615–1625, 2013.

[133] X.-Q. Wang and A. S. Mujumdar, "Heat transfer characteristics of nanofluids: A review," *Int. J. Therm. Sci.*, vol. 46, no. 1, pp. 1–19, 2007.

[134] M. Chopkar, S. Sudarshan, P. K. Das, and I. Manna, "Effect of particle size on thermal conductivity of nanofluid," *Metall. Mater. Trans. A*, vol. 39A, no. July, pp. 1535–1542, 2008.

[135] H. E. Patel, S. K. Das, T. Sundararajan, A. Sreekumaran Nair, B. George, and T. Pradeep, "Thermal conductivities of naked and monolayer protected metal nanoparticle based nanofluids: Manifestation of anomalous enhancement and chemical effects," *Appl. Phys. Lett.*, vol. 83, no. 14, pp. 2931–2933, 2003.

[136] M. S. Liu, M. C. C. Lin, C. Y. Tsai, and C. C. Wang, "Enhancement of thermal conductivity with Cu for nanofluids using chemical reduction method," *Int. J. Heat Mass Transf.*, vol. 49, no. 17–18, pp. 3028–3033, 2006.

[137] A. N. Turanov and Y. V. Tolmachev, "Heat- and mass-transport in aqueous silica nanofluids," *Heat Mass Transf. und Stoffuebertragung*, vol. 45, no. 12, pp. 1583–1588, 2009.

[138] H. Xie, W. Yu, Y. Li, and L. Chen, “Discussion on the thermal conductivity enhancement of nanofluids,” *Nanoscale Res. Lett.*, vol. 6, no. 1, p. 124, 2011.

[139] J. A. Eastman, S. U. S. Choi, S. Li, W. Yu, and L. J. Thompson, “Anomalously increased effective thermal conductivities of ethylene glycol-based nanofluids containing copper nanoparticles,” *Appl. Phys. Lett.*, vol. 78, no. 6, pp. 718–720, 2001.

[140] H. Xie, J. Wang, T. Xi, Y. Liu, F. Ai, and Q. Wu, “Thermal conductivity enhancement of suspensions containing nanosized alumina particles,” *J. Appl. Phys.*, vol. 91, no. 7, pp. 4568–4572, 2002.

[141] S. K. Das, N. Putra, P. Thiesen, and W. Roetzel, “Temperature dependence of thermal conductivity enhancement for nanofluids,” *J. Heat Transfer*, vol. 125, no. August, pp. 567–574, 2003.

[142] S. Sen Gupta *et al.*, “Thermal conductivity enhancement of nanofluids containing graphene nanosheets,” *J. Appl. Phys.*, vol. 110, no. 8, 2011.

[143] S. M. S. Murshed, K. C. Leong, and C. Yang, “Enhanced thermal conductivity of TiO2- Water based nanofluids,” *Int. J. Therm. Sci.*, vol. 44, no. 4, pp. 367–373, 2005.

[144] H. A. Mintsa, G. Roy, C. T. Nguyen, and D. Doucet, “New temperature dependent thermal conductivity data for water-based nanofluids,” *Int. J. Therm. Sci.*, vol. 48, no. 2, pp. 363–371, 2009.

[145] T. K. Hong, H. S. Yang, and C. J. Choi, “Study of the enhanced thermal

conductivity of Fe nanofluids," *J. Appl. Phys.*, vol. 97, no. 6, 2005.

[146] M. H. Hong *et al.*, "Nano-patterning by pulsed laser irradiation in near field," *J. Phys. Conf. Ser.*, vol. 59, no. 1, pp. 64–67, 2007.

[147] W. Duangthongsuk and S. Wongwises, "Heat transfer enhancement and pressure drop characteristics of TiO2-water nanofluid in a double-tube counter flow heat exchanger," *Int. J. Heat Mass Transf.*, vol. 52, no. 7–8, pp. 2059–2067, 2009.

[148] C. H. Chon, K. D. Kihm, S. P. Lee, and S. U. S. Choi, "Empirical correlation finding the role of temperature and particle size for nanofluid (Al2O3) thermal conductivity enhancement," *Appl. Phys. Lett.*, vol. 87, no. 15, pp. 1–3, 2005.

[149] J. Avsec, "The combined analysis of phonon and electron heat transfer mechanism on thermal conductivity for nanofluids," *Int. J. Heat Mass Transf.*, vol. 51, no. 19–20, pp. 4589–4598, 2008.

[150] L. Syam Sundar, M. T. Naik, K. V. Sharma, M. K. Singh, and T. C. Siva Reddy, "Experimental investigation of forced convection heat transfer and friction factor in a tube with Fe3O4magnetic nanofluid," *Exp. Therm. Fluid Sci.*, vol. 37, pp. 65–71, 2012.

[151] P. D. Shima, J. Philip, and B. Raj, "Role of microconvection induced by Brownian motion of nanoparticles in the enhanced thermal conductivity of stable nanofluids," *Appl. Phys. Lett.*, vol. 94, no. 22, pp. 2007–2010, 2009.

[152] W. Williams, J. Buongiorno, and L.-W. Hu, "Experimental investigation of turbulent convective heat transfer and pressure loss of alumina/water and

zirconia/water nanoparticle colloids (nanofluids) in horizontal tubes," *J. Heat Transfer*, vol. 130, no. 4, pp. 042412, 1–7, 2008.

[153] M. P. Beck, Y. Yuan, P. Warrier, and A. S. Teja, "The effect of particle size on the thermal conductivity of alumina nanofluids," *J. Nanoparticle Res.*, vol. 11, no. 5, pp. 1129–1136, 2009.

[154] D. Wen, L. Zhang, and Y. He, "Flow and migration of nanoparticle in a single channel," *Heat Mass Transf.*, vol. 45, no. 8, pp. 1061–1067, 2009.

[155] S. Xi, J. Zhou, Y. Li, S. Tung, and E. Schneider, "A review on development of nanofluid preparation and characterization," *Powder Technol.*, vol. 196, no. 2, pp. 89–101, 2009.

[156] S. Kakaç and A. Pramuanjaroenkij, "Review of convective heat transfer enhancement with nanofluids," *Int. J. Heat Mass Transf.*, vol. 52, no. 13–14, pp. 3187–3196, 2009.

[157] X. Wei and L. Wang, "Synthesis and thermal conductivity of microfluidic copper nanofluids," *Particuology*, vol. 8, no. 3, pp. 262–271, 2010.

[158] W. Yu and H. Xie, "A Review on nanofuids: preparation, stability mechanisms, and applications," *J. Nanomater.*, vol. 2012, no. Article ID 435873, pp. 1–17, 2012.

[159] Z. Han, "Nanofluids with Enhanced Thermal Transport Properties," University of Maryland, 2008.

[160] X.-Q. Q. Wang and A. S. Mujumdar, “A review on nanofluids - part I: Theoretical and numerical investigations,” *Brazilian J. Chem. Eng.*, vol. 25, no. 4, pp. 613–630, 2008.

[161] D. Bruggeman, “Calculation of different physical constants of heterogeneous substances. I. Dielectric constants and conductivities of the mixed bodies of isotropic substances,” *Ann. Phys. (N. Y).*, vol. 24, pp. 636–664, 1935.

[162] Y. Xuan, Q. Li, X. Zhang, and M. Fujii, “Stochastic thermal transport of nanoparticle suspensions,” *J. Appl. Phys.*, vol. 100, no. 4, 2006.

[163] R. . L. Hamilton and O. K. Crosser, “Thermal Conductivity of Hetrogenous Two-Component Systems,” *I EC Fundam.*, vol. 1, no. 3, pp. 187–191, 1962.

[164] R. T. Bonnecaze and J. F. Brady, “A method for determining the effective conductivity of dispersions of particles,” in *The Royal Society A: Mathematical, Physical and Engineering Sciences*, 1990, vol. 430, pp. 285–313.

[165] R. T. Bonnecaze and J. F. Brady, “The effective conductivity of random suspensions of spherical particles,” in *The Royal Society A: Mathematical, Physical and Engineering Sciences*, 1991, vol. 432, pp. 445–465.

[166] C. W. Nan, R. Birringer, D. R. Clarke, and H. Gleiter, “Effective thermal conductivity of particulate composites with interfacial thermal resistance,” *J. Appl. Phys.*, vol. 81, no. 10, pp. 6692–6699, 1997.

[167] W. Yu and S. U. S. Choi, “The role of interfacial layers in the enhanced thermal conductivity of nanofluids: A renovated Maxwell model,” *J. Nanoparticle Res.*,

vol. 5, pp. 167–171, 2004.

[168] D. J. Jeffrey, “Conduction through a random suspension of spheres,” in *Proceedings of the Royal Society of London. Series A, Mathematical and Physical Sciences*, 1973, vol. 335, pp. 355–367.

[169] R. H. Davis, “The effective thermal conductivity of a composite material with spherical inclusions,” *Int. J. Thermophys.*, vol. 7, no. 3, pp. 609–620, 1986.

[170] S. Y. Lu and H. C. Lin, “Effective conductivity of composites containing aligned spheroidal inclusions of finite conductivity,” *J. Appl. Phys.*, vol. 79, no. 9, pp. 6761–6769, 1996.

[171] K. Khanafer and K. Vafai, “A critical synthesis of thermophysical characteristics of nanofluids,” *Int. J. Heat Mass Transf.*, vol. 54, no. 19–20, pp. 4410–4428, 2011.

[172] K. Abbaspoursani, M. Allahyari, M. Rahmani, and K. Abbaspoursani, “An Improved Model for Prediction of the Effective Thermal Conductivity of Nanofluids,” *Int. J. Mech. Mechatronics Eng.*, vol. 5, no. 10, p. 4, 2011.

[173] H. Masuda, E. Ebata, K. Teramae, N. Hishinuma, and Y. Ebata, “Alteration of thermal conductivity and viscosity of liquid by dispersing ultra-fine particles (dispersion of γ-Al2O3, SiO2 and TiO2 ultra-fine particles),” *Netsu Bussei*, vol. 7, no. 4, pp. 227–233, 1993.

[174] X. Zhang, H. Gu, and M. Fujii, “Experimental study on the effective thermal conductivity and thermal diffusivity of nanofluids,” *Int. J. Thermophys.*, vol. 27, no. 2, pp. 569–580, 2006.

[175] A. Turgut, I. Tavman, M. Chirtoc, H. P. Schuchmann, C. Sauter, and S. Tavman, “Thermal conductivity and viscosity measurements of water-based TiO2 nanofluids,” *Int. J. Thermophys.*, vol. 30, no. 4, pp. 1213–1226, 2009.

[176] D. W. Oh, A. Jain, J. K. Eaton, K. E. Goodson, and J. S. Lee, “Thermal conductivity measurement and sedimentation detection of aluminum oxide nanofluids by using the 3ω method,” *Int. J. Heat Fluid Flow*, vol. 29, no. 5, pp. 1456–1461, 2008.

[177] B. Shen, “Minimum quantity lubrication grinding using nanofluids,” The University Of Michigan, 2008.

[178] V. Bianco, O. Manca, S. Nardini, and M. Roma, “Numerical investigation of transient thermal and fluidynamic fields in an executive aircraft cabin,” *Appl. Therm. Eng.*, vol. 29, no. 16, pp. 3418–3425, 2009.

[179] M. Bahiraei and S. M. Hosseinalipour, “Effects of various forces on particle distribution and thermal features of suspensions containing alumina nanoparticles,” *J. Dispers. Sci. Technol.*, vol. 35, no. 6, pp. 859–867, 2014.

[180] A. Celen, N. Kayaci, A. Çebi, H. Demir, A. S. Dalkiliç, and S. Wongwises, “Numerical investigation for the calculation of TiO2-water nanofluids’ pressure drop in plain and enhanced pipes,” *Int. Commun. Heat Mass Transf.*, vol. 53, pp. 98–108, 2014.

[181] W. C. Chen and W. T. Cheng, “Numerical simulation on forced convective heat transfer of titanium dioxide/water nanofluid in the cooling stave of blast furnace,”

Int. Commun. Heat Mass Transf., vol. 71, pp. 208–215, 2016.

[182] S. K. Choi, S. O. Kim, T. H. Lee, and D. H. Dohee, "Computation of the natural convection of nanofluid in a square cavity with homogeneous and nonhomogeneous models," *Numer. Heat Transf. Part A Appl.*, vol. 65, no. 4, pp. 287–301, 2014.

[183] L. Colla, L. Fedele, O. Manca, L. Marinelli, and S. Nardini, "Experimental and numerical investigation on forced convection in circular tubes with nanofluids," in *4th Micro and Nano Flows Conference*, 2014, vol. 37, no. September, pp. 1–8.

[184] M. Corcione, M. Cianfrini, and A. Quintino, "Two-phase mixture modeling of natural convection of nanofluids with temperature-dependent properties," *Int. J. Therm. Sci.*, vol. 71, pp. 182–195, 2013.

[185] Z.-G. Feng and E. E. Michaelides, "A numerical study on the transient heat transfer from a sphere at high Reynolds and Peclet numbers," *Int. J. Heat Mass Transf.*, vol. 43, no. 2, pp. 219–229, 2000.

[186] A. Elsayed, R. K. Al-Dadah, S. Mahmoud, and A. Rezk, "Numerical investigation of turbulent flow heat transfer and pressure drop of Al2O3/water nanofluid in helically coiled tubes," *Int. J. Low-Carbon Technol.*, vol. 10, no. 3, pp. 1–8, 2014.

[187] M. H. Fard, M. N. Esfahany, and M. R. Talaie, "Numerical study of convective heat transfer of nanofluids in a circular tube two-phase model versus single-phase model," *Int. Commun. Heat Mass Transf.*, vol. 37, no. 1, pp. 91–97, 2010.

[188] M. H. Fard, M. R. Talaie, and S. Nasr, "Numerical and experimental investigation

of heat transfer of zno/water nanofluid in the concentric tube and plate heat exchangers," *Therm. Sci.*, vol. 15, no. 1, pp. 183–194, 2011.

[189] O. Ghaffari, A. Behzadmehr, and H. Ajam, "Turbulent mixed convection of a nanofluid in a horizontal curved tube using a two-phase approach," *Int. Commun. Heat Mass Transf.*, vol. 37, no. 10, pp. 1551–1558, 2010.

[190] I. Gherasim, N. Galanis, and C. T. Nguyen, "Numerical study of nanofluid flow and heat transfer in plate heat exchanger.pdf," *Comput. Therm. Ecience*, vol. 5, no. 4, pp. 317–332, 2013.

[191] J. Guiet, M. Reggio, and P. Vasseur, "Natural convection of nanofluids in a square enclosure with a protruding heater," *Adv. Mech. Eng.*, vol. 2012, 2012.

[192] P. Gunnasegaran, N. H. Shuaib, M. F. Abdul Jalal, and E. Sandhita, "Numerical study of fluid dynamic and heat transfer in a compact heat exchanger using nanofluids," *Int. Sch. Res. Netw. Mech. Eng.*, no. Article ID 585496, pp. 1–11, 2012.

[193] W. K. Hasan and M. A. Mahmood, "Transient Natural Convection Heat Transfer of Al2O3-Water Nanofluid in Enclosure: A Numerical Study," *Int. Ref. J. Eng. Sci.*, vol. 3, no. 3, pp. 41–50, 2014.

[194] F. Akbaridoust, M. Rakhsha, A. Abbassi, and M. Saffar-Avval, "Experimental and numerical investigation of nanofluid heat transfer in helically coiled tubes at constant wall temperature using dispersion model," *Int. J. Heat Mass Transf.*, vol. 58, no. 1–2, pp. 480–491, 2013.

[195] Y. He, Y. Men, Y. Zhao, H. Lu, and Y. Ding, “Numerical investigation into the convective heat transfer of TiO2nanofluids flowing through a straight tube under the laminar flow conditions,” *Appl. Therm. Eng.*, vol. 29, no. 10, pp. 1965–1972, 2009.

[196] S. Z. Heris, M. N. Esfahany, and G. Etemad, “Numerical investigation of nanofluid laminar convective heat transfer through a circular tube,” *Numer. Heat Transf. Part A Appl.*, vol. 52, no. 11, pp. 1043–1058, 2007.

[197] S. B. Islami, B. Dastvareh, and R. Gharraei, “Numerical study of hydrodynamic and heat transfer of nanofluid flow in microchannels containing micromixer,” *Int. Commun. Heat Mass Transf.*, vol. 43, pp. 146–154, 2013.

[198] M. Ismail, S. Fotowat, and A. Fartaj, “Simulation of Al2O3-ATF nanofluid in a compact heat exchanger,” *Int. Conf. Fluid Flow, Heat Mass Transf.*, no. 149, pp. 1–8, 2015.

[199] M. Ismail, S. Fotowat, and A. Fartaj, “Transient response of minichannel heat exchanger using Al2O3-EG/W nanofluid,” in *SAE Technical Paper*, 2016, vol. 2016-01–02.

[200] M. Izadi, A. Behzadmehr, and D. Jalali-Vahida, “Numerical study of developing laminar forced convection of a nanofluid in an annulus,” *Int. J. Therm. Sci.*, vol. 48, no. 11, pp. 2119–2129, 2009.

[201] A. Jafari, T. Tynjälä, S. M. Mousavi, and P. Sarkomaa, “Simulation of heat transfer in a ferrofluid using computational fluid dynamics technique,” *Int. J. Heat*

Fluid Flow, vol. 29, no. 4, pp. 1197–1202, 2008.

[202] R. Y. Jou and S. C. Tzeng, “Numerical research of nature convective heat transfer enhancement filled with nanofluids in rectangular enclosures,” *Int. Commun. Heat Mass Transf.*, vol. 33, no. 6, pp. 727–736, 2006.

[203] M. Kalbasi and A. Saeedi, “Numerical investigation into the convective heat transfer of CuO nanofluids flowing through a straight tube with uniform heat flux,” *Indian J. Sci. Technol.*, vol. 5, no. S3, pp. 2455–2458, 2012.

[204] R. Kamali and A. R. Binesh, “Numerical investigation of heat transfer enhancement using carbon nanotube-based non-Newtonian nanofluids,” *Int. Commun. Heat Mass Transf.*, vol. 37, no. 8, pp. 1153–1157, 2010.

[205] M. N. Labib, M. J. Nine, H. Afrianto, H. Chung, and H. Jeong, “Numerical investigation on effect of base fluids and hybrid nanofluid in forced convective heat transfer,” *Int. J. Therm. Sci.*, vol. 71, pp. 163–171, 2013.

[206] R. Lotfi, Y. Saboohi, and A. M. Rashidi, “Numerical study of forced convective heat transfer of Nanofluids: Comparison of different approaches,” *Int. Commun. Heat Mass Transf.*, vol. 37, no. 1, pp. 74–78, 2010.

[207] Q. S. Mahdi, S. A. Fattah, and F. Jumia, “Numerical investigation to evaluate the performance of helical coiled tube heat exchanger with and without nanofluid,” in *The ASME 2013 International Mechanical Engineering Congress and Exposition IMECE2013*, 2013, pp. 1–11.

[208] A. H. Mahmoudi, M. Shahi, and F. Talebi, “Effect of inlet and outlet location on

the mixed convective cooling inside the ventilated cavity subjected to an external nanofluid," *Int. Commun. Heat Mass Transf.*, vol. 37, no. 8, pp. 1158–1173, 2010.

[209] S. E. B. Maïga, C. T. Nguyen, N. Galanis, and G. Roy, "Heat transfer behaviours of nanofluids in a uniformly heated tube," *Superlattices Microstruct.*, vol. 35, no. 3–6, pp. 543–557, 2004.

[210] M. A. Mansour, M. A. Bakeir, and A. Chamkha, "Natural convection inside a C-shaped nanofluid-filled enclosure with localized heat sources," *Int. J. Numer. Methods Heat Fluid Flow*, vol. 24, no. 8, pp. 1954–1978, 2014.

[211] Y. He, Y. Men, Y. Zhao, H. Lu, and Y. Ding, "Numerical investigation into the convective heat transfer of CuO nanofluids flowing through a straight tube with uniform heat flux," *Int. Commun. Heat Mass Transf.*, vol. 37, no. 10, pp. 1–8, 2009.

[212] M. H. Matin and I. Pop, "Numerical study of mixed convection heat transfer of a nanofluid in an eccentric annulus," *Numer. Heat Transf. Part A Appl.*, vol. 65, no. 1, pp. 84–105, 2014.

[213] R. M. Moghari, A. Akbarinia, M. Shariat, F. Talebi, and R. Laur, "Investigation effect of nanoparticle mean diameter on mixed convection Al2O3-water nanofluid flow in an annulus by two phase mixture model," *Int. Commun. Heat Mass Transf.*, vol. 49, pp. 25–35, 2013.

[214] R. M. Moghari, A. Akbarinia, M. Shariat, F. Talebi, and R. Laur, "Two phase mixed convection Al2O3-water nanofluid flow in an annulus," *Int. J. Multiph.*

Flow, vol. 37, no. 6, pp. 585–595, 2011.

[215] R. M. Moghari, F. Talebi, R. Rafee, and M. Shariat, “Numerical study of pressure drop and thermal characteristics of Al2O3-water nanofluid flow in horizontal annuli,” *Heat Transf. Eng.*, vol. 36, no. 2, pp. 166–177, 2015.

[216] S. K. Mohammadian, H. Reza Seyf, and Y. Zhang, “Performance augmentation and optimization of aluminum oxide-water nanofluid flow in a two-fluid microchannel heat exchanger,” *J. Heat Transfer*, vol. 136, no. February, pp. 021701,1–9, 2014.

[217] H. A. Mohammed, G. Bhaskaran, N. H. Shuaib, and R. Saidur, “Numerical study of heat transfer enhancement of counter nanofluids flow in rectangular microchannel heat exchanger,” *Superlattices Microstruct.*, vol. 50, no. 3, pp. 215–233, 2011.

[218] S. M. Aminossadati and B. Ghasemi, “Enhanced natural convection in an isosceles triangular enclosure filled with a nanofluid,” *Comput. Math. with Appl.*, vol. 61, no. 7, pp. 1739–1753, 2011.

[219] A. Mokmeli and M. Saffar-Avval, “Prediction of nanofluid convective heat transfer using the dispersion model,” *Int. J. Therm. Sci.*, vol. 49, no. 3, pp. 471–478, 2010.

[220] T. G. Myers, M. M. MacDevette, and H. Ribera, “A time-dependent model to determine the thermal conductivity of a nanofluid,” *J. Nanoparticle Res.*, vol. 15, no. 7, 2013.

[221] K. Narrein, S. Sivasankaran, and P. Ganesan, “Two-phase analysis of a helical microchannel heat sink using nanofluids,” *Numer. Heat Transf. Part A Appl.*, vol. 68, no. 11, pp. 1266–1279, 2015.

[222] R. Nasrin, S. Parvin, M. A. Alim, and A. J. Chamkha, “Transient analysis on forced convection phenomena in a fluid valve using nanofluid,” *Numer. Heat Transf. Part A Appl.*, vol. 62, no. 7, pp. 589–604, 2012.

[223] C. T. Nguyen and M. Le Menn, “Two-phase modelling of nanofluid heat transfer in a microchannel heat sink,” *WIT Trans. Modelling Simul.*, vol. 48, pp. 451–460, 2009.

[224] S. J. Palm, G. Roy, and C. T. Nguyen, “Heat transfer enhancement with the use of nanofluids in radial flow cooling systems considering temperature-dependent properties,” *Appl. Therm. Eng.*, vol. 26, no. 17–18, pp. 2209–2218, 2006.

[225] C. V. Popa, C. T. Nguyen, S. Fohanno, and G. Polidori, “Transient mixed convection flow of nanofluids in a vertical tube,” *Int. J. Numer. Methods Heat Fluid Flow*, vol. 24, no. 2, pp. 376–389, 2014.

[226] M. Rahimi-Esbo, A. A. Ranjbar, A. Ramiar, M. Rahgoshay, and A. Arya, “Numerical study of the turbulent forced convection jet flow of nanofluid in a converging duct,” *Numer. Heat Transf. Part A Appl.*, vol. 62, no. 1, pp. 60–79, 2012.

[227] P. Rana and R. Bhargava, “Numerical study of heat transfer enhancement in mixed convection flow along a vertical plate with heat source/sink utilizing nanofluids,”

Commun. Nonlinear Sci. Numer. Simul., vol. 16, no. 11, pp. 4318–4334, 2011.

[228] M. M. Rashidi, A. Hosseini, I. Pop, S. Kumar, and N. Freidoonimehr, “Comparative numerical study of single and two-phase models of nanofluid heat transfer in wavy channel,” *Appl. Math. Mech. (English Ed.*, vol. 35, no. 7, pp. 831–848, 2014.

[229] W. H. Azmi, K. V. Sharma, P. K. Sarma, R. Mamat, S. Anuar, and L. Syam Sundar, “Numerical validation of experimental heat transfer coefficient with SiO2nanofluid flowing in a tube with twisted tape inserts,” *Appl. Therm. Eng.*, vol. 73, no. 1, pp. 294–304, 2014.

[230] M. M. Rashidi, M. Nasiri, M. Khezerloo, and N. Laraqi, “Numerical investigation of magnetic field effect on mixed convection heat transfer of nanofluid in a channel with sinusoidal walls,” *J. Magn. Magn. Mater.*, vol. 401, pp. 159–168, 2016.

[231] B. Rimbault, C. T. Nguyen, and N. Galanis, “Numerical modelling of nanofluid heat transfer inside a microchannel heat sink,” in *The ASME 2012 10th International Conference on Nanochannels, Microchannels, and Minichannels, ICNMM2012*, 2012, no. 21, pp. 1–10.

[232] A. P. Sasmito, J. C. Kurnia, and A. S. Mujumdar, “Numerical evaluation of laminar heat transfer enhancement in nanofluid flow in coiled square tubes,” *Nanoscale Res. Lett.*, vol. 6, pp. 1–14, 2011.

[233] I. O. Sert, N. Sezer-Uzol, and S. Kakaç, “Numerical analysis of transient laminar

forced convection of nanofluids in circular ducts," *Heat Mass Transf.*, vol. 49, no. 10, pp. 1405–1417, 2013.

[234] M. Shahi, A. H. Mahmoudi, and F. Talebi, "Numerical simulation of steady natural convection heat transfer in a 3-dimensional single-ended tube subjected to a nanofluid," *Int. Commun. Heat Mass Transf.*, vol. 37, no. 10, pp. 1535–1545, 2010.

[235] M. Shahi, A. H. Mahmoudi, and F. Talebi, "A numerical investigation of conjugated-natural convection heat transfer enhancement of a nanofluid in an annular tube driven by inner heat generating solid cylinder," *Int. Commun. Heat Mass Transf.*, vol. 38, no. 4, pp. 533–542, 2011.

[236] M. Shariat, A. Akbarinia, A. H. Nezhad, A. Behzadmehr, and R. Laur, "Numerical study of two phase laminar mixed convection nanofluid in elliptic ducts," *Appl. Therm. Eng.*, vol. 31, no. 14–15, pp. 2348–2359, 2011.

[237] S. Tahir and M. Mital, "Numerical investigation of laminar nanofluid developing flow and heat transfer in a circular channel," *Appl. Therm. Eng.*, vol. 39, pp. 8–14, 2012.

[238] F. Talebi, A. H. Mahmoudi, and M. Shahi, "Numerical study of mixed convection flows in a square lid-driven cavity utilizing nanofluid," *Int. Commun. Heat Mass Transf.*, vol. 37, no. 1, pp. 79–90, 2010.

[239] R. S. Vajjha, D. K. Das, and P. K. Namburu, "Numerical study of fluid dynamic and heat transfer performance of Al2O3 and CuO nanofluids in the flat tubes of a

radiator," *Int. J. Heat Fluid Flow*, vol. 31, no. 4, pp. 613–621, 2010.

[240] M. Bahiraei, "A numerical study of heat transfer characteristics of CuO-water nanofluid by Euler-Lagrange approach," *J. Therm. Anal. Calorim.*, vol. 123, no. 2, pp. 1591–1599, 2016.

[241] Y. T. Yang and F. H. Lai, "Numerical investigation of cooling performance with the use of Al2O3/water nanofluids in a radial flow system," *Int. J. Therm. Sci.*, vol. 50, no. 1, pp. 61–72, 2011.

[242] Y. T. Yang, Y. H. Wang, and B. Y. Huang, "Numerical optimization for nanofluid flow in microchannels using entropy generation minimization," *Numer. Heat Transf. Part A Appl.*, vol. 67, no. 5, pp. 571–588, 2015.

[243] Z. T. Yu, W. Wang, X. Xu, L. W. Fan, Y. C. Hu, and K. F. Cen, "A numerical investigation of transient natural convection heat transfer of aqueous nanofluids in a differentially heated square cavity," *Int. Commun. Heat Mass Transf.*, vol. 38, no. 5, pp. 585–589, 2011.

[244] Z. T. Yu, X. Xu, Y. C. Hu, L. W. Fan, and K. F. Cen, "A numerical investigation of transient natural convection heat transfer of aqueous nanofluids in a horizontal concentric annulus," *Int. J. Heat Mass Transf.*, vol. 55, no. 4, pp. 1141–1148, 2012.

[245] W. I. A. Aly, "Numerical study on turbulent heat transfer and pressure drop of nanofluid in coiled tube-in-tube heat exchangers," *Energy Convers. Manag.*, vol. 79, pp. 304–316, 2014.

[246] Z. Alloui, P. Vasseur, and M. Reggio, “Natural convection of nanofluids in a shallow cavity heated from below,” *Int. J. Therm. Sci.*, vol. 50, no. 3, pp. 385–393, 2011.

[247] J. Koo and C. Kleinstreuer, “Viscous dissipation effects in microtubes and microchannels,” *Int. J. Heat Mass Transf.*, vol. 47, no. 14–16, pp. 3159–3169, 2004.

[248] V. Bianco, F. Chiacchio, O. Manca, and S. Nardini, “Numerical investigation of nanofluids forced convection in circular tubes,” *Appl. Therm. Eng.*, vol. 29, no. 17–18, pp. 3632–3642, 2009.

[249] V. Bianco, O. Manca, and S. Nardini, “Numerical investigation of transient single phase forced convection of nanofluids in circular tubes,” *WIT Trans. Eng. Sci.*, vol. 61, pp. 3–12, 2008.

[250] J. Koo and C. Kleinstreuer, “A new thermal conductivity model for nanofluids,” *J. Nanoparticle Res.*, vol. 6, no. 6, pp. 577–588, 2004.

[251] H. C. Brinkman, “The viscosity of concentrated suspensions and solutions,” *J. Chem. Phys.*, vol. 20, no. 4, p. 571, 1952.

[252] A. Einstein, “Investigation on the theory of Brownian movement,” 1956.

[253] G. K. Batchelor, “The effect of Brownian motion on the bulk stress in a suspension of spherical particles,” *J. Fluid Mech.*, vol. 83, no. 1, pp. 97–117, 1977.

[254] T. S. Lundgren, “Slow flow through stationary random beds and suspensions of

spheres," *J. Fluid Mech.*, vol. 51, no. 2, pp. 273–299, 1972.

[255] A. L. Graham and R. Byron Bird, "Particle clusters in concentrated suspensions. 1. Experimental observations of particle clusters," *Ind. Eng. Chem. Fundam.*, vol. 23, no. 4, pp. 406–410, 1984.

[256] C. T. Nguyen *et al.*, "Temperature and particle-size dependent viscosity data for water-based nanofluids - Hysteresis phenomenon," *Int. J. Heat Fluid Flow*, vol. 28, no. 6, pp. 1492–1506, 2007.

[257] N. Masoumi, N. Sohrabi, and A. Behzadmehr, "A new model for calculating the effective viscosity of nanofluids," *J. Phys. D. Appl. Phys.*, vol. 42, no. 5, 2009.

[258] S. U. S. Choi, "Nanofluid technology: Current status and future research.," *Argonne National Laboratory, ANL/ET/CP-97466*. The U.S. Department of Energy, Argonne, Illinois, 1998.

[259] Z. H. Han, F. Y. Cao, and B. Yang, "Synthesis and thermal characterization of phase-changeable indium/polyalphaolefin nanofluids," *Appl. Phys. Lett.*, vol. 92, no. 24, 2008.

[260] W. Yu and H. Xie, "A Review on nanofuids: preparation, stability mechanisms, and applications," *J. Nanofluids*, vol. 2012, no. Article ID 435873, pp. 1–17, 2012.

[261] A. K. Singh and V. S. Raykar, "Microwave synthesis of silver nanofluids with polyvinylpyrrolidone (PVP) and their transport properties," *Colloid Polym. Sci.*, vol. 286, no. 14–15, pp. 1667–1673, 2008.

[262] D. Li and R. B. Kaner, “Processable stabilizer-free polyaniline nanofiber aqueous colloids,” *Chem. Commun.*, no. 26, pp. 3286–3288, 2005.

[263] D. Kim *et al.*, “Convective heat transfer characteristics of nanofluids under laminar and turbulent flow conditions,” *Curr. Appl. Phys.*, vol. 9, no. 2 SUPPL., pp. e119–e123, 2009.

[264] L. Wang and X. Wei, “Nanofluids: Synthesis, heat conduction, and extension,” *J. Heat Transfer*, vol. 131, no. 3, pp. 033102, 1–7, 2009.

[265] D. Zhu, X. Li, N. Wang, X. Wang, J. Gao, and H. Li, “Dispersion behavior and thermal conductivity characteristics of Al2O3-H2O nanofluids,” *Curr. Appl. Phys.*, vol. 9, no. 1, pp. 131–139, 2009.

[266] M. Bahiraei, “A comprehensive review on different numerical approaches for simulation in nanofluids: Traditional and novel techniques,” *J. Dispers. Sci. Technol.*, vol. 35, no. 7, pp. 984–996, 2014.

[267] M. S. Mojarrad, A. Keshavarz, and A. Shokouhi, “Nanofluids thermal behavior analysis using a new dispersion model along with single-phase,” *Heat Mass Transf. und Stoffuebertragung*, vol. 49, no. 9, pp. 1333–1343, 2013.

[268] K. V. Wong and O. De Leon, “Applications of nanofluids: Current and future,” *Adv. Mech. Eng.*, vol. 2010, 2010.

[269] W. Yu, D. M. France, E. V. Timofeeva, D. Singh, and J. L. Routbort, “Thermophysical property-related comparison criteria for nanofluid heat transfer enhancement in turbulent flow,” *Appl. Phys. Lett.*, vol. 96, no. 21, pp. 3–5, 2010.

[270] R. Saidur, S. N. Kazi, M. S. Hossain, M. M. Rahman, and H. A. Mohammed, "A review on the performance of nanoparticles suspended with refrigerants and lubricating oils in refrigeration systems," *Renew. Sustain. Energy Rev.*, vol. 15, no. 1, pp. 310–323, 2011.

[271] R. Saidur, K. Y. Leong, and H. A. Mohammad, "A review on applications and challenges of nanofluids," *Renew. Sustain. Energy Rev.*, vol. 15, no. 3, pp. 1646–1668, 2011.

[272] M. Chopkar, P. K. Das, and I. Manna, "Synthesis and characterization of nanofluid for advanced heat transfer applications," *Scr. Mater.*, vol. 55, no. 6, pp. 549–552, 2006.

[273] W. Yu, D. M. France, J. L. Routbort, and S. U. S. Choi, "Review and comparison of nanofluid thermal conductivity and heat transfer enhancements," *Heat Transf. Eng.*, vol. 29, no. 5, pp. 432–460, 2008.

[274] N. M. Mishra, Purna ChandraSantosh Kumar, "Thermal conductivity of nanofluids-An extensive literature review," *Int. J. Eng. Res. Technol.*, vol. 2, no. 9, pp. 734–745, 2013.

[275] D. Singh *et al.*, "An investigation of silicon carbide-water nanofluid for heat transfer applications," *J. Appl. Phys.*, vol. 105, no. 6, pp. 1–6, 2009.

[276] W. Yu, D. M. France, S. U. S. Choi, and J. L. Routbort, "Review and assessment of nanofluid technology for transportation and other applications.," *Argonne Natl. Lab. ANL/ESD/07-9*, no. April, 2007.

[277] W. Yu, D. M. France, D. S. Smith, D. Singh, E. V. Timofeeva, and J. L. Routbort, "Heat transfer to a silicon carbide/water nanofluid," *Int. J. Heat Mass Transf.*, vol. 52, no. 15–16, pp. 3606–3612, 2009.

[278] H. Chen, Y. Ding, A. Lapkin, and X. Fan, "Rheological behaviour of ethylene glycol-titanate nanotube nanofluids," *J. Nanoparticle Res.*, vol. 11, no. 6, pp. 1513–1520, 2009.

[279] M. Kole and T. K. Dey, "Thermal conductivity and viscosity of Al2O3 nanofluid based on car engine coolant," *J. Phys. D. Appl. Phys.*, vol. 43, no. 31, 2010.

[280] E. Ollivier, J. Bellettre, M. Tazerout, and G. C. Roy, "Detection of knock occurrence in a gas SI engine from a heat transfer analysis," *Energy Convers. Manag.*, vol. 47, no. 7–8, pp. 879–893, 2006.

[281] M. J. Kao, H. Chang, Y. Y. Wu, T. T. Tsung, and H. M. Lin, "Producing Aluminum-oxide brake nanofluids using plasma charging system," *J. Chinese Soc. Mech. Eng.*, vol. 28, no. 2, pp. 123–131, 2007.

[282] M. J. Kao, C. H. Lo, T. T. Tsung, Y. Y. Wu, C. S. Jwo, and H. M. Lin, "Copper-oxide brake nanofluid manufactured using arc-submerged nanoparticle synthesis system," *J. Alloys Compd.*, vol. 434–435, no. SPEC. ISS., pp. 672–674, 2007.

[283] M. J. Gupta H.K, Agrawal G.D, "An overview of nanofluids: A new media towards green environment," *Int. J. Enviromental Sci.*, vol. 3, no. 1, pp. 433–440, 2012.

[284] Y. Gan and L. Qiao, "Combustion characteristics of fuel droplets with addition of

nano and micron-sized aluminum particles," *Combust. Flame*, vol. 158, no. 2, pp. 354–368, 2011.

[285] P. Selvakumar and S. Suresh, "Use of Al2O3-Cu/Water Hybrid nanofluid in an electronic heat sink," *IEEE Trans. Components, Packag. Manuf. Technol.*, vol. 2, no. 10, pp. 1600–1607, 2012.

[286] Z. Zhang, Q. Xue, and J. Zhang, "Synthesis, structure and lubricating properties of dialkyldithiophosphate-modified Mo-S compound nanoclusters," *Wear*, vol. 209, no. 1–2, pp. 8–12, 1997.

[287] A. H. Battez, J. L. Viesca, R. González, D. Blanco, E. Asedegbega, and A. Osorio, "Friction reduction properties of a CuO nanolubricant used as lubricant for a NiCrBSi coating," *Wear*, vol. 268, no. 1, pp. 325–328, 2010.

[288] M. J. Kao and C. R. Lin, "Evaluating the role of spherical titanium oxide nanoparticles in reducing friction between two pieces of cast iron," *J. Alloys Compd.*, vol. 483, no. 1–2, pp. 456–459, 2009.

[289] J. L. Routbort, D. Singh, E. V. Timofeeva, W. Yu, and D. M. France, "Pumping power of nanofluids in a flowing system," *J. Nanoparticle Res.*, vol. 13, no. 3, pp. 931–937, 2011.

[290] K. Q. Ma and J. Liu, "Nano liquid-metal fluid as ultimate coolant," *Phys. Lett. Sect. A Gen. At. Solid State Phys.*, vol. 361, no. 3, pp. 252–256, 2007.

[291] S. shan Bi, L. Shi, and L. li Zhang, "Application of nanoparticles in domestic refrigerators," *Appl. Therm. Eng.*, vol. 28, no. 14–15, pp. 1834–1843, 2008.

[292] W. Jiang, G. Ding, and H. Peng, “Measurement and model on thermal conductivities of carbon nanotube nanorefrigerants,” *Int. J. Therm. Sci.*, vol. 48, no. 6, pp. 1108–1115, 2009.

[293] J. Wang, J. K. Carson, M. F. North, and D. J. Cleland, “A new approach to modelling the effective thermal conductivity of heterogeneous materials,” *Int. J. Heat Mass Transf.*, vol. 49, no. 17–18, pp. 3075–3083, 2006.

[294] K. J. Park and D. Jung, “Boiling heat transfer enhancement with carbon nanotubes for refrigerants used in building air-conditioning,” *Energy Build.*, vol. 39, no. 9, pp. 1061–1064, 2007.

[295] H. Peng, G. Ding, W. Jiang, H. Hu, and Y. Gao, “Heat transfer characteristics of refrigerant-based nanofluid flow boiling inside a horizontal smooth tube,” *Int. J. Refrig.*, vol. 32, no. 6, pp. 1259–1270, 2009.

[296] P. Naphon, D. Thongkum, and P. Assadamongkol, “Heat pipe efficiency enhancement with refrigerant-nanoparticles mixtures,” *Energy Convers. Manag.*, vol. 50, no. 3, pp. 772–776, 2009.

[297] D. P. Kulkarni, D. K. Das, and R. S. Vajjha, “Application of nanofluids in heating buildings and reducing pollution,” *Appl. Energy*, vol. 86, no. 12, pp. 2566–2573, 2009.

[298] D. Jung and D. N. Assanis, “Numerical modeling of cross flow compact heat exchanger with louvered fins using thermal resistance concept,” *SAE Tech. Pap.*, no. 724, 2006.

[299] M. Mishra, P. K. Das, and S. Sarangi, “Transient behaviour of crossflow heat exchangers due to perturbations in temperature and flow,” *Int. J. Heat Mass Transf.*, vol. 49, no. 5–6, pp. 1083–1089, 2006.

[300] J. T. Pearson, R. G. Leonard, and R. D. McCutchan, “Gain and time constant for finned serpentine crossflow heat exchangers.pdf,” *ASHRAE Trans.*, vol. 80, no. 11, pp. 255–267, 1974.

[301] W. Roetzel, M. Li, and X. Luo, “Dynamic behaviour of heat exchangers,” *Adv. Comput. Methods Heat Transf.*, pp. 451–460, 2002.

[302] Y. Xuan and W. Roetzel, “Dynamics of shell-and-tube heat exchangers to arbitrary temperature and step flow variations,” *AIChE J.*, vol. 39, no. 3, pp. 413–421, 1993.

[303] K. Silaipillayarputhur and S. A. Idem, “Step response of a single-pass crossflow heat exchanger with variable inlet temperatures and mass flow rates,” *J. Therm. Sci. Eng. Appl.*, vol. 4, pp. 044501, 1–6, 2012.

[304] T. Gao, B. G. Sammakia, J. F. Geer, A. Ortega, and R. Schmidt, “Dynamic analysis of cross flow heat exchangers in data centers using transient effectiveness Method,” *IEEE Trans. Components, Packag. Manuf. Technol.*, vol. 4, no. 12, pp. 1925–1935, 2014.

[305] A. L. Ondon, R. M. Cima, and A. J. Oberg, “The transient response of a two-fluid counter flow heat exchanger, the gas-turbine regenerator,” *Trans. Amer. Soc. Mech. Eng.*, vol. 80, pp. 1169–1179, 1957.

[306] J. S. Turton, “A method of evaluating transient response of gas-to-gas heat

exchangers," *J. Mech. Eng. Sci.*, vol. 2, no. 4, pp. 349–358, 1960.

[307] J. R. Gartner and H. L. Harrison, "Dynamics characteristics of water to air cross-flow heat exchanger," *ASHRAE Trans.*, vol. 71, pp. 212–224, 1965.

[308] G. E. Myers, J. W. Mitchell, and R. F. Norman, "The transient response of crossflow heat exchangers, evaporators, and condensers," *J. Heat Transfer*, no. February, pp. 75–80, 1967.

[309] F. E. Romie, "Transient response of gas-to-gas crossflow heat exchangers with neither gas mixed," *J. Heat Transfer*, vol. 105, no. August, pp. 563–570, 1983.

[310] M. Mishra, P. K. Das, and S. Sarangi, "Transient behavior of crossflow heat exchangers with longitudinal conduction and axial dispersion," *J. Heat Transfer*, vol. 126, no. June, pp. 425–433, 2004.

[311] T. Gao, B. G. Sammakia, B. T. Murray, A. Ortega, and R. Schmidt, "Cross flow heat exchanger modeling of transient temperature input conditions," *IEEE Trans. Components, Packag. Manuf. Technol.*, vol. 4, no. 11, pp. 1796–1807, 2014.

[312] T. Gao, B. Sammakia, and J. Geer, "Dynamic response and control analysis of cross flow heat exchangers under variable temperature and flow rate conditions," *Int. J. Heat Mass Transf.*, vol. 81, pp. 542–553, 2015.

[313] V. I. Sharma, J. Buongiorno, T. J. McKrell, and L. W. Hu, "Experimental investigation of transient critical heat flux of water-based zinc-oxide nanofluids," *Int. J. Heat Mass Transf.*, vol. 61, no. 1, pp. 425–431, 2013.

[314] H. Hassan and S. Harmand, “3D transient model of vapour chamber: Effect of nanofluids on its performance,” *Appl. Therm. Eng.*, vol. 51, no. 1–2, pp. 1191–1201, 2013.

[315] K. S. Suganthi and K. S. Rajan, “Improved transient heat transfer performance of ZnO-propylene glycol nanofluids for energy management,” *Energy Convers. Manag.*, vol. 96, pp. 115–123, 2015.

[316] R. Hajian, M. Layeghi, and K. Abbaspour Sani, “Experimental study of nanofluid effects on the thermal performance with response time of heat pipe,” *Energy Convers. Manag.*, vol. 56, pp. 63–68, 2012.

[317] Q. S. Liu, M. Shibahara, and K. Fukuda, “Transient heat transfer for forced convection flow of helium gas over a horizontal plate,” *Exp. Heat Transf.*, vol. 21, no. 3, pp. 206–219, 2008.

[318] C. H. Li, W. Williams, J. Buongiorno, L.-W. Hu, and G. P. Peterson, “Transient and steady-state experimental comparison study of effective thermal conductivity of Al2O3⁄water nanofluids,” *J. Heat Transfer*, vol. 130, no. April, pp. 042407, 1–7, 2008.

[319] T. M. Adams, S. I. Abdel-Khalik, S. M. Jeter, and Z. H. Qureshi, “An experimental investigation of single-phase forced convection in microchannels,” *Int. J. Heat Mass Transf.*, vol. 41, no. 6–7, pp. 851–857, 1998.

[320] J. Tu, G. H. Eoh, and C. Liu, *Computational fluid dynamics: A practical approach*, 1st ed. Burlington, MA 01803, U.S.A.: Butterworth-Heinemann, 2008.

[321] E. S. Dasgupta, “Experimental study on heat transfer and flow characteristics of air cooling through cross-flow microchannel heat exchanger,” University of Windsor, 2011.

[322] S. Fotowat, S. Askar, and A. Fartaj, “Experimental transient response of a minichannel heat exchanger with step flow variation,” *Exp. Therm. Fluid Sci.*, vol. 89, pp. 128–139, 2017.

[323] J. Peiro and S. Sherwin, *Handbook of materials modeling. Volume I: Methods and models,* S. Yip. Netherlands: Springer, 2005.

[324] ANSYS Inc., *ANSYS Fluent Theory Guide*, R15 ed. Canonsburg, PA, USA, 2013.

[325] ANSYS Inc., *ANSYS Fluent User’ s Guide*, R15 ed. Canonsburg, PA, USA, 2013.

[326] H. Versteeg and W. Malalasekera, *Introduction to computational fluid dynamics-The finite volume method*, 2nd ed. Harlow, England: Pearson Education Limited, 2007.

[327] AIAA (1998), “Guide for the verification and validation of computational fluid dynamics simulations,” *AIAA G-077-1998(2002).*

[328] W. L. Oberkampf, T. G. Trucano, and C. Hirsch, “Verification and validation for modeling and simulation in computational science and engineering,” in *Foundations for Verification and Validation in the 21st Century Workshop*, 2002, pp. 1–74.

[329] S. Fotowat, S. Askar, and A. Fartaj, “Transient response of a meso heat exchanger

with temperature step variation," *Int. J. Heat Mass Transf.*, vol. 122, pp. 1172–1181, 2018.

[330] H. Han, B. Li, and W. Shao, "Multi-objective optimization of outward convex corrugated tubes using response surface methodology," *Appl. Therm. Eng.*, vol. 70, no. 1, pp. 250–262, 2014.

[331] M. Sheikholeslami, M. Gorji-Bandpy, and D. D. Ganji, "Review of heat transfer enhancement methods: Focus on passive methods using swirl flow devices," *Renew. Sustain. Energy Rev.*, vol. 49, pp. 444–469, 2015.

[332] A. Dewan and P. Srivastava, "A review of heat transfer enhancement through flow disruption in a microchannel," *J. Therm. Sci.*, vol. 24, no. 3, pp. 203–214, 2015.

[333] L. Ventola *et al.*, "Rough surfaces with enhanced heat transfer for electronics cooling by direct metal laser sintering," *Int. J. Heat Mass Transf.*, vol. 75, pp. 58–74, 2014.

[334] N. R. Kuppusamy, "Thermal Enhancement in a Microchannel," University of Malaya, Kualalumpur, 2016.

APPENDICES

Appendix A: Copyright Permissions for Previously Published Materials

A1: Copyright Permission for Ismail et al. 2016, doi: 10.11159/jffhmt.2016.005

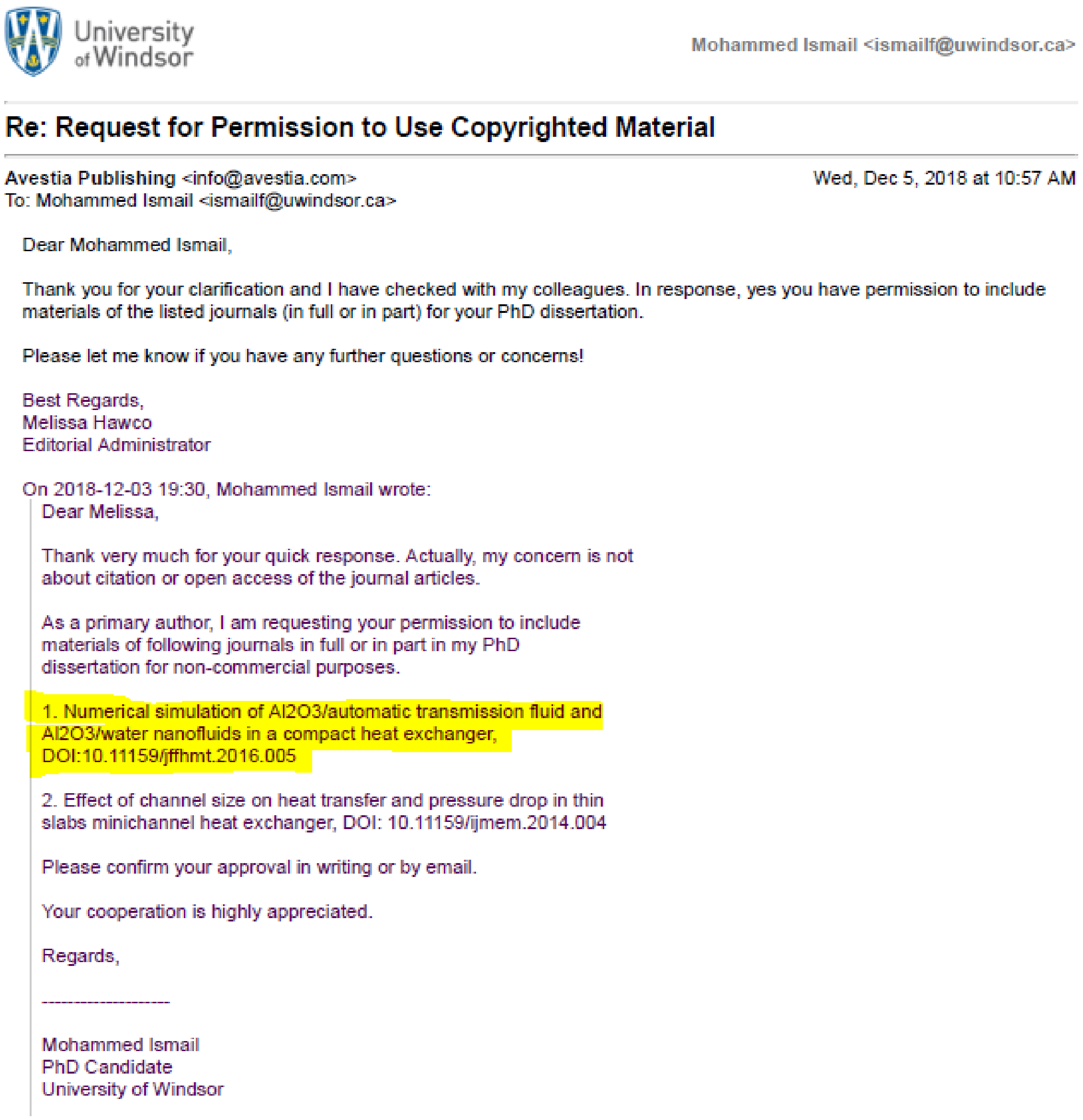

University of Windsor

Mohammed Ismail <ismailf@uwindsor.ca>

Re: Request for Permission to Use Copyrighted Material

Avestia Publishing <info@avestia.com>
Wed, Dec 5, 2018 at 10:57 AM
To: Mohammed Ismail <ismailf@uwindsor.ca>

Dear Mohammed Ismail,

Thank you for your clarification and I have checked with my colleagues. In response, yes you have permission to include materials of the listed journals (in full or in part) for your PhD dissertation.

Please let me know if you have any further questions or concerns!

Best Regards,
Melissa Hawco
Editorial Administrator

On 2018-12-03 19:30, Mohammed Ismail wrote:

> Dear Melissa,
>
> Thank very much for your quick response. Actually, my concern is not about citation or open access of the journal articles.
>
> As a primary author, I am requesting your permission to include materials of following journals in full or in part in my PhD dissertation for non-commercial purposes.
>
> 1. Numerical simulation of Al2O3/automatic transmission fluid and Al2O3/water nanofluids in a compact heat exchanger, DOI:10.11159/jffhmt.2016.005
>
> 2. Effect of channel size on heat transfer and pressure drop in thin slabs minichannel heat exchanger, DOI: 10.11159/ijmem.2014.004
>
> Please confirm your approval in writing or by email.
>
> Your cooperation is highly appreciated.
>
> Regards,
>
> --------------------
>
> Mohammed Ismail
> PhD Candidate
> University of Windsor

A2: Copyright Permission for Ismail et al. 2016, doi:10.4271/2016-01-0229

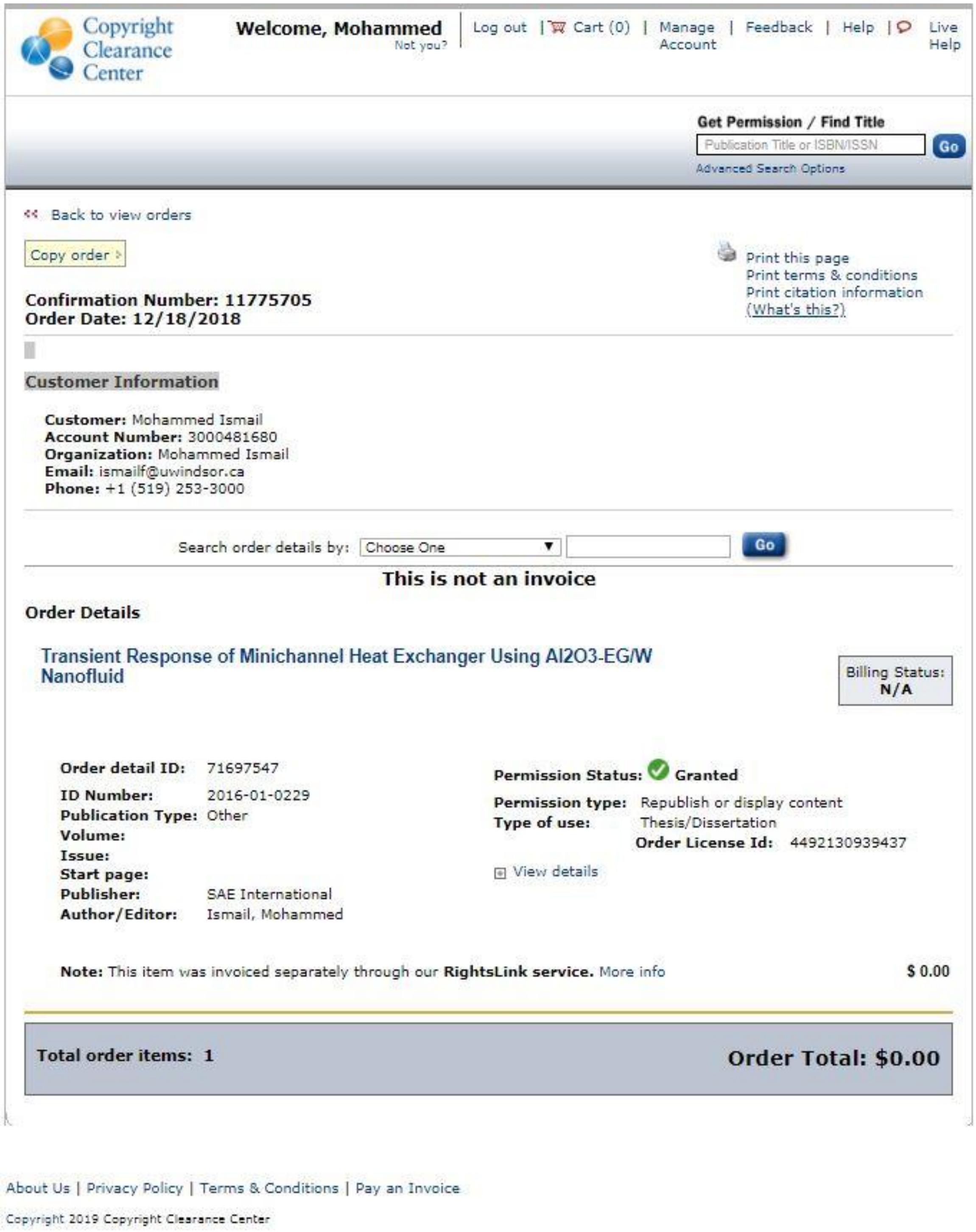

Confirmation Number: 11775705
Order Date: 12/18/2018

Customer Information

Customer: Mohammed Ismail
Account Number: 3000481680
Organization: Mohammed Ismail
Email: ismailf@uwindsor.ca
Phone: +1 (519) 253-3000

This is not an invoice

Order Details

Transient Response of Minichannel Heat Exchanger Using Al2O3-EG/W Nanofluid

Billing Status: **N/A**

Order detail ID: 71697547
ID Number: 2016-01-0229
Publication Type: Other
Volume:
Issue:
Start page:
Publisher: SAE International
Author/Editor: Ismail, Mohammed

Permission Status: ✓ **Granted**
Permission type: Republish or display content
Type of use: Thesis/Dissertation
Order License Id: 4492130939437

Note: This item was invoiced separately through our **RightsLink service.** More info $ 0.00

Total order items: 1 **Order Total: $0.00**

A3: Copyright Permission for Ismail et al. 2014, doi: 10.11159/ijmem.2014.004

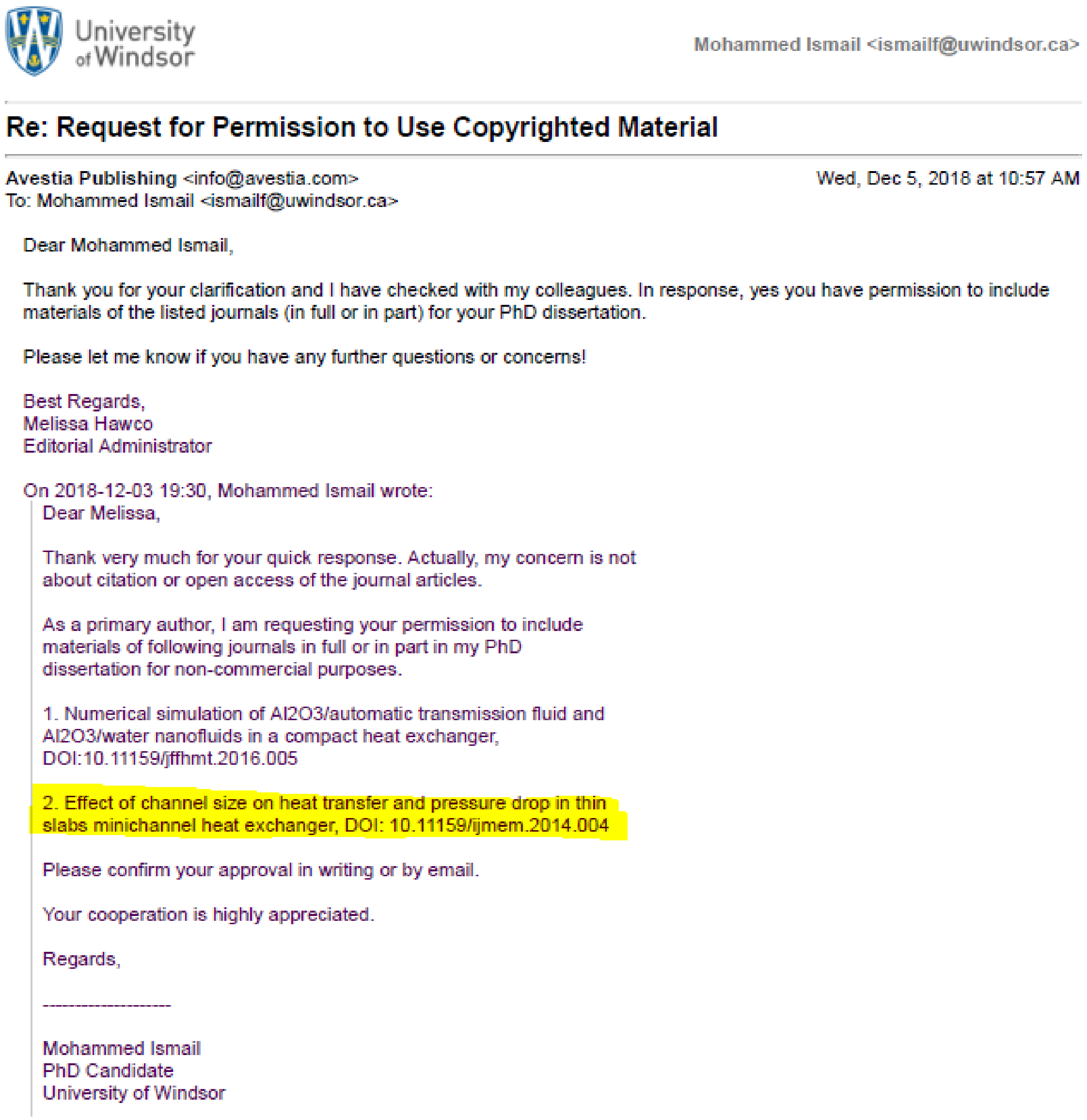

University of Windsor

Mohammed Ismail <ismailf@uwindsor.ca>

Re: Request for Permission to Use Copyrighted Material

Avestia Publishing <info@avestia.com> Wed, Dec 5, 2018 at 10:57 AM
To: Mohammed Ismail <ismailf@uwindsor.ca>

Dear Mohammed Ismail,

Thank you for your clarification and I have checked with my colleagues. In response, yes you have permission to include materials of the listed journals (in full or in part) for your PhD dissertation.

Please let me know if you have any further questions or concerns!

Best Regards,
Melissa Hawco
Editorial Administrator

On 2018-12-03 19:30, Mohammed Ismail wrote:

> Dear Melissa,
>
> Thank very much for your quick response. Actually, my concern is not about citation or open access of the journal articles.
>
> As a primary author, I am requesting your permission to include materials of following journals in full or in part in my PhD dissertation for non-commercial purposes.
>
> 1. Numerical simulation of Al2O3/automatic transmission fluid and Al2O3/water nanofluids in a compact heat exchanger, DOI:10.11159/jffhmt.2016.005
>
> 2. Effect of channel size on heat transfer and pressure drop in thin slabs minichannel heat exchanger, DOI: 10.11159/ijmem.2014.004
>
> Please confirm your approval in writing or by email.
>
> Your cooperation is highly appreciated.
>
> Regards,
>
> --------------------
>
> Mohammed Ismail
> PhD Candidate
> University of Windsor

A4: Copyright Permission for Ismail et al. 2013, doi: 10.2316/P.2013.802-073

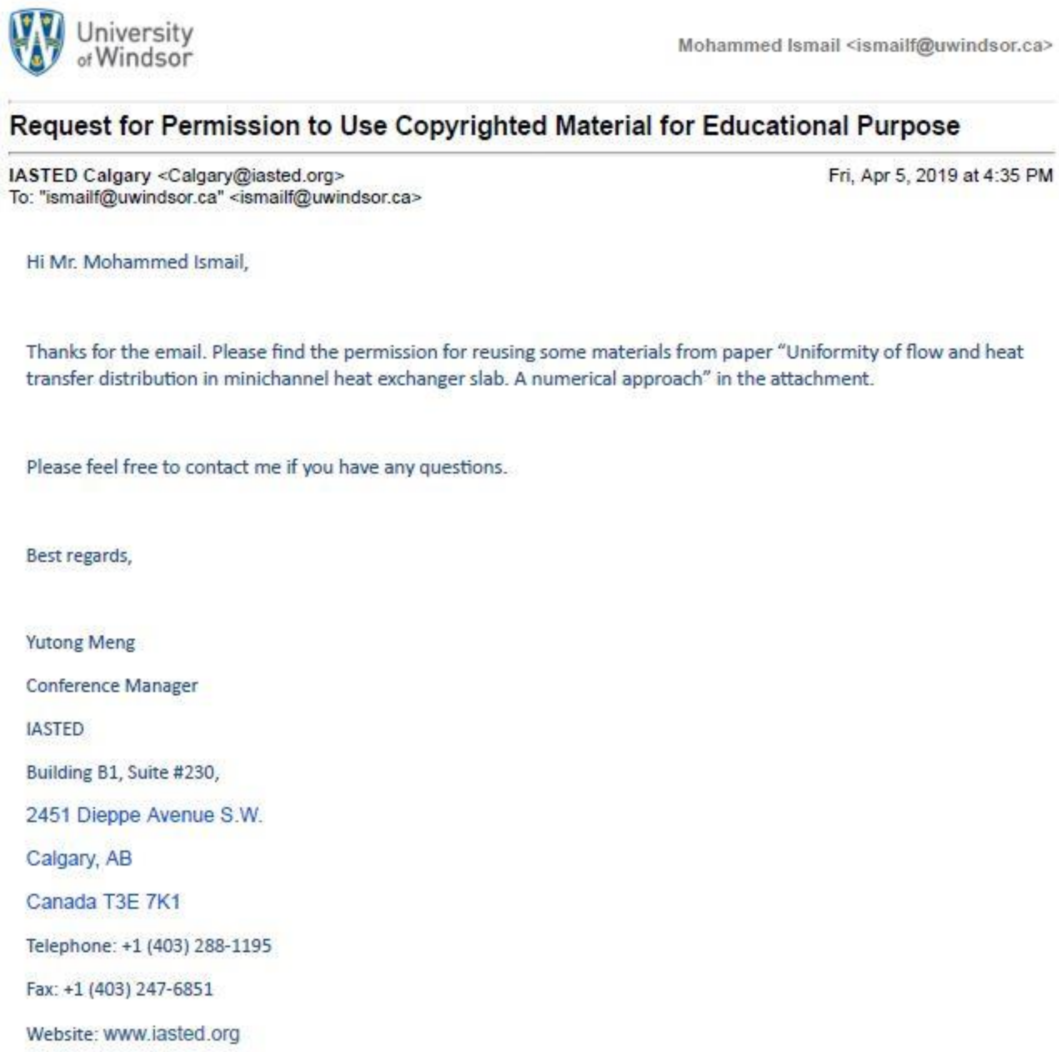

University of Windsor

Mohammed Ismail <ismailf@uwindsor.ca>

Request for Permission to Use Copyrighted Material for Educational Purpose

IASTED Calgary <Calgary@iasted.org>
To: "ismailf@uwindsor.ca" <ismailf@uwindsor.ca>

Fri, Apr 5, 2019 at 4:35 PM

Hi Mr. Mohammed Ismail,

Thanks for the email. Please find the permission for reusing some materials from paper "Uniformity of flow and heat transfer distribution in minichannel heat exchanger slab. A numerical approach" in the attachment.

Please feel free to contact me if you have any questions.

Best regards,

Yutong Meng

Conference Manager

IASTED

Building B1, Suite #230,

2451 Dieppe Avenue S.W.

Calgary, AB

Canada T3E 7K1

Telephone: +1 (403) 288-1195

Fax: +1 (403) 247-6851

Website: www.iasted.org

Appendix B: Tabular Representation of the Heat Transfer Intensification Techniques in Available Literature

Table B: Summary of the heat transfer intensification technique

Intensification techniques	**Description/function/purpose** [330–334]
I. Active techniques	
Surface vibration	A low or high frequency is employed to create surface vibrations, which results in elevated convective heat transfer coefficient. Heat transfer enhancement depends on the vibration intensity. This method is primarily used in single-phase heat transfer and flow process.
Flow pulsation and oscillations	Instead of applying surface vibrations, flow pulsations and oscillations are created in the fluid itself by means of ultrasonic vibrations, mechanical vibrations, stirring the fluid, or rotating the surface. This type of vibration is also applied for single-phase flows to enhance heat transfer.
Electrostatic fields	Electric field or magnetic field or a combination of the both fields from AC or DC sources is employed in heat exchangers, which induces better bulk mixing, electromagnetic pumping, or forced convection to intensify heat transfer. This method is appropriate in heat transport process comprising dielectric fluids.
Injection	In this procedure, similar or dissimilar fluid is injected into the primary fluid through a porous heat transport interface or upstream of the heat transfer unit. This method is employed for single phase heat transfer process.
Suction	Two phase nucleate boiling involves the vapor removal through a porous heated surface whereas in single phase flows fluid is withdrawn through the porous heated surface. This method is used for both two phase heat transfer and single phase heat transfer process.

II. Passive techniques	
Surface roughness	Multi-objective optimal designs of greater efficiency heat exchangers applied in nuclear plants by means of corrugated tube.
Extended surfaces	Fin, louvered strip and winglet etc. are employed to produce extended surfaces and create swirl turbulence as well as secondary flow, which support to elevate heat transfer.
Flow disruptions	Flow disruption can be developed by surface modifications, including protrusions, dimple surfaces, ribs, cavities and groove structures. These techniques promotes free stream separation at the leading edge, which result boundary layer development, boost mixing and increase heat transfer.
Channel curvature	Serpentine channels generate secondary flow, which support higher heat transfer coefficient. These are suitable for compact heat exchangers.
Re-entrant obstructions	At the re-entrant obstructions, flow fluctuations occur due to development of new boundary layer and flow mixing, which enhance the heat transfer.
Coiled tubes	Helical coiled tubes generate secondary flow, which support higher heat transfer coefficient. They are suitable for compact heat exchangers.
Fluid additives	Higher thermal conductivity nanoparticles are employed in basefluid, which increase the heat transfer coefficient.

Appendix C: Regression Analysis

C1: Evaluation of C_1 and D_1 for the Correlation of $T^*_{h,o}(t)$ under MR

The correlations for the ratio of $T^*_{h,o}(t)$ to $T^*_{h,o}(\infty)$ corresponding to each mass flow step are as follows:

$$T^*_{h,o}(t) = T^*_{h,o}(\infty)\{1 - 0.35e^{-0.09t^*}\} \text{ with } R^2 = 0.99, \text{ for MR=1.5} \tag{6.5.5}$$

$$T^*_{h,o}(t) = T^*_{h,o}(\infty)\{1 - 0.54e^{-0.13t^*}\} \text{ with } R^2 = 0.97, \text{ for MR=2.0} \tag{6.5.6}$$

$$T^*_{h,o}(t) = T^*_{h,o}(\infty)\{1 - 0.62e^{-0.17t^*}\} \text{ with } R^2 = 0.98, \text{ for MR=2.5} \tag{6.5.7}$$

$$T^*_{h,o}(t) = T^*_{h,o}(\infty)\{1 - 0.67e^{-0.18t^*}\} \text{ with } R^2 = 0.97, \text{ for MR=3.0} \tag{6.5.8}$$

The generalized form of above equations is as follows:

$$T^*_{h,o}(t) = T^*_{h,o}(\infty)\{1 - C_1e^{-D_1t^*}\} \tag{6.5.9}$$

The values of C_1 and D_1 from Equations 6.5.5 to 6.5.8 are shown in Table C-1.

Table C-1: The values of C_1 and D_1 in the correlation of $T^*_{h,o}(t)$ under MR

Mass flow rate step	MR	C_1	D_1
20g/s-30g/s	1.5	0.35	0.09
20g/s-40g/s	2.0	0.54	0.13
20g/s-50g/s	2.5	0.62	0.17
20g/s-60g/s	3.0	0.67	0.18

The relationship of MR with C_1 and D_1 in the correlation of $T^*_{h,o}(t)/\ T^*_{h,o}(\infty)$ are illustrated in Figures C-1 and C-2 as follows;

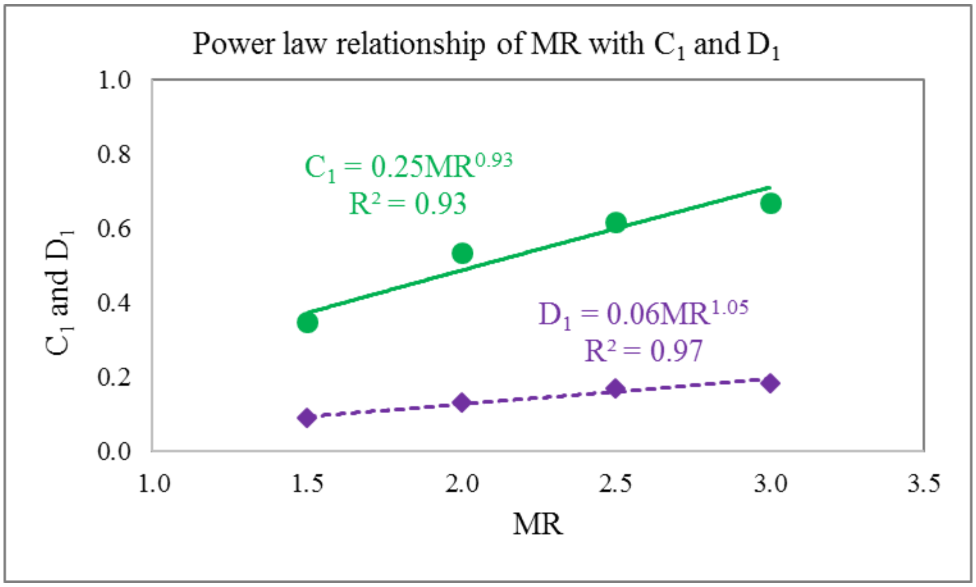

Figure C-1: Power law relationship of MR with coefficient C_1 and exponent D_1 in the correlation of transient dimensionless temperature

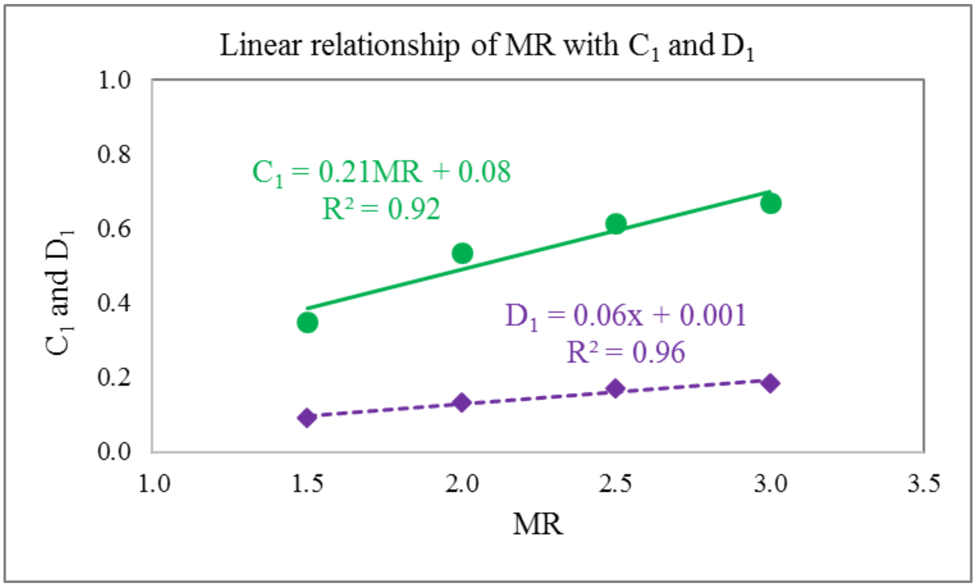

Figure C-2: Linear relationship of MR with coefficient C_1 and exponent D_1 in the correlation of transient dimensionless temperature

The relationship between MR and C_1 is taken from the best curve fit with R^2-value of 0.93, which follows power law relationship as

$$C_1 = 0.25 \mathrm{MR}^{0.93} \tag{6.5.10}$$

The relationship between MR and D_1 is also taken from the best curve fit with R^2-value of 0.97, which follows power law relationship as

$$D_1 = 0.06 \mathrm{MR}^{1.05} \tag{6.5.11}$$

C2: Evaluation of C_2 and D_2 in the Transient Correlation for Nu under MR

The correlations for the ratio of $\mathrm{Nu_h}(t)$ to $\mathrm{Nu_h}(\infty)$ corresponding to each mass flow step are as follows:

$$\mathrm{Nu_h}(t) = \mathrm{Nu_h}(\infty)\left\{1 + 0.24e^{-0.24t^*}\right\} \text{ with } R^2 = 0.96, \text{ for } \mathrm{MR} = 1.5 \tag{6.5.13}$$

$$\mathrm{Nu_h}(t) = \mathrm{Nu_h}(\infty)\left\{1 + 0.26e^{-0.20t^*}\right\} \text{ with } R^2 = 0.96, \text{ for } \mathrm{MR} = 2.0 \tag{6.5.14}$$

$$\mathrm{Nu_h}(t) = \mathrm{Nu_h}(\infty)\left\{1 + 0.28e^{-0.17t^*}\right\} \text{ with } R^2 = 0.95, \text{ for } \mathrm{MR} = 2.5 \tag{6.5.15}$$

$$\mathrm{Nu_h}(t) = \mathrm{Nu_h}(\infty)\left\{1 + 0.29e^{-0.13t^*}\right\} \text{ with } R^2 = 0.99, \text{ for } \mathrm{MR} = 3.0 \tag{6.5.16}$$

The generalized form of above equations is as follows:

$$\mathrm{Nu_h}(t) = \mathrm{Nu_h}(\infty)\left\{1 + C_2 e^{-D_2 t^*}\right\} \tag{6.5.17}$$

The values of C_2 and D_2 for Eqs. 6.5.11 to 6.5.15 are summarized in Table C-2.

Table C-2: The values of C_2 and D_2 in the correlation of $Nu_h(t)$ under MR

Mass flow rate step	MR	C_2	D_2
20g/s-30g/s	1.5	0.24	0.24
20g/s-40g/s	2.0	0.26	0.20
20g/s-50g/s	2.5	0.28	0.17
20g/s-60g/s	3.0	0.29	0.13

The relationship of MR with C_2 and D_2 in the correlation of $Nu_h(t)/Nu_h(\infty)$ are illustrated in Figures C-3 and C-4.

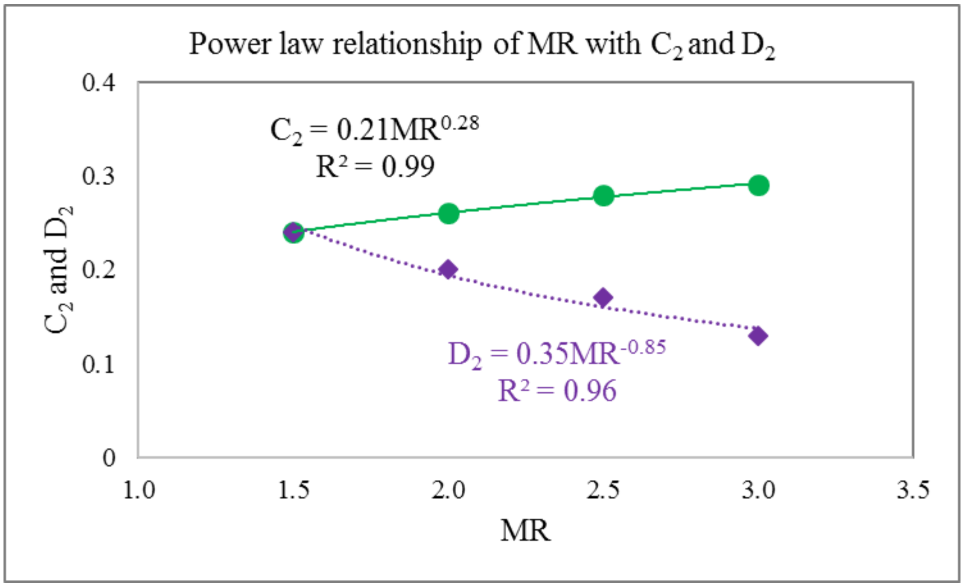

Figure C-3: Power law relationship of MR with coefficient C_2 and exponent D_2 in the correlation of $Nu_h(t)/Nu_h(\infty)$

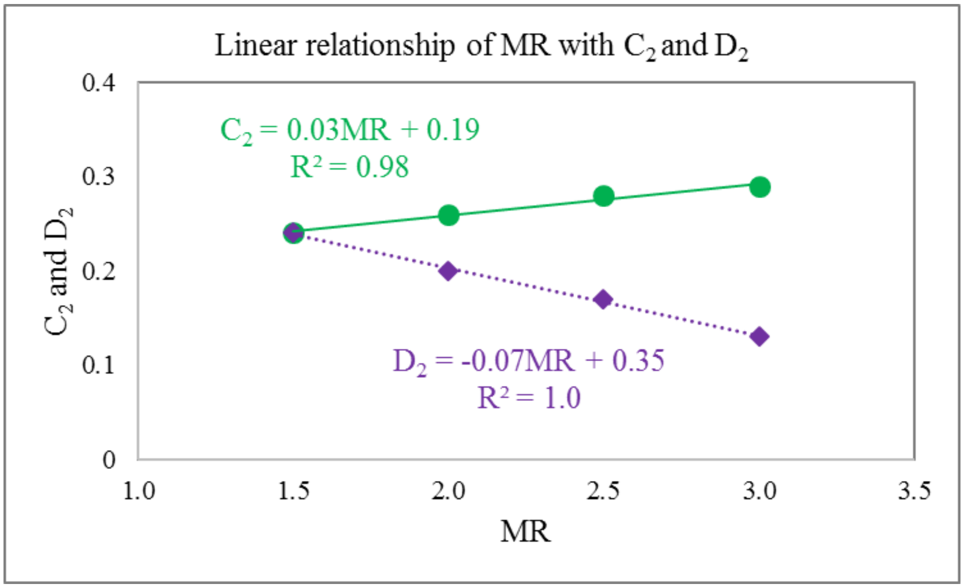

Figure C-4: Linear relationship of MR with coefficient C_2 and exponent D_2 in the correlation of $Nu_h(t)/Nu_h(\infty)$

The coefficient C_2 and exponent D_2, both depend on MR. The relationship of MR with C_2 and D_2 are evaluated from the best curve fit. The coefficient C_2 follows power law relationship with R^2-value of 0.99, while the exponent D_2 follows linear relationship with R^2-value of 1.0.

$$C_2 = 0.21MR^{0.28} \tag{6.5.18}$$

$$D_2 = -0.07MR + 0.35 \tag{6.5.19}$$

C3: Evaluation of C_3 and D_3 in the Transient Correlation of $T^*_{(h,o)}$ under TR for t*≤5

The correlations for the ratio of $T^*_{h,o}(t)$ to $T^*_{h,o}(\infty)$ corresponding to each temperature step for $t^* \leq 5$ are as follows:

For TR = 1.5: $$T^*_{h,o}(t) = T^*_{h,o}(\infty)\,\{0.001t^* + 0.45\} \quad (6.5.21)$$

For TR = 2.0: $$T^*_{h,o}(t) = T^*_{h,o}(\infty)\,\{0.001t^* + 0.29\} \quad (6.5.22)$$

For TR = 2.5: $$T^*_{h,o}(t) = T^*_{h,o}(\infty)\,\{0.002t^* + 0.21\} \quad (6.5.23)$$

For TR = 3.0: $$T^*_{h,o}(t) = T^*_{h,o}(\infty)\,\{0.003t^* + 0.16\} \quad (6.5.24)$$

For TR = 3.5: $$T^*_{h,o}(t) = T^*_{h,o}(\infty)\,\{0.003t^* + 0.13\} \quad (6.5.25)$$

For $t^* \leq 5$, The generalized form of above equations is as follows:

$$T^*_{h,o}(t) = T^*_{h,o}(\infty)\,\{C_3 t^* + D_3\} \quad (6.5.26)$$

The values of C_3 and D_3 from Eqs. 6.5.21 to 6.5.25 are summarized in Table C-3.

Table C-3: The values of C_3 and D_3 in the correlation of $T^*_h(t)$ under TR for $t^* \leq 5$

Temperature steps	TR	C_3	D_3
22^0C-33^0C	1.5	0.001	0.45
22^0C-44^0C	2.0	0.001	0.29
22^0C-55^0C	2.5	0.002	0.21
22^0C-66^0C	3.0	0.003	0.16
22^0C-77^0C	3.5	0.003	0.13

The relationships of TR with coefficient C_3 and exponent D_3 in the correlation of $T^*_{h,o}(t)/T^*_{h,o}(\infty)$ for t*≤5 are shown in Figure C-5.

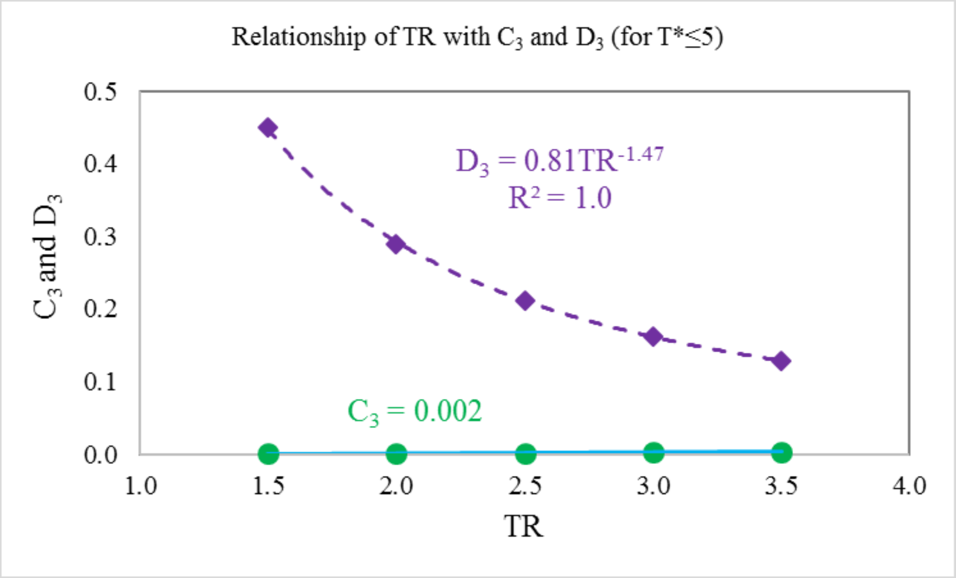

Figure C-5: Relationship of TR with C_3 and D_3 in the correlation of $T^*_{h,o}(t)/T^*_{h,o}(\infty)$ for t*≤5

The Figure C-5 displays that the coefficient C_3 is approximately constant, which is ≈ 0.002. However, the values of D_3 follow the power law relationship. The relationships of TR with C_3 and D_3 are as follows

$$C_3 = 0.002 \tag{6.5.27}$$

$$D_3 = 0.81\mathrm{TR}^{-1.47} \tag{6.5.28}$$

C4: Evaluation of C_4 and D_4 in the Transient Correlation of $T^*_{(h,o)}$ under TR for t*>5

The correlations for the ratio of $T^*_{h,o}(t)$ to $T^*_{h,o}(\infty)$ corresponding to each temperature step for $t^* > 5$ are as follows:

$$\text{For TR} = 1.5: \quad T^*_{h,o}(t) = T^*_{h,o}(\infty)\{1 - 1.84e^{-0.21t^*}\} \text{ with } R^2 = 0.98 \tag{6.5.29}$$

For TR = 2.0: $T^*_{h,o}(t) = T^*_{h,o}(\infty)\left\{1 - 2.24e^{-0.21t^*}\right\}$ with $R^2 = 0.97$ (6.5.30)

For TR = 2.5: $T^*_{h,o}(t) = T^*_{h,o}(\infty)\left\{1 - 2.50e^{-0.20t^*}\right\}$ with $R^2 = 0.98$ (6.5.31)

For TR = 3.0: $T^*_{h,o}(t) = T^*_{h,o}(\infty)\left\{1 - 2.77e^{-0.21t^*}\right\}$ with $R^2 = 0.97$ (6.5.32)

For TR = 3.5: $T^*_{h,o}(t) = T^*_{h,o}(\infty)\left\{1 - 2.92e^{-0.21t^*}\right\}$ with $R^2 = 0.97$ (6.5.33)

For $t^* > 5$, the generalized form of above equations is as follows:

$$T^*_{h,o}(t) = T^*_{h,o}(\infty)\left\{1 - C_4 e^{-D_4 t^*}\right\} \tag{6.5.34}$$

The values of C_4 and D_4 from Eqs. 6.5.29 to 6.5.33 are summarized in Table C-4.

Table C-4: Coefficient C_4 and exponent D_4 in the correlation of $T^*_h(t)$ under TR for $t^*>5$

Temperature steps	TR	C_4	D_4
22^0C-33^0C	1.5	1.84	0.21
22^0C-44^0C	2.0	2.24	0.21
22^0C-55^0C	2.5	2.50	0.20
22^0C-66^0C	3.0	2.77	0.21
22^0C-77^0C	3.5	2.92	0.21

The relationships of TR with coefficient C_4 and exponent D_4 in the correlation of the ratio of $T^*_{h,o}(t)$ to $T^*_{h,o}(\infty)$ for $t^*>5$ are shown in Figure C-6 as below;

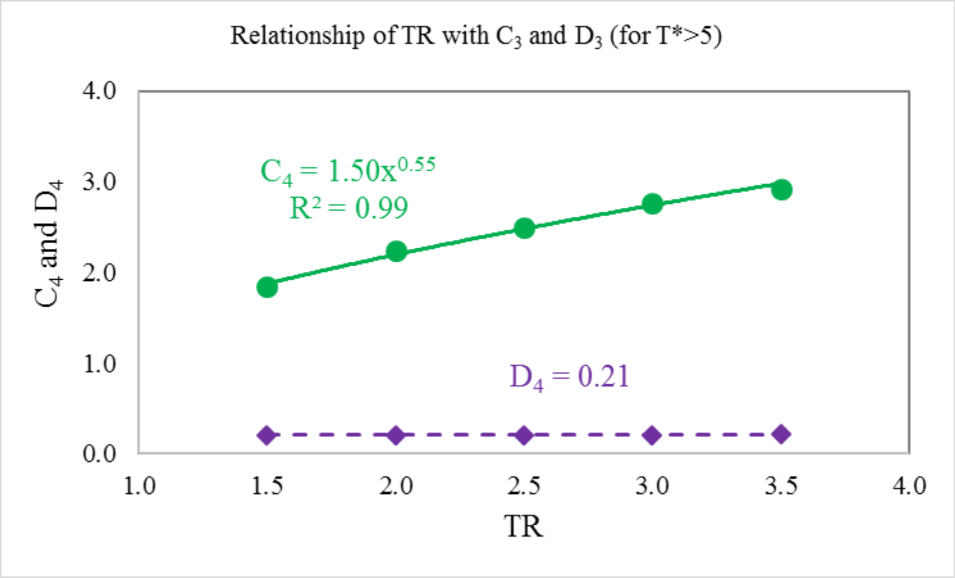

Figure C-6: Relationship of TR with coefficient C_4 and exponent D_4 in the correlation of $T^*_{h,o}(t)/T^*_{h,o}(\infty)$ for t*>5

Figure C-6 shows that the coefficient C_4 is strongly dependent on temperature steps and follows the power law relationship with R^2-value of 0.99. Whereas, the exponent D_4 is approximately a constant, which is ≈ 0.21. The relationships are as follows

$$C_4 = 1.50\mathrm{TR}^{0.55} \tag{6.5.35}$$

$$D_4 = 0.21 \tag{6.5.36}$$

C5: Evaluation of C_5 and D_5 in the Transient Correlation for Nu under TR

The correlations for the ratio of $\mathrm{Nu_h}(t)$ to $\mathrm{Nu_h}(\infty)$ corresponding to each temperature step are as follows:

$$\mathrm{Nu_h(t) = Nu_h(\infty)\{1 + 0.53e^{-0.20t^*}\}}\text{ with }\mathrm{R^2 = 0.97}\text{, for }\mathrm{TR = 1.5} \quad (6.5.39)$$

$$\mathrm{Nu_h(t) = Nu_h(\infty)\{1 + 0.64e^{-0.21t^*}\}}\text{ with }\mathrm{R^2 = 0.99}\text{, for }\mathrm{TR = 2.0} \quad (6.5.40)$$

$$\mathrm{Nu_h(t) = Nu_h(\infty)\{1 + 0.67e^{-0.22t^*}\}}\text{ with }\mathrm{R^2 = 0.98}\text{, for }\mathrm{TR = 2.5} \quad (6.5.41)$$

$$\mathrm{Nu_h(t) = Nu_h(\infty)\{1 + 0.77e^{-0.24t^*}\}}\text{ with }\mathrm{R^2 = 0.98}\text{, for }\mathrm{TR = 3.0} \quad (6.5.42)$$

$$\mathrm{Nu_h(t) = Nu_h(\infty)\{1 + 0.99e^{-0.26t^*}\}}\text{ with }\mathrm{R^2 = 0.96}\text{, for }\mathrm{TR = 3.0} \quad (6.5.43)$$

The generalized form of above equations is as follows:

$$\mathrm{Nu_h(t) = Nu_h(\infty)\{1 + C_5 e^{D_5 t^*}\}} \quad (6.5.44)$$

The values of C_5 and D_5 from Eqs. 6.5.39 to 6.5.43 are summarized in Table C-5.

Table C-5: The values of C_5 and D_5 in the correlation of $Nu_h(t)$ under TR

Temperature steps	TR	C_5	D_5
22^0C-33^0C	1.5	0.53	0.20
22^0C-44^0C	2.0	0.64	0.21
22^0C-55^0C	2.5	0.67	0.22
22^0C-66^0C	3.0	0.77	0.24
22^0C-77^0C	3.5	0.99	0.26

The relationships of TR with coefficient C_5 and exponent D_5 in the relationship of the ratio of $Nu_h(t)$ to $Nu_h(\infty)$ are illustrated in Figures C-7 and C-8 as follows;

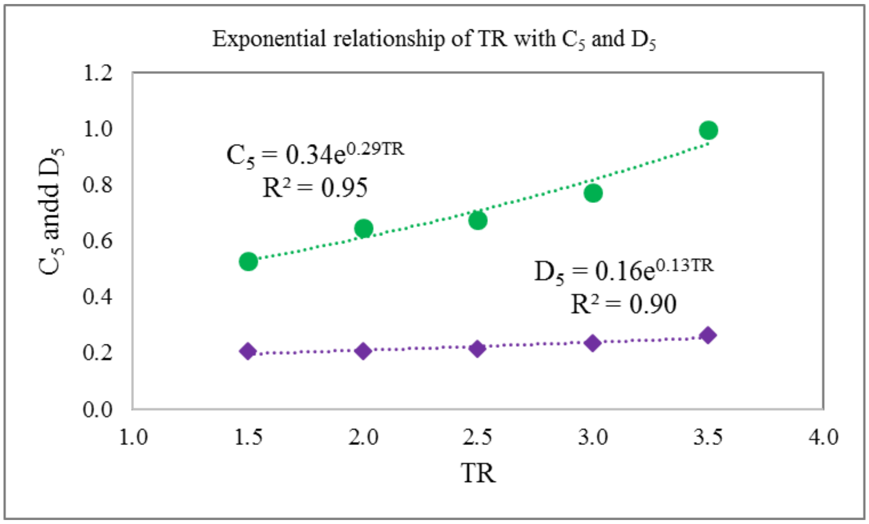

Figure C-7: Relationship of TR with C_5 and D_5 in the correlation of the ratio of $Nu_h(t)$ to $Nu_h(\infty)$

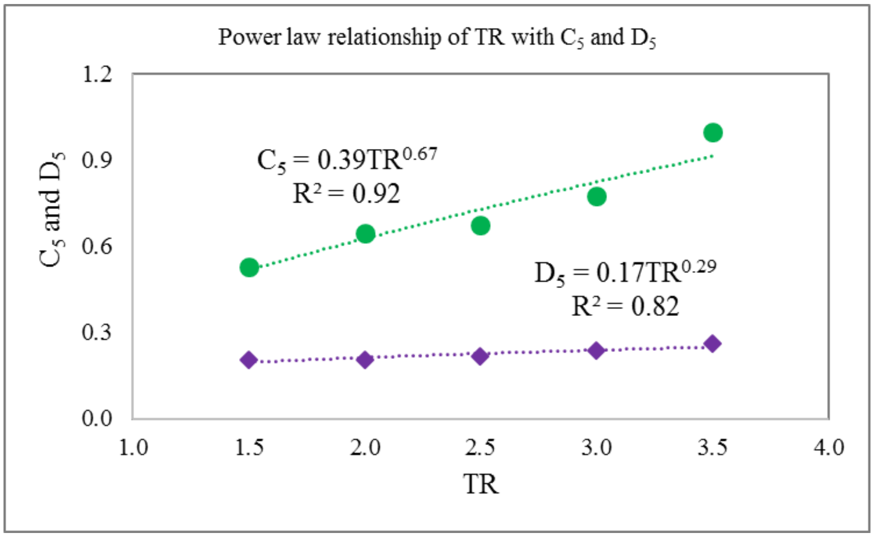

Figure C-8: Relationship of TR with C_5 and D_5 in the correlation of the ratio of $Nu_h(t)$ to $Nu_h(\infty)$

The coefficient C_5 and exponent D_5, both depend on TR. The relationship of TR with C_5 and D_5 are evaluated from the best curve fit with R^2-value of 0.95 for C_5 and 0.90 for D_5. Both the C_5 and the D_5 exponentially vary with TR as follows:

$$C_5 = 0.34TR^{0.29} \tag{6.5.45}$$

$$D_5 = 0.16TR^{0.13} \tag{6.5.46}$$

Appendix D: Derivation of the Governing Equations

Consider, the mass is flowing into and out of a physically infinitesimal volume element, dV through the sides dx, dy, and dz.

The mass density ρ at the centroid (x, y, z) of the volume element is assumed to be almost uniform throughout the volume element. The total mass contained within dV is

$$M = \int \rho dV = \int \rho dxdydz \qquad \text{(D1)}$$

There are no sources or sinks of mass within dV,

The mass flux (mass/unit area/unit time) through a surface is ρu, and the mass flow per unit time through dS is

$$\rho u \cdot dS = \rho u \cdot nds \qquad \text{(D2)}$$

where u, dS, n, and ds represent the fluid velocity, a side of the infinitesimal volume element, a unit vector normal (perpendicular) to the surface. and the surface area, respectively. n is assumed to point out of the volume element (i.e., from inside to outside).

The total mass flow rate out of the volume dV is

$$\sum \rho u \cdot dS = \oint \rho u \cdot dS = \oint \rho u \cdot nds \qquad \text{(D3)}$$

D1: Conservation of Mass or Continuity Equation:

Since the mass flow rate enters or leaves through the surface ds is equal to dM/dt, we have,

$$\frac{dM}{dt} = \frac{d}{dt}\int \rho dV = -\oint \rho u \cdot nds \qquad \text{(D4)}$$

For a fixed surface, the total time derivative inside the volume integral as a partial derivative:

$$\int \frac{\partial \rho}{\partial t} dV = -\oint \rho u \, . \, nds \tag{D5}$$

By Gauss' theorem,

$$\oint \rho u \cdot nds = \int \nabla \cdot (\rho u) dV \tag{D6}$$

Incorporating Equations (D5) and (D6),

$$\int \frac{\partial \rho}{\partial t} dV + \int \nabla \cdot (\rho u) dV = 0 \tag{D7}$$

$$\int \left(\frac{\partial \rho}{\partial t} + \nabla \cdot (\rho u) \right) dV = 0 \tag{D8}$$

The above Equation (D8) must hold for any control volume regardless of shape and size. It can only be satisfied if the integrand is equal to zero, i.e.,

$$\frac{\partial \rho}{\partial t} = -\nabla \cdot (\rho u) \tag{D9}$$

This is the conservation of mass or continuity equation.

D2: Momentum Equation:

Momentum per volume $= \rho u$ (D10)

Momentum in control volume $= \int \rho u dV$ (D11)

The rate of increase of momentum $= \frac{\partial}{\partial t} \int \rho u dV$ (D12)

Net influx of momentum: Consider a small rectangle outside the boundary. During time Δt it flows into the control volume. Momentum flow through the boundary ΔA during Δt is

$$(\rho u)U_x\Delta t\Delta A = -(\rho u)u \cdot n\Delta t\Delta A \tag{D13}$$

Net influx of momentum per unit time $= -\oint(\rho u)u \cdot nds$ (D14)

Total body force $= \int \rho fdV$ (D15)

Surface forces: The viscous surface force is the dot product of the normal, n with the stress tensor, T.

Total stress force $= \oint T \cdot nds$ (D16)

Rate of momentum increase = Net momentum influx + body force + surface force

$[D12 = D14 + D15 + D16]$

$$\frac{\partial}{\partial t}\int \rho udV = -\oint(\rho u)u \cdot nds + \int \rho fdV + \oint T \cdot nds \tag{D17}$$

Stress tensor, T can be defined as

$$T = (-p + \lambda\nabla \cdot u)I + 2\mu D \tag{D18}$$

For incompressible flow, $\nabla \cdot u = 0$

Therefore, Equation (D18) becomes,

$$T = -pI + 2\mu D \tag{D19}$$

The pressure surface force, p is the normal force on the control surface. The total pressure force $= \oint \mathrm{pnds}$.

$$\frac{\partial}{\partial \mathrm{t}}\int \rho \mathrm{udV} = -\oint(\rho \mathrm{u})\mathrm{u}\cdot \mathrm{nds} + \int \rho \mathrm{fdV} - \oint \mathrm{pnds} + \oint 2\mu \mathrm{D}\cdot \mathrm{nds}$$

where the components of deformation tensor, D are $\mathrm{D_y} = \frac{1}{2}\left(\frac{\partial \mathrm{u_i}}{\partial \mathrm{x_j}} + \frac{\partial \mathrm{u_j}}{\partial \mathrm{x_i}}\right)$

Recall Equation (D17),

$$\frac{\partial}{\partial \mathrm{t}}\int \rho \mathrm{udV} = \int \rho \mathrm{fdV} + \oint \mathrm{T}\cdot \mathrm{nds} - \oint(\rho \mathrm{u})\mathrm{u}\cdot \mathrm{nds}$$

$$= \int \rho \mathrm{fdV} + \oint(\mathrm{nT} - (\rho \mathrm{u})(\mathrm{u}\cdot \mathrm{n}))\mathrm{ds}$$

$$= \int \rho \mathrm{fdV} + \int \nabla\cdot(\mathrm{T} - \rho \mathrm{uu})\mathrm{dV}$$

Therefore, the differential form of the momentum equation is

$$\frac{\partial \rho \mathrm{u}}{\partial \mathrm{t}} = \rho \mathrm{f} + \nabla\cdot(\mathrm{T} - \rho \mathrm{uu})$$

$$\frac{\partial \rho \mathrm{u}}{\partial \mathrm{t}} + \nabla\cdot\rho \mathrm{uu} = \rho \mathrm{f} + \nabla\cdot \mathrm{T} \qquad \text{(D20)}$$

The advection part can be written as

$$\frac{\partial \rho \mathrm{u}}{\partial \mathrm{t}} + \nabla\cdot\rho \mathrm{uu} = \mathrm{u}\frac{\partial \rho}{\partial \mathrm{t}} + \mathrm{u}\nabla\cdot\rho \mathrm{u} + \rho\frac{\partial \mathrm{u}}{\partial \mathrm{t}} + \rho \mathrm{u}\cdot\nabla \mathrm{u}$$

$$\frac{\partial \rho \mathrm{u}}{\partial \mathrm{t}} + \nabla\cdot\rho \mathrm{uu} = \mathrm{u}\left(\frac{\partial \rho}{\partial \mathrm{t}} + \nabla\cdot\rho \mathrm{u}\right) + \rho\left(\frac{\partial \mathrm{u}}{\partial \mathrm{t}} + \mathrm{u}\cdot\nabla \mathrm{u}\right) \qquad \text{(D21)}$$

Since $\frac{\partial \rho}{\partial \mathrm{t}} + \nabla\cdot\rho \mathrm{u} = 0$, by Eq. (D9) of mass conservation, Eq. (D21) becomes,

$$\frac{\partial \rho u}{\partial t} + \nabla \cdot \rho uu = \rho\left(\frac{\partial u}{\partial t} + u \cdot \nabla u\right) = \rho\frac{Du}{Dt} \qquad \text{(D22)}$$

Since $\frac{\partial \rho u}{\partial t} + \nabla \cdot \rho uu = \rho f + \nabla \cdot T$, by Equation (D20)

Therefore, Equation (D22) becomes

$$\rho\frac{Du}{Dt} = \rho f + \nabla \cdot T \qquad \text{(D23)}$$

where, $\rho\frac{Du}{Dt} = \rho\left(\frac{\partial u}{\partial t} + u \cdot \nabla u\right)$

D3: Energy Equation

$$\frac{\partial}{\partial t}\int \rho\left(e + \frac{u^2}{2}\right) dV = \int u \cdot \rho f dV + \oint n \cdot \left(uT - \rho\left(e + \frac{u^2}{2}\right) - q\right) ds$$

It can be rewritten as

$$\frac{\partial \rho}{\partial t}\left(e + \frac{u^2}{2}\right) = \nabla \cdot \left(\rho\left(e + \frac{u^2}{2}\right) u - uT + q\right) \qquad \text{(D24)}$$

Similarly, the energy equation can be derived as a differential form. It is generally simplified by subtracting the mechanical energy.

The equation of mechanical energy can be obtained by taking the dot product of the velocity and the momentum equation as

$$u \cdot \left(\rho\left(\frac{\partial u}{\partial t} + u \cdot \nabla u\right)\right) = u \cdot (\rho f + \nabla \cdot T)$$

$$\rho\frac{\partial}{\partial t}\left(\frac{u^2}{2}\right) + \rho u \cdot \nabla\left(\frac{u^2}{2}\right) = \rho u \cdot f + u \cdot (\nabla \cdot T)$$

$$\rho\frac{\partial}{\partial t}\left(\frac{u^2}{2}\right) = -\rho u \cdot \nabla\left(\frac{u^2}{2}\right) + \rho u \cdot f + u \cdot (\nabla \cdot T) \qquad \text{(D25)}$$

Subtracting mechanical energy Equation (D25) from the energy Equation (D24),

$$\rho \frac{De}{\partial t} T \cdot \nabla u + \nabla \cdot q = 0 \tag{D26}$$

We know from the stress tensor and Fourie's law for the heat conduction

$T = (-p + \lambda \nabla \cdot u)I + 2\mu D$ and $q = -k\nabla T$

$$\therefore \rho \frac{De}{\partial t} + p\nabla \cdot u = \Phi + \nabla \cdot k\nabla T \tag{D26}$$

where the dissipation function Φ is the rate at which work is converted into heat.

$$\Phi = \lambda(\nabla \cdot u)^2 + 2\mu D \cdot D \tag{D27}$$

D4: Summary of Steady-state Governing Equations

Integral form of governing equations:

Continuity: $\frac{\partial}{\partial t} \int \rho \, dV = -\oint \rho u \, . \, nds$

Momentum: $\frac{\partial}{\partial t} \int \rho u dV = \int \rho f dV + \oint (nT - (\rho u)(u \cdot n))ds$

Energy: $\frac{\partial}{\partial t} \int \rho \left(e + \frac{u^2}{2}\right) dV = \int u \cdot \rho f dV + \oint n \cdot \left(uT - \rho \left(e + \frac{u^2}{2}\right) - q\right) ds$

Conservative form of governing equations:

Continuity: $\frac{\partial \rho}{\partial t} + \nabla . (\rho u) = 0$

Momentum: $\frac{\partial \rho u}{\partial t} = \rho f + \nabla \cdot (T - \rho u u)$

Energy: $\frac{\partial \rho}{\partial t}\left(e + \frac{u^2}{2}\right) = \nabla \cdot \left(\rho \left(e + \frac{u^2}{2}\right) u - uT + q\right)$

D5: Time-dependent Equations

The governing equations need to be discretized in both space and time for transient simulations. For the time-dependent equations, the spatial discretization is similar to the steady-state situation.

Time-based discretization includes the integration of every single term in the differential equations over a time step, Δt. A general expression for the time advancement of a variable Φ is given by

$$\frac{\partial \Phi}{\partial t} = F(\Phi)$$

where Φ denotes a scalar quantity and the function F includes any spatial discretization. Using backward differences, the first-order accurate discretization of the time derivative is given by

$$\frac{\Phi^{n+1} - \Phi^{n}}{\Delta t} = F(\Phi)$$

and the second-order temporal discretization is given by

$$\frac{3\Phi^{n+1} - 4\Phi^{n} + \Phi^{n-1}}{2\Delta t} = F(\Phi)$$

where,

$n =$ value at the current time level, t

$n + 1 =$ value at the next time level, $t + \Delta t$

$n - 1 =$ value at the previous time level, $t - \Delta t$

The implicit discretized form of the general transport equation used for the pressure based solver in ANSYS FLUENT [324] is

$$\int_V \frac{\partial \rho \Phi}{\partial t} dV + \oint \rho \Phi \vec{v} \cdot d\vec{A} = \oint \Gamma_\Phi \nabla \Phi \cdot d\vec{A} + \int_V S_\Phi \, dV$$

where,

$\frac{\partial \rho \Phi}{\partial t}$ is the conservative form of transient derivative of transported variable

ρ = density of working fluid

$\vec{v}$ = velocity vector $\left(u\hat{i} + v\hat{j} + w\hat{k} \text{ in 3D}\right)$

$\vec{A}$ = surface area vector

Γ_Φ = diffusion coefficient for Φ

$\nabla\Phi$ = gradient of φ $\left(= (\partial\varphi/\partial x)\hat{i} + (\partial\varphi/\partial y)\hat{j} + (\partial\varphi/\partial z)\hat{k} \text{ in 3D}\right)$

S_Φ = source of per unit volume

All convective, diffusive, and source terms are computed from the fields for time level $n + 1$ as

$$\int_V \frac{\partial \rho \Phi}{\partial t} dV + \oint \rho^{n+1} \Phi^{n+1} \vec{v}^{n+1} \cdot d\vec{A} = \oint {\Gamma_\Phi}^{n+1} \nabla \Phi^{n+1} \cdot d\vec{A} + \int_V {S_\Phi}^{n+1} \, dV$$

Appendix E: Residuals of Different Variables

E 1: Plots of Iterations vs Residuals for Different Turbulence Models

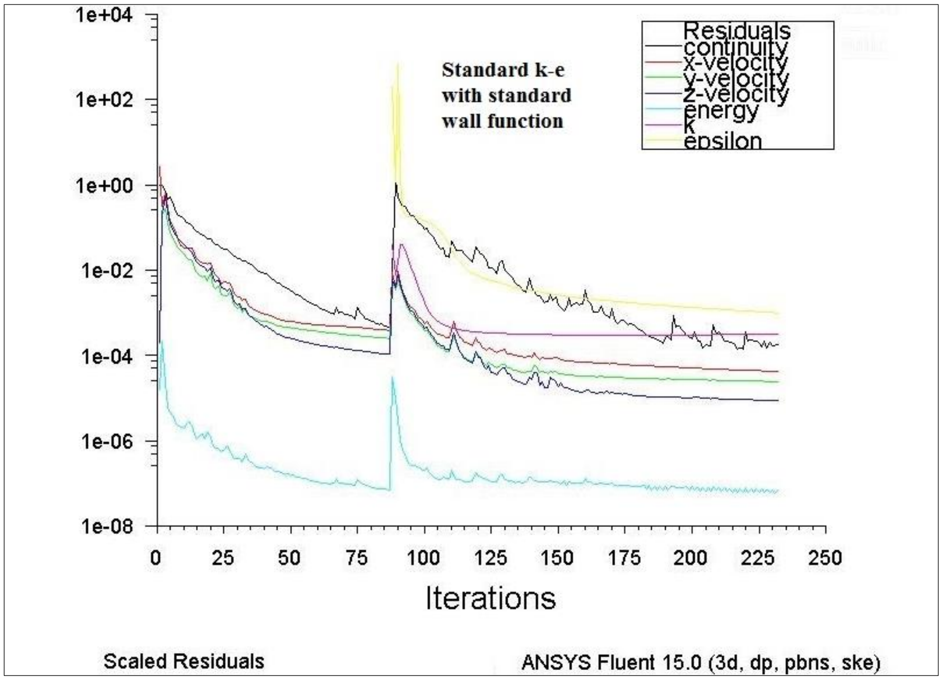

Figure E - 1: Iterative residuals for Standard k-ε turbulence model with standard wall function

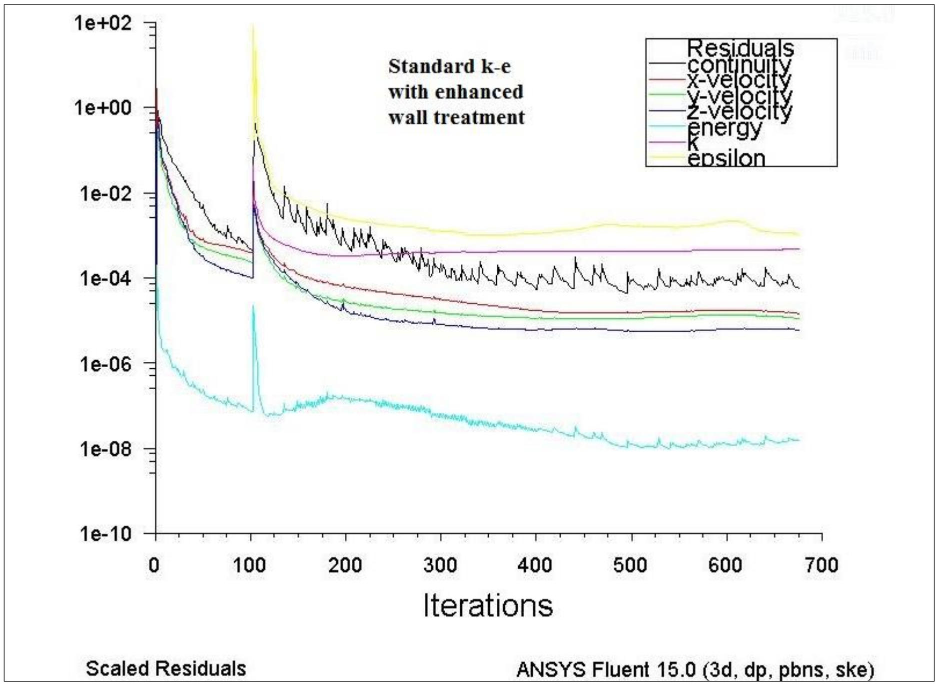

Figure E - 2: Iterative residuals for standard k-ε turbulence model with enhanced wall treatment

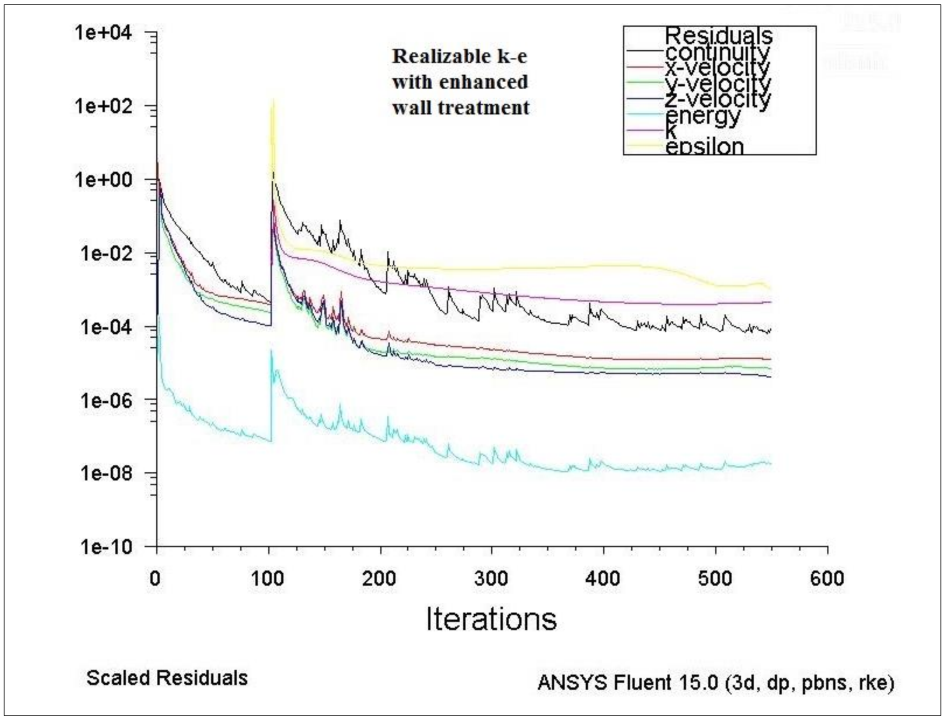

Figure E - 3: Iterative residuals for realizable k-ε turbulence model with enhanced wall treatment

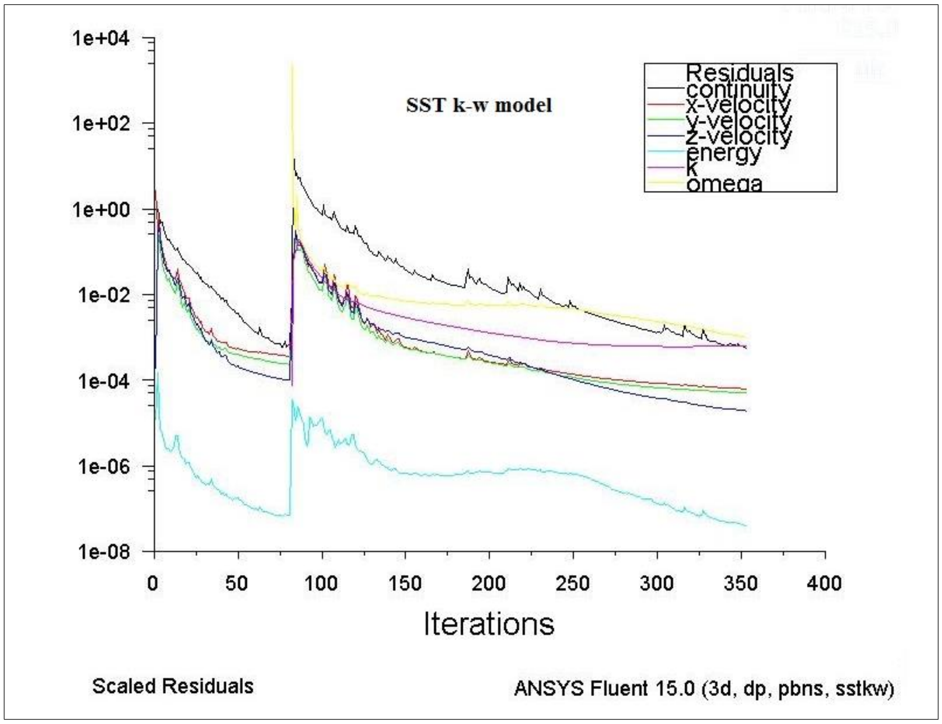

Figure E - 4: Iterative residuals for the shear stress transport (SST) k-ω turbulence model

E 2: Sample Residuals of Different Variables

```
 iter  continuity  x-velocity  y-velocity  z-velocity     energy          k     epsilon     time/iter
  701  4.57e-05    1.30e-05    1.12e-05    5.95e-06    3.01e-08   4.75e-04   8.85e-04   1:31:52   299
  702  4.57e-05    1.30e-05    1.12e-05    5.95e-06    2.97e-08   4.75e-04   8.85e-04   1:30:55   298
  703  4.57e-05    1.30e-05    1.12e-05    5.95e-06    2.93e-08   4.75e-04   8.85e-04   1:29:58   297
  704  4.57e-05    1.30e-05    1.12e-05    5.95e-06    2.89e-08   4.75e-04   8.85e-04   1:29:01   296
  705  4.57e-05    1.30e-05    1.12e-05    5.94e-06    2.85e-08   4.75e-04   8.84e-04   1:28:04   295
  706  4.57e-05    1.30e-05    1.11e-05    5.94e-06    2.81e-08   4.75e-04   8.84e-04   1:27:07   294
  707  4.57e-05    1.30e-05    1.11e-05    5.94e-06    2.77e-08   4.74e-04   8.84e-04   1:26:10   293
  708  4.57e-05    1.30e-05    1.11e-05    5.94e-06    2.73e-08   4.74e-04   8.84e-04   1:25:13   292
  709  4.57e-05    1.29e-05    1.11e-05    5.94e-06    2.69e-08   4.74e-04   8.84e-04   1:24:16   291
  710  4.57e-05    1.29e-05    1.11e-05    5.94e-06    2.65e-08   4.74e-04   8.84e-04   1:23:19   290
 iter  continuity  x-velocity  y-velocity  z-velocity     energy          k     epsilon     time/iter
  711  4.57e-05    1.29e-05    1.11e-05    5.94e-06    2.61e-08   4.74e-04   8.84e-04   1:22:22   289
  712  4.56e-05    1.29e-05    1.11e-05    5.94e-06    2.56e-08   4.74e-04   8.84e-04   1:21:25   288
  713  4.56e-05    1.29e-05    1.11e-05    5.94e-06    2.52e-08   4.74e-04   8.84e-04   1:20:28   287
  714  4.56e-05    1.29e-05    1.11e-05    5.94e-06    2.48e-08   4.74e-04   8.84e-04   1:19:31   286
  715  4.56e-05    1.29e-05    1.11e-05    5.94e-06    2.44e-08   4.73e-04   8.83e-04   1:18:34   285
  716  4.56e-05    1.29e-05    1.11e-05    5.94e-06    2.40e-08   4.73e-04   8.83e-04   1:17:37   284
  717  4.56e-05    1.29e-05    1.11e-05    5.94e-06    2.36e-08   4.73e-04   8.83e-04   1:16:40   283
  718  4.56e-05    1.28e-05    1.11e-05    5.94e-06    2.32e-08   4.73e-04   8.83e-04   1:15:43   282
  719  4.56e-05    1.28e-05    1.11e-05    5.94e-06    2.28e-08   4.73e-04   8.83e-04   1:14:46   281
  720  4.56e-05    1.28e-05    1.11e-05    5.94e-06    2.24e-08   4.73e-04   8.83e-04   1:13:49   280
 iter  continuity  x-velocity  y-velocity  z-velocity     energy          k     epsilon     time/iter
  721  4.56e-05    1.28e-05    1.11e-05    5.94e-06    2.20e-08   4.73e-04   8.83e-04   1:12:52   279
  722  4.56e-05    1.28e-05    1.10e-05    5.93e-06    2.16e-08   4.73e-04   8.83e-04   1:11:55   278
  723  4.56e-05    1.28e-05    1.10e-05    5.93e-06    2.12e-08   4.72e-04   8.83e-04   1:10:58   277
  724  4.56e-05    1.28e-05    1.10e-05    5.93e-06    2.08e-08   4.72e-04   8.82e-04   1:10:01   276
  725  4.56e-05    1.28e-05    1.10e-05    5.93e-06    2.04e-08   4.72e-04   8.82e-04   1:09:04   275
  726  4.56e-05    1.28e-05    1.10e-05    5.93e-06    2.00e-08   4.72e-04   8.82e-04   1:08:07   274
  727  4.56e-05    1.27e-05    1.10e-05    5.93e-06    1.96e-08   4.72e-04   8.82e-04   1:07:10   273
  728  4.56e-05    1.27e-05    1.10e-05    5.93e-06    1.92e-08   4.72e-04   8.82e-04   1:06:13   272
  729  4.56e-05    1.27e-05    1.10e-05    5.93e-06    1.88e-08   4.72e-04   8.82e-04   1:05:16   271
  730  4.56e-05    1.27e-05    1.10e-05    5.93e-06    1.84e-08   4.72e-04   8.82e-04   1:04:19   270
 iter  continuity  x-velocity  y-velocity  z-velocity     energy          k     epsilon     time/iter
  731  4.56e-05    1.27e-05    1.10e-05    5.93e-06    1.80e-08   4.71e-04   8.82e-04   1:03:22   269
  732  4.56e-05    1.27e-05    1.10e-05    5.93e-06    1.75e-08   4.71e-04   8.82e-04   1:02:25   268
  733  4.56e-05    1.27e-05    1.10e-05    5.93e-06    1.71e-08   4.71e-04   8.81e-04   1:01:28   267
  734  4.56e-05    1.27e-05    1.10e-05    5.93e-06    1.67e-08   4.71e-04   8.81e-04   1:00:31   266
  735  4.56e-05    1.27e-05    1.10e-05    5.93e-06    1.63e-08   4.71e-04   8.81e-04   0:59:34   265
  736  4.55e-05    1.26e-05    1.10e-05    5.93e-06    1.59e-08   4.71e-04   8.81e-04   0:58:37   264
```

```
 737   4.55e-05   1.26e-05   1.10e-05   5.93e-06   1.55e-08   4.71e-04   8.81e-04   0:57:40   263
 738   4.56e-05   1.26e-05   1.10e-05   5.92e-06   1.51e-08   4.70e-04   8.81e-04   0:56:43   262
 739   4.55e-05   1.26e-05   1.09e-05   5.92e-06   1.47e-08   4.70e-04   8.81e-04   0:55:46   261
 740   4.55e-05   1.26e-05   1.09e-05   5.92e-06   1.43e-08   4.70e-04   8.81e-04   0:54:49   260
 iter  continuity  x-velocity  y-velocity  z-velocity     energy          k     epsilon      time/iter
 741   4.55e-05   1.26e-05   1.09e-05   5.92e-06   1.39e-08   4.70e-04   8.81e-04   0:53:52   259
 742   4.55e-05   1.26e-05   1.09e-05   5.92e-06   1.35e-08   4.70e-04   8.80e-04   0:52:55   258
 743   4.56e-05   1.26e-05   1.09e-05   5.92e-06   1.31e-08   4.70e-04   8.80e-04   0:51:58   257
 744   4.55e-05   1.26e-05   1.09e-05   5.92e-06   1.27e-08   4.70e-04   8.80e-04   0:51:01   256
 745   4.55e-05   1.25e-05   1.09e-05   5.92e-06   1.23e-08   4.70e-04   8.80e-04   0:50:04   255
 746   4.55e-05   1.25e-05   1.09e-05   5.92e-06   1.19e-08   4.69e-04   8.80e-04   0:49:07   254
 747   4.55e-05   1.25e-05   1.09e-05   5.92e-06   1.15e-08   4.69e-04   8.80e-04   0:48:10   253
 748   4.55e-05   1.25e-05   1.09e-05   5.92e-06   1.11e-08   4.69e-04   8.80e-04   0:47:13   252
 749   4.55e-05   1.25e-05   1.10e-05   5.92e-06   1.07e-08   4.69e-04   8.80e-04   0:46:16   251
 750   4.55e-05   1.25e-05   1.09e-05   5.92e-06   1.03e-08   4.69e-04   8.80e-04   0:45:19   250
 iter  continuity  x-velocity  y-velocity  z-velocity     energy          k     epsilon      time/iter
 751   4.55e-05   1.25e-05   1.09e-05   5.92e-06   9.85e-09   4.69e-04   8.79e-04   0:44:22   249
 752   4.56e-05   1.25e-05   1.09e-05   5.92e-06   9.45e-09   4.69e-04   8.79e-04   0:43:25   248
 753   4.55e-05   1.25e-05   1.09e-05   5.92e-06   9.04e-09   4.69e-04   8.79e-04   0:42:28   247
 754   4.55e-05   1.25e-05   1.09e-05   5.92e-06   8.64e-09   4.68e-04   8.79e-04   0:41:31   246
 755   4.55e-05   1.24e-05   1.09e-05   5.92e-06   8.23e-09   4.68e-04   8.79e-04   0:40:34   245
 756   4.55e-05   1.24e-05   1.10e-05   5.91e-06   7.83e-09   4.69e-04   8.79e-04   0:39:37   244
 757   4.55e-05   1.24e-05   1.08e-05   5.91e-06   7.42e-09   4.68e-04   8.80e-04   0:38:40   243
 758   4.55e-05   1.24e-05   1.08e-05   5.91e-06   7.02e-09   4.68e-04   8.79e-04   0:37:43   242
 759   4.55e-05   1.24e-05   1.08e-05   5.92e-06   6.61e-09   4.68e-04   8.79e-04   0:36:46   241
 760   4.54e-05   1.24e-05   1.08e-05   5.91e-06   6.21e-09   4.69e-04   8.78e-04   0:35:49   240
 iter  continuity  x-velocity  y-velocity  z-velocity     energy          k     epsilon      time/iter
 761   4.54e-05   1.25e-05   1.09e-05   5.91e-06   5.80e-09   4.67e-04   8.78e-04   0:34:52   239
 762   4.56e-05   1.24e-05   1.08e-05   5.91e-06   5.40e-09   4.67e-04   8.78e-04   0:33:55   238
 763   4.54e-05   1.24e-05   1.10e-05   5.92e-06   4.99e-09   4.67e-04   8.78e-04   0:32:58   237
 764   4.55e-05   1.23e-05   1.08e-05   5.91e-06   4.59e-09   4.69e-04   8.80e-04   0:32:01   236
 765   4.54e-05   1.23e-05   1.10e-05   5.91e-06   4.18e-09   4.68e-04   8.79e-04   0:31:04   235
 766   4.56e-05   1.24e-05   1.08e-05   5.91e-06   3.78e-09   4.67e-04   8.78e-04   0:30:07   234
 767   4.54e-05   1.23e-05   1.08e-05   5.91e-06   3.37e-09   4.67e-04   8.78e-04   0:29:10   233
 768   4.55e-05   1.23e-05   1.10e-05   5.91e-06   2.97e-09   4.67e-04   8.80e-04   0:28:13   232
 769   4.54e-05   1.25e-05   1.09e-05   5.92e-06   2.56e-09   4.69e-04   8.77e-04   0:27:16   231
 770   4.54e-05   1.24e-05   1.08e-05   5.91e-06   2.16e-09   4.68e-04   8.80e-04   0:26:19   230
 iter  continuity  x-velocity  y-velocity  z-velocity     energy          k     epsilon      time/iter
 771   4.55e-05   1.23e-05   1.08e-05   5.91e-06   1.75e-09   4.67e-04   8.79e-04   0:25:22   229
 772   4.54e-05   1.23e-05   1.07e-05   5.90e-06   1.35e-09   4.66e-04   8.78e-04   0:24:25   228
 773   4.54e-05   1.22e-05   1.07e-05   5.90e-06   9.40e-10   4.66e-04   8.77e-04   0:23:28   227
```

VITA AUCTORIS

NAME: Mohammed Ismail

PLACE OF BIRTH: Khadghor, Comilla, Bangladesh

YEAR OF BIRTH: 1968

EDUCATION:

1977 Completed Elementary School (Grade Five) from Kutumbapur Govt. Primary School, Comilla, Bangladesh

1983 Completed Secondary School Certificate (SSC) in Science from Gumta Ishaquia High School, Comilla, Bangladesh

1985 Completed Higher Secondary School Certificate (HSC) in Science from Comilla Victoria Govt. College, Comilla, Bangladesh

1993 Received Bachelor of Science (BSc) degree in Mechanical Engineering from Bangladesh University of Engineering & Technology (BUET), Dhaka, Bangladesh

2010 Received Master of Engineering (MEng) degree in Mechanical Engineering from University of Windsor, Windsor, Ontario, Canada

2012 Received Master of Applied Science (MASc) degree in Mechanical Engineering from University of Windsor, Windsor, Ontario, Canada

EXPERIENCE

1094-2006 Served as Mechanical Engineer and Senior Mechanical Engineer in Bangladesh

2009-2010 Served as Product Engineer at EDAT Solutions Inc. Ontario, Canada

2018 Served as Test Engineer, Innovation & Research Centre, Carrier Corporation, UTC CCS, NY, USA.

CURRENT

2019 PhD in Mechanical Engineering, University of Windsor, Ontario, Canada.